THE CHARACTERIZATION OF SEISMIC EARTH STRUCTURES AND NUMERICAL MANTLE CONVECTION EXPERIMENTS USING TWO-POINT CORRELATION FUNCTIONS

by

PETER PUSTER

Vordiplom in Geophysik, Universität Fridericiana, Karlsruhe, 1986

Submitted to the Department of
Earth, Atmospheric, and Planetary Sciences
in partial fulfillment of the requirements for the degree of

DOCTOR OF PHILOSOPHY

at the

MASSACHUSETTS INSTITUTE OF TECHNOLOGY

February 1995

Signature of Author____
Department of Earth, Atmospheric, and Planetary Sciences
November, 1994

Certified by____
Thomas H. Jordan
Thesis Supervisor

Certified by____
Bradford H. Hager
Thesis Co-Supervisor

Accepted by____
Thomas H. Jordan
Department Head

To my parents, Christel and Wolf Puster.

THE CHARACTERIZATION OF SEISMIC EARTH STRUCTURES AND NUMERICAL MANTLE CONVECTION EXPERIMENTS USING TWO-POINT CORRELATION FUNCTIONS

PETER PUSTER

Submitted to the Department of Earth, Atmospheric, and Planetary Sciences in partial fulfillment of the requirements for the degree of Doctor of Philosophy

ABSTRACT

We consider a time-dependent random field, $f(r,\Omega,t)$, defined on a spherical shell $[\Omega=(\theta,\varphi),\ 0\leq\theta\leq\pi,\ -\pi<\varphi\leq\pi]$ or cylindrical annulus $[\Omega=\varphi,\ -\pi<\varphi\leq\pi]$. Examples are the temperature distribution, $T(r,\Omega,t)$, or the radial component of the flow velocity, $u(r,\Omega,t)$, obtained from numerical simulations of high Rayleigh number convection. For such a field the spatio-temporal two-point correlation function, $C_{ff}(r,r',\Delta,t^*)$, is constructed by averaging over rotational transformations of this ensemble. To assess the structural differences among mantle convection experiments we construct three spatial subfunctions of $C_{ff}(r,r',\Delta,t^*)$: the rms variation, $\sigma_f(r) = \sqrt{C_{ff}(r,r,0,0)}$, the radial correlation function, $R_f(r,r') = C_{ff}(r,r',0,0)\,/\,\sigma_f(r)\sigma_f(r')$, and the angular correlation function, $A_f(r,\Delta) = C_{ff}(r,r,\Delta,0)\,/\,\sigma_f^2(r)$. The integral transform of $A_f(r,\Delta)$ is the angular power spectrum. $R_f(r,r')$ and $A_f(r,\Delta)$ are symmetric about the loci $r=r'$ and $\Delta=0$, respectively, where they achieve their maximum value of unity. The fall-off of R_f and A_f away from their symmetry axes can be quantified by a correlation length $\rho_f(r)$ and a correlation angle $\alpha_f(r)$, which we define to be the halfwidths of the central peaks at the correlation level 0.75. The behavior of ρ_f is a diagnostic of radial structure, while α_f measures average plume width.

We use two-point correlation functions of the temperature field (T-diagnostics) and flow velocity fields (V-diagnostics) to quantify some important aspects of mantle convection experiments. We explore the dependence of different correlation diagnostics on Rayleigh number, internal heating rate, radial viscosity variations, temperature-dependent rheology, phase changes, and plates. For isoviscous flows in an annulus, we show how radial averages of σ_T, ρ_T, and α_T scale with Rayleigh number for various internal heating rates. A rapid 10-fold to 30-fold viscosity increase with depth yields weakly stratified flows, quantified by σ_u, which is a measure of radial flux. The horizontal flux diagnostic σ_w reveals that the flow organization is sensitive to the depth of the viscosity increase. We illustrate that T-diagnostics, which are more easily relatable to geophysical observables, can serve as proxies for the V-diagnostics. A viscosity increase with depth is evident as an increase in the T-diagnostics in the high-viscosity region. For numerical experiments with a temperature-dependent rheology we employ a mobilization scheme for the upper boundary layer. Temperature dependence does not appreciably perturb the σ-diagnostics or α_T in the convecting interior. Changes in the radial correlation length are two-fold. First, the greater viscosity of cold downwellings leads to an increase in height and width of the radial correlation maximum near the top. Second, the increase in ρ_T associated with a viscosity jump is markedly reduced. An endothermic phase transition manifests itself in the correlation diagnostics as a local minimum in σ_u and ρ_T and local maxima in σ_T and α_T around the phase transition depth. Temperature-dependent rheology reduces the amount of layering, however, the phase-change induced layering is still apparent in the two-point correlation diagnostics. When the phase change coincides with a rapid viscosity increase the effects of the latter dominate. We investigate the influence of surface plates on the organization of mantle flow. Plates whose geometries evolve with time are modeled by using a temperature-dependent viscosity combined with weak zones (small regions of low viscosity) advected by the flow. The two-point correlation diagnostics obtained from these flows are similar to the temperature-dependent runs with a mobilized upper boundary layer. Differences include an increase in σ_w and α_T near the surface, and a shift of the maximum in σ_u to shallower depths. The main influence of plates is to organize the large-scale flow structure. This is best documented in the angular power spectrum, which has more power concentrated at low wavenumbers. We also quantify some statistics of the plate system, such as plate-size and relative plate-velocity distributions. Average plate velocities decrease nearly monotonically with increasing plate size for cases without a viscosity stratification. Viscously stratified systems exhibit a more uniform average plate-velocity distribution. Comparing plate system statistics from numerical convection calculations to the plate tectonic record for the past 120 Ma favors models with a 30-fold viscosity increase in the lower mantle over those with a viscosity that is constant with depth.

We calculate the two-point moment functions for global and regional models of seismic shear velocity heterogeneity, $\delta\beta(r,\Omega)$. The radial correlation function is least sensitive to the low-pass filtering required when comparing convection experiments to low-resolution seismic images, making it the most useful tool for comparisons between the two. As long as thermal anomalies are predominantly responsible for seismic velocity heterogeneity, a direct comparison between ρ_T and ρ_β is meaningful. We find significant differences between the tomographic models, which frustrate a detailed interpretation of individual features of ρ_β. The overall morphology of the ρ_β-profiles, however, whereas consistent with ρ_T curves for convection models with a 30-fold to 100-fold viscosity increase at 670 km depth, rules out convection models with a viscosity that is constant with depth. We define stratification indices for the radial correlation length, $S(\rho)$, and average radial flux, $S(|u|)$, at 670 km depth. Using stratification values for the seismic models ($S(\rho_\beta) \leq 0.12$), we infer $S(|u|) \leq 0.1$, indicating that the present-day style of convection is dominantly whole-mantle. Together with $A(|\tilde{u}|_S)$, a measure of the asymmetry of the radial flux distribution at 670 km depth, $S(|u|)$ furthermore suggests that it is unlikely for the earth to be in an intermittently layered regime.

Thesis committee:

Dr. Thomas H. Jordan, Professor of Geophysics (thesis supervisor)
Dr. Bradford H. Hager, Professor of Geophysics (thesis co-supervisor)
Dr. Daniel H. Rothman, Professor of Geophysics
Dr. John Grotzinger, Professor of Geology
Dr. Richard J. O'Connell, Professor of Geophysics, Harvard University

Table of contents

Chapter 2 Two-point correlation functions

Chapter 3 Convection models

Chapter 4 Tomographic earth structures

Appendix A Field equations of mantle convection

CHAPTER 1

INTRODUCTION

One goal of structural seismology is to map the aspherical variations in the seismic wave speeds in sufficient detail to resolve diagnostic properties of the mantle convection. The most fundamental issue, posed forty-three years ago by Birch [1951], is the degree to which the large-scale flow is stratified by changes in mineralogical phase and/or bulk chemistry across the mid-mantle transition zone from depths of 400 to 700 km. The first data on seismic heterogeneity directly addressing this issue became available in the mid-1970's through early attempts to detect the penetration of cold, subducted lithosphere into the lower mantle beneath zones of plate convergence [Jordan and Lynn, 1974; Jordan, 1977]. Recent tomographic studies of subduction zones in the western Pacific [van der Hilst et al., 1991; Fukao et al., 1992] and beneath the Americas [Grand, 1987; Grand, 1994] have confirmed the existence of high-velocity anomalies, presumably slab-related, extending below the 660-km seismic discontinuity in several subduction regions. In other locations, however, tomographic images seem to reveal near-horizontal high-velocity anomalies above 660 km, interpreted as slabs deflected sideways by the interface [van der Hilst et al., 1991; Fukao et al., 1992]. Because of these apparent complexities in the seismic data pertaining to the deep structure of subduction zones, no consensus has yet developed regarding the extent to which the 660-km discontinuity forms a barrier to mantle flow [Olson et al., 1990].

The most plausible mineralogical explanation for the jump in elastic parameters at the 660-km discontinuity is the endothermic dissociation of spinel-structured $(Mg,Fe)_2SiO_4$ (γ-olivine) into $(Mg,Fe)O$ (magnesiowüstite) plus perovskite-structured $(Mg,Fe)SiO_3$. Laboratory measurements of the Clapeyron slope, γ, for the spinel - post-spinel transition yield values of –2.8 MPa/K [*Ito and Takahashi*, 1989] and –3±1 MPa/K [*Akaogi and Ito*, 1993]. Convection calculations incorporating phase-change dynamics with two-dimensional [*Christensen and Yuen*, 1985; *Machetel and Weber*, 1991; *Peltier and Solheim*, 1992; *Zhao et al.*, 1992] and three-dimensional [*Honda et al.*, 1993; *Tackley et al.*, 1993; *Tackley et al.*, 1994] flow geometries indicate that an endothermic transition of this magnitude acts to inhibit convection through the phase boundary.

The 660-km discontinuity could also mark a compositional boundary between the upper and lower mantle [*Richter and Johnson*, 1974], at least in some average sense [*Jeanloz*, 1991]. The strongest evidence favoring a chemical difference is a discrepancy between the lower-mantle density profile predicted for an upper-mantle (pyrolitic) composition and the seismically determined density profile. According to some studies [*Jeanloz and Knittle*, 1989; *Stixrude et al.*, 1992], the former is 3-7% lower than the latter, implying an increase in either the iron/magnesium ratio or the silica content of the lower mantle, or both (see, however, *Chopelas and Boehler* [1992]). Numerical simulations suggest that a density difference near the upper end of this range would imply layered convection with deformation of the chemical boundary but very little mass exchange [*Christensen and Yuen*, 1984], while a density contrast near the lower end might be maintained by some form of penetrative convection [*Christensen and Yuen*, 1984; *Silver et al.*, 1988]. The seismic mapping of subduction zones has been sufficiently ambiguous that compositionally stratified models—even the end-member hypothesis of layered convection—remain in contention.

Another mechanism for impeding vertical flow is an increase of viscosity with depth. Most radial viscosity structures obtained from modeling the earth's non-hydrostatic geoid [*Hager et al.*, 1985; *Hager and Richards*, 1989; *Ricard and Wuming*, 1991; *King and Masters*, 1992; *Forte et al.*, 1993] exhibit a rapid viscosity increase from the upper to the lower mantle.

Seismic observations have been a principal tool for probing the earth's deep interior and addressing questions regarding the organization of convection currents in the mantle. Global maps of mantle shear-wave velocity heterogeneity, $\delta\beta$, [e.g., *Tanimoto*, 1990; *Masters et al.*, 1992; *Su et al.*, 1992] provide snapshots of mantle dynamics, assuming that $\delta\beta$ is proportional to convectively induced temperature anomalies δT. (This assumption should be a good working hypothesis in the mantle's interior away from the chemical boundary layers at the free surface and core-mantle boundary.) Numerical convection experiments, on the other hand, give insight into the dynamics of the mantle flow system. Because our understanding of mantle convection is still crude, numerical simulations cannot reproduce the exact geographical details, but only the grosser aspects of the flow pattern. Therefore, quantification schemes that measure the effect of different parameters on convective flow organization and structure are necessary. Examples of flow diagnostics are the angular power spectrum [e.g. *Jarvis and Peltier*, 1986; *Tanimoto*, 1990] and the root-mean-square (rms) variation on horizontal surfaces [*Honda*, 1987]. Recently, *Jordan et al.* [1993] and *Puster and Jordan* [1994] have introduced two-point correlation diagnostics, the radial and angular correlation functions, that are invariant with respect to the temperature coefficient of shear-wave speed, $(\partial\beta / \partial T)_P$, and thus well-suited for comparison to seismic observations.

In chapter 2 we introduce the complete spatio-temporal two-point correlation functions of the temperature and flow velocity fields as tools for studying high-Rayleigh number fluid flow and illustrate the concepts with an example calculation of infinite Prandtl number thermal convection in a cylindrical annulus. We also investigate the influence of geometry on the flow by quantifying the second-order statistics of 2D and 3D convection calculations.

Chapter 3 applies this formalism to characterize the second-order statistics of mantle convection experiments encompassing a large number of different effects. In particular, we quantify the effects of Rayleigh number and internal heating rate and present scaling relations for different correlation diagnostics. We also investigate the influence of both depth-dependent and depth- and temperature-dependent viscosities on flow structure and correlation functions. A lot of recent attention has been paid to mantle flow models incorporating the effects of phase changes. We show that two-point correlation functions are sensitive indicators of the degree of flow stratification due to an endothermic phase boundary. The influence of surface plates on the mantle flow is another important effect.

We present flow models of rigid surface plates, whose geometries evolve with time and characterize the second-order properties of the resulting flow fields.

In chapter 4 we quantify the second-order properties of several recent global and regional seismic earth models. As global tomographic models can only constrain the large-scale pattern of mantle flow it is important to investigate the effects of filtering on two-point correlation diagnostics. We also address the issues of model resolution and model parameterization. Using two-point correlation functions also allows us to quantitatively compare the different seismic structures.

Chapter 5 gives a brief summary of the main results of chapters 3 and 4 and discusses some implications about the importance of various effects on the style of mantle convection.

REFERENCES

Akaogi, M., and E. Ito, Refinement of enthalpy measurement of MgSiO3 perovskite and negative pressure-temperature slopes for perovskite-forming reactions, *Geophys. Res. Lett.*, *20*, 1839-1842, 1993.

Birch, F., Remarks on the structure of the mantle, and its bearing upon the possibility of convection currents, Trans. Am. Geophys. Union, 32, 533-534, 1951.

Chopelas, A., and R. Boehler, Thermal expansivity in the lower mantle, *Geophys. Res. Lett.*, *19*, 1347-1350, 1992.

Christensen, U. R., and D. A. Yuen, The interaction of a subducting lithospheric slab with a chemical or phase boundary, *J. Geophys. Res.*, *89*, 4389-4402, 1984.

Christensen, U. R., and D. A. Yuen, Layered convection induced by phase transitions, *J. Geophys. Res.*, *90*, 10, 1985.

Forte, A. M., A. M. Dziewonski, and R. L. Woodward, Aspherical structure of the mantle, tectonic plate motions, nonhydrostatic geoid, and topography of the core-mantle boundary, in *Dynamics of Earth's deep interior and Earth rotation*, edited by J. L. LeMouel, D. E. Smylie, and T. Herring, *Geophysical Monograph*, *72*, pp. 135-166, 1993.

Fukao, Y., M. Obayashi, H. Inoue, and M. Nenbai, Subducted slabs stagnant in the mantle transition zone, *J. Geophys. Res.*, *97*, 4809-4822, 1992.

Grand, S. P., Tomographic inversions for shear structure beneath the North American plate, *J. Geophys. Res.*, *92*, 14065-14090, 1987.

Grand, S. P., Mantle shear structure beneath the Americas and surrounding oceans, *J. Geophys. Res.*, *99*, 11591-11621, 1994.

Hager, B. H., R. W. Clayton, M. A. Richards, R. P. Comer, and A. M. Dziewonski, Lower mantle heterogeneity, dynamic topography and the geoid, *Nature*, *313*, 541-545, 1985.

Hager, B. H., and M. A. Richards, Long-wavelength variations in Earth's geoid; physical models and dynamical implications, *Philos. Trans. R. Soc. London, Ser. A*, *328*, 309-327, 1989.

Honda, S., The RMS residual temperature in the convecting mantle and seismic heterogeneities, *J. Phys. Earth*, *35*, 195-207, 1987.

Honda, S., D. A. Yuen, S. Balachandar, and D. Reuteler, Three-dimensional instabilities of mantle convection with multiple phase transitions, *Science*, *259*, 1308-1311, 1993.

Ito, E., and E. Takahashi, Postspinel transformations in the system Mg2SiO4-Fe2SiO4 and some geophysical implications, *J. Geophys. Res.*, *94*, 10637-10646, 1989.

Jarvis, G. T., and W. R. Peltier, Lateral heterogeneity in the convecting mantle, *J. Geophys. Res.*, *91*, 435-451, 1986.

Jeanloz, R., Effects of phase transitions and possible compositional changes on the seismological structure near 650 km depth, *Geophys. Res. Lett.*, *18*, 1743-1746, 1991.

Jeanloz, R., and E. Knittle, Density and composition of the lower mantle, *Philos. Trans. R. Soc. London, Ser. A*, *328*, 377-389, 1989.

Jordan, T. H., Lithospheric slab penetration into the lower mantle beneath the Sea of Okhotsk, *J. Geophys.*, *43*, 473-496, 1977.

Jordan, T. H., and W. S. Lynn, A velocity anomaly in the lower mantle, *J. Geophys. Res.*, *79*, 2679-2685, 1974.

Jordan, T. H., P. Puster, G. A. Glatzmaier, and P. J. Tackley, Comparisons between seismic Earth structures and mantle flow models based on radial correlation functions, *Science*, *261*, 1427-1431, 1993.

King, S. D., and T. G. Masters, An inversion for radial viscosity structure using seismic tomography, *Geophys. Res. Lett.*, *19*, 1551-1554, 1992.

Machetel, P., and P. Weber, Intermittent layered convection in a model mantle with an endothermic phase change at 670 km, *Nature*, *350*, 55-57, 1991.

Masters, T. G., H. Bolton, and P. Shearer, Large-scale 3-dimensional structure of the mantle, *Eos Trans. AGU*, *73*, 201, 1992.

Olson, P., P. G. Silver, and R. W. Carlson, The large-scale structure of convection in the Earth's mantle, *Nature*, *344*, 209-215, 1990.

Peltier, W. R., and L. P. Solheim, Mantle phase transitions and layered chaotic convection, *Geophys. Res. Lett.*, *19*, 321-324, 1992.

Puster, P., and T. H. Jordan, Stochastic analysis of mantle convection experiments using two-point correlation functions, *Geophys. Res. Lett.*, *21*, 305-308, 1994.

Ricard, Y., and B. Wuming, Inferring the viscosity and 3-D density structure of the mantle from geoid, topography and plate velocities, *Geophys. J. Int.*, *105*, 561-571, 1991.

Richter, F. M., and C. E. Johnson, Stability of a chemically layered mantle, *J. Geophys. Res.*, *79*, 1635-1639, 1974.

Silver, P. G., R. W. Carlson, and P. Olson, Deep slabs, geochemical heterogeneity, and the large-scale structure of mantle convection; investigation of an enduring paradox, *Ann. Rev. Earth Planet. Sci.*, *16*, 477-541, 1988.

Stixrude, L. S., R. J. Hemley, Y. Fei, and H. K. Mao, Thermoelasticity of silicate perovskite and magnesiowustite and stratification of the earth's mantle, *Science*, *257*, 1099-1101, 1992.

Su, W.-J., R. L. Woodward, and A. M. Dziewonski, Joint inversions of travel-time and waveform data for the 3-D models of the Earth up to degree 12, *Eos Trans. AGU*, *73*, 201, 1992.

Tackley, P. J., D. J. Stevenson, G. Glatzmaier, and G. Schubert, Effects of an endothermic phase transition at 670 km depth in a spherical model of convection in the Earth's mantle, *Nature*, *361*, 699-704, 1993.

Tackley, P. J., D. J. Stevenson, G. A. Glatzmaier, and G. Schubert, Effects of multiple phase transitions in a 3-D spherical model of convection in the Earth's mantle, *J. Geophys. Res.*, *99*, 15877-15901, 1994.

Tanimoto, T., Long-wavelength S-wave velocity structure throughout the mantle, *Geophys. J. Int.*, *100*, 327-336, 1990.

van der Hilst, R. D., R. Engdahl, W. Spakman, and G. Nolet, Tomographic imaging of subducted lithosphere below Northwest Pacific island arcs, *Nature*, *353*, 37-43, 1991.

Zhao, W., D. A. Yuen, and S. Honda, Multiple phase transitions and the style of mantle convection, *Phys. Earth Planet. Inter.*, *72*, 185-210, 1992.

CHAPTER 2

TWO-POINT CORRELATION FUNCTIONS

INTRODUCTION

Seismic observations have been a principal tool for probing the earth's deep interior and addressing questions regarding the organization of convection currents in the mantle. The features of mantle shear-wave velocity heterogeneity, $\delta\beta$, are now being mapped on a global scale with increasing precision and resolution [e.g., *Tanimoto*, 1990; *Masters et al.*, 1992; *Su et al.*, 1994] provide snapshots of mantle dynamics, assuming that $\delta\beta$ is proportional to convectively induced temperature anomalies δT. This should be a good approximation in the interior away from the boundary layers, but it is invalid in the uppermost mantle, where the continental chemical boundary layer exerts a strong control on aspherical heterogeneity [*Jordan*, 1981], and perhaps at the base of the mantle, where chemical heterogeneity may also dominate [*Jordan*, 1979; *Lay*, 1989]. Numerical convection experiments, on the other hand, give insight into the dynamics of the mantle flow system. Because mantle convection is spatially and temporally chaotic [e.g., *Vincent and Yuen*, 1988] and our understanding of mantle dynamics is still crude, numerical simulations cannot reproduce the exact geographical details, but only the grosser aspects of the flow pattern. Therefore, quantification schemes that measure the effect of different parameters on convective flow organization and structure are necessary. Attention has thus far been focused primarily on power spectra [e.g. *Jarvis and Peltier*, 1986; *Tanimoto*, 1990] and the root-mean-square (rms) variation on horizontal surfaces [*Honda*, 1987]. Recently, *Jordan et al.* [1993] and *Puster and Jordan* [1994] have introduced two-point correlation diagnostics, the radial and angular correlation functions, that are invariant with respect to the temperature coefficient of shear-wave speed, $(\partial\beta / \partial T)_P$, and thus well-suited for comparison to seismic observations.

The spatial two-point correlation functions are useful for capturing the flow characteristics of mantle convection experiments in a succinct yet comprehensive manner. Instead of gigabytes of snapshots of the time-dependent flow field, useful for obtaining qualitative insight into a convective system, two-point correlation functions provide a means for quantitative analysis of a flow regime that can be directly compared to seismic observations.

A statistical approach for analyzing fluid flow has been used for many years in the study of turbulence (see *Monin and Yaglom* [1971; 1975] for a comprehensive summary). The focus of statistical fluid mechanics has been on moment functions, or equivalently power spectral densities, arising from a stochastic analysis of the equations of fluid dynamics. The simplest examples are the Reynolds equations, which are derived by ensemble-averaging the Navier-Stokes equations for an incompressible fluid. Moments arising in this context are, for example, the mean velocity, $\langle \mathbf{v}(\mathbf{r},t)\rangle$, or the covariance of velocity fluctuations, $\left\langle \delta v_i(\mathbf{r},t)\delta v_j(\mathbf{r}',t')\right\rangle$. The fundamental problem arising from statistical averaging of the momentum equations is that any finite system of equations contains more unknowns than equations (a problem referred to as the closure problem in the turbulence literature) and is thus unsolvable. We, therefore, determine the statistical properties of the flow by analyzing numerical solutions of the primitive equations instead.

In the following section we introduce the complete spatio-temporal two-point correlation functions of the temperature and flow velocity fields as tools for studying high-Rayleigh number fluid flow and illustrate the concepts with an example calculation of infinite Prandtl number thermal convection in a cylindrical annulus.

DEFINITIONS

We consider a time-dependent random field, $f(r,\Omega,t)$, defined on a spherical shell $[\Omega=(\theta,\varphi),\ \ 0\le\theta\le\pi,\ \ -\pi<\varphi\le\pi]$ or cylindrical annulus $[\Omega=\varphi,\ \ -\pi<\varphi\le\pi]$

extending over a radial interval $b \leq r \leq 1$. Examples are the temperature distribution, $T(r,\Omega,t)$, or the radial component of the flow velocity, $u(r,\Omega,t)$, obtained from numerical simulations of high Rayleigh number convection. To characterize the statistical properties of $f(r,\Omega,t)$, represented by the N-dimensional probability density function, $p_{X_1 \dots X_N}(f)$, we can calculate the N-point moment functions,

$$C_{f \dots f}(X_1,\dots,X_N) = \left\langle \left[f(X_1)-\langle f(X_1)\rangle\right] \dots \left[f(X_N)-\langle f(X_N)\rangle\right] \right\rangle, \tag{2.1}$$

where $X = (r,\Omega,t)$, and the brackets $\langle \dots \rangle$ denote ensemble average. While a complete knowledge of $p_{X_1 \dots X_N}(f)$ is desirable, much can be learned from examining its low-order moments. In particular, we focus on determining the one-point and two-point moment functions. If $f(r,\Omega,t)$ is a Gaussian random field, second-order statistics completely describe its properties. Conversely, if $f(r,\Omega,t)$ is characterized by a distinctly non-Gaussian probability distribution, bimodal for example, the probability that the snapshot estimates will differ from the ensemble average can be significant. We invoke an ergodic hypothesis [*Beran*, 1968], which allows us to estimate the statistical properties of a random process using observations from a single realization, replacing ensemble averages with time averages. Ergodicity demands that all states available to an ensemble of realizations be available to each realization. While difficult to prove formally, ergodicity is commonly assumed in the analysis of turbulent fluid flow [e.g., *Monin and Yaglom*, 1971].

In estimating the low-order properties of $p_{X_1 \dots X_N}(f)$ we further assume that $f(r,\Omega,t)$ is (weakly) stationary with respect to temporal translations and rigid-body rotations. The physical meaning of stationarity is that all conditions governing the physical process which has the function $f(r,\Omega,t)$ as its numerical characteristic will be time-independent and rotationally symmetric. For the example of thermal convection in a spherical shell this implies that reference states, internal heating rates, and boundary conditions are temporally invariant and rotationally symmetric. Furthermore, the average flow characteristics (e.g., mean temperature, average kinetic energy) must show no secular behavior over time. For each radius, we define the mean value

$\int\int f(r,\Omega,t)d\Omega\,dt \,/ \int\int d\Omega\,dt \equiv \bar{f}(r)$, and the angular fluctuation, $\delta f(r,\Omega,t) \equiv f(r,\Omega,t) - \bar{f}(r)$. Temporal and rotational invariance of the underlying statistics imply that $\delta f(r,\Omega,t)$ has zero mean, $\langle \delta f(r,\Omega,t)\rangle = 0$, and that its spatio-temporal autocovariance or two-point correlation function,

$$C_{ff}(r,r',\Delta,t^*) \;=\; \langle \delta f(r,\Omega,t)\,\delta f(r',\Omega',t')\rangle, \tag{2.2}$$

depends only on radial coordinates, angular separation $\Delta = \arccos(\Omega \cdot \Omega')$, and time lag $t^* = t - t'$.

Most of the useful information about spatial characteristics of the field is contained in three subfunctions of $C_{ff}(r,r',\Delta,t^*)$: the rms variation,

$$\sigma_f(r) \;\equiv\; \langle \delta f^2(r,\Omega,t)\rangle^{1/2} \;=\; \sqrt{C_{ff}(r,r,0,0)}, \tag{2.3}$$

the radial correlation function,

$$R_f(r,r') \;=\; C_{ff}(r,r',0,0) \,/\, \sigma_f(r)\,\sigma_f(r'), \tag{2.4}$$

and the angular correlation function,

$$A_f(r,\Delta) \;=\; C_{ff}(r,r,\Delta,0) \,/\, \sigma_f^2(r). \tag{2.5}$$

Both radial and angular correlation functions are invariant with respect to scaling by a radially varying function, $h(r) \neq 0$; i.e., $R_{\hat{f}} = R_f$, and $A_{\hat{f}} = A_f$, where $\hat{f}(r) = f(r)/h(r)$. $R_f(r,r')$ and $A_f(r,\Delta)$ are symmetric about the loci $r = r'$ and $\Delta = 0$, respectively, where they achieve their maximum value of unity. As their radial and angular separations increase, structures on spherical surfaces decorrelate at a rate measured by a correlation length, $\rho_f(r)$, and a correlation angle $\alpha_f(r)$, which we define to be the halfwidths of the central peaks at the correlation level $x < 1$:

$$\rho_f \;=\; \min[\,|\delta r| : R_f(r - \delta r/\sqrt{2},\, r + \delta r/\sqrt{2}) = x\,], \tag{2.6}$$

$$\alpha_f \;=\; \min[\,|\Delta| : A_f(r,\Delta) = x\,]. \tag{2.7}$$

The $\sqrt{2}$ scaling factor appears in (2.6) because we measure the halfwidth of $R_f(r,r')$ perpendicular to its diagonal. For $0.5 \lesssim x \lesssim 0.9$, the diagnostic properties of $\rho_f(r)$ and $\alpha_f(r)$ are insensitive to the specific choice of the correlation level; we adopt $x = 0.75$.

Rotational invariance implies the existence of an angular power spectrum, $S_f(r,l)$, which can be obtained by a suitable transform of $A_f(r,\Delta)$. In a spherical geometry, the nondimensional wavenumber is the spherical-harmonic degree $l = 1,2,\ldots$, and $\{S_f\}$ are the coefficients in the Legendre expansion

$$A_f(r,\Delta) = \frac{1}{4\pi\sigma_f^2(r)} \sum_{l=1}^{\infty} S_f(r,l)\, P_l(\cos\Delta). \qquad \text{(spherical domain)} \qquad (2.8a)$$

In the case of a circular geometry, the harmonic functions are cosines, and the expression is

$$A_f(r,\Delta) = \frac{2}{\sigma_f^2(r)} \sum_{l=1}^{\infty} S_f(r,l) \cos(l\Delta). \qquad \text{(cylindrical domain)} \qquad (2.8b)$$

The simplest two-point moment function involving temporal correlations is,

$$\mathcal{T}_f(r,t^*) = C_{ff}(r,r,0,t^*) \,/\, \sigma_f^2(r). \qquad (2.9)$$

$\mathcal{T}_f(r,t^*)$ is symmetric about $t^*= 0$, the correlation time, $\tau_f(r)$, is defined as the halfwidth of $\mathcal{T}_f(r,t^*)$ at the correlation level 0.5, i.e., $\tau_f(r) = \min[|t^*| : \mathcal{T}_f(r,t^*) = 0.5]$.

We have used these two-point correlation functions to characterize time-dependent, high-Rayleigh number convection in a cylindrical annulus. In particular, we have calculated two-point correlation diagnostics of the temperature field (T-diagnostics) and of the radial (u) and horizontal (w) components of the flow velocity field (V-diagnostics). The stochastic analysis of fluid flow in terms of two-point moment functions can be extended in an obvious way to the calculation of higher order moments, which constrain the non-Gaussian properties of the fields.

EXAMPLE CALCULATION

We illustrate the concepts developed in the previous section with an example of convection at high Rayleigh number in a cylindrical shell of inner radius $b = 0.5$ having a

30-fold viscosity increase at depth $z = 1 - r = 0.25$. The coupled system of equations describing incompressible convection at infinite Prandtl number is solved using a version of the ConMan finite element code of *King et al.* [1990] adapted to cylindrical coordinates (r, φ) by *Gurnis and Zhong* [1991]. The governing equations for the conservation of mass, momentum and energy in cylindrical geometry can be found in Appendix A. Top and bottom boundaries are free-slip and isothermal. For Boussinesq convection, Bénard and internal-heating Rayleigh numbers are defined as $Ra_B = \rho_0 g \alpha d^3 \Delta T / \kappa \eta$ and $Ra_H = Ra_B H d^2 / k \Delta T$, respectively. Here ρ_0 is the reference density, g is the gravitational acceleration, α is the thermal expansivity, ΔT is the temperature drop across the fluid layer of thickness d, κ is the thermal diffusivity, η is the dynamic viscosity, H is the heating rate per unit volume, and k is the thermal conductivity. Based on the viscosity in the top layer the Rayleigh numbers for this run are $Ra_B = 5 \times 10^6$ and $Ra_H = 1.5 \times 10^8$, with an internal heat generation that is 83% of the time-averaged surface heat flux. The effective Rayleigh number, $Ra_{B_{eff}}$, defined as the Bénard-Rayleigh number using the time-averaged strain-rate-averaged viscosity [*Christensen*, 1984] is 1.1×10^6. The finite element mesh used for this calculation consists of 532×56 elements.

We monitored the volume-averaged temperature, total kinetic energy, and surface and bottom heat flux throughout the simulation. We assumed stationarity was achieved when the running means of these quantities showed no significant secular change. Figure 2.1 displays three snapshots of the temperature field $T(r, \varphi, t)$ and velocity field $\mathrm{v}(r, \varphi, t)$ taken at widely separated times in the stationary regime. The temperature fields are characterized by a set of four or five strong, nearly vertical upwellings in the high-viscosity lower zone, which narrow and are distorted as they travel through the low-viscosity (upper) zone, and a more numerous set of downwellings, which spread out and become diffuse upon entering the high-viscosity region. Upwellings and downwellings in the low-viscosity upper layer are regions of the highest radial velocities, while horizontal velocities are largest near the surface. Flow velocities in the high-viscosity layer are much smaller than in the upper layer. Weaker downwellings, unable to penetrate the viscosity barrier at mid-depth, lead to horizontal return flow in the upper half of the annulus.

For temporal averaging to extract faithfully the low-order ensemble properties, it is important that a sufficiently long time series of the flow field is available. After the convection reached stationarity the run was continued for 59 overturn times, defined as the time needed for a fluid parcel traveling at the rms-velocity to traverse the layer [*Balachandar and Sirovich*, 1991]. We extracted 167 snapshots at equal time intervals from this part of the run. We subtracted the mean radial variation in temperature from each snapshot to form a temperature anomaly $\delta T(r,\varphi,t)$ and averaged the products $\delta T(r,\varphi,t)\,\delta T(r',\varphi',t')$ over t and φ for a fixed angular separation $\Delta = \varphi' - \varphi$ and temporal separation $t^* = t' - t$ to obtain $C_{TT}(r,r',\Delta,t^*)$. Most of the spatial information contained in $C_{TT}(r,r',\Delta,0)$ is accessible by viewing its subfunctions $R_T(r,r')$ and $A_T(r,\Delta)$, depicted in Figures 2.2*a* and 2.2*d*, and computed according to equations (2.4) and (2.5), respectively. Similarly, we calculate the V-diagnostics $R_u(r,r')$, $A_u(r,\Delta)$ and $R_w(r,r')$, $A_w(r,\Delta)$, shown in Figures 2.2*b* and 2.2*e* and Figures 2.2*c* and 2.2*f*, respectively. The normalized angular power spectra $S_T(r,l)/\sigma_T^2$, $S_u(r,l)/\sigma_u^2$, and $S_w(r,l)/\sigma_w^2$ calculated from the angular correlation functions via equation (2.8b) are shown in Figures 2.2*g*-2.2*i*. Information on the temporal correlation structure as captured by $\mathcal{T}_T(r,t^*)$ is shown in Figure 2.3. Figure 2.4 plots the horizontally averaged temperature, $\overline{T}$, the rms variation of radial and horizontal velocity, σ_u and σ_w, the rms temperature variation, σ_T, and the radial correlation length, ρ_T, and horizontal correlation angle, α_T, of the temperature field, as a function of normalized depth z. We check whether the flow is in a stationary regime by comparing two-point correlation diagnostics calculated for subsets of the ensemble.

The weak convective stratification caused by the viscosity jump at $z = 0.25$ is manifested in all two-point diagnostics of the temperature and velocity fields. It also leads to a kink in the $\overline{T}$ profile, evident in Figure 2.4*a*. σ_u, which measures the radial flux, peaks halfway through the upper layer and shows a distinct kink at the viscosity interface (Figure 2.4*b*). (Note that σ_u uses horizontal averages of $u^2(r,\varphi)$, whereas the radial flux diagnostic defined by *Peltier and Solheim* [1992] is based on horizontal averages of $|u(r,\varphi)|$.) For comparison, the unnormalized, time-averaged radial mass flux is also plotted in Figure 2.4*b*.) σ_w shows local maxima near the bottom and the top, associated with increased horizontal velocities at the boundaries of convection cells. Another local maximum is evident directly above the viscosity increase. This feature is related to horizontal return flow induced by weak downwellings unable to penetrate the viscosity barrier. σ_T shows a weak maximum just above the interface, associated with the disruption of the downwellings at the base of the low-viscosity zone (Figure 2.4*d*). The peak-width of σ_T in the lower boundary layer is larger than the upper-boundary peak owing to the smaller effective Rayleigh number in the high-viscosity zone. Away from the boundary layers, A_T is dominated by plumes, and α_T measures the effective plume halfwidth, which varies from 0.04 radian (2.3°) in the interior of the high-viscosity zone to as low as 0.01 radian (0.6°) in the upper part of the low-viscosity zone (Figure 2.4*f*). Near the top and bottom boundaries the increased angular correlation associated with horizontal flow in the boundary layers causes α_T to increase and the spectrum to redden [*Jarvis and Peltier*, 1986]. While α_T describes the angular correlation structure at small lags, A_T, A_u and A_w (or equivalently S_T, S_u and S_w) contain useful information on the average cell size at larger angular separations. An octapolar pattern, strongest in A_u, indicates that on average the flow is organized in eight convection cells (Figures 2.2*d*-2.2*f*). The normalized angular power spectra, S_T/σ_T^2, S_u/σ_u^2 and S_w/σ_w^2, attain their maxima at angular degree 4, as expected (Figures 2.2*h*-2.2*i*). This can be also seen in Figure 2.5, which shows the radial average of the angular power spectrum normalized to unit power at each depth (i.e. $\int_b^a S_f/\sigma_f^2\, r dr$) and the angular power spectrum at five depths normalized accordingly, for S_T, S_u and S_w.

The temporal correlation (Figure 2.3) also shows the effects of the viscosity increase. In the high-viscosity layer, $\mathcal{T}_T(r,t^*)$ is increased and achieves its maximum in the lower boundary layer. The correlation time, defined by τ_T is ~0.28 overturn times in the upper layer, and ~0.82 overturn times in the high-viscosity layer. The temporal correlation is also a useful indicator of episodicities in the flow. The most obvious feature associated with the stratification is the larger vertical coherence of the flow in the lower layer, displayed as a distinctive broadening in R_T, R_u and R_w, and an increase in ρ_T at the viscosity discontinuity. In the upper layer ρ_T has a local maximum near the top, which reflects the strong downwellings and scales with the internal heating rate. In the lower layer, ρ_T increases monotonically to a maximum at $z = 0.41$ where the upwelling plumes are best developed. R_w shows a widening of the central correlation ridge, associated with increased horizontal flow above the viscosity interface.

As evident from this example, the effects viscous stratification has on the average flow structure can be quantified by the two-point correlation functions of the temperature and velocity fields. The velocity field defines flow structure, but it cannot be directly measured by remote-sensing methods. The radial and angular correlation functions of the temperature field can be constrained seismically. For the remainder of this study we therefore focus on the T-diagnostics as a proxy for the V-diagnostics and investigate the signatures associated with varying different flow parameters on these two-point correlation functions.

GEOMETRY

The numerical convection calculation described above was performed in a cylindrical annulus. The earth's mantle, however, is a spherical shell. While the next generation of supercomputers will provide both the speed and memory required for three-dimensional mantle convection simulations with temperature-dependent viscosity at earth-like Rayleigh numbers, current 3D calculations either do not account for a temperature-dependent rheology [*Tackley et al.*, 1993] or use a limited aspect-ratio Cartesian box [*Tackley et al.*, 1994] at Rayleigh numbers approximately an order of magnitude below the earth's. Furthermore, when characterizing the properties of a flow regime, it is important that the flow evolution is followed for several tens of overturn times [*Balachandar and Sirovich*, 1991], a condition not satisfied by most 3D experiments to date. Lastly, 3D calculations, especially with temperature-dependent rheology, are too time-consuming to allow a systematic exploration of parameter space, desirable when quantifying the effects of many variables on the flow structure. For these reasons we study mantle convection in a cylindrical annulus. It is important, however, to understand the effects of the two-dimensional geometry on the flow structure as quantified by two-point correlation functions. In this section we illustrate differences between two-point correlation diagnostics calculated for flows using a cylindrical annulus (2D) and a spherical shell (3D), respectively.

Figure 2.6 shows a comparison between the radial and angular correlation functions calculated according to equations (2.4)-(2.5) for a compressible mantle convection experiment in a spherical shell [*Tackley et al.*, 1993] and an incompressible run in cylindrical geometry. Both experiments were performed at a volume-averaged Rayleigh number [*Glatzmaier*, 1988] of 1.1×10^6. An endothermic phase change at 670 km depth with a Clapeyron slope of –4 MPa/K impedes flow across it. Viscosity, thermal expansivity, and thermal diffusivity vary smoothly with depth. Further details on the reference state can be found in *Tackley et al.* [1994]. Both runs are predominantly heated from within, with 25% and 40% of the time-averaged heat flux supplied from the core for the 2D and 3D experiments, respectively. The radial correlation functions for the 2D and 3D runs show similar characteristics (Figures 2.6*a*, *b*). The effect of the phase transition is expressed by a pinching of the central correlation ridge at the phase boundary depth. Below the phase change, the correlation increases in the mid-mantle, reaches another minimum around 2000 km depth, and widens again in the lowermost mantle. The angular correlation functions (Figures 2.6*c*, *d*) attain a local maximum at the phase boundary and increase monotonically in the lower mantle. Figure 2.7 shows rms temperature variation, σ_T, radial correlation length, ρ_T, and horizontal correlation angle, α_T. σ_T has a local maximum above the phase transition and increases in the lower mantle attaining a maximum both wider and smaller than the peak in the surface boundary layer. ρ_T and α_T show the same behavior as the radial and angular correlation functions. One goal of characterizing mantle convection experiments with two-point correlation functions is a comparison to seismically derived correlation functions.

Seismic models have a limited angular and radial resolution; therefore, we calculated the two-point correlation functions for fields truncated at angular degree 10 and radial (Chebyshev) order 13 (Figures 2.7*b*, *d*, *f*). Note that ρ_T and σ_T retain most of their characteristic signatures, while α_T is altered more significantly. A detailed investigation of the effects of filtering on the two-point correlation functions will be presented in chapter 4.

The signatures of an endothermic phase change (local maximum in σ_T and α_T, local minimum in ρ_T) and of a viscosity increase with depth (increase in ρ_T and α_T, widening of the σ_T-maximum in the high-viscosity region) are evident for both 2D and 3D experiments. However, some differences in these diagnostics caused by the different geometries (and possibly the effects of compressibility) are also apparent. The radial correlation function for the 2D run shows less pinching at the phase boundary and a smaller increase in the mid-mantle than the 3D run. (The radial numerical resolution of the 3D run is notably inferior in the lower mantle, especially between ~1100 and ~2400 km depth where the half-wavelength of the highest-order Chebyshev polynomial reaches 110 km, twice the grid spacing of the 2D run.) These differences in the two-point correlation functions are caused by the following differences in the flow structures. In the 3D experiment, the phase transition is only penetrated by cylindrical downwellings that form at intersections of the sheet-like downwellings. These cylindrical features broaden as the viscosity increases with depth and surround the core with cold material, inhibiting hot upwelling plumes [*Tackley et al.*, 1994]. Thus, for the 3D run, the radial correlation function in the mid-mantle is dominated by cold, cylindrical downwellings. For the 2D experiment, upwelling plumes are more important for the overall flow structure. Due to geometry and high viscosity, stable (sheet-like) upwellings contribute significantly to the radial correlation function in the high-viscosity lower mantle. Furthermore, the fractional surface-area of the core is larger for the 2D case (50%) than for the 3D case (35%), making a disruption of upwelling plumes by cold downwelling material more difficult in two dimensions. Both factors, a change from sheet-like to cylindrical features in the 3D model and an overemphasis of upwellings in the 2D model, are responsible for differences in the two-point correlation diagnostics. As we shall see in chapter 3, a temperature-dependent rheology greatly reduces the importance of upwellings for 2D flows. It should also result in sheet-like high-viscosity downwellings (slabs), as opposed to the cylindrical features observed for this 3D experiment. Thus the differences between the 2D and 3D runs are likely to be diminished for a more realistic temperature-dependent rheology. Nonetheless, as noted above, the general features of an endothermic phase change and a viscosity increase with depth are evident in the correlation diagnostics for both 2D and 3D experiments.

Figure 2.8 shows a comparison of the radially averaged normalized angular power spectra, S_T/σ_T^2. It is interesting that the spectral roll-off between angular degrees 25 and 75 is approximately the same for both 2D and 3D experiments. Both runs show an increase in the power at low angular degrees [*Tackley et al.*, 1993]. Details of the spectra at low angular degrees ($l \leq 20$), however, differ between the 2D and 3D experiments both in location of the spectral maximum and spectral roll-off. As we shall document in the next chapter, both a viscosity increase with depth and an endothermic phase change are responsible for this reddening of the angular power spectrum.

REFERENCES

Balachandar, S., and L. Sirovich, Probability distribution functions in turbulent convection, *Phys. Fluids A*, *3*, 919-927, 1991.

Beran, M. J., *Statistical Continuum Theories*, 424 pp., Wiley-Interscience, New York, 1968.

Christensen, U., Convection with pressure- and temperature-dependent non-Newtonian rheology, *Geophys. J. R. Astron. Soc.*, *77*, 343-384, 1984.

Glatzmaier, G. A., Numerical simulations of mantle convection: time-dependent, three-dimensional, compressible, spherical shell, *Geophys. Astrophys. Fluid Dynamics*, *43*, 223-264, 1988.

Gurnis, M., and S. Zhong, Generation of long wavelength heterogeneity in the mantle by the dynamic interaction between plates and convection, *Geophys. Res. Lett.*, *18*, 581-584, 1991.

Honda, S., The RMS residual temperature in the convecting mantle and seismic heterogeneities, *J. Phys. Earth*, *35*, 195-207, 1987.

Jarvis, G. T., and W. R. Peltier, Lateral heterogeneity in the convecting mantle, *J. Geophys. Res.*, *91*, 435-451, 1986.

Jordan, T. H., Structural geology of the earth's interior, *Proc. Natl. Acad. Sci. USA*, *76*, 4192-4200, 1979.

Jordan, T. H., Continents as a chemical boundary layer, *Philos. Trans. R. Soc. London, Ser. A*, *301*, 359-373, 1981.

Jordan, T. H., P. Puster, G. A. Glatzmaier, and P. J. Tackley, Comparisons between seismic Earth structures and mantle flow models based on radial correlation functions, *Science*, *261*, 1427-1431, 1993.

King, S. D., A. Raefsky, and B. H. Hager, ConMan: vectorizing a finite element code for incompressible two-dimensional convection in the Earth's mantle, *Phys. Earth Planet. Inter.*, *59*, 195-207, 1990.

Lay, Structure of the core-mantle transition zone: a chemical and thermal boundary layer, *Eos Trans. AGU*, *70*, 49-59, 1989.

Masters, T. G., H. Bolton, and P. Shearer, Large-scale 3-dimensional structure of the mantle, *Eos Trans. AGU*, *73*, 201, 1992.

Monin, A. S., and A. M. Yaglom, *Statistical fluid mechanics: Mechanics of turbulence I*, 769 pp., MIT Press, Cambridge, 1971.

Monin, A. S., and A. M. Yaglom, *Statistical fluid mechanics: Mechanics of turbulence II*, 874 pp., MIT Press, Cambridge, 1975.

Peltier, W. R., and L. P. Solheim, Mantle phase transitions and layered chaotic convection, *Geophys. Res. Lett.*, *19*, 321-324, 1992.

Puster, P., and T. H. Jordan, Stochastic analysis of mantle convection experiments using two-point correlation functions, *Geophys. Res. Lett.*, *21*, 305-308, 1994.

Su, W.-J., R. L. Woodward, and A. M. Dziewonski, Degree 12 model of shear velocity heterogeneity in the mantle, *J. Geophys. Res.*, *99*, 6945-6980, 1994.

Tackley, P. J., D. J. Stevenson, G. Glatzmaier, and G. Schubert, Effects of an endothermic phase transition at 670 km depth in a spherical model of convection in the Earth's mantle, *Nature*, *361*, 699-704, 1993.

Tackley, P. J., D. J. Stevenson, G. A. Glatzmaier, and G. Schubert, Effects of multiple phase transitions in a 3-D spherical model of convection in the Earth's mantle, *J. Geophys. Res.*, *99*, 15877-15901, 1994.

Tanimoto, T., Long-wavelength S-wave velocity structure throughout the mantle, *Geophys. J. Int.*, *100*, 327-336, 1990.

Vincent, A. P., and D. A. Yuen, Thermal attractor in chaotic convection with high-Prandtl-number fluids, *Phys. Rev. A*, *38*, 328-334, 1988.

FIGURE CAPTIONS

Fig. 2.1. Three snapshots of the temperature field, $T(z,\varphi,t)$, and velocity field, $\mathrm{v}(z,\varphi,t)$, for convection in a cylindrical shell where the viscosity increases by a factor of 30 at normalized depth $z = 1 - r = 0.25$. Grayscale varies from cold (dark) to warm (light) dimensionless temperatures ($T \in [0,1]$). Velocity arrows are normalized by the maximum velocity at each instant. Horizontal velocities were constrained to yield zero net horizontal fluid motion.

Fig. 2.2. Radial correlation functions, $R_f(z,z')$, angular correlation functions, $A_f(z,\Delta)$, and normalized power spectrum, $S_f(z,l)/\sigma_f^2$, as functions of normalized depth $z = 1 - r$, angular lag Δ, and angular order l, calculated from the ensemble-averaged fields. $R_f(z,z')$ and $A_f(z,\Delta)$ are unity on the loci $z = z'$, and $\Delta = 0$, respectively, and decrease away from these axes of symmetry. (*a*) R_T, (*b*) R_u, (*c*) R_w, (*d*) A_T, (*e*) A_u, (*f*) A_w, (*g*) S_T/σ_T^2, (*h*) S_u/σ_u^2, and (*i*) S_w/σ_w^2. Contours in (*a*)-(*f*) are in increments of 0.2. The scale in (*g*)-(*i*) is logarithmic.

Fig. 2.3. Temporal correlation function, $\mathcal{T}_T(z,t^*)$, for the same convection run as a function of normalized depth $z = 1 - r$, and temporal lag t^*. $\mathcal{T}_T(z,t^*)$ is unity for $t^* = 0$, and decreases away from this axis of symmetry. Contours are in increments of 0.2. The temporal correlation function is shown only for time-lags up to 30 overturn times, to focus on the region where it has appreciable amplitude.

Fig. 2.4. (*a*) Horizontally averaged temperature, $\overline{T}$, (*b*) rms variation of radial velocity, σ_u, (*c*) rms variation horizontal of velocity, σ_w, (*d*) rms temperature variation, σ_T, (*e*) radial correlation length, ρ_T, and (*f*) horizontal correlation angle, α_T, as a function of normalized depth $z = 1 - r$ for the same convection run shown in Figures 2.1-2.3. The horizontal dotted line marks the depth of the 30-fold viscosity increase in the stratified

model. For comparison, the (unnormalized, time-averaged) radial mass flux diagnostic of *Peltier and Solheim* [1992] is shown as a dashed line in (*b*). Units are dimensionless temperature, dimensionless amplitude, dimensionless length, and radians, respectively.

Fig. 2.5. Angular power spectrum, $S_T(z,l)$. (*a*) Radial average of normalized spectrum, S_T/σ_T^2. (*b*) $S_T(z=0.009,l)$, (*c*) $S_T(z=0.125,l)$, (*d*) $S_T(z=0.25,l)$, (*e*) $S_T(z=0.375,l)$, and (*f*) $S_T(z=0.491,l)$. All plots are normalized to a maximum power of unity.

Fig. 2.6. (*a*), (*b*) Radial correlation functions, $R_T(z,z')$, and (*c*), (*d*) angular correlation functions, $A_T(z,\Delta)$, as functions of depth z and angular lag Δ for a convection run with an endothermic phase transition at 670 km depth with a phase buoyancy parameter P = –0.147. (*a*), (*c*) Experiment performed in a cylindrical annulus (2D). (*b*), (*d*) Experiment performed in a spherical shell (3D). Contours are in increments of 0.2.

Fig. 2.7. (*a*), (*b*) Rms temperature variation, σ_T, (*c*), (*d*) radial correlation length, ρ_T, and (*e*), (*f*) horizontal correlation angle, α_T, as a function of depth for the same convection runs shown in Figure 2.6. (*a*), (*c*), and (*e*) Correlation diagnostics calculated from unfiltered fields. (*b*), (*d*), and (*f*) Correlation diagnostics calculated from δT snapshots low-pass filtered at angular degree 10 and radial order 13 prior to averaging. 3D experiment (solid), 2D experiment (dotted). The horizontal dashed line marks the depth of the phase transition.

Fig. 2.8. Radial averages of the normalized angular power spectrum, S_T/σ_T^2 for the same convection runs shown in Figure 2.6. 2D (dashed lines, open symbols) and 3D (solid lines, filled symbols) experiments. All spectra are scaled to a maximum amplitude of unity.

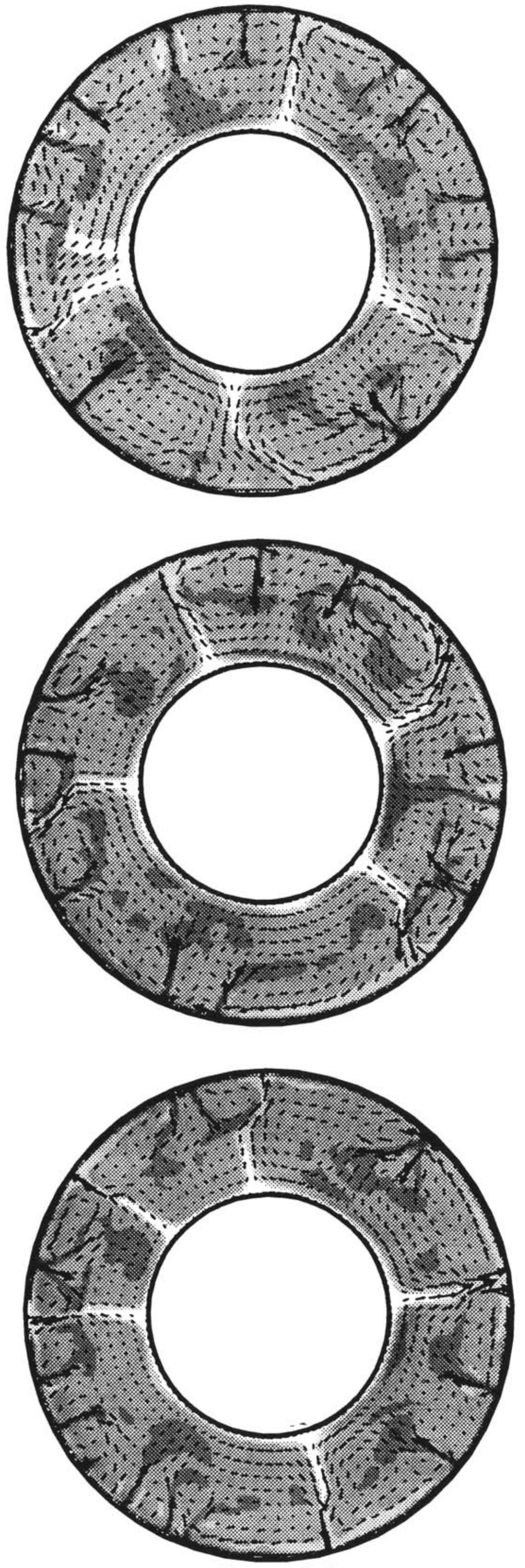

Figure 2.1

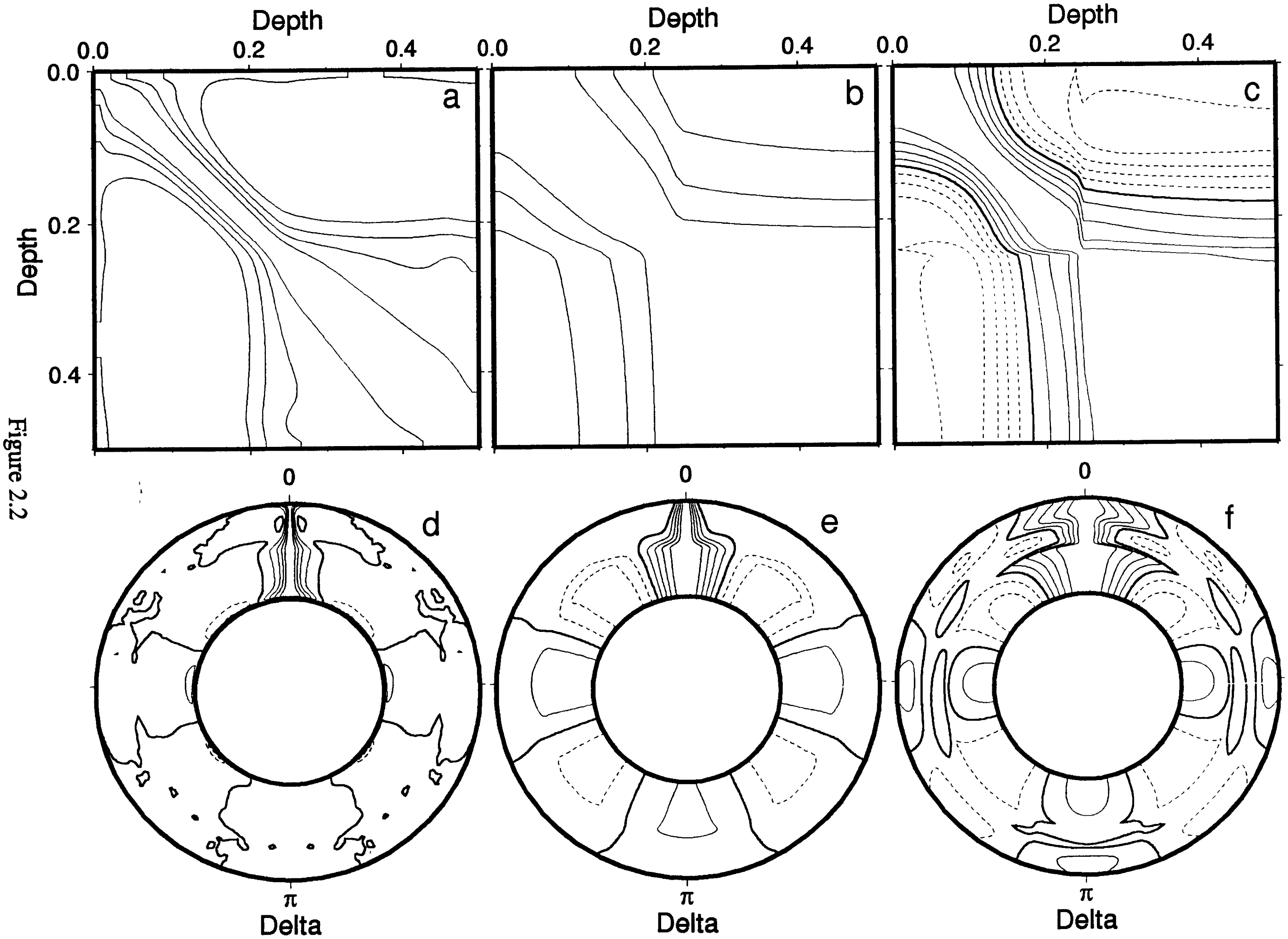
Depth
0.0
0.2
0.4
Depth
0.0
0.2
0.4
a
Depth
0.0
0.2
0.4
b
Depth
0.0
0.2
0.4
c
0
d
π
Delta
0
e
π
Delta
0
f
π
Delta

Figure 2.2

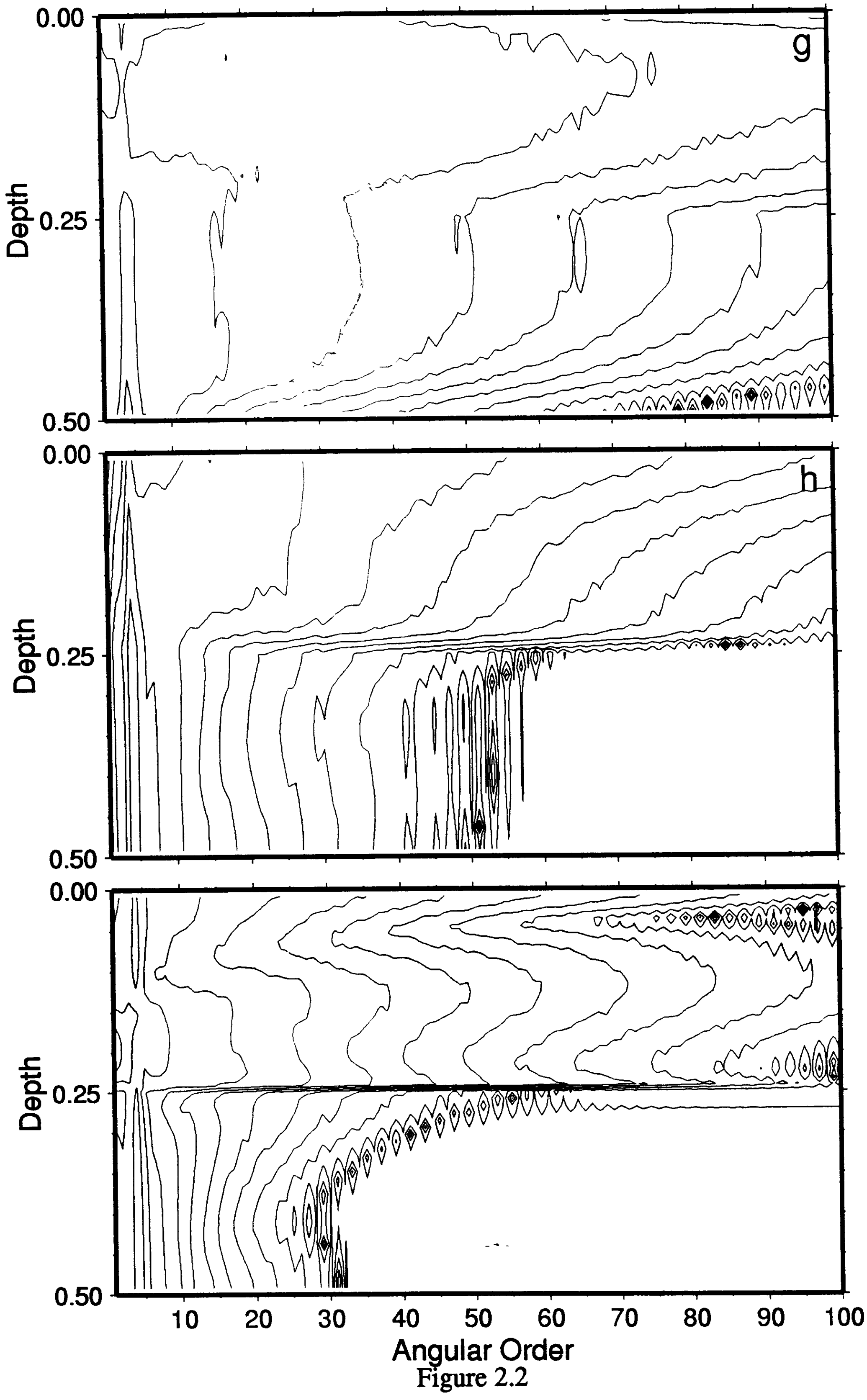

Figure 2.2

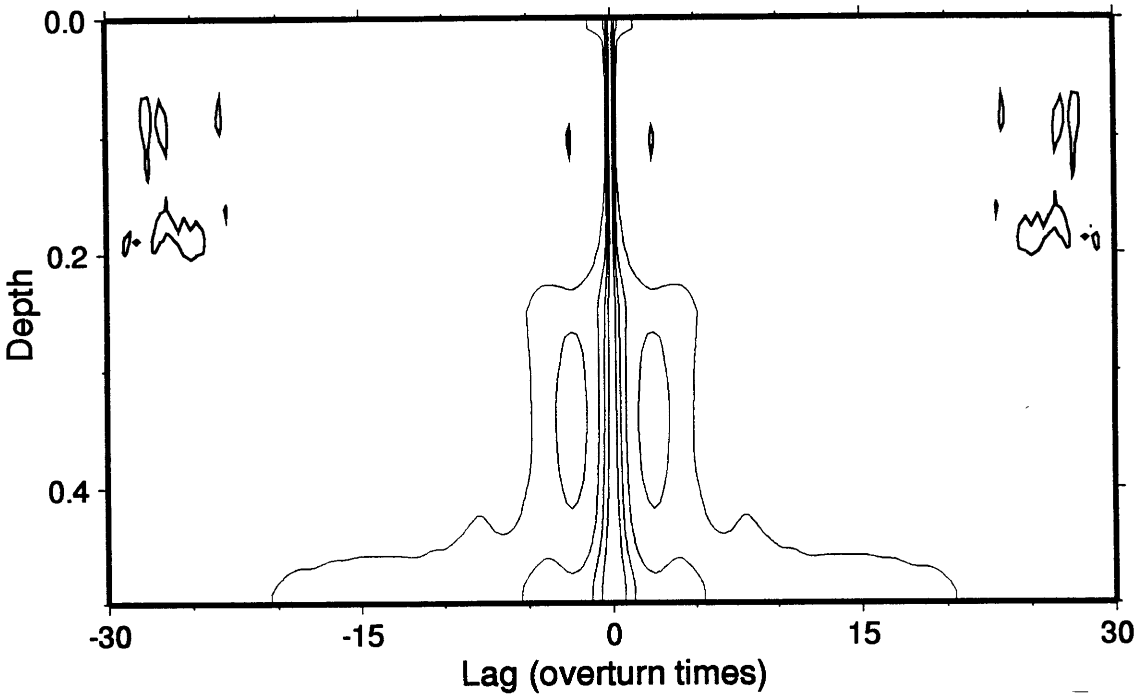

Figure 2.3

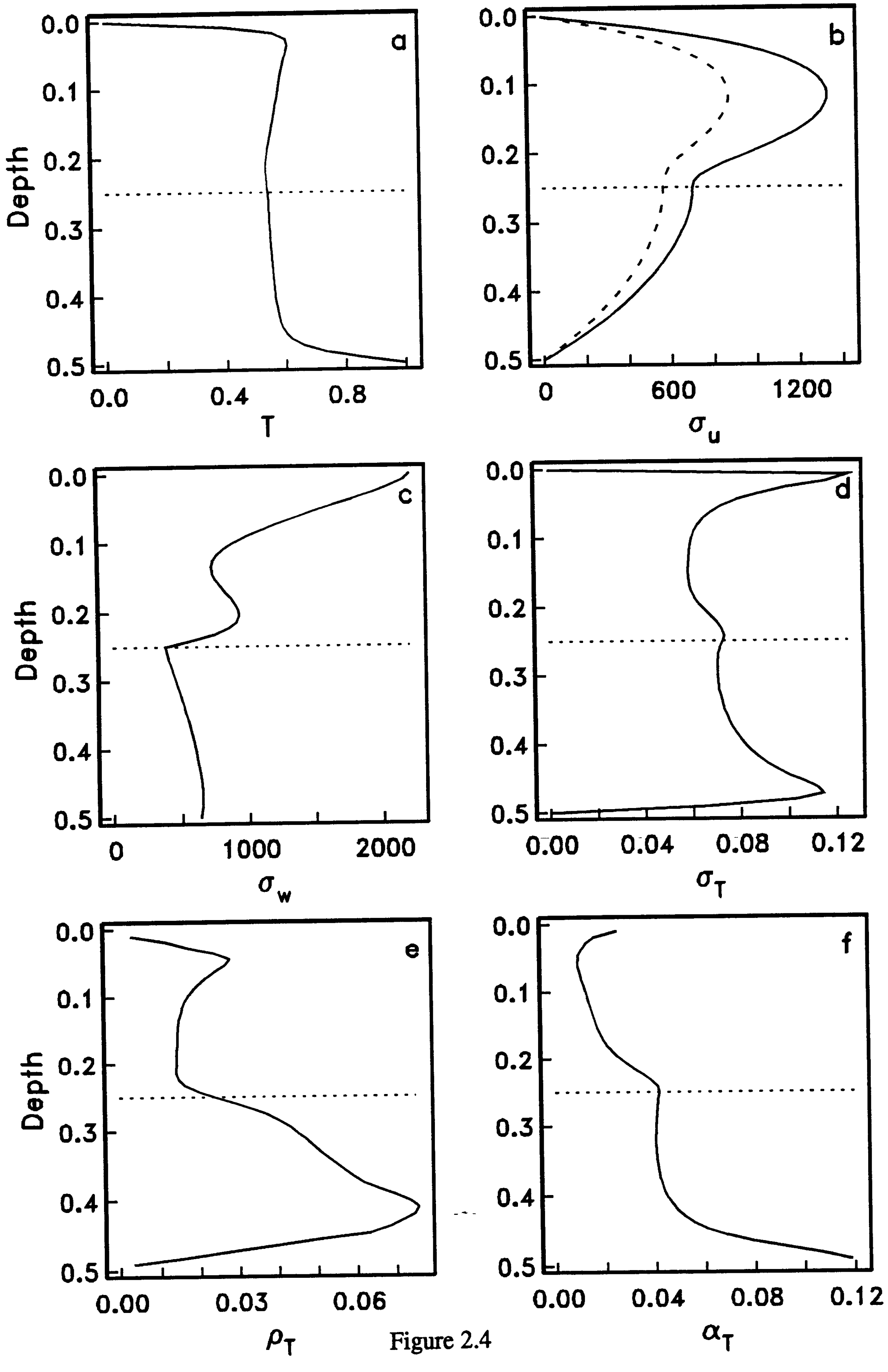
a
b
c
d
e
f
Depth
0.0
0.1
0.2
0.3
0.4
0.5
T
0.0
0.4
0.8
σ_u
0
600
1200
σ_w
0
1000
2000
σ_T
0.00
0.04
0.08
0.12
ρ_T
0.00
0.03
0.06
α_T
0.00
0.04
0.08
0.12

Figure 2.4

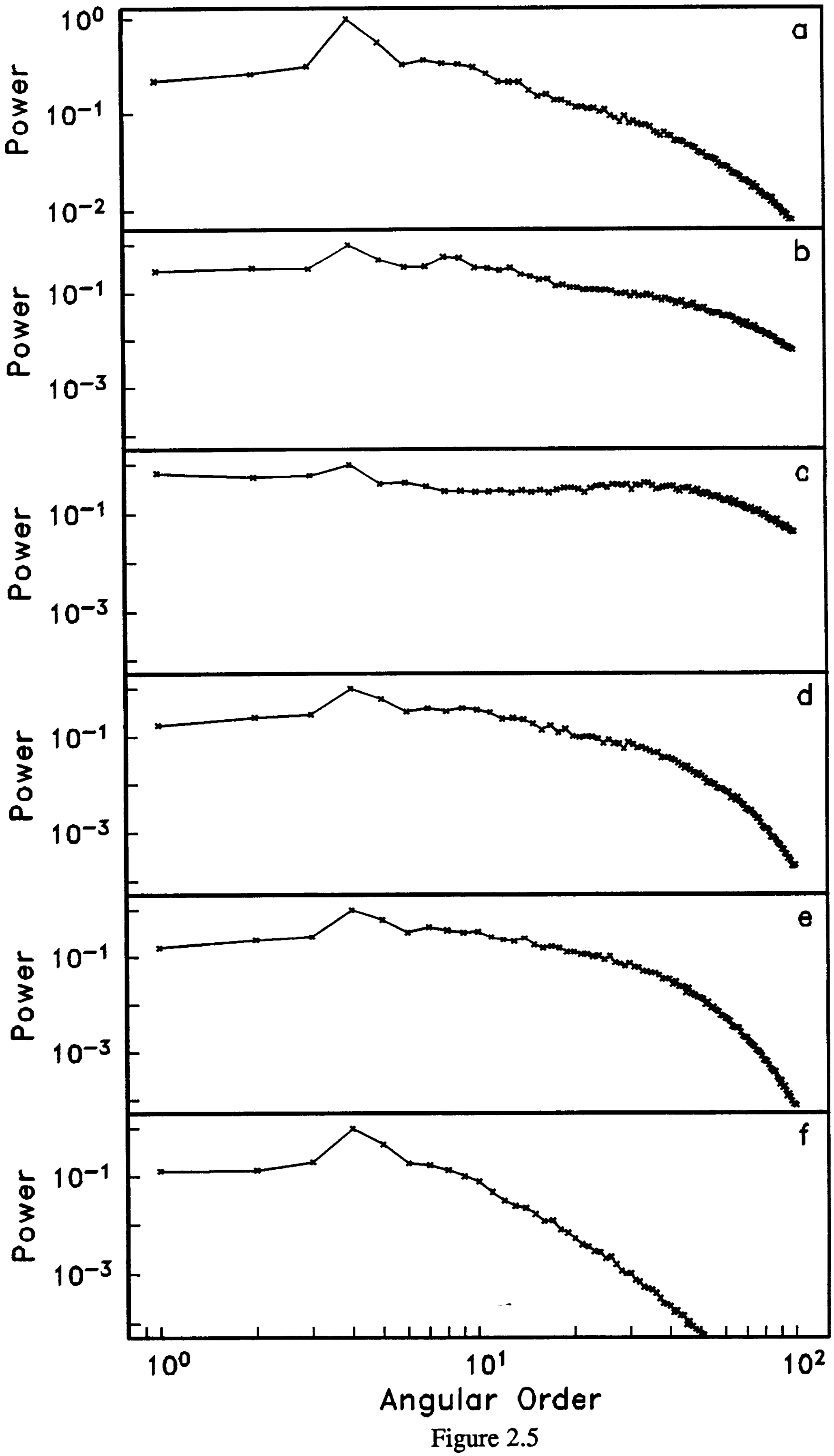

Figure 2.5

Figure 2.6

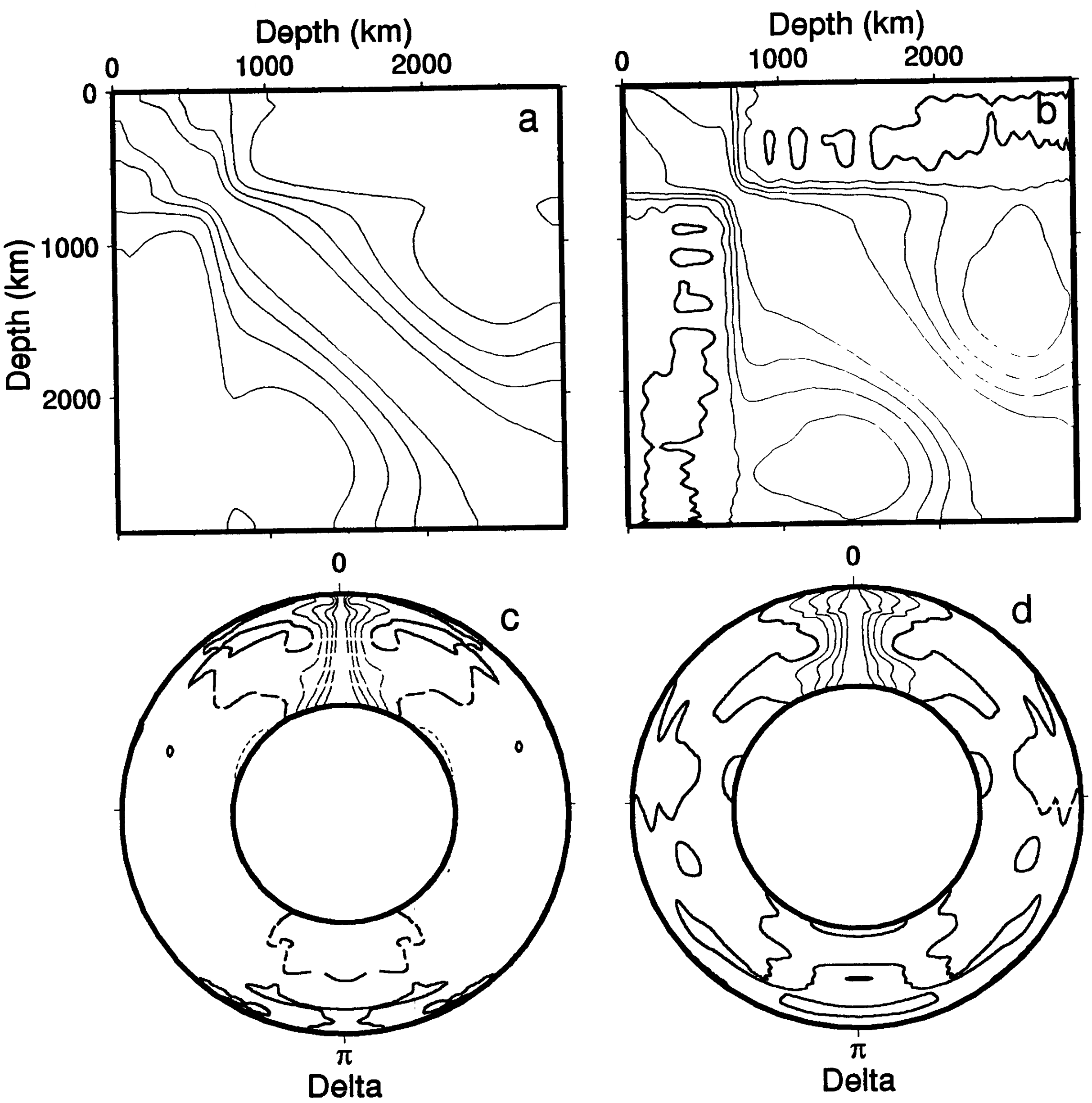
Depth (km)
0
1000
2000
a
b
Depth (km)
0
1000
2000
Depth (km)
0
1000
2000
0
c
d
π
Delta
π
Delta

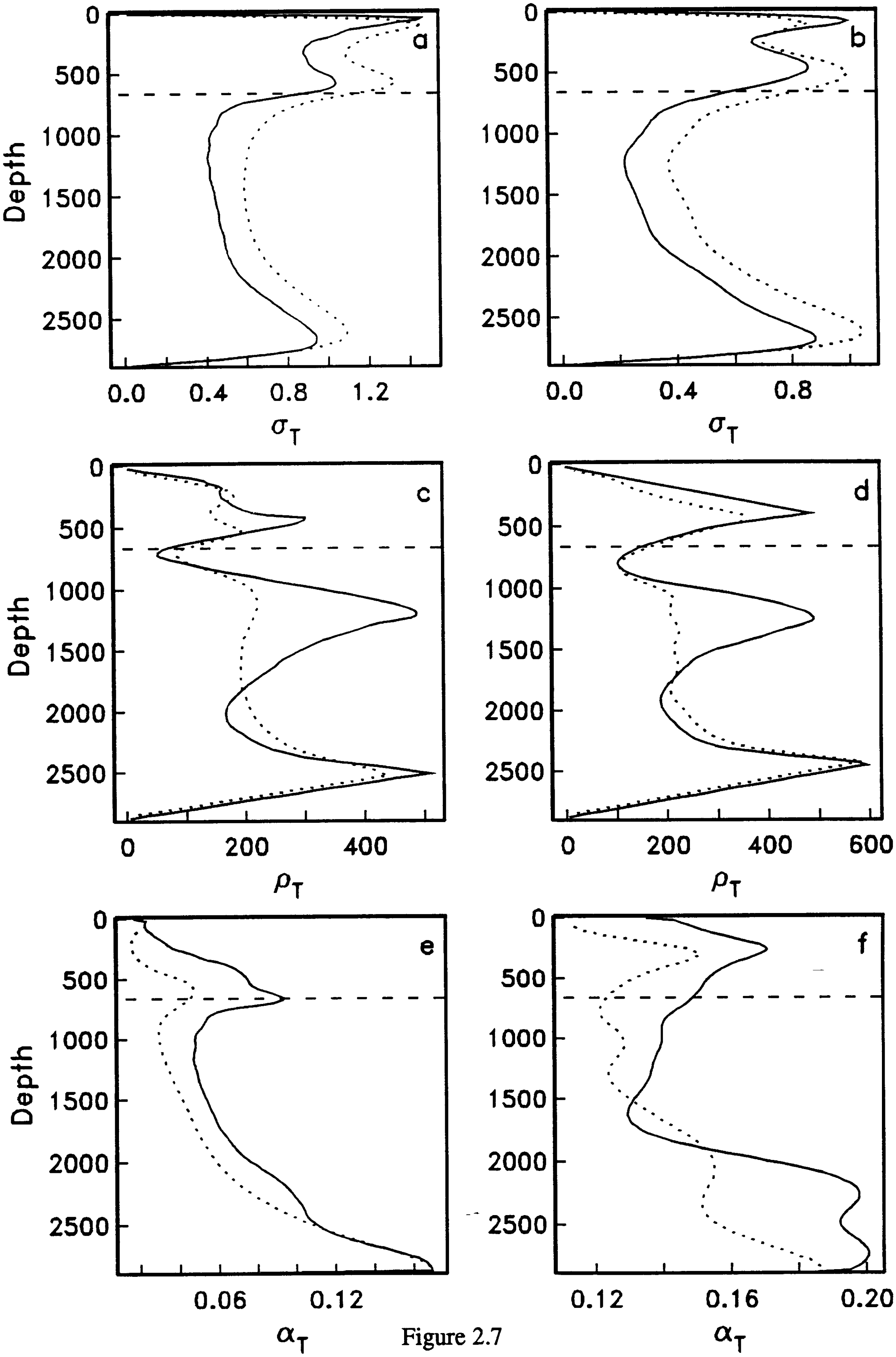
a
b
c
d
e
f
Depth
0
500
1000
1500
2000
2500
0.0
0.4
0.8
1.2
σ_T
0.0
0.4
0.8
σ_T
0
200
400
ρ_T
0
200
400
600
ρ_T
0.06
0.12
α_T
0.12
0.16
0.20
α_T

Figure 2.7

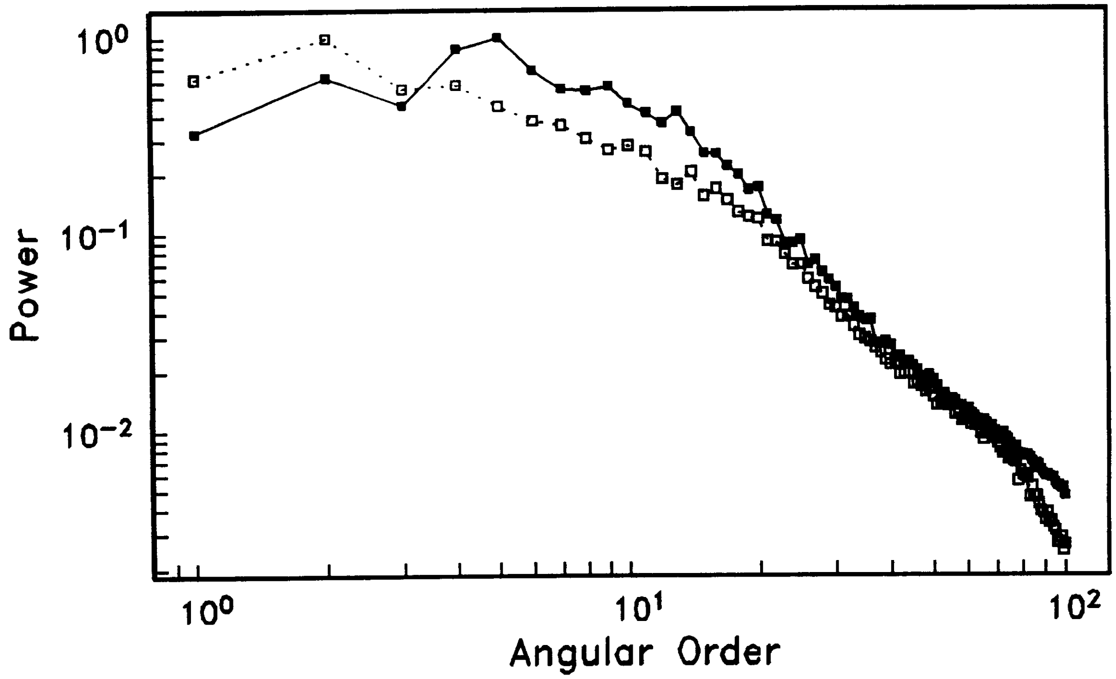

Figure 2.8

CHAPTER 3

CONVECTION MODELS

INTRODUCTION

Numerical modeling of mantle convection has been used for the past two decades [e.g., *McKenzie et al.*, 1974] to gain insight in the dynamical behavior of the earth interior. What makes this system particularly interesting is the wide range of physical processes and parameters potentially important to mantle flow. In this chapter we will undertake a systematic study of some of those effects on the flow structure and quantify the flow characteristics using the two-point correlation functions introduced in chapter 2. These diagnostics can then be compared to two-point correlation functions obtained from seismic earth structures and a quantitative assessment about the relative importance of different processes for mantle convection can be made. This will be the topic of chapter 4.

In the following section we apply the formalism developed in chapter 2 to characterize fields obtained from convection experiments at Bénard-Rayleigh numbers ranging from 5×10^4 to 5×10^6 (which includes the transition from a steady to a time-dependent convective regime) for varying degrees of internal heating, and present scaling relations for different correlation diagnostics. Other mechanisms modifying the flow field, which we investigate in subsequent sections are radial variations in viscosity, temperature-dependent rheology, phase transitions, and plates.

SCALING RELATIONSHIPS

Scaling relations, which play an important role in the study of convection, have been established for quantities such as the Nusselt number, boundary layer thickness and horizontal surface velocity; these often obey power-law relations as functions of Rayleigh number [e.g. *Howard*, 1966]. In this section we investigate the dependence of isoviscous flows on internal heating rate and Rayleigh number and establish scaling relations for various T-diagnostics of the flow properties. Numerical details of the convection calculations discussed in this section are in Table 3.1.

The time-averaged surface Nusselt number, a measure of convective vigor, is plotted as a function of Rayleigh number for different amounts of internal heat generation in Figure 3.1. For a convective system heated partially from within, the conventional definition of the surface Nusselt number as the surface heat flux normalized by the conductive heat flux is no longer appropriate. Instead we use a definition based on boundary layer thickness, $Nu_\delta = c/\delta$, where δ is the thickness of the surface boundary layer and c is a geometrical constant (for Cartesian geometry, $c = 1/2$; for cylindrical geometry, $c \approx 0.258$). This definition for Nu_δ can be derived from boundary layer arguments both for systems entirely heated from below (using the heat flux) and for systems entirely heated from within (using the ratio of conductive over convective temperature at the bottom). (For cylindrical geometry, c differs only slightly for the bottom heated and internally heated systems.) Power-law relations, indicated by straight-line fits on a log-log scale, are apparent for the Rayleigh-Bénard experiments, as well as for the internally heated runs. The power-law exponent for the bottom heated Nu_δ -Ra_B fit (0.242) is lower than the value predicted from boundary layer theory (1/3) or power-law exponents obtained from steady-state or time-dependent convection experiments in a fixed aspect-ratio geometry. *Hansen et al.* [1992], for example, obtain a value of 0.315 for experiments in a box of aspect-ratio 1.8. They show that steady-state and time-dependent experiments yield the same Nusselt number, provided that the cell sizes are the same and that a sufficiently long time interval is employed when calculating the time-averaged Nusselt number (several tens of overturn times). They also demonstrate the dependence of *Nu* on cell size, which follows closely the predictions of boundary layer theory [*Olson and Corcos*, 1980], with an inverse proportionality of *Nu* and cell size for aspect ratios larger than unity. This decrease of *Nu* with increasing cell size is the reason our power-law exponent is lower than for fixed, small aspect-ratio experiments. The flow system in an annulus has the freedom to find its preferred aspect-ratio, leading to convection cells with aspect-ratios larger than unity, which become larger with increasing Rayleigh number. This dependence of preferred cell size on convective vigor, leads to a Nu-Ra_B scaling law with a power law exponent lower than usually assumed for thermal history modeling of the earth, which would affect the results of parameterized convection. For runs partially heated from within, the preferred cell-aspect-ratio changes less with increasing Rayleigh number leading to a Nu-Ra_B scaling law with a power law exponent larger than for the Bénard case. In Figure 3.1*b* we use a Rayleigh number based on the heat flux (Q), $Ra_Q = Ra_B Qd/k\Delta T$, [e.g., *O'Connell and Hager*, 1980], which is more appropriate than Ra_B when comparing experiments with different amounts of internal heat generation. Least-squares fit parameters for the Nusselt number - Rayleigh number scaling relations are given in Table 3.2.

Figure 3.2 shows the variation of the two-point correlation diagnostics, σ_T, ρ_T, and α_T, for different amounts of internal heating, Ra_H/Ra_B, at constant Bénard-Rayleigh number, $Ra_B = 5 \times 10^6$. Increasing the amount of internal heating leads to an increase in the upper boundary layer peak in σ_T and a simultaneous decrease in the lower boundary layer peak. The maximum in ρ_T, which for internally heated experiments is near the top boundary, also increases with internal heat generation. The average plume half-width, measured by α_T, grows with depth for internally heated runs and is largest for the highest Ra_H/Ra_B. The features observed in the T-diagnostics are caused by downwellings whose strength and number increases with growing internal heating rate leading to their dominance over upwellings and resulting in the asymmetries observed above. For internally heated experiments, contributions to α_T for example, are primarily due to downwellings; as these cold plumes sink toward the bottom boundary they widen leading to an increase in α_T. The observed asymmetry in the correlation diagnostics for the bottom heated run shows the effects of the cylindrical geometry (for Cartesian geometry the correlation diagnostics are symmetric about mid-depth). Figure 3.3 shows the influence of varying the Bénard-Rayleigh number on the T-diagnostics, for Ra_H/Ra_B =

15. All three diagnostics show the largest asymmetry due to internal heating at the lowest Rayleigh number, which for constant Ra_H/Ra_B has the largest internal heating fraction (see Table 3.1). With increasing Rayleigh number boundary layers become thinner, resulting in an overall decrease in the magnitude of σ_T, ρ_T, and α_T. The radial correlation length (Figure 3.3*b*), while not a direct measure of boundary layer thickness, is influenced by the strength of downwellings, which are more easily distorted as plumes become thinner. The correlation angle (Figure 3.3*c*) measures average plume width and is thus directly related to boundary layer thickness and Rayleigh number.

Figures 3.4-3.6 show the scaling behavior for radial averages of rms temperature variation, $\overline{\sigma}_T$, radial correlation length, $\overline{\rho}_T$, and correlation angle, $\overline{\alpha}_T$, for Rayleigh numbers, Ra_Q, varying over more than two orders of magnitude and for different internal heating rates. Least-squares fit parameters for the power laws relating $\overline{\sigma}_T$, $\overline{\rho}_T$ and $\overline{\alpha}_T$ to Ra_Q are given in Table 3.2. All of the two-point correlation diagnostics decrease with increasing Rayleigh number. $\overline{\sigma}_T$ shows the least variability with respect to internal heating (Figure 3.4). Not only does $\overline{\rho}_T$ vary more strongly for the different internal heating rates, also evident in Figure 3.2, but there is also a difference between experiments that lead to a steady-state and runs in a time-dependent regime. We obtained steady-state results only for the Rayleigh-Bénard experiments at Ra_B below 10^6. The large aspect ratio of our computational domain [e.g., *Hansen and Ebel*, 1988], the annular geometry, and internal heating lead to time-dependent solutions for most cases. The variation of $\overline{\alpha}_T$ with Ra_Q is shown in Figure 3.6. Again, a difference in the power-law relations for steady-state and time-dependent Rayleigh-Bénard experiments is apparent, while both the *Nu-Ra* and the $\overline{\sigma}_T$-Ra_Q scaling law show no change in power-law behavior between the steady and time-dependent regimes.

As the results presented in this section make clear, varying the amount of internal heating and the Rayleigh number leave distinct fingerprints on the correlation diagnostics of the temperature field. While one might hope to infer such fundamental parameters as the average Rayleigh number or the average internal heating fraction of the earth's mantle from comparing seismic observations of $\rho_\beta(r)$ or $\alpha_\beta(r)$ to those derived from convection calculations, the actual situation is more complicated. As we shall see below, other effects such as depth- and temperature-dependent viscosity also have a significant influence on flow structure and two-point correlation diagnostics.

DEPTH- AND TEMPERATURE-DEPENDENT VISCOSITY

Convection in the earth's mantle is, of course, far more complicated than what is modeled in the experiments above. Those experiments made no attempt to mimic details of mantle flow, but rather to isolate different parameters and study their influence on the correlation diagnostics. As demonstrated above, two-point correlation functions are sensitive indicators of modulations in the flow characteristics introduced by Rayleigh number and internal heating rate.

In this section we investigate the effects on mantle flow due to variations of viscosity with depth and temperature. Observational evidence from studies of the earth's geoid [*Hager et al.*, 1985; *Hager and Richards*, 1989; *King and Masters*, 1992] indicates that the radially averaged viscosity increases with depth. Experimental studies of mantle constituents such as olivine show that viscosity is strongly temperature-, pressure-, and probably stress-dependent (see Ranalli, [1991]for a recent review). We explore the effects of radial viscosity variations on the flow structure using simple two-layer viscosity models. The temperature dependence of viscosity leads to cold, high-viscosity downwellings and hot, low-viscosity upwellings. Modeling subduction of strong, high-viscosity plates in a dynamically self-consistent way in a geometry where plate boundaries are free to rearrange themselves will be investigated in a later section. Here we focus on the influence of strong, cold, high-viscosity downwellings ("slabs") on the flow structure.

One way of modeling the earth's strong, viscous lithosphere in a numerical simulation is to employ a temperature-dependent viscosity. To study the effects of slabs we parameterize the temperature dependence of viscosity as $\eta_1(T) = \exp[5.23/(T+0.23)-5.23/1.23]$. The dimensionless constants correspond to an activation energy of 52.2 kJ, a surface temperature of 273 K, and a superadiabatic temperature drop of 1200 K. Using experimentally determined values for the activation energy (for olivine *Ashby and Verrall* [1977] find an activation energy of 522 kJ) would lead to extreme viscosity variations, which probably exaggerate actual mantle conditions, since at low temperatures the dominant deformation mechanism no longer follows an exponential creep law. Furthermore, the stress-weakening of viscosity due to non-Newtonian effects partially counteracts the temperature behavior. *Christensen* [1984] showed that for steady-state experiments, non-Newtonian, temperature-dependent rheology and Newtonian, temperature-dependent rheology with reduced activation energy yielded similar temperature and flow fields. In our calculations we allow viscosity variations due to temperature by four orders of magnitude; the exponential viscosity law implies that a cold downwelling of non-dimensional temperature $T = 0.25$ in a fluid of ambient temperature $T = 0.5$ has a viscosity contrast of approximately 40. Even with the reduced activation energy used here a stagnant lid with little or no surface motion [e.g., *Nataf and Richter*, 1982] would develop in a temperature-dependent viscosity calculation. Since our focus here is not to model surface plates but rather subducting slabs, we mobilize the flow near the surface by limiting the maximum viscosity in the upper boundary layer, δ_{bl}, to a lower value, η_{bl}, that enables surface motion; i.e., we use the viscosity law,

$$\eta(r,T) = \begin{cases} \min[\eta_{bl}, \eta_0(r)\eta_1(T)] & 1-\delta_{bl} \le r \le 1 \\ \eta_0(r)\eta_1(T) & b \le r < 1-\delta_{bl} \end{cases}. \tag{3.1}$$

This form is ad hoc, but successful in permitting the significant surface motion important for allowing boundary layer instabilities to develop, grow and become high-viscosity downwellings simulating slabs. Furthermore, this formalism does not impose geometrical constraints onto the convecting system which might introduce artifacts into the two-point correlation functions, and it is computationally faster than calculations where the viscosity is both stress- and temperature-dependent. We will see in a later section that the resulting flow fields have an average structure that is remarkably similar to experiments where the cold, high-viscosity surface boundary layer consists of variable-sized plates.

Numerical calculations using a temperature-dependent rheology are more than an order of magnitude more expensive than those with depth-dependent properties; therefore, some of the calculations are performed in a semi-annulus with reflecting boundary conditions rather than a full annulus with periodic boundary conditions. The smaller computational domain enables us to perform experiments of sufficient length in a stationary regime. Two-point correlation diagnostics calculated for semi-annulus and annulus runs were compared for some cases and found to be in close agreement.

Temperature, flow velocity, and viscosity fields for three snapshots from a convection experiment with depth- and temperature-dependent viscosity taken at widely separated times in the stationary regime are shown in Figure 3.7. The effective Rayleigh number for this run was 1.2×10^6; 78% of the time-averaged surface heat flux was generated internally. $\eta_0(r)$ is a two-layer model with a 30-fold viscosity increase at $r = 0.75$, identical to the non-temperature-dependent run at similar Rayleigh number and internal heating rate shown in Figure 2.1. A visual comparison of the temperature and velocity fields for the two runs illustrates the effects of the temperature dependence of viscosity. Cold downwellings are stronger and thus able to penetrate the high-viscosity region more easily. Simultaneously, hot upwellings are mobilized, leading to weaker, less stationary plumes.

Before investigating the effects of both depth- and temperature-dependent rheology on the flow structure as quantified by the two-point correlation functions, we first examine variations in the flow due to changes in the viscosity law (equation 3.1). Figure 3.8 shows σ_T, ρ_T, and α_T for a suite of temperature-dependent viscosity simulations obtained by varying η_{bl} and δ_{bl} together with an isoviscous calculation for which Rayleigh number and internal heating rate matched most closely those of the temperature-dependent experiments. Parameters and results for these experiments can be found in Table 3.3. (Since the effective Rayleigh number and internal heating fraction are results of the calculations rather than input parameters, the different experiments were not run at exactly the same values of these parameters.) We notice that the peak in ρ_T is higher and wider for the temperature-dependent rheology cases. This is due to the fact that the downwellings, which are about two orders of magnitude more viscous than the ambient fluid throughout the upper half of the domain, are able to reach greater depths before they are disturbed by the return flow. The greater strength of the downwellings is also evident in the maximum in σ_T near the surface and in the increased correlation angle near the top. α_T also shows a large increase near the bottom compared to the isoviscous run, which, can be attributed to the strongest slabs which traverse the entire fluid layer and pile up near the bottom boundary. Comparing the temperature-dependent calculations with each other, it can be seen that varying δ_{bl} from 0.027 to 0.045 and η_{bl} from 10-100 results in minor differences in σ_T, ρ_T and α_T, although some of the variability is attributable to the different heating rates, average temperatures and Rayleigh numbers. For subsequent calculations we adopt $\delta_{bl} = 0.036$ and $\eta_{bl} = 50$, which leads to strong downwellings that have both a high viscosity contrast with respect to the ambient fluid and are sufficiently narrow to mimic slabs.

Figures 3.9-3.14 show a compilation of flow diagnostics for predominantly internally heated experiments with depth-dependent viscosity and both temperature-independent rheology (dashed lines) and temperature-dependent rheology (solid lines). The numerical details of these experiments are listed in Table 3.4. Figures 3.9*a*-3.14*a* show $\overline{T}$, σ_u, σ_w, σ_T, ρ_T, and α_T, as a function of depth for $\eta_0(r) = 1$. Figures 3.9*b*-3.14*b* depict the same diagnostics for a two-layer viscosity structure with a 30-fold viscosity increase at $r = 0.875$. In Figures 3.9*c*-3.14*c* the two-layer viscosity structure has a 10-fold viscosity increase at mid-depth ($r = 0.75$), while in Figures 3.9*d*-3.14*d* the viscosity increases by a factor of 30 at mid-depth. We attempted to use similar effective Rayleigh numbers and internal heating rates for corresponding cases with and without temperature-dependent rheology; an exact agreement is difficult to achieve since both effective viscosity and internal heating rate are results of the calculations rather than input parameters.

When rheology is a function of depth alone, a viscosity increase with depth results in a flow pattern with large aspect-ratio cells defined by a few strong, nearly stationary upwellings and numerous weak downwellings [*Hansen et al.*, 1993]. The viscosity increase leads to a drop in the average temperature and a decrease of the velocity in the high-viscosity region, also observed in steady, square-cell Bénard convection [*Gurnis and Davies*, 1986]. Both cases with a 30-fold viscosity increase show a kink in the $\bar{T}$ profile above the viscosity step (Figures 3.9*b* and 3.9*d*). If the rheology is a function of temperature alone, the average temperature is raised significantly due to the cold, high-viscosity lid, which inhibits heat transport (Figure 3.9*a*). The depth- and temperature-dependent cases show a smaller increase in the interior temperature compared to the experiments where viscosity was solely a function of depth. This is in part due to a self-regulating mechanism of temperature-dependent convection, which leads to more vigorous motion and thus more efficient heat transport as temperatures increase and viscosity decreases. Note, however, that $\bar{T}$ varied appreciably for different choices of η_{bl} in equation (3.1) for the purely temperature-dependent experiments described above. The temperature-dependent experiment with the 30-fold viscosity increase at mid-depth still shows a kink in the $\bar{T}$ profile above the high-viscosity region.

The models where the viscosity increase occurs at mid-depth exhibit corresponding local extrema in the V-diagnostics (Figures 3.10*c*-3.10*d* and Figures 3.11*c*-3.11*d*). The local minima in σ_u and the local maxima in σ_w above the high viscosity region can be attributed to material being transported laterally as the flow encounters the rapid viscosity increase, which impedes radial mass transport. The model with the viscosity contrast at $r = 0.875$ on the other hand shows no distinct expression of horizontal return-flow induced by the viscosity barrier, but rather a rapid decrease in σ_w from the low-viscosity to the high-viscosity region (Figure 3.11*b*). Thus the depth of viscous stratification has a major influence on the overall flow organization. σ_u and σ_w are remarkably similar for depth-dependent and depth- and temperature dependent cases (Figures 3.10*b*-3.10*d* and Figures 3.11*b*-3.11*d*). The drop in σ_u from the upper layer to the high-viscosity layer is smaller for the temperature-dependent runs (Figures 3.10c-3.10d). This can be explained by the strong, coherent slabs being able to overcome the viscosity barrier more easily. The temperature-dependent runs have slightly smaller (larger) horizontal rms velocity variations near the upper (lower) boundary than their purely depth-dependent counterparts. However, near-surface values for σ_w are significant – a result of the mobilization achieved with the viscosity law (equation 3.1).

Figures 3.12-3.14 show the rms temperature variation, radial correlation length, and correlation angle, respectively. The largest effect of temperature-dependent viscosity on σ_T is a widening of the upper boundary-layer peak, a manifestation of the strong, high-viscosity downwellings. Aside from this feature temperature-dependence has only a minor influence on the shape of σ_T. A viscosity increase with depth has only a weak signature in σ_T. The effects of incorporating temperature-dependent rheology in the constitutive relations is most pronounced for ρ_T. As noted earlier when comparing temperature-dependent and isoviscous experiments, the strong, high-viscosity downwellings result in wider and higher peaks in the radial correlation length near the top boundary. Sharp increases in ρ_T due to the step-function increase in $\eta_0(r)$ are also evident, but greatly diminished compared to the cases without temperature dependence (Figures 3.13*b*-3.13*d*). In fact, the peak in the lower layer which exceeded the upper peak by nearly a factor of three for the case with a 30-fold viscosity increase at mid-depth is barely larger than the upper peak when temperature-dependent rheology is incorporated. The decrease in ρ_T in the lower layer compared to the purely depth-dependent experiments is caused by the less viscous, less stationary hot upwellings. The largest effect of temperature-dependent rheology on α_T (Figure 3.14) is a decrease directly above the lower boundary (except for the case $\eta_0(r) = 1$ discussed earlier). This feature can be attributed to the mobilization of the lower boundary layer due to the temperature-dependent viscosity. Note that a stress-dependent rheology would counteract this effect as it would stabilize the lower boundary layer [e.g., *Christensen*, 1984]. The viscosity increase with depth also manifests itself in a larger correlation angle in the high-viscosity layer, which is in agreement with the scaling relation derived earlier (Figure 3.6) that predicts larger α_T at higher viscosity (lower Rayleigh number).

α_T characterizes the angular correlation function for small angles and is thus diagnostic of the average plume-width. To describe the angular correlation properties at large scales, either A_T (or its spectral counterpart, the angular power spectrum, S_T) are required. Figure 3.15 compares the radial averages of the normalized spectrum, S_T / σ_T^2, for the experiments with (*a*) $\eta_0(r) = 1$, (*b*) a 30-fold viscosity increase at $r = 0.875$, and (*c*) a 30-fold viscosity increase at mid-depth. Both cases with a constant background viscosity are characterized by a "white" spectrum, which only begins to roll-off around angular degree 30. The viscously layered experiments have more power concentrated at long wavelengths. The predominance of strong, nearly stationary upwellings for the experiments without temperature-activated rheology expresses itself in the dominance of a single angular degree (Figures 3.15*b* and 3.15*c*). These plumes are weakened in a temperature-dependent regime, thus reducing the dominance of a single wavenumber.

To summarize, the effects of a combined depth-and temperature dependent rheology on the flow structure as diagnosed by two-point correlation functions are two-fold. First, cold downwellings are stronger and thus able to reach greater depths relatively undisturbed compared to their non-temperature-dependent counterparts, leading to an increase in height and width of the radial correlation maximum near the top associated primarily with those downwellings. Second, temperature-dependent rheology mobilizes hot upwellings in high-viscosity regions, which leads to a decrease of the maxima for ρ_T and α_T in the lower layer. The decreased radial correlation length in the high-viscosity region for the temperature-dependent experiments suggests that in the purely depth-dependent runs the large radial correlation length in the lower layer is primarily due to nearly stationary upwellings, while in the temperature-dependent cases ρ_T is dominated by strong downwellings. Note, that the two runs with a viscosity step at $r = 0.875$, where the relative contribution to ρ_T from downwellings may be expected to be largest, differ the least. We verified that for temperature-dependent rheology the contributions to ρ_T – even in the lower layer – are dominated by downwellings by considering only positive or negative temperature anomalies when calculating the correlation diagnostics. The stratification boundary due to the abrupt viscosity increase with depth is still easily discernible in ρ_T and α_T. The size of the near-surface peaks, however, which has been shown earlier to scale with the amount of internal heating, is strongly influenced by temperature-dependent rheology. This makes a direct attempt to estimate the amount of internal heating from radial correlation functions of seismic earth models problematic.

PHASE TRANSITIONS

Major discontinuities in the radial variations of seismic wave-speeds observed to occur in the earth at depths of 410 km and 660 km are now widely regarded to be due to mineralogical phase transformations. The effects of these phase transitions on mantle flow have received much recent attention [*Machetel and Weber*, 1991; *Peltier and Solheim*, 1992; *Honda et al.*, 1993; *Tackley et al.*, 1993; *Tackley et al.*, 1994], as the degree to which phase boundaries enforce flow stratification has important ramifications for the earth's thermal and chemical evolution and structure. The shallower phase boundary is associated with the exothermic transformation of α-olivine to its β-phase, while the deeper transition is due to the endothermic dissociation of spinel-structured $(Mg,Fe)_2SiO_4$ (γ-olivine) into (Mg,Fe)O (magnesiowüstite) plus perovskite-structured $(Mg,Fe)SiO_3$. Exothermic phase changes enhance, while endothermic phase changes inhibit material flow across them. Laboratory measurements of the Clapeyron slope, γ, for the spinel - post-spinel transition yield values of –2.8 MPa/K [*Ito and Takahashi*, 1989] and –3±1 MPa/K [*Akaogi and Ito*, 1993]. *Bina and Helffrich* [1994] recently reexamined some of the earlier measurements and found values for the Clapeyron slope to be somewhat reduced (–1.9 to –2.7 MPa/K). Laboratory experiments [*Ito and Takahashi*, 1989] require the phase-loop width (the depth interval over which the multivariant phase change occurs) to be a few km or less, consistent with seismic observations [*Benz and Vidale*, 1993]. As the role of the 410-km phase transition in determining the degree of convective stratification has been found to be less important than variations in the strength of the 660-km phase change [*Tackley et al.*, 1994], we will concentrate on studying the influence of an endothermic phase transition at a depth similar to the γ-olivine/perovskite transition on mantle flow.

We begin by investigating the effects of varying the strength of an endothermic phase change at a non-dimensional depth $r = 0.875$. The effectiveness of a phase transition in inhibiting or assisting flow due to the buoyancy associated with its vertical deflection can be described by the non-dimensional phase buoyancy parameter, $P = \gamma \Delta\rho / \alpha\rho^2 g(a-b)$ [*Christensen and Yuen*, 1985], where $\Delta\rho$ is the density increase across the phase boundary, α is thermal expansivity, ρ is density, g is gravitational acceleration, and b and a are the inner and outer radii, respectively. Details of the numerical implementation of phase boundary effects are given in Appendix A. Figure 3.16 shows the influence of the phase buoyancy for three bottom-heated experiments with P ranging from -0.1 to -0.2 (corresponding to Clapeyron slopes ranging from –2.5 MPa/K to –5 MPa/K, with the other parameters fixed to their reference values (see Table A.1)). For comparison, results for a run without a phase change ($P = 0$) are also shown. Increasing the magnitude of the phase buoyancy parameter leads to an increased flow stratification. This is evident in the $\overline{T}$-profile (Figure 3.16*a*) where a temperature increase indicating the development of a boundary layer takes place around $r = 0.875$. σ_u decreases and develops a kink, diagnostic of flow stratification, at the same depth (Figure 3.16*b*). σ_T and α_T both show an increase in the region above the phase transition approaching values of the reference run ($P = 0$) below the phase boundary (Figures 3.16*d,f*). ρ_T exhibits a distinct minimum around the phase transition, indicating a decorrelation of features across this depth, characteristic of stratified flows (Figure 3.16*e*). Figure 3.17 shows experiments predominantly heated from within for the same values of P. The overall influence of the phase boundary on the correlation diagnostics is similar. Owing to the emphasized downwellings, characteristic of predominantly internally heated systems, being closer to the phase boundary, the phase-change-induced stratification is enhanced compared to the corresponding bottom-heated runs. A pronounced episodicity in the time series of the non-dimensional radial mass flux, as found by *Peltier and Solheim* [1992], was only observed for the experiments with $P = -0.2$. Their parameterization of the phase transition uses the "phase-function" method [*Christensen and Yuen*, 1985], while the experiments described above use the "sheet-mass-anomaly" method [*Tackley et al.*, 1993]. A comparison between the two formulations is shown in Figure 3.18. For the parameters chosen the two methods yield almost identical results. The agreement is expected to be less good once the phase deflection becomes comparable in size to the characteristic scale of convective features at higher Rayleigh numbers and the phase-loop width is decreased to approach earth-like values [*Peltier and Solheim*, 1992].

A principal shortcoming of the experiments described above is that cold downwellings have the same strength as the surrounding material. One might expect stiff, high-viscosity slabs to penetrate an endothermic phase boundary more easily than weak downwellings. The only numerical experiments to date that have investigated the interaction of a strong high-viscosity downwelling with an endothermic phase boundary, used a specialized geometry with a two-sided high-viscosity slab forced to subduct vertically along a side-wall boundary [*Christensen and Yuen*, 1984; *Zhong and Gurnis*, 1994]. To study the influence of strong, cold, high-viscosity downwellings ("slabs") on phase-change modulated flows in a more realistic subduction geometry, we use a temperature-dependent rheology employing the same mobilization scheme as above (equation 3.1). Figure 3.19 shows the comparison of correlation diagnostics between two experiments with temperature-dependent viscosity and their isoviscous counterparts for values of $P = -0.1$ and -0.15. All parameters diagnostic of stratification show that the amount of layering is reduced for the temperature-dependent cases. However, the phase-change induced layering is still apparent in the two-point correlation diagnostics of flows with a temperature-dependent viscosity (most pronounced in the correlation minimum in ρ_T). This diagnostic also reveals that the relative decrease around $r = 0.875$ can be even larger for a temperature-dependent rheology than for constant viscosity (Figure 3.19*e*). Reducing the maximum viscosity contrast due to temperature dependence from 10^4 to 10^3 does not alter the correlation diagnostics significantly.

Another aspect of phase-change modulated flow that has received little attention is the combination of a phase transition and a rapid viscosity increase at the same depth. Experimental studies indicate that an abrupt viscosity increase at a phase transition may be expected due to an increase in the activation energy, which is related to the density increase across the phase transition [*Sammis et al.*, 1977; ***Ranalli and Fischer***, 1984]. With the phase boundary fixed in depth, the "sheet-mass-anomaly" method allows us to investigate the effects of a combined phase transition with a step-function viscosity increase. Figure 3.20 shows a comparison between an experiment with an endothermic phase change ($P = -0.1$) plus a 30-fold viscosity increase at $r = 0.875$ and a run with the depth-dependent viscosity only. The combination of the phase boundary and the viscosity increase lead to a system slightly more stratified than with a viscosity increase alone, indicated by a small temperature increase in $\overline{T}$, a local minimum in σ_u, local maxima in σ_T and α_T, and a larger increase in ρ_T across $r = 0.875$ (see Figures 3.20*a-b*, *c-f*). However, the influence of the viscosity increase on determining the flow structure is clearly dominant as can be seen by comparing Figure 3.20 to Figure 3.17, where the corresponding correlation diagnostics for isoviscous flows are depicted. The same step-function viscosity increase and phase buoyancy parameter were used for the experiments analyzed in Figure 3.21. In these simulations the rheology also depends on temperature according to equation 3.1. Again, the presence of an endothermic phase transition slightly increases the propensity for layering, evident in the boundary layer structure discernible for $\overline{T}$, the stronger local minimum in σ_u, local maxima in σ_T and α_T, as well as in the larger increase in ρ_T across $r = 0.875$ for the experiment with an endothermic phase transition (see Figures 3.21*a-b*, *c-f*). However, as for the case without temperature-dependent rheology, the step-function viscosity increase alone is clearly responsible for most of the stratification features observed (compare to Figure 3.19). This should come as no surprise, as the local buoyancy force due to a phase change with $P = -0.1$ is altered by 10%, while a 30-fold viscosity increase leads to a change in Ra_B by a factor of 30.

Figure 3.22 shows the effects of a phase transition on radial averages of the normalized angular power spectrum. Both the isoviscous run (Figure 3.22*a*) and the experiment with a 30-fold viscosity increase at $r = 0.875$ (Figure 3.22*b*) show a reddening of the power spectrum relative to their counterparts without a phase change. This effect has also been observed in 3D spherical-shell experiments [*Tackley et al.*, 1993; *Tackley et* *al.*, 1994]. The peaks in the power spectra with a high-viscosity lower layer, are again due to the dominance of strong upwellings. As discussed in the previous section, a mobilizing, temperature-activated rheology would diminish their importance on the flow structure.

In summary, two-point correlation functions are well-suited for capturing the effects of phase transitions on mantle flow simulations. Diagnostics of the temperature field, in particular ρ_T, document phase change effects as well as diagnostics based on the velocity field. Plus, the temperature diagnostics can be compared directly to seismic observations. As have others [e.g., *Solheim and Peltier*, 1994], we find that internal heating increases the propensity for layering. Strong, cold "slabs" are able to penetrate a phase boundary more readily, as expected. However, the flow modulation due to the phase change is still quite apparent for experiments with temperature-dependent rheology. We also find that combining an endothermic phase change with a rapid viscosity increase does not alter the flow significantly with respect to the case without a phase boundary. Adding an exothermic phase transition at 410 km depth, which reduces the propensity for layering [*Solheim and Peltier*, 1994; *Tackley et al.*, 1994], should further diminish the net importance of phase transitions for modulating flow.

SUPERCONTINENTS

One feature distinguishing convection in the earth's mantle from other terrestrial planets, is the participation of its outer boundary layer in the flow. The earth's lithosphere, the cold thermal boundary layer of the convecting mantle, is divided into several plates. Due to the thermally activated viscosity these plates are strong, with surface deformation concentrated at plate boundaries. The interaction of surface plates with the mantle flow is expected to have important consequences for the observed flow structure. Modeling mantle convection with surface plates where plates geometries evolve with time is a previously unconquered challenge. We will present one approach for modeling plates with evolving geometry in the next section. Here, we study a simplified system: the influence of a single large, non-subducting plate ("supercontinent") on the flow system. *Gurnis and Zhong* [1991]and *Zhong and Gurnis* [1993] have performed this type of numerical experiment for a constant viscosity fluid. They found that the presence of a supercontinent results in a reorganization of the large-scale flow structure leading to a reddening of the angular power spectrum (which they calculated for individual temperature snapshots). We extend this analysis to the complete two-point correlation function, and calculate the angular power spectrum from the angular correlation function for flows with depth-dependent and depth- and temperature-dependent rheologies. The supercontinent is modeled as a high-viscosity cap of size, s, defined as the ratio of horizontal plate dimension and depth of the convecting layer, and a dimensionless thickness of 0.036. For further details on the model parameterization see *Zhong and Gurnis* [1993].

Figure 3.23 shows a comparison of correlation diagnostics between two flows with a 30-fold viscosity increase at r = 0.75, one with supercontinent. Owing to its high viscosity the supercontinent thickens the cold thermal boundary layer leading to a lower average temperature, $\bar{T}$ (Figure 3.23*a*). While σ_u is nearly unchanged (Figure 3.23*b*), σ_w exhibits a disappearance of the return flow peak above the viscosity increase at mid-depth (Figure 3.23*c*). This is due to the fact that the supercontinent organizes the large-scale flow structure beneath it, usually leading to a single, large convection cell aligned with the plate with most of the return flow in the high-viscosity lower layer. σ_T shows an increase near the surface, where horizontal temperature contrasts are enhanced by the presence of the supercontinent (3.23*d*). α_T is affected in a similar manner (Figure 3.23*f*). The size of these near-surface maxima is directly related to the size of the high-viscosity plate. ρ_T shows a local maximum within the supercontinent and a minimum just below it. This can be explained by the thermal blanketing effect of the plate, which leads to hotter than average material below the continent, while the continent itself has a negative temperature anomaly throughout.

Figure 3.24 shows a comparison between two flows with temperature-dependent viscosity, one with a supercontinent. We employ the viscosity law introduced in equation

3.1. The two-point correlation diagnostics are modified in a manner similar to that described above. We have also investigated flows with constant and depth-and temperature-dependent rheology and found similar modifications of the two-point correlation functions. Figure 3.25 shows a comparison between radial averages of S_T/σ_T^2 for these four rheologies. Three isoviscous runs, predominantly heated from within, are compared in Figure 3.25*a*. The presence of a supercontinent significantly reddens the angular power spectrum. For the larger plate ($s = 4$), the power decreases rapidly from its peak at angular degree, $l = 1$, with $l = 3$ being reduced by an order of magnitude. This decrease in power is somewhat lessened for the smaller plate ($s = 2$), where the power is reduced by a factor of three at $l = 5$ and stays relatively constant out to about angular degree 30. The case without a supercontinent has its power-spectral peak around $l = 20$. Similar trends can be observed for the other experiments, with depth-dependent rheology (Figure 3.25*b*), temperature-dependent rheology (Figure 3.25*c*), or depth- and temperature-dependent rheology (Figure 3.25*d*). The principal influence of the supercontinent is to increase the power at the lowest harmonics (always peaking at $l =$ 1). The power spectrum then decreases rapidly with a roll-off and corner-wave number that depends on plate size. The addition of a high-viscosity, non-subducting plate to the convective system introduces a second characteristic scale, which dominates the power spectrum out to wave-numbers characteristic of its size, relatively unaffected by other variations in rheology.

EVOLVING PLATES

Using a single, large non-subducting supercontinent we gained some preliminary insight into the influence of surface plates on the mantle flow system. However, supercontinents were not present for extended periods of time in the earth's history and thus a more realistic modeling approach with a larger number of plates whose geometries vary with time, mimicking the evolution of plates on the earth's surface, is clearly warranted. While the presence of a supercontinent leads to a reorganization of the flow system, it mainly affects the flow structure beneath the plate. Elesewhere in the fluid small-aspect-ratio convection cells still dominate. While the large supercontinent leads to a reddening of the angular power spectrum, the spectrum rolls-off rapidly from the maximum, which always occurs at angular degree one.

In this section we describe an approach that allows a more realistic modeling of mantle convection. We model plates by using a temperature-dependent viscosity combined with weak zones (small regions of low viscosity) advected by the flow. This results in rigid plates whose geometries evolve with time. The low-viscosity regions mimic plate boundary regions, where the lithosphere may be weakened due to faulting and brittle failure or non-linear effects of stress-dependent rheology creating a lower effective viscosity [*King and Hager*, 1990]. Past studies have used low-viscosity weak zones fixed to the numerical grid to allow upwellings and downwellings of an otherwise immobile, high-viscosity lid [*Kopitzke*, 1979; *Schmeling and Jacoby*, 1981]. This approach has been shown to yield similar results to other methods for modeling plate-like behavior [*King et al.*, 1992]. Novel to our study are that we use a number of weak zones not fixed to the grid, but advected by the mantle flow. This leads to a flow system with cold, strong, high-viscosity surface plates, separated by regions of low viscosity, which can be identified with ridges and trenches. As the weak zones are advected with the flow, plate geometries change with time in a dynamically self-consistent manner (i.e., not by the variation of prescribed boundary conditions). When two weak zones collide, one is relocated to the region of maximum horizontal stress in the plate system. The viscosity law takes the form

$$\eta(r,T) = \begin{cases} \eta_0(r)\eta_1(T)[1+(\frac{\eta_w}{\eta_0}-1)\sum_i^{N_w} \mathrm{H}(\varphi-\varphi_{w_i})\mathrm{H}(\varphi_{w_i}+\Delta\varphi_w-\varphi)] & 1-\delta_{bl} \le r \le 1 \\ \eta_0(r)\eta_1(T) & b \le r < 1-\delta_{bl} \end{cases} ,(3.2)$$

where $\eta_0(r)$ and $\eta_1(T)$ have the same form as before, φ_{w_i} is the position of the left side of the ith weak-zone of width $\Delta\varphi_w$ and viscosity η_w, N_w is the total number of weak zones, and H is the Heavyside step function.

Figure 3.26 shows an example of a convection experiment employing this formulation with 10 plates. The effective Rayleigh number for this run was 1.5×10^6;

73% of the time-averaged surface heat flux was generated internally. $\eta_0(r)$ is a two-layer model with a 30-fold viscosity increase at $r = 0.75$, identical to the temperature-dependent run without plates but a mobilized upper boundary layer at similar Rayleigh number and internal heating rate shown in Figure 3.7. Temperature and velocity fields (Figure 3.26*a*) and corresponding viscosity fields (Figure 3.26*b*) show three snapshots widely separated in time. The variable-sized plates can be best identified in the viscosity field, where the high-viscosity plates (dark gray) are separated by low-viscosity weak zones (white). A visual comparison of Figures 3.26 and 3.7 reveals the main differences: while the experiment without plates has numerous downwellings, leading to many convection cells of small aspect-ratio, only a few downwellings are present at any one time for the run using the viscosity law (3.2). Consequently, the aspect ratio of convection cells is larger. On the other hand, the relative strength of upwellings and downwellings, and in particular the ability of the strong downwellings to penetrate the viscosity barrier at mid-depth is similar for both viscosity laws. Before investigating similarities and differences between flows resulting from the viscosity laws (3.2) and (3.1) with two-point correlation diagnostics, we first discuss the effects of varying different parameters in equation (3.2).

Figure 3.27 shows the two-point correlation diagnostics for three convection runs with different numbers of weak zones. The overall effect of changing N_w from six to ten to fourteen is relatively small. $\bar{T}$ decreases slightly with increasing N_w, as the convective system becomes more efficient in removing heat (Figure 3.27*a*). The time-averaged amount of heat generated internally drops from 56% for $N_w = 6$ to 52% for $N_w = 14$. σ_u, σ_w, and σ_T are remarkably similar for the different number of plates (Figures 3.27*b*-*d*). The peak of ρ_T is slightly reduced/increased for the cases with six/fourteen plates, as downwellings (which dominate ρ_T for temperature-dependent systems without a viscosity increase with depth) are less/more numerous compared to the run with $N_w = 10$ (Figure 3.27*e*). The main difference in α_T occurs near the surface, where the correlation angle is proportional to the average plate size (Figure 3.27*f*). We also studied the influence of modifying the weak-zone size, weak zone viscosity, and plate viscosity on the flow structure. We found that if the low-viscosity regions were too small or not weak enough, the plate system would evolve towards a state where a single plate encompasses most of the surface with many small plates clustered closely together, with little or no horizontal motion between them. Modifying the plate viscosity, by varying the maximum viscosity contrast due to temperature-dependence from 10^3 to 10^4 has a smaller effect on the flow structure. For subsequent experiments we used $Nw = 10$, $\Delta\varphi_w \times \delta_{bl} = 0.052 \times 0.036$, $\eta_w = 10^{-2}$.and allowed $\eta_1(T)$ to vary by three orders of magnitude.

Figure 3.28 shows the comparison of two-point correlation diagnostics for the two convection experiments with temperature-dependent viscosity and a 30-fold viscosity increase at $r = 0.75$, depicted in Figures 3.7 and 3.26. While similar in overall character, some small, but notable differences exist. The $\bar{T}$ profile for the run with ten plates has a slightly thicker boundary layer and a somewhat larger negative temperature gradient in the interior (Figure 3.28*a*). σ_u is increased near the surface, as the weak zones allow for both ridges and trenches to develop, while the viscosity law (3.1) does not facilitate for upwellings to reach the surface (Figure 3.28*b*). The influence of plates in organizing the flow structure leads to larger horizontal flow velocities. This is documented as an increase in σ_w near the surface (Figure 3.28*c*). It is remarkable how similar the velocity diagnostics for the temperature-dependent flow with plates and the equivalent non-temperature-dependent run shown in Figures 3.10*c* and 3.11*c* are. As the rms-velocity variations, σ_T shows increased near-surface variability and is reduced in the interior for the case using the viscosity law (3.2) (Figure 3.28*d*). A similar decrease in the interior is also evident for ρ_T (Figure 3.28*e*). This can be explained by the smaller number of downwellings for the case with plates. Owing to the presence of plates, α_T shows a large increase near the surface (Figure 3.28*f*). While all these differences are readily apparent, it should be emphasized that the first-order features of the two-point correlation functions, namely features associated with the step-function viscosity increase with depth, are the same for both experiments employing different rheology laws. This may also serve as an a posteriori validation of the ad-hoc viscosity law (3.1).

Two experiments with surface plates, differing only in the presence of an endothermic phase transition ($P = -0.1$) at $r = 0.875$ for one run, are shown in Figure 3.29. The differences in the two-point correlation diagnostics are similar to those documented in the section on phase changes. Namely, σ_T, ρ_T, and α_T show small local extrema around the phase transition depth (see Figures 3.28*d-f*).

Figure 3.30 shows two experiments with an endothermic phase transition ($P = -0.1$) and a 30-fold viscosity increase at r = 0.875, using viscosity laws (3.1) and (3.2), respectively. As in Figure 3.27 for the experiments without a stratification boundary, results from the two formulations agree in the first-order features of the correlation diagnostics, with similar differences in detail as those described above.

From our results in the section on supercontinents, we might anticipate the angular power spectrum to be altered significantly by the presence of surface plates. First we determined the influence of the number of variable-sized plates on the radial averages of S_T/σ_T^2. Figure 3.31*a* shows power spectra for cases with six, ten and fourteen plates. The spectral roll-off from the maximum ($l = 1$ for $N_w = 6$, $l = 2$ for $N_w = 10$ and 14) to angular degree $l = 20$ decreases as the number of plates increases. This is not surprising, considered that the largest plate is of size $s = 4$ or greater for approximately 90% of the time for the run with six plates, and only 6% of the time for the run with fourteen plates. Figure 3.31*b* shows a comparison between an experiment with ten plates, and two runs using the viscosity law (3.1), one with a supercontinent ($s = 4$). The case with variable-sized plates of has a spectrum significantly redder than the case without plates, however, the spectrum is richer in the low angular degrees and does not roll-off as rapidly as for the case with a supercontinent.

Figure 3.32 shows radially averaged normalized power spectra for runs with temperature-dependent rheology and a 30-fold, step-function viscosity increase with depth. Comparisons between experiments with ten plates, with a supercontinent and without any plates for cases with a viscosity increase at mid-depth (Figure 3.32*a*) are similar to those discussed above. Figure 3.32*b* compares two runs with ten plates and a viscosity increase at $r = 0.875$, one run also has an endothermic phase change ($P = -0.1$)

at this depth. The spectral roll-off is reduced for the case with an endothermic phase change. The same result was obtained for the equivalent experiments without the step-function viscosity increase, albeit differences between the spectra were somewhat smaller. This result is somewhat surprising, as we found earlier that for experiments with non-temperature-dependent viscosity the presence of a phase change caused the spectrum to redden. This illustrates that for non-linear systems such as mantle convection a combination of isolated effects does not necessarily yield the results expected from a linear superposition.

Modeling convection with surface plates whose geometries evolve with time in a dynamically self-consistent manner allows, for the first time, the investigation of plate-system statistics. Although somewhat beyond the scope of this thesis, we will introduce some statistics that have the potential of being compared to the geologic record. Examples of statistics that may be constrained by observations are the distribution of plate-sizes and relative plate-velocities with time. Figure 3.33 shows histograms of plate-size and relative plate-velocity for runs with six, ten, and fourteen plates. The statistics are compiled from the stationary part of the experiments also used for the two-point correlation analysis. Plate information is output at every timestep making $O(10^5)$ measurements available for each run. The size-frequency distribution shows that for all three cases, small plates dominate (Figures 3.33*a*, *c*, *e*). As N_w increases the prevalence of small plates increases. While for $N_w = 6$ a single plate occupied as much as 85% of the total plate area, for $N_w = 14$ no plate ever exceeded a fractional size of 0.4. The plate-velocity histogram follows a similar distribution (Figures 3.33*b*, *d*, *f*). Peaked at the lowest velocity bin, it decreases exponentially with increasing velocity. Figure 3.34 shows the same plate statistics for three experiments with ten plates and a 30-fold viscosity increase with depth. Both the plate-size and plate velocity distributions are less one-sided. This is particularly evident for the cases with a viscosity increase at $r = 0.875$ (Figures 3.34*c*-*f*). Another statistic of interest is the average relative plate velocity as a function of plate size (Figure 3.35). Average plate velocities were calculated for the same size bins used above. The average plate velocities decrease nearly monotonically for cases without a viscosity stratification (Figure 3.35*a*). Viscously stratified systems exhibit a more uniform average plate-velocity distribution (Figure 3.35*b*).

Plate statistics such as those shown above illustrate some potential applications of this modeling approach. Being able to model mantle convection with surface plates in a dynamically self-consistent manner, offers the possibility of applying a new data set to constrain the range of possible convection models – the plate tectonic record. It is intriguing that at present, for example, plate velocity is not a function of plate size.

The plate system modeled above can be most closely identified with oceanic plates. An interesting question is how the presence of non-subducting continental plates (perhaps with thick roots) would modify the flow system and its effects on the plate statistics. One of the better established facts about the earth's plate tectonic system is, that at present (and throughout the Cenozoic) continental plates move slower than oceanic plates [*Gordon and Jurdy*, 1986]. Incorporating continents into the convection model is important for another reason. As global plate-reconstructions are available only for the last 180 million years [*Engebretson et al.*, 1992], it would be important to use plate motion information from continents to extend this record back in time.

We introduced a new approach to modeling plates by using a temperature-dependent viscosity combined with weak zones advected by the flow. This results in rigid plates whose geometries evolve with time. The main influence of plates is to organize the large-scale flow structure, resulting in a reddening of the angular power spectrum of thermal anomalies. The long-wavelength component of the radially averaged power spectrum shows a structure similar to that calculated from global tomographic models, but differs from numerical experiments with a single supercontinent, which exhibit a power spectrum that rolls off rapidly from the maximum at $l = 1$.

The average flow properties can be quantified using two-point correlation functions. Comparing calculations incorporating surface plates to other temperature-dependent experiments where the surface boundary layer is mobilized by limiting its viscosity (which allows strong, high-viscosity downwellings to form), we find many of the characteristic features of the two-point correlation functions to be similar. The main differences are an increase in the near-surface rms-variation of the horizontal velocity and angular correlation length, and a shift of the maximum in the radial rms-velocity to shallower depths.

This approach to modeling mantle convection with surface plates lends itself to a statistical analysis of the plate system, which may be used for comparison to the earth's plate tectonic history. An analysis of plate-size and plate-velocity distributions reveals differences between models with a step-function viscosity increase with depth and those with constant η_0.

DISCUSSION

In this chapter we have shown that the two-point averages of the temperature fields (T-diagnostics) and flow velocity fields (V-diagnostics) quantify some important aspects of mantle convection experiments. As an example, we have investigated the effects of a discontinuity in the radial viscosity profile. The radial flux diagnostic σ_u indicates that a viscosity increase of a factor of 30 or less yields a weakly stratified flow (Figure 3.10). The horizontal flux diagnostic σ_w reveals that the flow organization is sensitive to the depth of the viscosity increase (Figure 3.11). A jump at mid-depth induces a significant horizontal return flow at the base of the upper layer, which is absent in the model with a jump at quarter-depth. The latter approximates the viscosity increase at the 660-km discontinuity in the viscosity model of *Hager et al.* [1985]. We also obtained no return-flow peak in σ_w for simulations based on the more elaborate radial viscosity structures recently proposed by *King and Masters* [1992] and *Forte et al.* [1993]. These results suggest that viscosity increases comparable to those that have been proposed for the earth's transition zone might have only a minor effect on the overall flow organization, whereas rapid increases in the lower mantle could significantly influence the pattern of the return flow.

We have used the two-point averages to quantify the effects of temperature-dependent viscosity. To avoid the development of a stagnant lid typical of strongly-temperature-dependent fluids (but not the earth) we have employed two different approaches. In one method the viscosity in the surface boundary layer is limited to a value low enough for downwellings to develop. In the second approach a mobilization of the is achieved by inserting low-viscosity regions into the cold boundary layer. These weak zones are advected by the flow. This leads to plates whose geometries evolve with time. The correlation diagnostics obtained from convection experiments using these two methods are remarkably similar. The most notable differences are an increase in σ_T and α_T and a reduction in ρ_T near the surface, for cases with plates (Figures 3.28 and 3.30). Surface plates also influence the overall flow organization, leading to larger aspect-ratio convection cells. This results in a reddening of the angular power spectrum of thermal anomalies. Power spectra for experiments with evolving plates differ distinctly from both cases without plates or runs with a single supercontinent (Figure 3.31). Modeling mantle convection with surface plates also allows a statistical analysis of the plate system, which may be used for a comparison with the earth's plate tectonic history. An analysis of plate-size and plate-velocity histograms reveals differences between flow models with a step-function viscosity increase with depth and experiments with constant η_0 (Figure 3.34).

The effects of temperature-dependent viscosity on the σ-diagnostics (Figures 3.10-3.12) or the α_T diagnostic (average plume width) in the convecting interior (Figure 3.14) are small. Changes in the radial correlation length are more pronounced (Figure 3.13). The near-surface peak in ρ_T is amplified owing to the greater viscosity of the cold downwellings, and the increase in ρ_T associated with a viscosity jump at mid-depth (Figures 3.13*c*,*d*) is markedly reduced. The latter effect can be explained by comparing Figures 2.1 and 3.7: the hot upwellings, which are strong and nearly stationary when the viscosity is temperature independent, are mobilized by the temperature-dependent viscosity and disrupted by the cold, high-viscosity downwellings. This suggests that the hypothesis, that the apparent fixing of upwelling plumes results from the temperature dependence of viscosity, needs to be reevaluated with three-dimensional flow calculations. Experiments with a high-viscosity lower layer but without temperature dependent rheology greatly emphasize the role of upwellings for the overall flow organization, especially in a 2D geometry.

Another mechanism for a radial stratification of mantle flow are phase changes. We have investigated flow systems with an endothermic phase transition at a depth approximating the depth of the spinel - post-spinel transition in the earth. The effects of an endothermic phase transition are well documented in the two-point correlation functions, most notably in ρ_T. This is true even when the rheology is temperature-dependent, although the flow stratification is weaker in this case. Combining an endothermic phase change with a rapid viscosity increase does not alter the flow significantly compared to the case with no phase boundary.

Our experiments have shown that the two-point correlation functions are diagnostic of radial flow stratification. To define the degree of layering in a convecting system, both V-diagnostics, such as σ_u (or, equivalently, *Peltier and Solheim's* [1992] radial flux diagnostic) and T-diagnostics, ρ_T for example, can be used. While either is suitable to characterize numerical convection experiments, T-diagnostics are, through the dependence of seismic wave speeds on temperature, easily related to mantle observations. In chapter 4 we will focus on determining two-point correlation functions for global and regional tomographic models.

Another area (not further pursued in this thesis) where the techniques employed here might find further application in the study of turbulence. For example, a transition from soft to hard turbulence has been observed at high Rayleigh numbers, characterized by the breakup of continuous plumes traversing the fluid layer [*Heslot et al.*, 1987; *Castaing et al.*, 1989; *Hansen et al.*, 1990]. From a visual inspection of the temperature fields, the transition is seen to occur at $Ra_B \sim 10^7$ for infinite Prandtl number convection in a small aspect-ratio box [*Hansen et al.*, 1992]. To date, laboratory experiments [e.g., *Heslot et al.*, 1987], numerical simulations [e.g., *DeLuca et al.*, 1990; *Hansen et al.*, 1990; *Vincent and Meneguzzi*, 1991], and theoretical studies [e.g., *Castaing et al.*, 1989] have investigated the shape of the probability density functions (PDFs) of flow variables, the slope of the kinetic energy wavenumber spectrum, and the *Nu-Ra* scaling law as diagnostics for the transition to hard turbulence. Most of the quantitative analyses have focused on the local structure of the temperature and velocity fields at only a few points, and several of the diagnostics have been called into question [*DeLuca et al.*, 1990; *Solomon and Gollub*, 1991; *Hansen et al.*, 1992]. A global measure, like the two-point averages described in this paper, may be better suited for this purpose. We have seen that there is a clear break in the power-law relationships for $\overline{\rho}_T$ and $\overline{\alpha}_T$, but not in those for Nu_δ or $\overline{\sigma}_T$, at the transition from steady-state to time-dependence (cf. Figures 3.1, 3.4-3.6). We speculate that the transition to hard turbulence might be similarly reflected in a change of the power-law behavior for $\overline{\rho}_T$ and $\overline{\alpha}_T$.

REFERENCES

Akaogi, M., and E. Ito, Refinement of enthalpy measurement of MgSiO3 perovskite and negative pressure-temperature slopes for perovskite-forming reactions, *Geophys. Res. Lett.*, *20*, 1839-1842, 1993.

Ashby, M. F., and R. A. Verrall, Micromechanisms of flow and fracture and their relevance to the rheology of the upper mantle, *Philos. Trans. R. Soc. London, Ser. A*, *288*, 59-95, 1977.

Balachandar, S., and L. Sirovich, Probability distribution functions in turbulent convection, *Phys. Fluids A*, *3*, 919-927, 1991.

Benz, H. M., and J. E. Vidale, Sharpness of upper-mantle discontinuities determined from high-frequency reflections, *Nature*, *365*, 147-150, 1993.

Bina, C. R., and G. Helffrich, Phase transition Clapeyron slopes and transition zone seismic discontinuity topography, *J. Geophys. Res.*, *99*, 15853-15860, 1994.

Castaing, B., G. Gunaratne, F. Heslot, L. Kadanoff, A. Libchaber, S. Thomae, X.-Z. Wu, S. Zaleski, and G. Zanetti, Scaling of hard turbulence in Rayleigh-Bénard convection, *J. Fluid Mech.*, *204*, 1-30, 1989.

Chave, A. D., and D. J. Thomson, Some comments on magnetotelluric response function estimation, *J. Geophys. Res.*, *94*, 14215-14225, 1989.

Christensen, U., Convection with pressure- and temperature-dependent non-Newtonian rheology, *Geophys. J. R. Astron. Soc.*, *77*, 343-384, 1984.

Christensen, U. R., and D. A. Yuen, The interaction of a subducting lithospheric slab with a chemical or phase boundary, *J. Geophys. Res.*, *89*, 4389-4402, 1984.

Christensen, U. R., and D. A. Yuen, Layered convection induced by phase transitions, *J. Geophys. Res.*, *90*, 10, 1985.

DeLuca, E. E., J. Werne, R. Rosner, and F. Cattaneo, Numerical simulations of soft and hard turbulence: Preliminary results for two-dimensional convection, *Phys. Rev. Lett.*, *64*, 2370-2373, 1990.

Engebretson, D. C., K. P. Kelley, H. J. Cashman, and M. A. Richards, 180 million years of subduction, *GSA Today*, *2*, 93-95, 1992.

Forte, A. M., A. M. Dziewonski, and R. L. Woodward, Aspherical structure of the mantle, tectonic plate motions, nonhydrostatic geoid, and topography of the core-mantle boundary, in *Dynamics of Earth's deep interior and Earth rotation*, edited by J. L. LeMouel, D. E. Smylie, and T. Herring, *Geophysical Monograph*, *72*, pp. 135-166, 1993.

Gordon, R. G., and D. M. Jurdy, Cenozoic global plate motions, *J. Geophys. Res.*, *91*, 12389-12406, 1986.

Gurnis, M., and G. F. Davies, Numerical study of high Rayleigh number convection in a medium with depth-dependent viscosity, *Geophys. J. R. Astron. Soc.*, *82*, 523-541, 1986.

Gurnis, M., and S. Zhong, Generation of long wavelength heterogeneity in the mantle by the dynamic interaction between plates and convection, *Geophys. Res. Lett.*, *18*, 581-584, 1991.

Hager, B. H., R. W. Clayton, M. A. Richards, R. P. Comer, and A. M. Dziewonski, Lower mantle heterogeneity, dynamic topography and the geoid, *Nature*, *313*, 541-545, 1985.

Hager, B. H., and M. A. Richards, Long-wavelength variations in Earth's geoid; physical models and dynamical implications, *Philos. Trans. R. Soc. London, Ser. A*, *328*, 309-327, 1989.

Hansen, U., and A. Ebel, Time-dependent thermal convection; a possible explanation for a multiscale flow in the Earth's mantle, *Geophys. J. R. Astron. Soc.*, *94*, 181-191, 1988.

Hansen, U., D. A. Yuen, and S. E. Kroening, Transition to hard turbulence in thermal convection at infinite Prandtl number, *Phys. Fluids A*, *2*, 2157-2163, 1990.

Hansen, U., D. A. Yuen, S. E. Kroening, and T. B. Larsen, Dynamical consequences of depth-dependent thermal expansivity and viscosity on mantle circulations and thermal structure, *Phys. Earth Planet. Inter.*, *77*, 205-223, 1993.

Hansen, U., D. A. Yuen, and A. V. Malevsky, Comparison of steady-state and strongly chaotic thermal convection at high Rayleigh number, *Phys. Rev. A*, *46*, 4742-4754, 1992.

Heslot, F., B. Castaing, and A. Libchaber, Transitions to turbulence in helium gas, *Phys. Rev. A*, *36*, 5870-5873, 1987.

Honda, S., D. A. Yuen, S. Balachandar, and D. Reuteler, Three-dimensional instabilities of mantle convection with multiple phase transitions, *Science*, *259*, 1308-1311, 1993.

Howard, L. N., Convection at high Rayleigh number, *11th Congress of Applied Mechanics*, 1109-1115, 1966.

Ito, E., and E. Takahashi, Postspinel transformations in the system Mg2SiO4-Fe2SiO4 and some geophysical implications, *J. Geophys. Res.*, *94*, 10637-10646, 1989.

King, S. D., C. W. Gable, and S. A. Weinstein, Models of convection-driven tectonic plates; a comparison of methods and results, *Geophys. J. Int.*, *109*, 481-487, 1992.

King, S. D., and B. H. Hager, The relationship between plate velocity and trench viscosity in Newtonian and power-law subduction calculations, *Geophys. Res. Lett.*, *17*, 2409-2412, 1990.

King, S. D., and T. G. Masters, An inversion for radial viscosity structure using seismic tomography, *Geophys. Res. Lett.*, *19*, 1551-1554, 1992.

Kopitzke, U., Finite element convection models; comparison of shallow and deep mantle convection, and temperatures in the mantle, *J. Geophys.*, *46*, 97-121, 1979.

Machetel, P., and P. Weber, Intermittent layered convection in a model mantle with an endothermic phase change at 670 km, *Nature*, *350*, 55-57, 1991.

McKenzie, D. P., J. M. Roberts, and N. O. Weiss, Convection in the earth's mantle: towards a numerical simulation, *J. Fluid Mech.*, *63*, 465-538, 1974.

Nataf, H. C., and F. M. Richter, Convection experiments in fluids with highly temperature-dependent viscosity and the thermal evolution of the planets, *Phys. Earth Planet. Inter.*, *29*, 320-329, 1982.

O'Connell, R. J., and B. H. Hager, On the thermal state of the earth, in *Physics of the Earth's Interior*, edited by A. M. Dziewonski, and E. Boschi, *Enrico Fermi International School of Physics*, *78*, pp. 270-317, Soc. Italiana di Fisica, Bologna, 1980.

Olson, P., and G. M. Corcos, A boundary layer model for mantle convection with surface plates, *Geophys. J. R. Astronom. Soc.*, *62*, 195-219, 1980.

Peltier, W. R., and L. P. Solheim, Mantle phase transitions and layered chaotic convection, *Geophys. Res. Lett.*, *19*, 321-324, 1992.

Ranalli, G., The microphysical approach to mantle rheology, in *Glacial isostasy, sea-level and mantle rheology*, edited by R. Sabadini, K. Lambeck, and E. Boschi, *NATO ASI Series*, *334*, pp. 343-378, Kluwer, Boston, 1991.

Ranalli, G., and B. Fischer, Diffusion creep, dislocation creep, and mantle rheology, *Physics of the Earth and Planetary Interiors*, *34*, 77-84, 1984.

Sammis, C. G., J. C. Smith, G. Schubert, and D. A. Yuen, Viscosity-depth profile of the Earth's mantle; effects of polymorphic phase transitions, *J. Geophys. Res.*, *82*, 3747-3761, 1977.

Schmeling, H., and W. R. Jacoby, On modelling the lithosphere in mantle convection with non-linear rheology, *J. Geophys.*, *50*, 89-100, 1981.

Solheim, L. P., and W. R. Peltier, Avalanche effects in phase transition modulated thermal convection: A model of earth's mantle, *J. Geophys. Res.*, *99*, 6997-7018, 1994.

Solomon, T. H., and J. P. Gollub, Thermal boundary layers and heat flux in turbulent convection: The role of recirculating flows, *Phys. Rev. A*, *43*, 6683-6693, 1991.

Tackley, P. J., D. J. Stevenson, G. Glatzmaier, and G. Schubert, Effects of an endothermic phase transition at 670 km depth in a spherical model of convection in the Earth's mantle, *Nature*, *361*, 699-704, 1993.

Tackley, P. J., D. J. Stevenson, G. A. Glatzmaier, and G. Schubert, Effects of multiple phase transitions in a 3-D spherical model of convection in the Earth's mantle, *J. Geophys. Res.*, *99*, 15877-15901, 1994.

Vincent, A., and M. Meneguzzi, The spatial structure and statistical properties of homogeneous turbulence, *J. Fluid Mech.*, *225*, 1-20, 1991.

Zhong, S., and M. Gurnis, Dynamic feedback between a continentlike raft and thermal convection, *J. Geophys. Res.*, *98*, 12, 1993.

Zhong, S., and M. Gurnis, Role of plates and temperature-dependent viscosity in phase change dynamics, *J. Geophys. Res.*, *99*, 15903-15917, 1994.

TABLES

Table 3.1. Convection experiments with constant material properties

Rayleigh number Ra_B	Internal heating rate Ra_H/Ra_B	Internal heat generation (%)	Numerical mesh $N_\varphi \times N_r$	Number of overturns†
5×10^4	0	0	200×32	0*
	7.5	71		156
	15	97		132
10^5	0	0	240×32	0*
	7.5	61		92
	15	88		135
2.5×10^5	0	0	270×36	0*
	7.5	51		111
	15	77		98
5×10^5	0	0	300×40	0*
	7.5	44		93
	15	69		92
10^6	0	0	360×48	196
	7.5	37		106
	15	61		88
	22.5	77		78
2.5×10^6	0	0	468×52	80
	7.5	30		78
	15	51		96
5×10^6	0	0	532×56	73
	7.5	27		84
	15	44		88
	22.5	58		80
	30	68		84

*Run reached a steady state.

†We adopt the definition of *Balachandar and Sirovich* [1991] for the overturn time.

Table 3.2. Power-law least-squares parameters for scaling relations

Relationship* $y \propto x$	Internal heating rate Ra_H/Ra_B	Power-law exponent m†	Power-law multiplier log$c$†
$Nu_S \propto Ra_B$	0	0.242 ± 0.006	-0.275 ± 0.039
	7.5	0.299 ± 0.007	-0.707 ± 0.041
	15	0.294 ± 0.008	-0.678 ± 0.048
$Nu_S \propto Ra_Q$	0	0.193 ± 0.003	-0.187 ± 0.026
	7.5	0.245 ± 0.006	-0.670 ± 0.044
	15	0.251 ± 0.008	-0.739 ± 0.059
$\bar{\sigma}_T \propto Ra_Q$	0 (steady-state)	-0.141 ± 0.005	-0.760 ± 0.031
	0 (time-dependent)	-0.137 ± 0.015	-0.770 ± 0.118
	7.5	-0.138 ± 0.001	-0.775 ± 0.004
	15	-0.151 ± 0.002	-0.804 ± 0.001
$\bar{\rho}_T \propto Ra_Q$	0 (steady-state)	-0.042 ± 0.028	-1.230 ± 0.184
	0 (time-dependent)	-0.276 ± 0.015	-0.144 ± 0.121
	7.5	-0.204 ± 0.002	-0.700 ± 0.018
	15	-0.196 ± 0.004	-0.742 ± 0.027
$\bar{\alpha}_T \propto Ra_Q$	0 (steady-state)	-0.107 ± 0.040	-1.193 ± 0.264
	0 (time-dependent)	-0.223 ± 0.062	-0.563 ± 0.488
	7.5	-0.253 ± 0.013	-0.387 ± 0.100
	15	-0.247 ± 0.011	-0.407 ± 0.083

*A power law relationship of the form $y = cx^m$ was assumed.

†Uncertainties in power-law exponent and multiplier were calculated using a delete–1 jackknife estimator [e.g., *Chave and Thomson*, 1989].

Table 3.3. Convection experiments with temperature-dependent viscosity*

Effective Rayleigh number $Ra_{B_{eff}}$†	Internal heat generation (%)	Boundary layer viscosity η_{bl}	Boundary layer thickness δ_{bl}	Number of overturns‡
4.0×10^6	78	50	0.036	38
2.9×10^6	79	50	0.027	13
4.6×10^6	82	50	0.045	12
3.3×10^6	68	10	0.036	17
3.6×10^6	86	100	0.036	11

*All calculations were performed using a semi-annulus with 266 × 56 elements using the viscosity law equation (3.1).

†The effective Rayleigh number, $Ra_{B_{eff}}$, is defined as the Bénard-Rayleigh number using the time-averaged strain-rate averaged viscosity [*Christensen*, 1984].

‡We adopt the definition of *Balachandar and Sirovich* [1991] for the overturn time.

Table 3.4. Convection experiments with depth-dependent and depth- and temperature-dependent viscosity

Viscosity profile	Effective Rayleigh number $Ra_{B_{eff}}$[*]	Internal heat generation (%)	Numerical mesh $N_\varphi \times N_r$[†]	Number of overturns[‡]
$\eta_0(r)=1 \quad 0.5 \le r \le 1$	5×10^6	68	532×56	84
	4.5×10^6	61	500×50[§]	35
$\eta_0(r)=\begin{cases} 1 & 0.75 \le r \le 1 \\ 10 & 0.5 \le r < 0.75 \end{cases}$	1.8×10^6	78	532×56	43
	2.6×10^6	71	266×56[§]	58
$\eta_0(r)=\begin{cases} 1 & 0.75 \le r \le 1 \\ 30 & 0.5 \le r < 0.75 \end{cases}$	1.1×10^6	83	532×56	59
	1.2×10^6	78	500×50[§]	38
$\eta_0(r)=\begin{cases} 1 & 0.875 \le r \le 1 \\ 30 & 0.5 \le r < 0.875 \end{cases}$	1.7×10^6	72	480×52	37
	0.9×10^6	69	480×52[§]	40

[*] The effective Rayleigh number, $Ra_{B_{eff}}$, is defined as the Bénard-Rayleigh number using the time-averaged strain-rate averaged viscosity [*Christensen*, 1984].

[†] The calculation using a 266×56 element mesh was performed in an semi-annulus with reflecting boundary conditions. All other calculation were performed in an annulus.

[‡] We adopt the definition of *Balachandar and Sirovich* [1991] for the overturn time.

[§] Viscosity was both depth-and temperature-dependent All calculations were performed using the viscosity law equation (3.1) with $\eta_{bl} = 50$ and $\delta_{bl} = 0.036$.

Table 3.5 Convection experiments with an endothermic phase change

Viscosity profile	Effective Rayleigh number $Ra_{B_{eff}}$[*]	Internal heat generation (%)	Numerical mesh $N_\varphi \times N_r$[†]	Phase buoyancy parameter P[‡]	Number of overturns N_{over}[§]
$\eta_0(r)=1 \quad 0.5 \le r \le 1$	5×10^6	0	240×56	−0.1	35
	5×10^6	0	240×56	−0.15	26
	5×10^6	0	240×56	−0.2	15
	5×10^6	69	240×56	−0.1	26
	5×10^6	69	480×56	−0.1	48
	5×10^6	71	240×56	−0.15	28
	5×10^6	71	266×78[‖]	−0.15	27
	5×10^6	73	240×56	−0.2	30
	3.3×10^6	62	240×56[¶]	−0.1	24
	2.3×10^6	60	240×56[¶]	−0.15	24
$\eta_0(r)=\begin{cases} 1 & 0.875 \le r \le 1 \\ 30 & 0.5 \le r < 0.875 \end{cases}$	1.3×10^6	78	240×56	−0.1	34
	2.2×10^6	70	480×56	−0.1	32
	1.3×10^6	78	240×56	−0.15	33
	0.9×10^6	69	240×56[¶]	−0.1	29

[*] The effective Rayleigh number, $Ra_{B_{eff}}$, is defined as the Bénard-Rayleigh number using the time-averaged strain-rate averaged viscosity [*Christensen*, 1984].

[†] The calculations using a 480×56 element mesh were performed in an annulus. All other calculations were performed in a semi-annulus with reflecting boundary conditions.

[‡] The ratio of phase-boundary Rayleigh number and Benard Rayleigh number, Ra_P / Ra_B, is 3.5 for all experiments. The phase change occurs at a non-dimensional depth of $r = 0.875$.

[§] We adopt the definition of *Balachandar and Sirovich* [1991] for the overturn time.

[‖] The "phase-function" method was used to parameterize the phase transition for this calculation. All other calculations were performed using the "sheet-mass anomaly" method.

[¶] Viscosity was both depth-and temperature-dependent All calculations were performed using the viscosity law equation (3.1) with $\eta_{bl} = 50$ and $\delta_{bl} = 0.036$.

Table 3.6. Convection experiments with a supercontinent

Viscosity profile	Effective Rayleigh number $Ra_{B_{eff}}$*	Internal heat generation (%)	Numerical mesh $N_\varphi \times N_r$	Plate Size s	Number of overturns N_{over}†
$\eta_0(r)=1 \quad 0.5\le r\le 1$	4.8×10^6	61	532×56‡	2	54
	4.4×10^6	65	532×56‡	4	70
	3.4×10^6	66	500×50§	4	34
$\eta_0(r)=\begin{cases}1 & 0.75\le r\le 1\\ 30 & 0.5\le r<0.75\end{cases}$	1.1×10^6	81	532×56‡	4	56
	2.1×10^6	79	500×50§	4	42
$\eta_0(r)=\begin{cases}1 & 0.875\le r\le 1\\ 30 & 0.5\le r<0.875\end{cases}$	5.3×10^5	80	532×56‡	4	46

*The effective Rayleigh number, $Ra_{B_{eff}}$, is defined as the Bénard-Rayleigh number using the time-averaged strain-rate averaged viscosity [*Christensen*, 1984].

†We adopt the definition of *Balachandar and Sirovich* [1991] for the overturn time.

‡Calculations were performed in an annulus with a purely depth-dependent viscosity.

§Calculations were performed in an annulus with a depth-and temperature-dependent rheology using the viscosity law equation (3.1) with $\eta_{bl}=50$ and $\delta_{bl}=0.036$.

Table 3.7. Convection experiments with evolving plates

Viscosity profile	Effective Rayleigh number $Ra_{B_{eff}}$*	Internal heat generation (%)	Numerical mesh $N_\varphi \times N_r$†	Number of weak zones N_w	Number of overturns N_{over}‡
$\eta_0(r)=1 \quad 0.5\le r\le 1$	3.3×10^6	54	480×52	10	55
	3.7×10^6	56	480×52	6	52
	3.0×10^6	52	480×52	14	44
	3.0×10^6	52	480×56§	10	54
$\eta_0(r)=\begin{cases}1 & 0.75\le r\le 1\\ 30 & 0.5\le r<0.75\end{cases}$	1.5×10^6	73	480×52	10	37
$\eta_0(r)=\begin{cases}1 & 0.875\le r\le 1\\ 30 & 0.5\le r<0.875\end{cases}$	1.6×10^6	70	480×52	10	32
	1.0×10^6	59	480×56§	10	31

*The effective Rayleigh number, $Ra_{B_{eff}}$, is defined as the Bénard-Rayleigh number using the time-averaged strain-rate averaged viscosity [*Christensen*, 1984].

†Calculations were performed in an annulus with temperature-dependent rheology using the viscosity law equation (3.2). Viscosity variations due to temperature-dependence are 10^3. Weak-zone size, $\Delta\varphi_w \times \delta_{bl} = 0.052\times0.036$, weak-zone viscosity, $\eta_w = 10^{-2}$.

‡We adopt the definition of *Balachandar and Sirovich* [1991] for the overturn time.

§An endothermic phase transition at $r = 0.875$ with phase buoyancy parameter, $P = -0.1$ was used.

FIGURE CAPTIONS

Fig. 3.1. Time-averaged surface Nusselt number, Nu_δ, as a function of (*a*) Bénard-Rayleigh number, Ra_B, and (*b*) Ra_Q, a Rayleigh number defined using the heat flux, for convection experiments in a cylindrical shell. Internal heating rates, Ra_H/Ra_B, are 0 (squares), 7.5 (circles), and 15 (triangles). Solid squares indicate that a steady state solution was reached. Further details of the convection calculations can be found in Table 3.1. Least-squares fit parameters are given in Table 3.2. For display reasons the $Ra_H/Ra_B = 15$ points were multiplied by 0.9.

Fig. 3.2. (*a*) Rms temperature variation, σ_T, (*b*) radial correlation length, ρ_T, and (*c*) horizontal correlation angle, α_T, as a function of normalized depth $z = 1 - r$ for convection experiments at $Ra_B = 5 \times 10^6$. Internal heating rates, Ra_H/Ra_B, are 0 (long dashed lines), 7.5 (intermediate dashed), 15 (short dashed), 22.5 (dotted), and 30 (solid). Further details of the convection calculations can be found in Table 3.1.

Fig. 3.3. (*a*) Rms temperature variation, σ_T, (*b*) radial correlation length, ρ_T, and (*c*) horizontal correlation angle, α_T, as a function of normalized depth $z = 1 - r$ for a suite of convection experiments at $Ra_H/Ra_B = 15$. Bénard-Rayleigh numbers are 10^5 (long dashed lines), 5×10^5 (short dashed), 10^6 (dotted), and 5×10^6 (solid). Further details of the convection calculations can be found in Table 3.1.

Fig. 3.4. Radially-averaged rms temperature variation, $\overline{\sigma}_T$, as a function of Ra_Q for convection experiments in a cylindrical shell. Internal heating rates, Ra_H/Ra_B, are 0 (squares), 7.5 (circles), 15 (triangles), and 22.5 and 30 (crosses). Solid squares indicate that a steady state solution was reached. A dashed line connects the least-squares lines for the steady and time-dependent bottom-heated regimes. Further details of the

convection calculations can be found in Table 3.1. Least-squares fit parameters are given in Table 3.2.

Fig. 3.5. Radially-averaged radial correlation length, $\bar{\rho}_T$, as a function of Ra_Q for convection experiments in a cylindrical shell. Internal heating rates, Ra_H/Ra_B, are 0 (squares), 7.5 (circles), 15 (triangles). Solid squares indicate that a steady state solution was reached. A dashed line connects the least-squares lines for the steady and time-dependent bottom-heated regimes. Values at the lowest Rayleigh numbers were not included in the least-squares fits for the internally heated runs. Further details of the convection calculations can be found in Table 3.1. Least-squares fit parameters are given in Table 3.2. For display reasons the $Ra_H/Ra_B = 7.5$ points were multiplied by 1.5, the $Ra_H/Ra_B = 15$ points were multiplied by 2.

Fig. 3.6. Radially-averaged horizontal correlation angle, $\bar{\alpha}_T$, as a function of Ra_Q for convection experiments in a cylindrical shell. Internal heating rates, Ra_H/Ra_B, are 0 (squares), 7.5 (circles), 15 (triangles). Solid squares indicate that a steady state solution was reached. A dashed line connects the least-squares lines for the steady and time-dependent bottom-heated regimes. Values at the lowest Rayleigh numbers were not included in the least-squares fits for the internally heated runs. Further details of the convection calculations can be found in Table 3.1. Least-squares fit parameters are given in Table 3.2. For display reasons the $Ra_H/Ra_B = 7.5$ points were multiplied by 1.5, the $Ra_H/Ra_B = 15$ points were multiplied by 2.

Fig. 3.7. Three snapshots for convection with depth- and temperature-dependent viscosity in an annulus. Viscosity varies according to equation (3.1), with $\eta_0(z)$ increasing by a factor of 30 at normalized depth $z = 1 - r = 0.25$ and $\eta_1(T)$ varying exponentially by four orders of magnitude. Numerical details of this convection run can be found in Table 3.4. (*a*) Temperature and velocity fields. Grayscale varies from cold (dark) to warm (light) relative temperatures ($T \in [0,1]$). Velocity arrows are normalized

by the maximum velocity at each instant. Horizontal velocities were constrained to yield zero net horizontal fluid motion. (*b*) Viscosity fields. Grayscale varies logarithmically from low viscosities (light) to high viscosities (dark) ($\eta \in [1,10^4]$).

Fig. 3.8. (*a*) Rms temperature variation, σ_T, (*b*) radial correlation length, ρ_T, and (*c*) horizontal correlation angle, α_T, as a function of normalized depth $z = 1 - r$ for convection experiments with a temperature-dependent viscosity. Viscosity varies according to equation (3.1), with $\eta_0(z) = 1$. Boundary layer viscosity, η_{bl}, and boundary layer thickness, δ_{bl}, are: $\eta_{bl} = 50$, $\delta_{bl} = 0.036$ (solid lines), $\eta_{bl} = 50$, $\delta_{bl} = 0.027$ (dotted lines), $\eta_{bl} = 50$, $\delta_{bl} = 0.045$ (thin short dashed lines), $\eta_{bl} = 10$, $\delta_{bl} = 0.036$ (intermediate dashed lines), and $\eta_{bl} = 100$, $\delta_{bl} = 0.036$ (long dashed lines). The isoviscous run at approximately the same Rayleigh number and internal heating rate is also shown (heavy solid lines). Further details of the convection calculations can be found in Table 3.3.

Fig. 3.9. Horizontally averaged temperature, $\overline{T}$, as a function of normalized depth $z = 1 - r$ for convection experiments with depth-dependent viscosity (dashed lines) and depth- and temperature-dependent viscosity (solid lines). For the temperature-dependent runs $\eta_1(T)$ varies exponentially by four orders of magnitude. Depth-dependent viscosity, $\eta_0(z)$, is: (*a*) uniform viscosity, (*b*) 30-fold viscosity increase at $z = 0.125$, (*c*) 10-fold viscosity increase at mid-depth ($z = 0.25$), and (*d*) 30-fold viscosity increase at mid-depth. Further details of the convection calculations can be found in Table 3.4.

Fig. 3.10. Rms variation of radial velocity, σ_u, as a function of normalized depth $z = 1 - r$ for convection experiments with depth-dependent viscosity (dashed lines) and depth- and temperature-dependent viscosity (solid lines). For the temperature-dependent runs, $\eta_1(T)$ varies exponentially by four orders of magnitude. Depth-dependent viscosity, $\eta_0(z)$, is: (*a*) uniform viscosity, (*b*) 30-fold viscosity increase at $z = 0.125$, (*c*) 10-fold

viscosity increase at mid-depth ($z = 0.25$), and (*d*) 30-fold viscosity increase at mid-depth. Further details of the convection calculations can be found in Table 3.4.

Fig. 3.11. Rms variation of horizontal velocity, σ_w, as a function of normalized depth $z = 1 - r$ for convection experiments with depth-dependent viscosity (dashed lines) and depth- and temperature-dependent viscosity (solid lines). For the temperature-dependent runs, $\eta_1(T)$ varies exponentially by four orders of magnitude. Depth-dependent viscosity, $\eta_0(z)$, is: (*a*) uniform viscosity, (*b*) 30-fold viscosity increase at $z = 0.125$, (*c*) 10-fold viscosity increase at mid-depth ($z = 0.25$), and (*d*) 30-fold viscosity increase at mid-depth. Further details of the convection calculations can be found in Table 3.4.

Fig. 3.12. Rms temperature variation, σ_T, as a function of normalized depth $z = 1 - r$ for convection experiments with depth-dependent viscosity (dashed lines) and depth- and temperature-dependent viscosity (solid lines). For the temperature-dependent runs, $\eta_1(T)$ varies exponentially by four orders of magnitude. Depth-dependent viscosity, $\eta_0(z)$, is: (*a*) uniform viscosity, (*b*) 30-fold viscosity increase at $z = 0.125$, (*c*) 10-fold viscosity increase at mid-depth ($z = 0.25$), and (*d*) 30-fold viscosity increase at mid-depth. Further details of the convection calculations can be found in Table 3.4.

Fig. 3.13. Radial correlation length, ρ_T, as a function of normalized depth $z = 1 - r$ for convection experiments with depth-dependent viscosity (dashed lines) and depth- and temperature-dependent viscosity (solid lines). For the temperature-dependent runs, $\eta_1(T)$ varies exponentially by four orders of magnitude. Depth-dependent viscosity, $\eta_0(z)$, is: (*a*) uniform viscosity, (*b*) 30-fold viscosity increase at $z = 0.125$, (*c*) 10-fold viscosity increase at mid-depth ($z = 0.25$), and (*d*) 30-fold viscosity increase at mid-depth. Further details of the convection calculations can be found in Table 3.4.

Fig. 3.14. Horizontal correlation angle, α_T, as a function of normalized depth $z = 1 - r$ for convection experiments with depth-dependent viscosity (dashed lines) and depth- and

temperature-dependent viscosity (solid lines). For the temperature-dependent runs, $\eta_1(T)$ varies exponentially by four orders of magnitude. Depth-dependent viscosity, $\eta_0(z)$, is: (*a*) uniform viscosity, (*b*) 30-fold viscosity increase at $z = 0.125$, (*c*) 10-fold viscosity increase at mid-depth ($z = 0.25$), and (*d*) 30-fold viscosity increase at mid-depth. Further details of the convection calculations can be found in Table 3.4.

Fig. 3.15. Radial average of normalized angular power spectrum, S_T / σ_T^2 for convection experiments with depth-dependent viscosity (dashed lines, open symbols) and depth- and temperature-dependent viscosity (solid lines, filled symbols). (*a*) uniform viscosity, (*b*) 30-fold viscosity increase at $z = 0.125$, and (*c*) 30-fold viscosity increase at mid-depth. All spectra are scaled to a maximum amplitude of unity. Further details of the convection calculations can be found in Table 3.4.

Fig. 3.16. (*a*) Horizontally averaged temperature, $\bar{T}$, (*b*) rms variation of radial velocity, σ_u, (*c*) rms variation of horizontal velocity, σ_w, (*d*) rms temperature variation, σ_T, (*e*) radial correlation length, ρ_T, and (*f*) horizontal correlation angle, α_T, as a function of normalized depth $z = 1 - r$ for convection experiments with an endothermic phase transition at $r = 0.875$ and $Ra_H/Ra_B = 0$. Phase buoyancy parameters are: $P = 0.0$ (solid), -0.1 (short dashed), -0.15 (intermediate dashed), and -0.2 (long dashed). Further details of the convection calculations can be found in Table 3.5.

Fig. 3.17. (*a*) Horizontally averaged temperature, $\bar{T}$, (*b*) rms variation of radial velocity, σ_u, (*c*) rms variation of horizontal velocity, σ_w, (*d*) rms temperature variation, σ_T, (*e*) radial correlation length, ρ_T, and (*f*) horizontal correlation angle, α_T, as a function of normalized depth $z = 1 - r$ for convection experiments with an endothermic phase transition at $r = 0.875$ and $Ra_H/Ra_B = 30$. Phase buoyancy parameters are: $P = 0.0$ (solid), -0.1 (short dashed), -0.15 (intermediate dashed), and -0.2 (long dashed). Further details of the convection calculations can be found in Table 3.5.

Fig. 3.18. Two different formulations for the phase transition are compared: "sheet-mass-anomaly" method (solid) and "phase-function" method (phase loop width 120 km) (dashed). (*a*) Horizontally averaged temperature, $\overline{T}$, (*b*) rms variation of radial velocity, σ_u, (*c*) rms variation of horizontal velocity, σ_w, (*d*) rms temperature variation, σ_T, (*e*) radial correlation length, ρ_T, and (*f*) horizontal correlation angle, α_T, as a function of normalized depth $z = 1 - r$ for convection experiments with an endothermic phase transition at $r = 0.875$, a phase buoyancy parameter $P = -0.15$, and $Ra_H/Ra_B = 30$. Further details of the convection calculations can be found in Table 3.5.

Fig. 3.19. (*a*) Horizontally averaged temperature, $\overline{T}$, (*b*) rms variation of radial velocity, σ_u, (*c*) rms variation of horizontal velocity, σ_w, (*d*) rms temperature variation, σ_T, (*e*) radial correlation length, ρ_T, and (*f*) horizontal correlation angle, α_T, as a function of normalized depth $z = 1 - r$ for convection experiments with an endothermic phase transition at $r = 0.875$. Phase buoyancy parameters and rheologies are: $P = -0.1$ and temperature-dependent viscosity (solid), $P = -0.10$ and constant viscosity (short dashed), $P = -0.15$ and temperature-dependent viscosity (intermediate dashed), and $P = -0.15$ and constant viscosity (long dashed). Further details of the convection calculations can be found in Table 3.5.

Fig. 3.20. (*a*) Horizontally averaged temperature, $\overline{T}$, (*b*) rms variation of radial velocity, σ_u, (*c*) rms variation of horizontal velocity, σ_w, (*d*) rms temperature variation, σ_T, (*e*) radial correlation length, ρ_T, and (*f*) horizontal correlation angle, α_T, as a function of normalized depth $z = 1 - r$ for convection experiments with an endothermic phase transition and a 30-fold viscosity increase at $r = 0.875$, and $Ra_H/Ra_B = 22.5$. Phase buoyancy parameters are: $P = 0.0$ (solid), and $P = -0.1$ (dashed). Further details of the convection calculations can be found in Table 3.5.

Fig. 3.21. (*a*) Horizontally averaged temperature, $\overline{T}$, (*b*) rms variation of radial velocity, σ_u, (*c*) rms variation of horizontal velocity, σ_w, (*d*) rms temperature variation, σ_T, (*e*)

radial correlation length, ρ_T, and (*f*) horizontal correlation angle, α_T, as a function of normalized depth $z = 1 - r$ for convection runs with a 30-fold viscosity increase at r = 0.875, and Ra_H/Ra_B = 22.5, and temperature-dependent rheology. Phase buoyancy parameters are: $P = 0.0$ (solid), and $P = -0.1$ (dashed). Further details of the convection calculations can be found in Table 3.5.

Fig. 3.22. Radial average of normalized angular power spectrum, S_T/σ_T^2 for convection experiments with an endothermic phase change at $r = 0.875$. $P = 0.0$ (dashed lines, open symbols) and $P = -0.1$ (solid lines, filled symbols). (*a*) uniform viscosity, (*b*) 30-fold viscosity increase at $r = 0.875$. All spectra are scaled to a maximum amplitude of unity. Further details of the convection calculations can be found in Table 3.5.

Fig. 3.23. (*a*) Horizontally averaged temperature, $\overline{T}$, (*b*) rms variation of radial velocity, σ_u, (*c*) rms variation of horizontal velocity, σ_w, (*d*) rms temperature variation, σ_T, (*e*) radial correlation length, ρ_T, and (*f*) horizontal correlation angle, α_T, as a function of normalized depth $z = 1 - r$ for convection runs with a 30-fold viscosity increase at r = 0.75. "Supercontinent" sizes are: $s = 4$ (solid), and $s = 0$ (dashed). Further details of the convection calculations can be found in Table 3.6.

Fig. 3.24. (*a*) Horizontally averaged temperature, $\overline{T}$, (*b*) rms variation of radial velocity, σ_u, (*c*) rms variation of horizontal velocity, σ_w, (*d*) rms temperature variation, σ_T, (*e*) radial correlation length, ρ_T, and (*f*) horizontal correlation angle, α_T, as a function of normalized depth $z = 1 - r$ for convection runs with a temperature-dependent rheology. "Supercontinent" sizes are: $s = 4$ (solid), and $s = 0$ (dashed). Further details of the convection calculations can be found in Table 3.6.

Fig. 3.25. Radial average of normalized angular power spectrum, S_T/σ_T^2 for convection experiments with a supercontinent. Sizes are: $s = 0$ (short dashed lines, open squares), $s = 2$ (long dashed lines, crosses) and $s = 4$ (solid lines, filled squares). (*a*) uniform

viscosity, (*b*) 30-fold viscosity increase at mid-depth, (*c*) temperature-dependent viscosity, and (*d*) temperature-dependent viscosity with a 30-fold viscosity increase at mid-depth. All spectra are scaled to a maximum amplitude of unity. Further details of the convection calculations can be found in Table 3.6.

Fig. 3.26. Three snapshots for convection with depth- and temperature-dependent viscosity in an annulus. Ten plates whose geometries evolve with time are present. Viscosity varies according to equation (3.2), with $\eta_0(z)$ increasing by a factor of 30 at normalized depth $z = 1 - r = 0.25$ and $\eta_1(T)$ varying exponentially by three orders of magnitude. Numerical details of this convection run can be found in Table 3.7. (*a*) Temperature and velocity fields. Grayscale varies from cold (dark) to warm (light) relative temperatures ($T \in [0,1]$). Velocity arrows are normalized by the maximum velocity at each instant. Horizontal velocities were constrained to yield zero net horizontal fluid motion. (*b*) Viscosity fields. Grayscale varies logarithmically from low viscosities (light) to high viscosities (dark) ($\eta \in [1,10^4]$).

Fig. 3.27. (*a*) Horizontally averaged temperature, $\bar{T}$, (*b*) rms variation of radial velocity, σ_u, (*c*) rms variation of horizontal velocity, σ_w, (*d*) rms temperature variation, σ_T, (*e*) radial correlation length, ρ_T, and (*f*) horizontal correlation angle, α_T, as a function of normalized depth $z = 1 - r$ for convection runs with a $Ra_H/Ra_B = 15$. Viscosity varies according to equation (3.2). Number of weak zones are: $N_w = 10$ (solid), $N_w = 6$ (short dashed), and $N_w = 14$ (long dashed). Further details of the convection calculations can be found in Table 3.7.

Fig. 3.28. (*a*) Horizontally averaged temperature, $\bar{T}$, (*b*) rms variation of radial velocity, σ_u, (*c*) rms variation of horizontal velocity, σ_w, (*d*) rms temperature variation, σ_T, (*e*) radial correlation length, ρ_T, and (*f*) horizontal correlation angle, α_T, as a function of normalized depth $z = 1 - r$ for convection runs with a $Ra_H/Ra_B = 22.5$ and a 30-fold viscosity increase at mid-depth. Viscosity varies according to equation (3.2), with N_w =

10 (solid), and equation (3.1) (dashed). Further details of the convection calculations can be found in Table 3.7.

Fig. 3.29. (*a*) Horizontally averaged temperature, $\bar{T}$, (*b*) rms variation of radial velocity, σ_u, (*c*) rms variation of horizontal velocity, σ_w, (*d*) rms temperature variation, σ_T, (*e*) radial correlation length, ρ_T, and (*f*) horizontal correlation angle, α_T, as a function of normalized depth $z = 1 - r$ for convection runs with an endothermic phase transition at $r = 0.875$, and $Ra_H/Ra_B = 15$. Viscosity varies according to equation (3.2), with $N_w = 10$. Phase buoyancy parameters are: $P = 0.0$ (solid), and $P = -0.1$ (dashed). Further details of the convection calculations can be found in Table 3.7.

Fig. 3.30. (*a*) Horizontally averaged temperature, $\bar{T}$, (*b*) rms variation of radial velocity, σ_u, (*c*) rms variation of horizontal velocity, σ_w, (*d*) rms temperature variation, σ_T, (*e*) radial correlation length, ρ_T, and (*f*) horizontal correlation angle, α_T, as a function of normalized depth $z = 1 - r$ for convection runs with an endothermic phase transition and a 30-fold viscosity increase at $r = 0.875$. Phase buoyancy parameter $P = -0.1$. Viscosity varies according to equation (3.2), with $N_w = 10$ (solid), and equation (3.1) (dashed). Further details of the convection calculations can be found in Table 3.7.

Fig. 3.31. Radial average of normalized angular power spectrum, S_T/σ_T^2 for convection experiments with temperature-dependent rheology. (*a*) Viscosity varies according to equation (3.2). Number of weak zones are: $N_w = 10$ (solid line, filled squares), $N_w = 6$ (dotted line, open squares), and $N_w = 14$ (dashed line, crosses). (*b*) Viscosity varies according to equation (3.2), with $N_w = 10$ (solid line, filled squares), and equation (3.1), with a supercontinent of size $s = 0$ (dotted line, open squares) and $s = 4$ (dashed line, crosses). All spectra are scaled to a maximum amplitude of unity. Further details of the convection calculations can be found in Table 3.7.

Fig. 3.32. Radial average of normalized angular power spectrum, S_T / σ_T^2 for convection experiments with temperature-dependent rheology and a 30-fold viscosity increase with depth. (*a*) Viscosity increase at mid-depth. Viscosity varies according to equation (3.2), with $N_w = 10$ (solid line, filled squares), and equation (3.1), with a supercontinent of size $s = 0$ (dotted line, open squares) and $s = 4$ (dashed line, crosses). (*b*) Endothermic phase transition and viscosity increase at $r = 0.875$. Viscosity varies according to equation (3.2) with $N_w = 10, P = 0.0$ (solid line, filled squares), and $P = -0.1$ (dotted line, open squares). All spectra are scaled to a maximum amplitude of unity. Further details of the convection calculations can be found in Table 3.7.

Fig. 3.33. (*a*), (*c*), (*e*) Histograms of fractional plate size, (*b*), (*d*), (*f*) histograms of relative plate velocity magnitude for runs with evolving plates. Viscosity varies according to equation (3.2). (*a*), (*b*) $N_w = 6$; (*c*), (*d*) $N_w = 10$; and (*e*), (*f*) $N_w = 14$. Further details of the convection calculations can be found in Table 3.7.

Fig. 3.34. (*a*), (*c*), (*e*) Histograms of fractional plate size, (*b*), (*d*), (*f*) histograms of relative plate velocity magnitude. Viscosity varies according to equation (3.2), with $N_w = 10$, and increases by a factor of 30 with depth. (*a*), (*b*) Viscosity increase at mid-depth; (*c*), (*d*) viscosity increase at $r = 0.875$; and (*e*), (*f*) endothermic phase transition with $P = -0.1$ and viscosity increase at $r = 0.875$. Further details of the convection calculations can be found in Table 3.7.

Fig. 3.35. Bin-average of relative plate velocity magnitude for runs with plates whose geometries evolve. Viscosity varies according to equation (3.2). (*a*) $N_w = 6$ (triangles), $N_w = 10$ (squares), $N_w = 14$ (circles), and $N_w = 10$ with an endothermic phase transition ($P = -0.1$) at $r = 0.875$ (crosses). (*b*) $N_w = 10$, and 30-fold viscosity increase with depth. Viscosity increase at mid-depth (open squares), viscosity increase and endothermic phase transition at $r = 0.875$ (filled symbols); $P = 0.0$ (squares) and $P = -0.1$ (triangles). Size of

fractional plate-size bin is 0.03. Further details of the convection calculations can be found in Table 3.7.

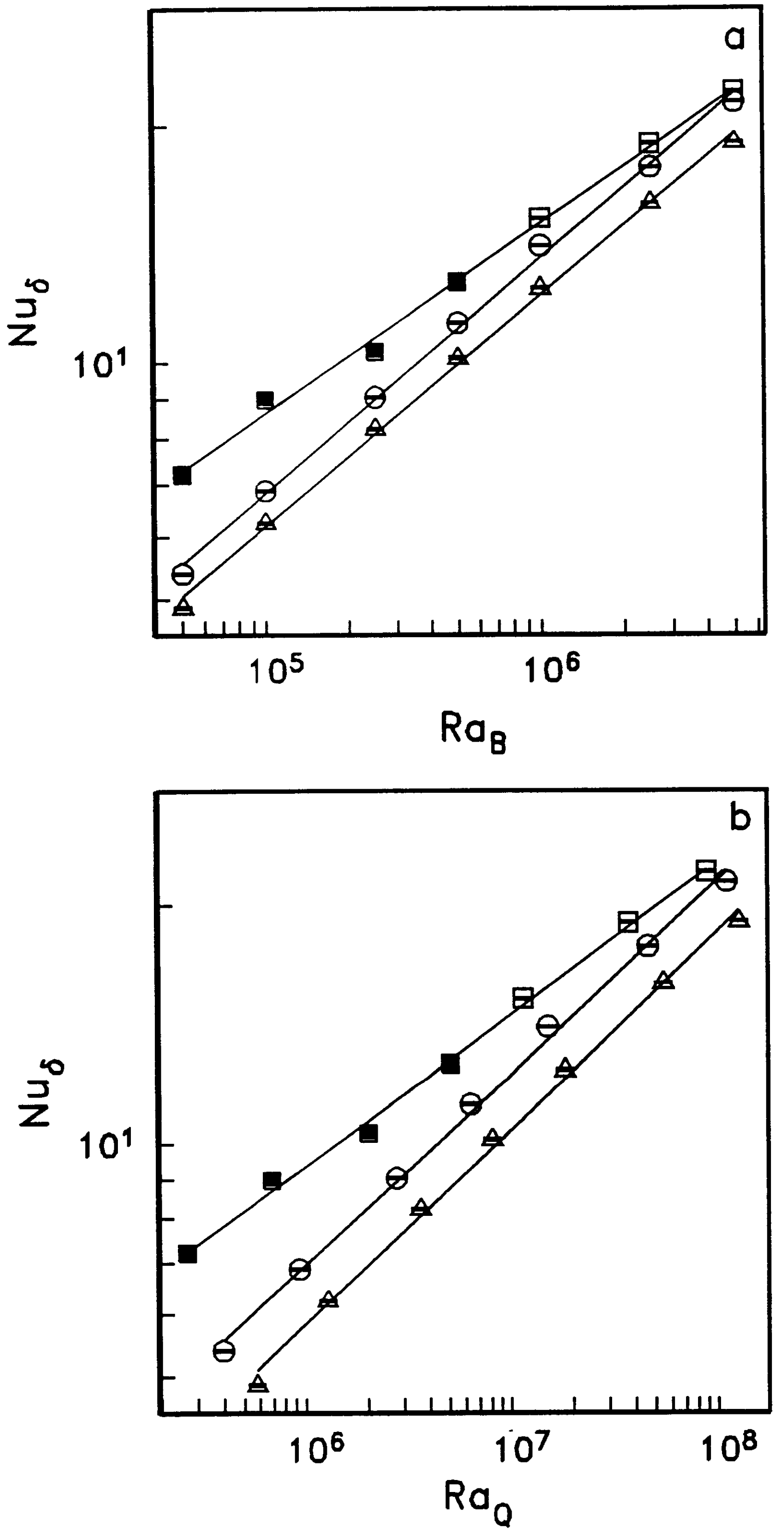

Figure 3.1

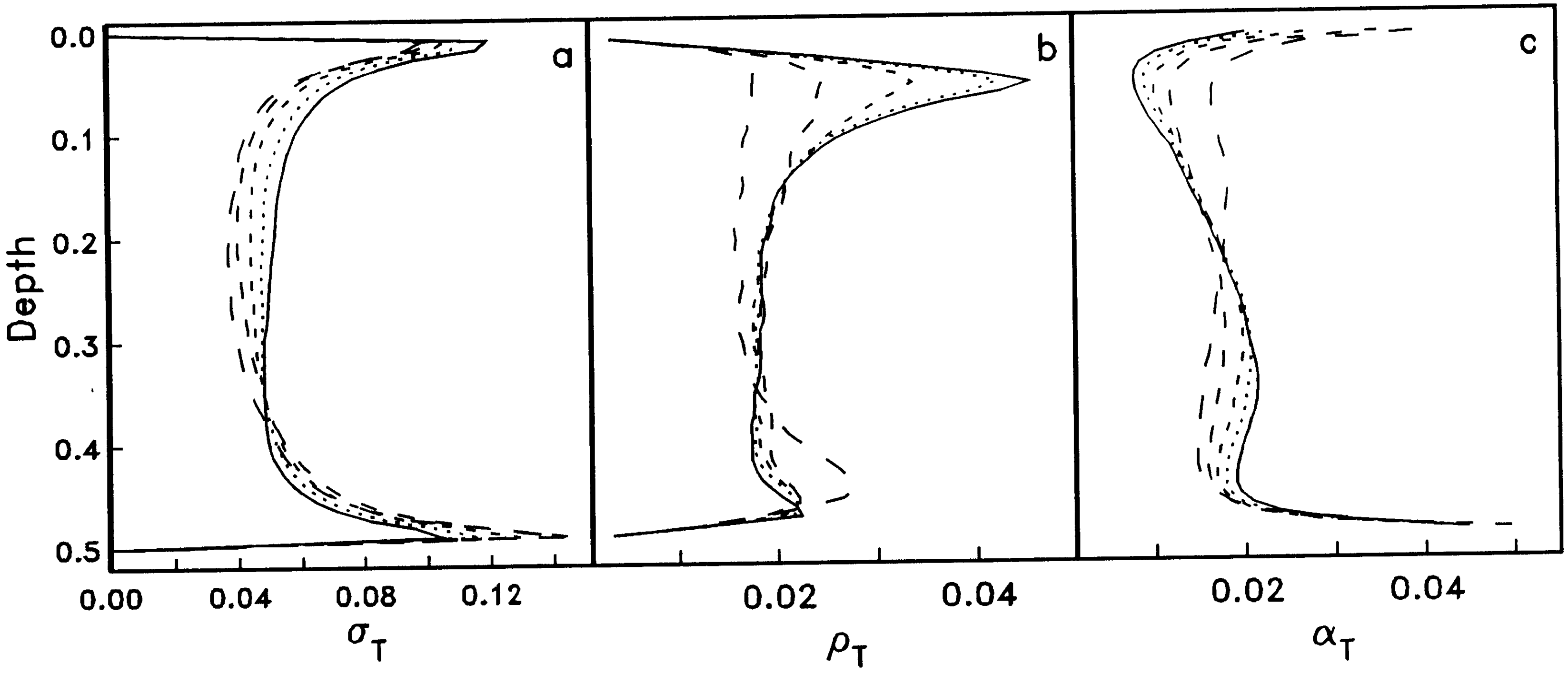
Depth
0.0
0.1
0.2
0.3
0.4
0.5
a
b
c
0.00
0.04
0.08
0.12
σ_T
0.02
0.04
ρ_T
0.02
0.04
α_T

Figure 3.2

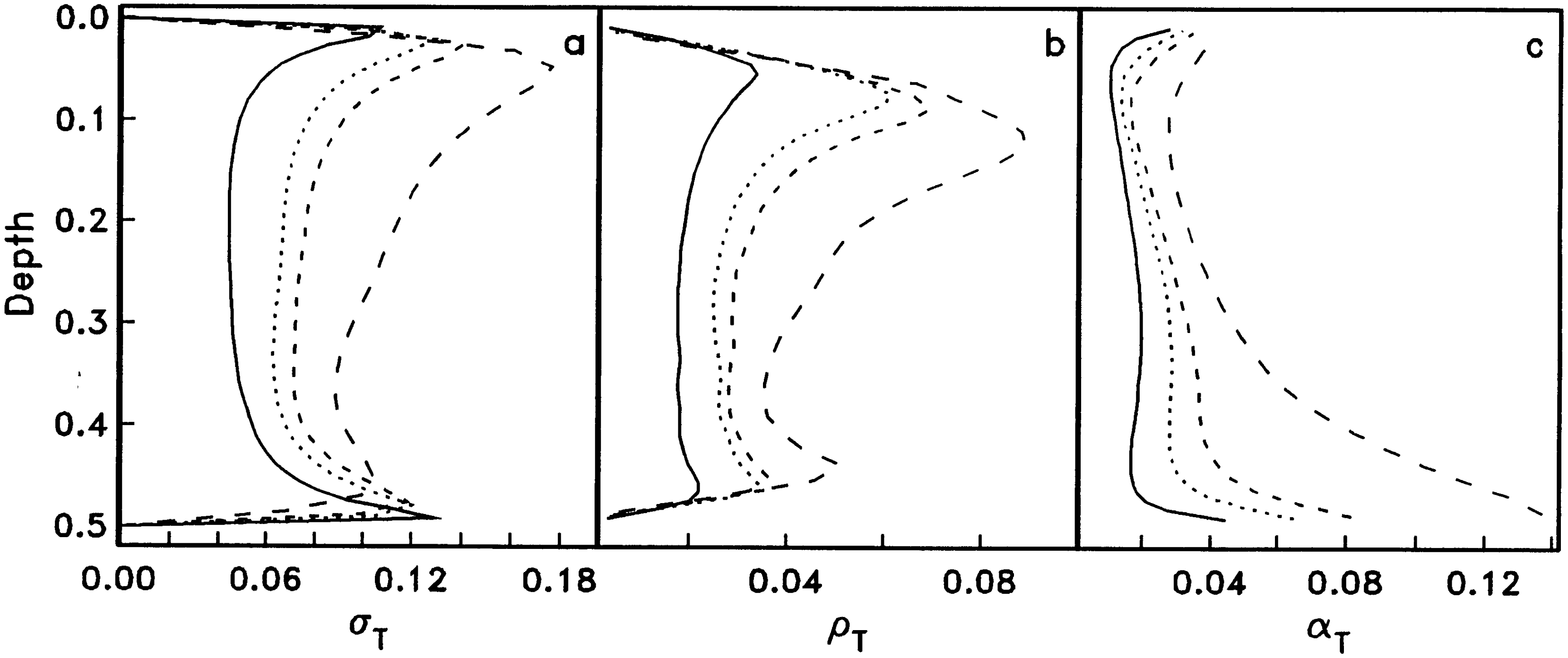
a
b
c
Depth
0.0
0.1
0.2
0.3
0.4
0.5
0.00
0.06
0.12
0.18
σ_T
0.04
0.08
ρ_T
0.04
0.08
0.12
α_T

Figure 3.3

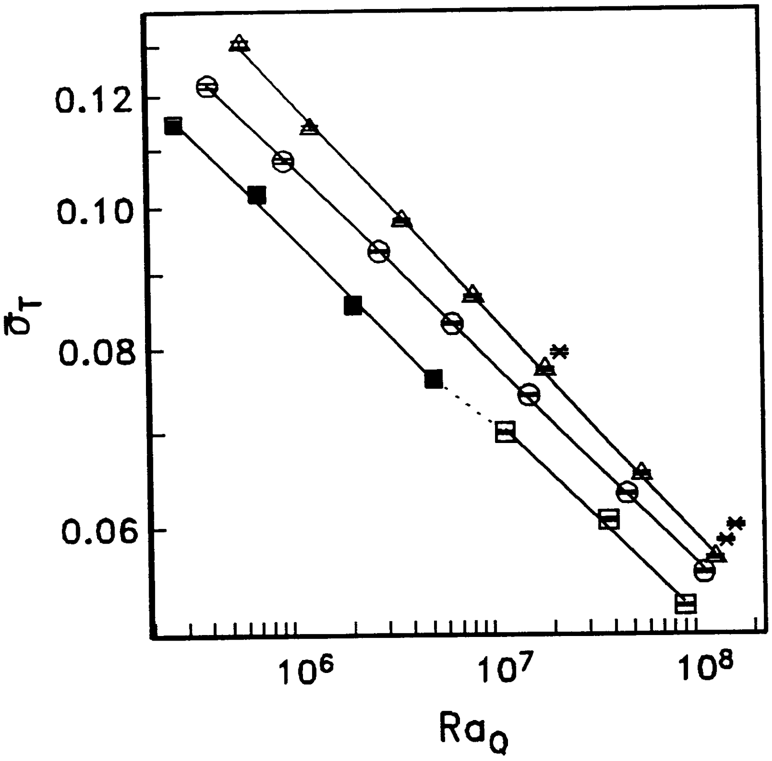

Figure 3.4

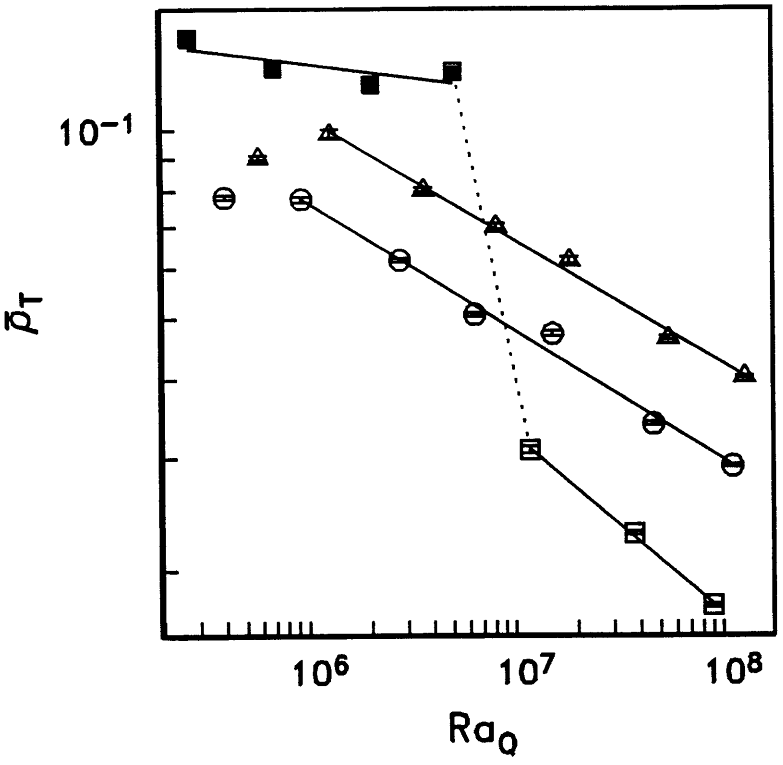

Figure 3.5

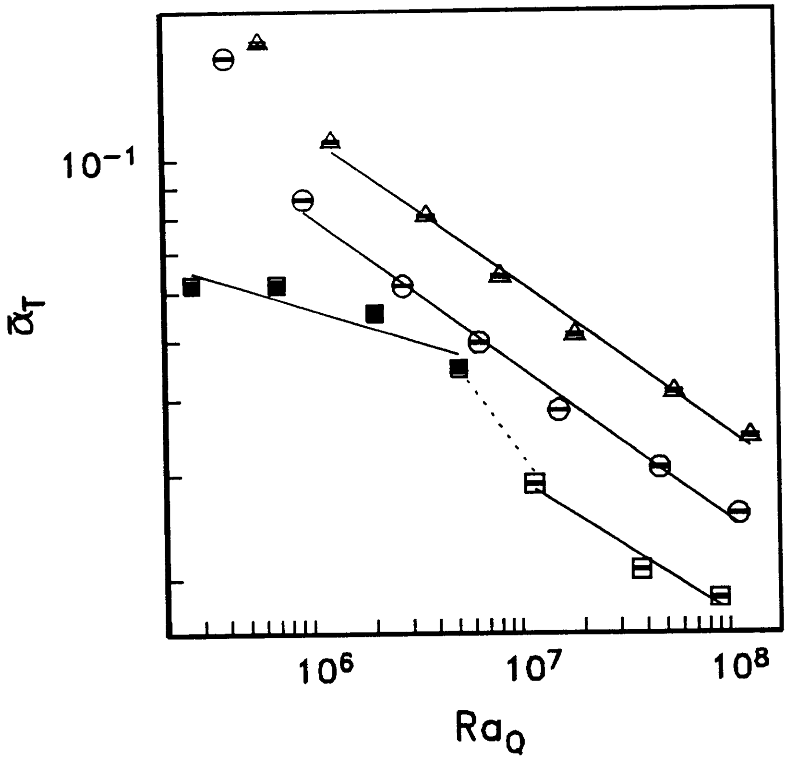

Figure 3.6

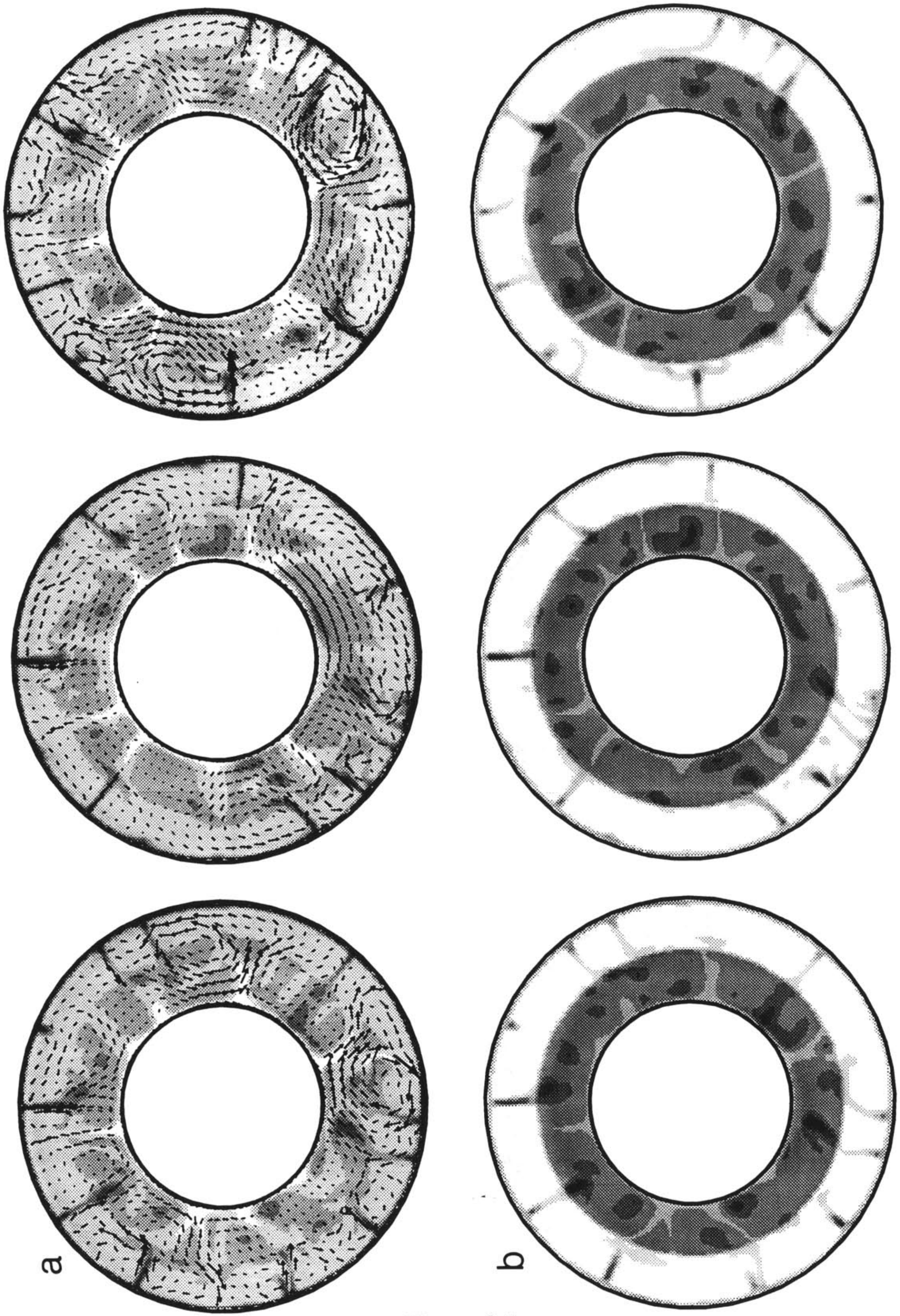

Figure 3.7

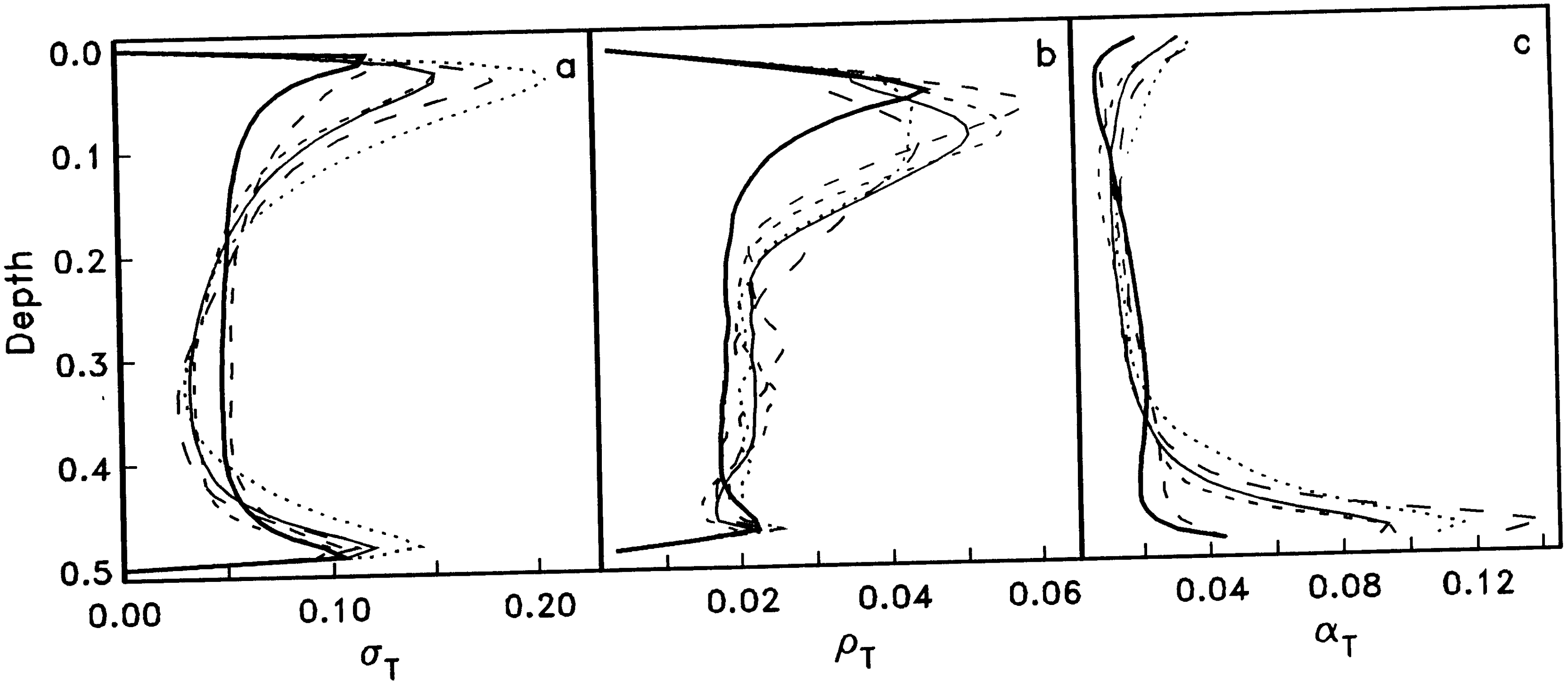
a
b
c
Depth
0.0
0.1
0.2
0.3
0.4
0.5
0.00
0.10
0.20
σ_T
0.02
0.04
0.06
ρ_T
0.04
0.08
0.12
α_T

Figure 3.8

Figure 3.9

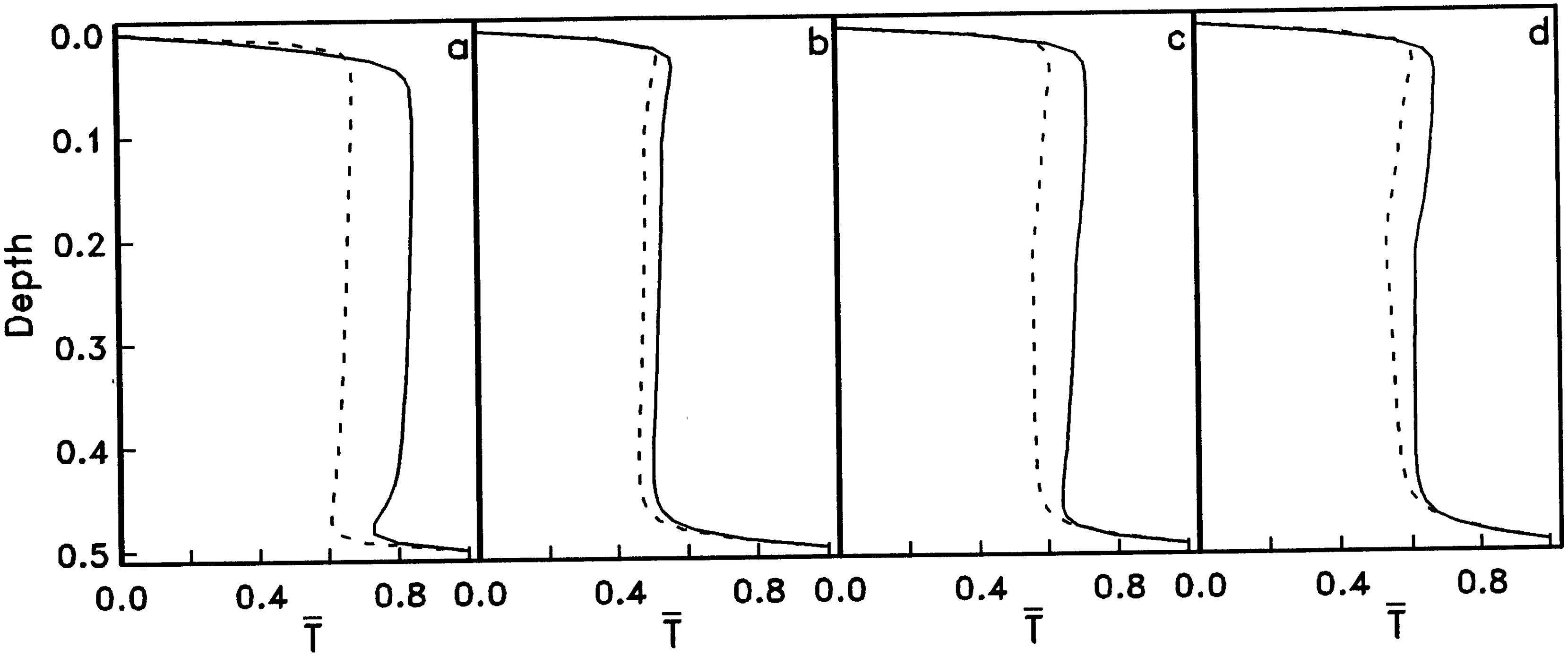

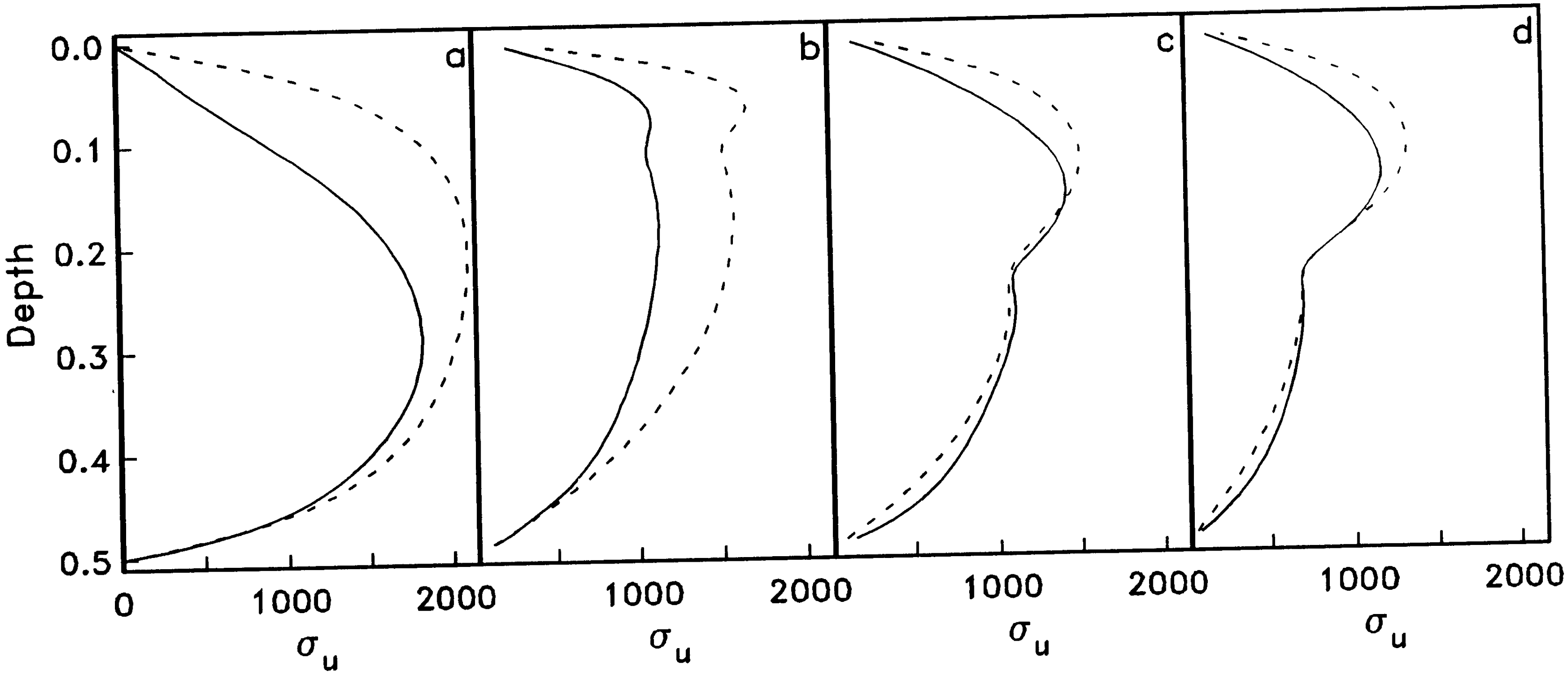
a
b
c
d
Depth
0.0
0.1
0.2
0.3
0.4
0.5
0
1000
2000
1000
2000
1000
2000
1000
2000
σ_u
σ_u
σ_u
σ_u

Figure 3.10

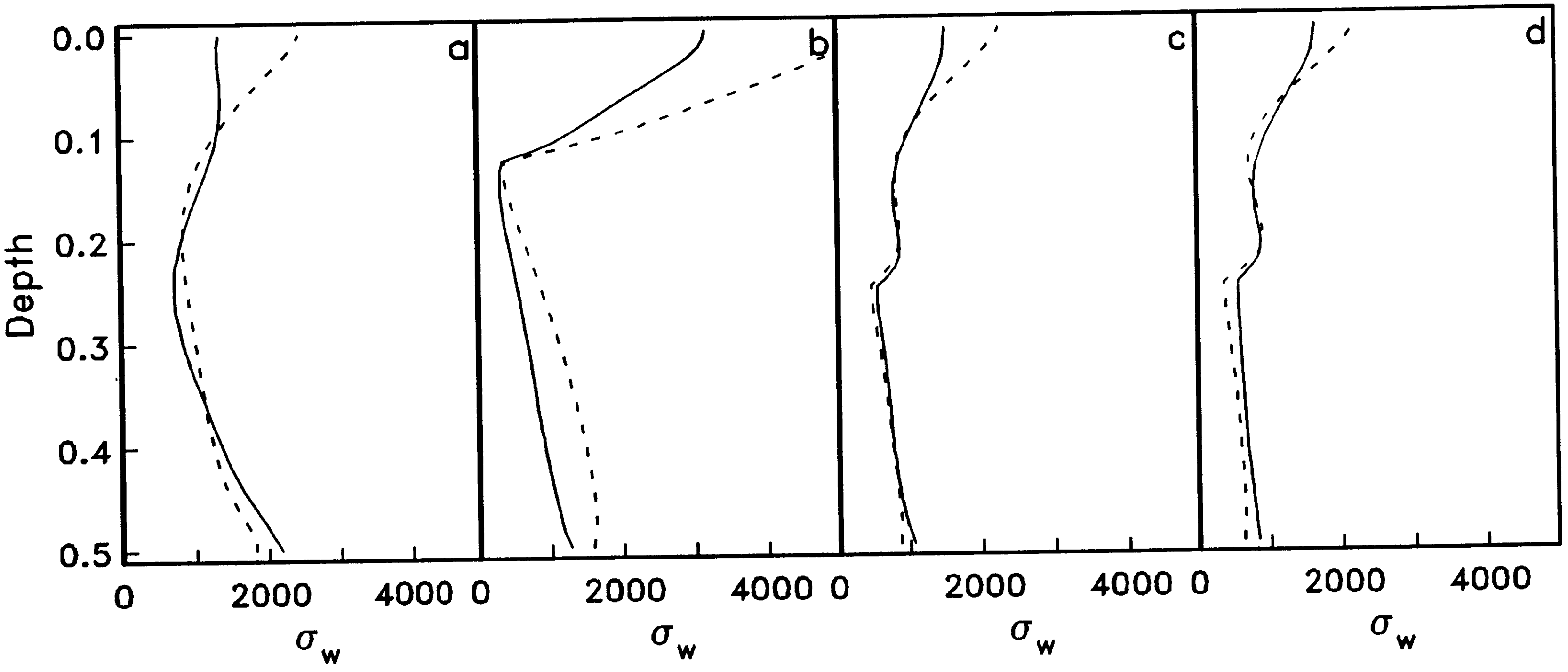

Figure 3.11

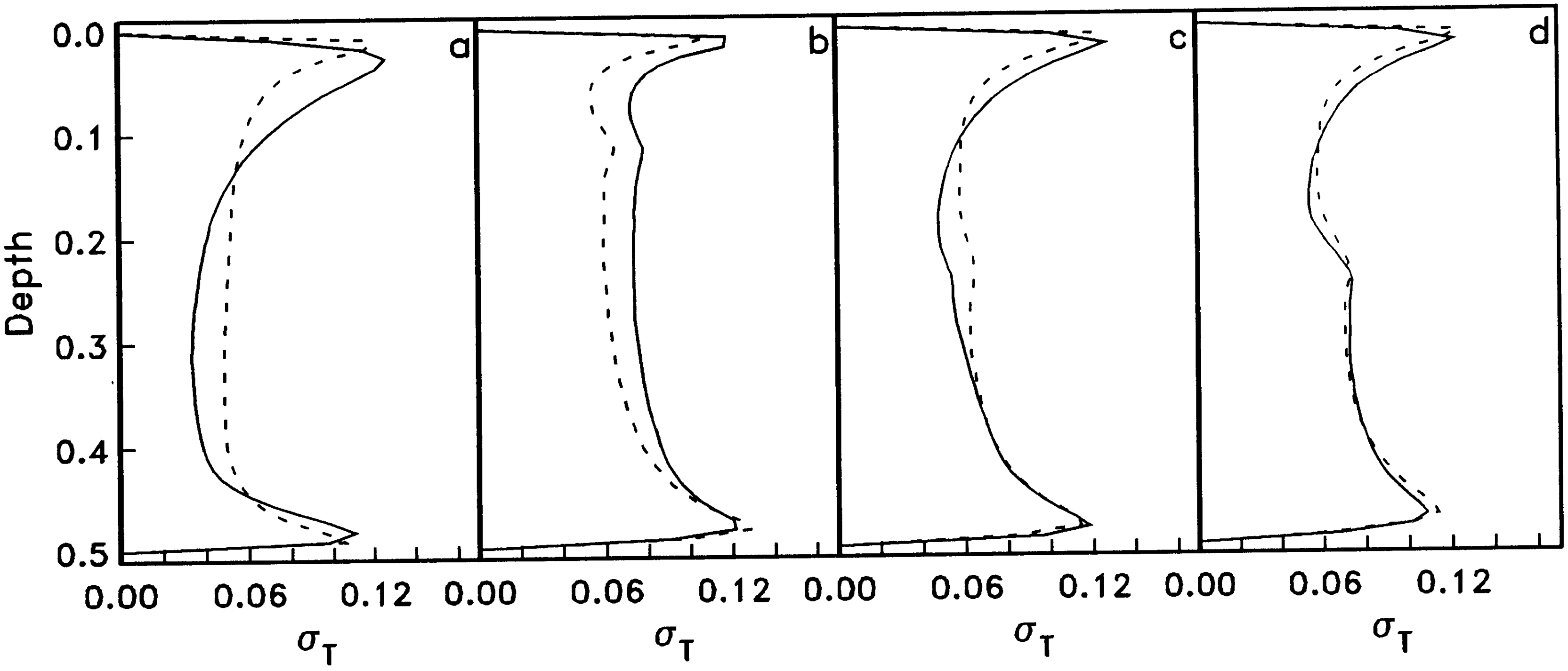

Figure 3.12

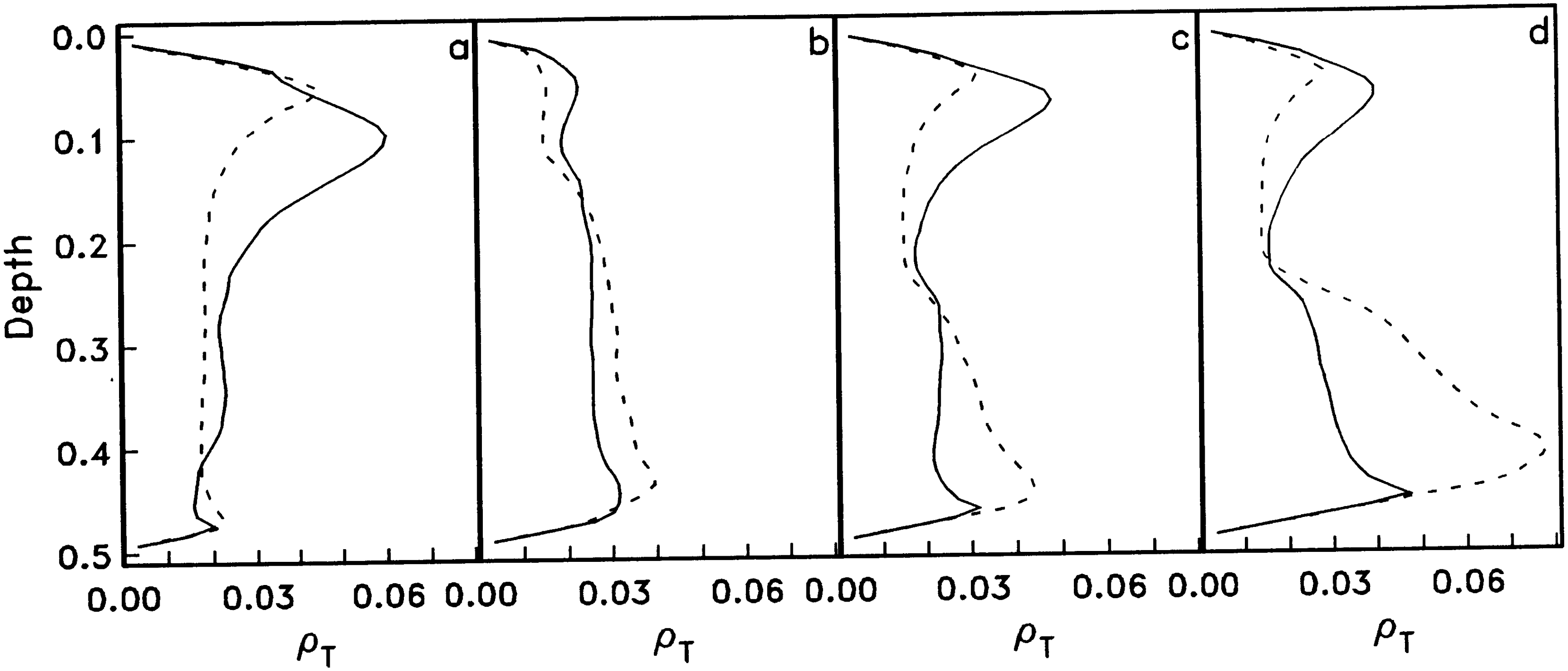
a
b
c
d
Depth
0.0
0.1
0.2
0.3
0.4
0.5
0.00
0.03
0.06
0.00
0.03
0.06
0.00
0.03
0.06
0.00
0.03
0.06
ρ_T
ρ_T
ρ_T
ρ_T

Figure 3.13

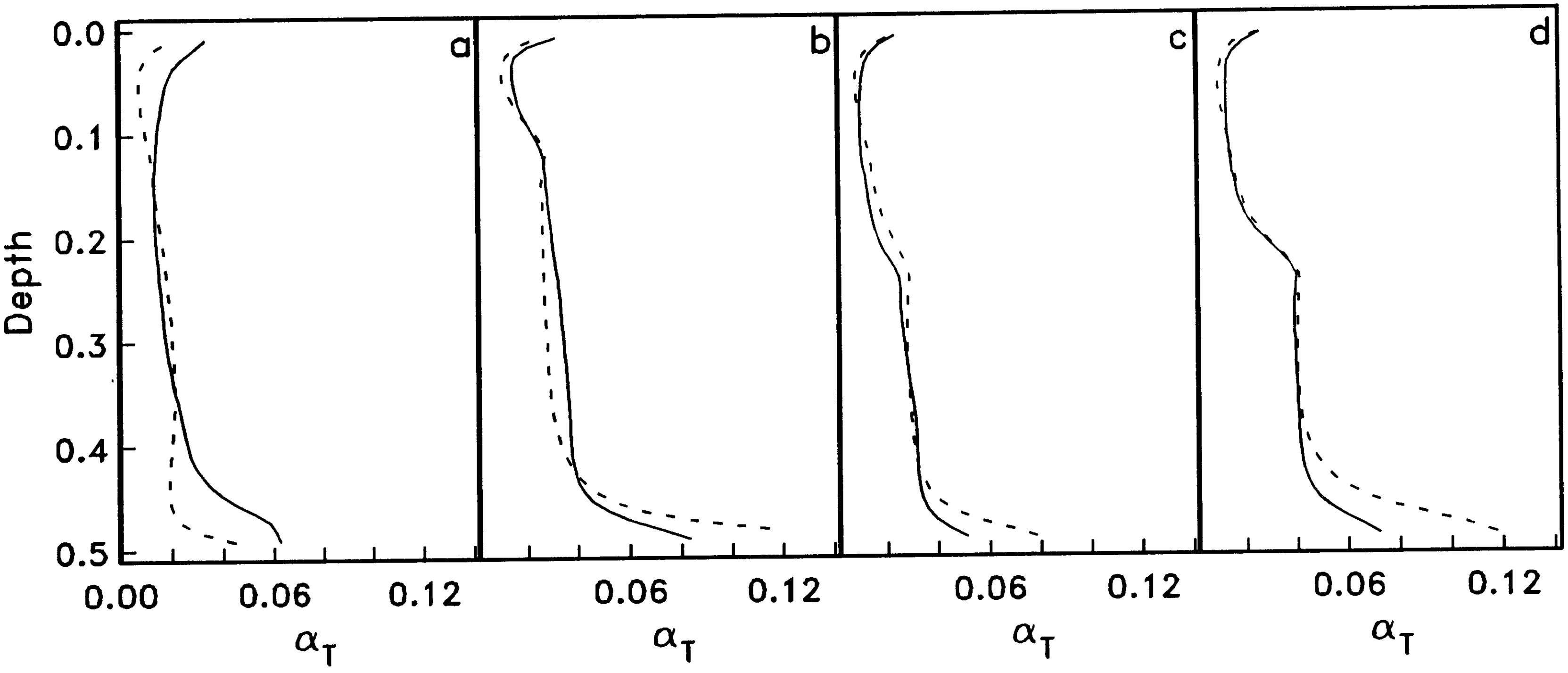
Depth
0.0
0.1
0.2
0.3
0.4
0.5
a
b
c
d
0.00
0.06
0.12
0.06
0.12
0.06
0.12
0.06
0.12
α_T
α_T
α_T
α_T

Figure 3.14

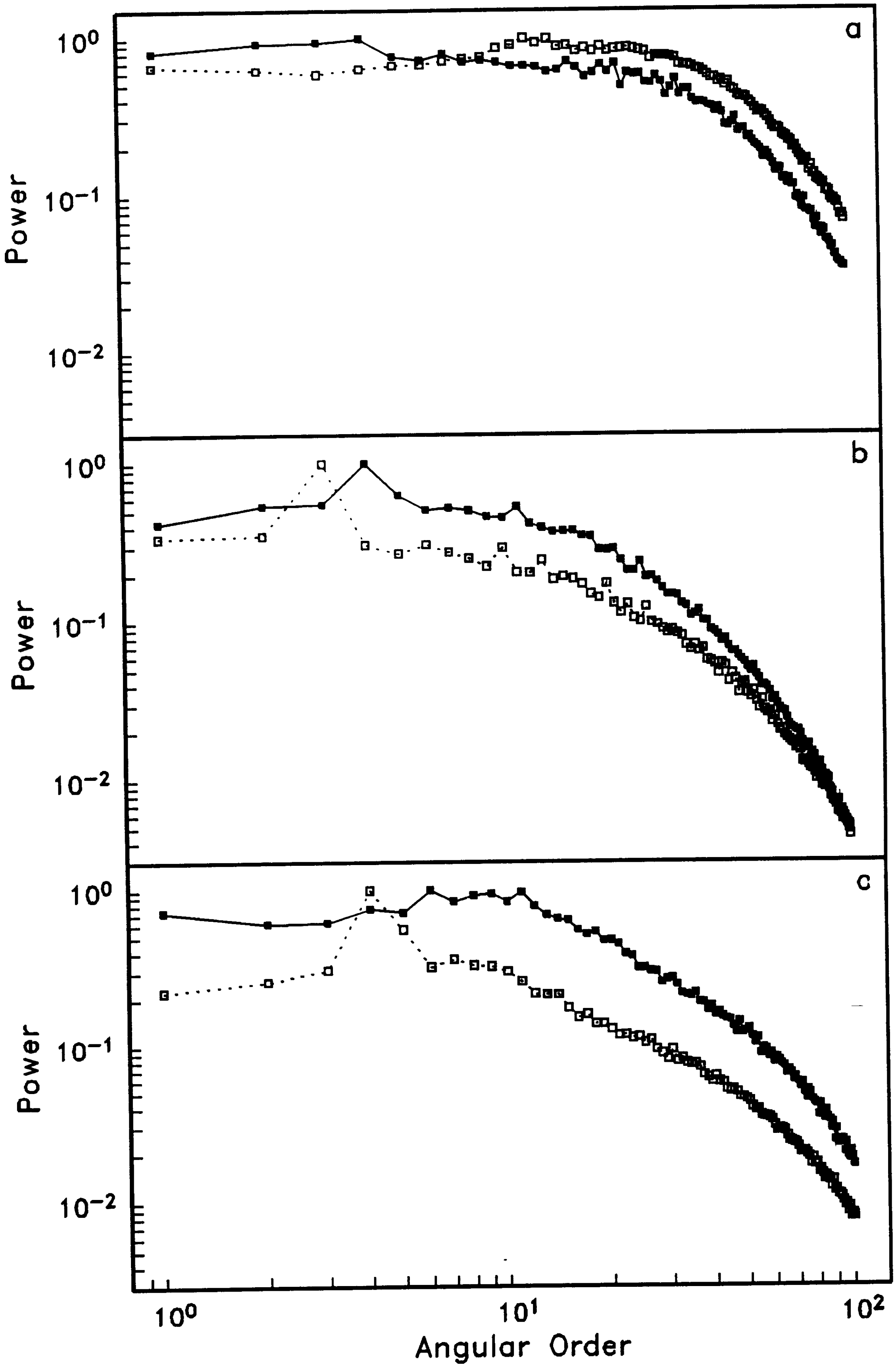
a
b
c
Power
Power
Power
10^0
10^{-1}
10^{-2}
10^0
10^{-1}
10^{-2}
10^0
10^{-1}
10^{-2}
10^0
10^1
10^2
Angular Order

Figure 3.15

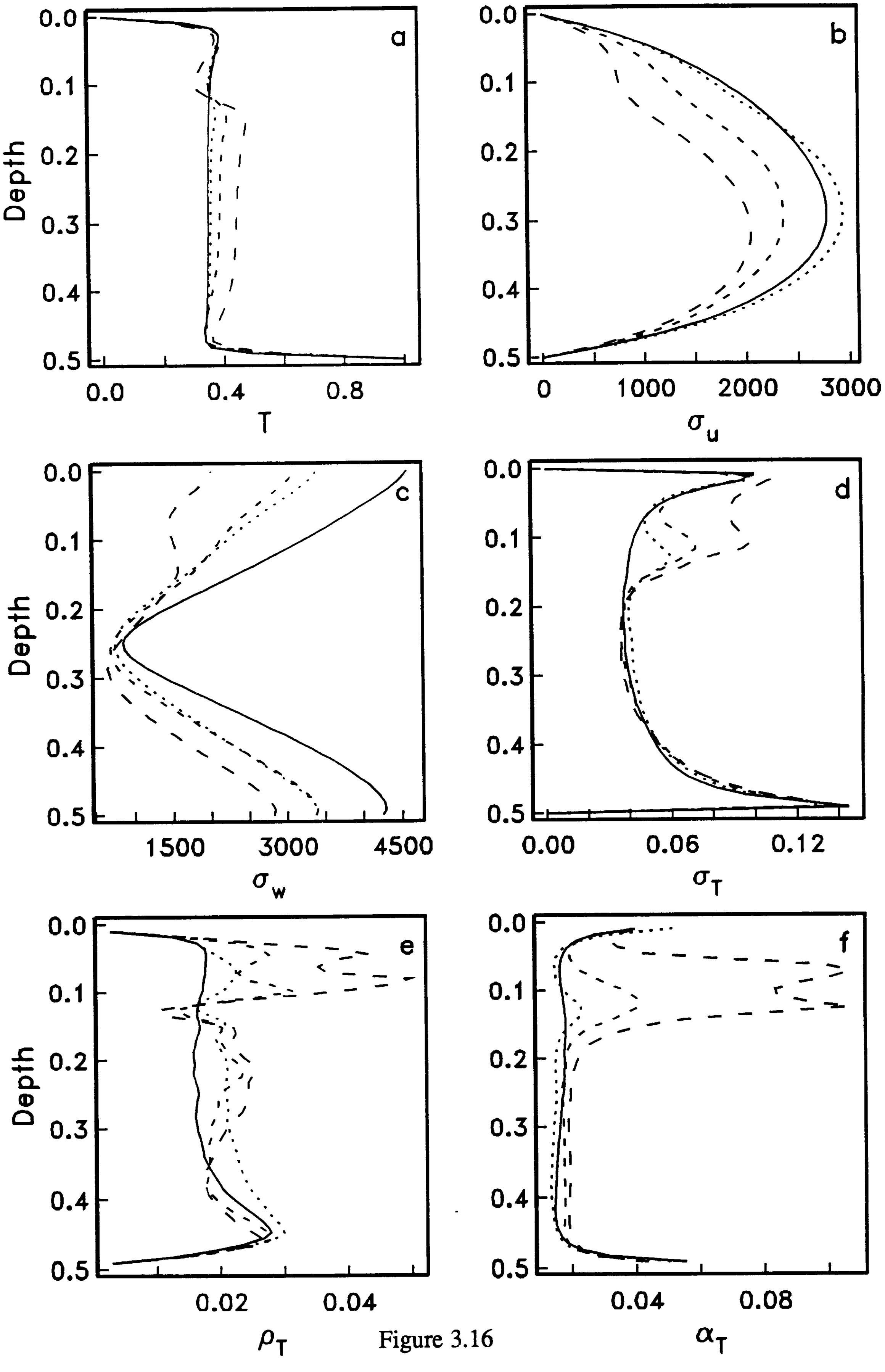
a
Depth
0.0
0.1
0.2
0.3
0.4
0.5
0.0
0.4
0.8
T
b
0
1000
2000
3000
σ_u
c
1500
3000
4500
σ_w
d
0.00
0.06
0.12
σ_T
e
0.02
0.04
ρ_T
f
0.04
0.08
α_T

Figure 3.16

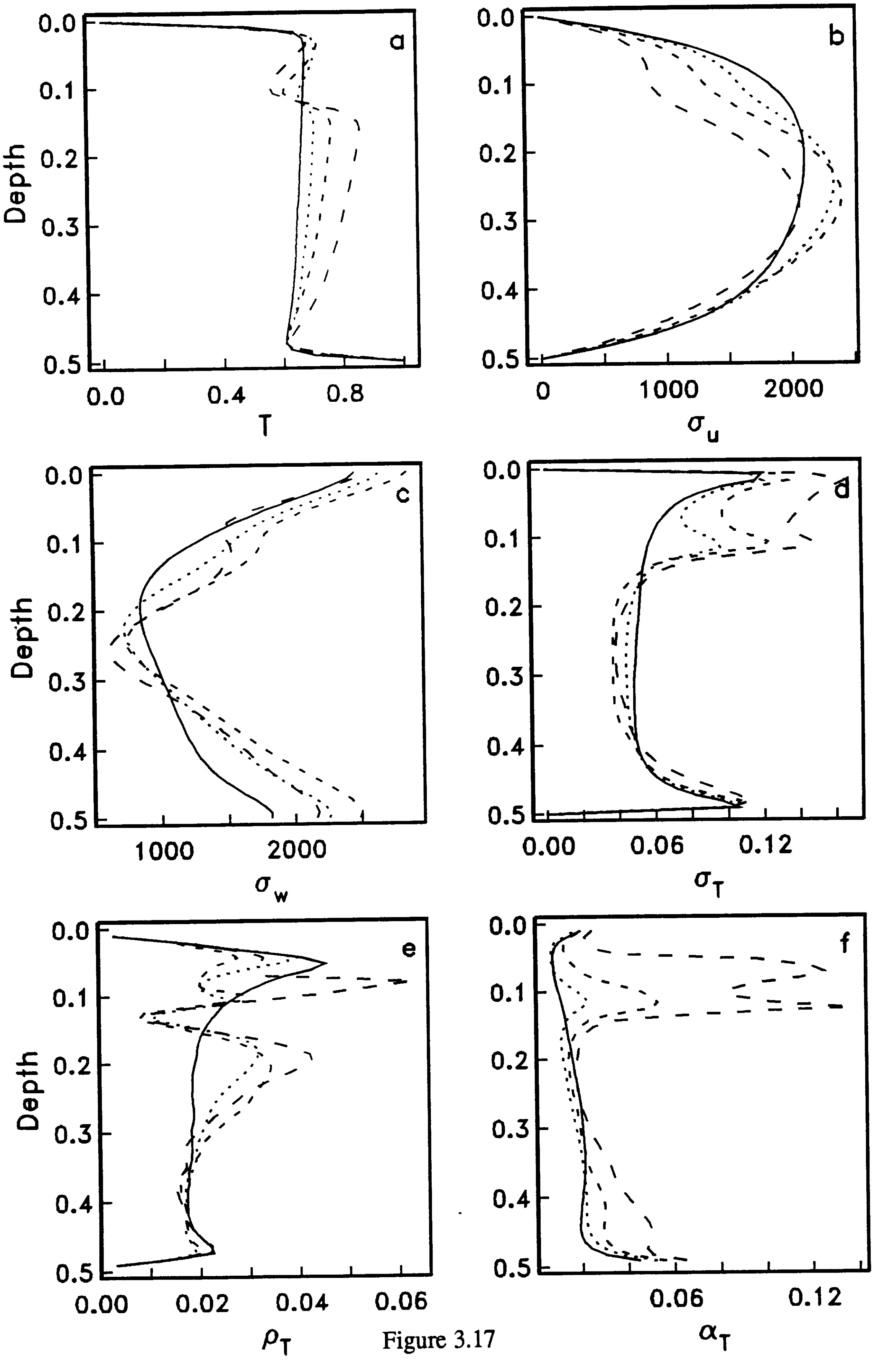
a
b
c
d
e
f
Depth
0.0
0.1
0.2
0.3
0.4
0.5
0.0
0.4
0.8
T
0
1000
2000
σ_u
1000
2000
σ_w
0.00
0.06
0.12
σ_T
0.00
0.02
0.04
0.06
ρ_T
0.06
0.12
α_T

Figure 3.17

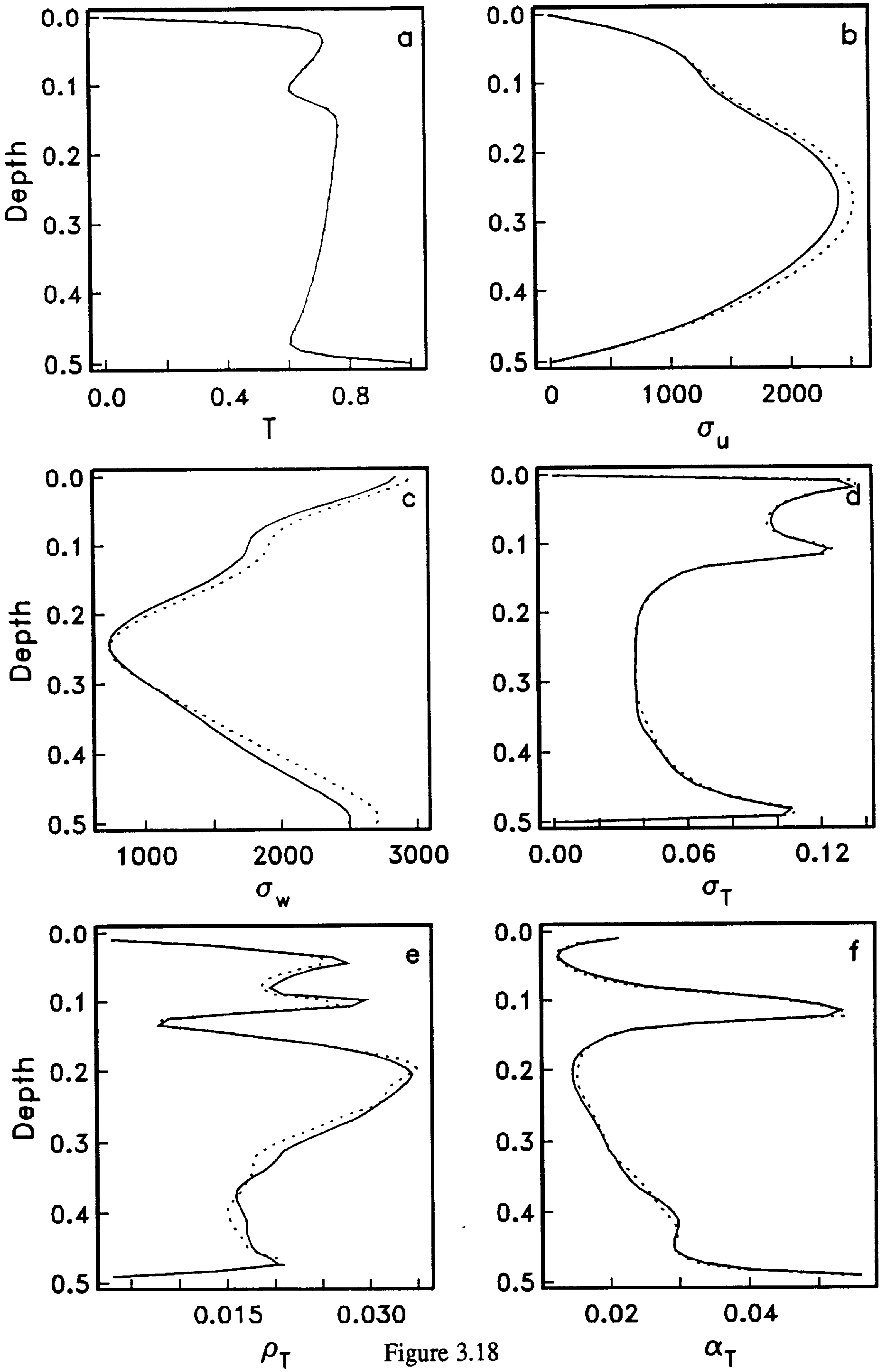
a
b
c
d
e
f
Depth
0.0
0.1
0.2
0.3
0.4
0.5
T
0.0
0.4
0.8
σ_u
0
1000
2000
σ_w
1000
2000
3000
σ_T
0.00
0.06
0.12
ρ_T
0.015
0.030
α_T
0.02
0.04

Figure 3.18

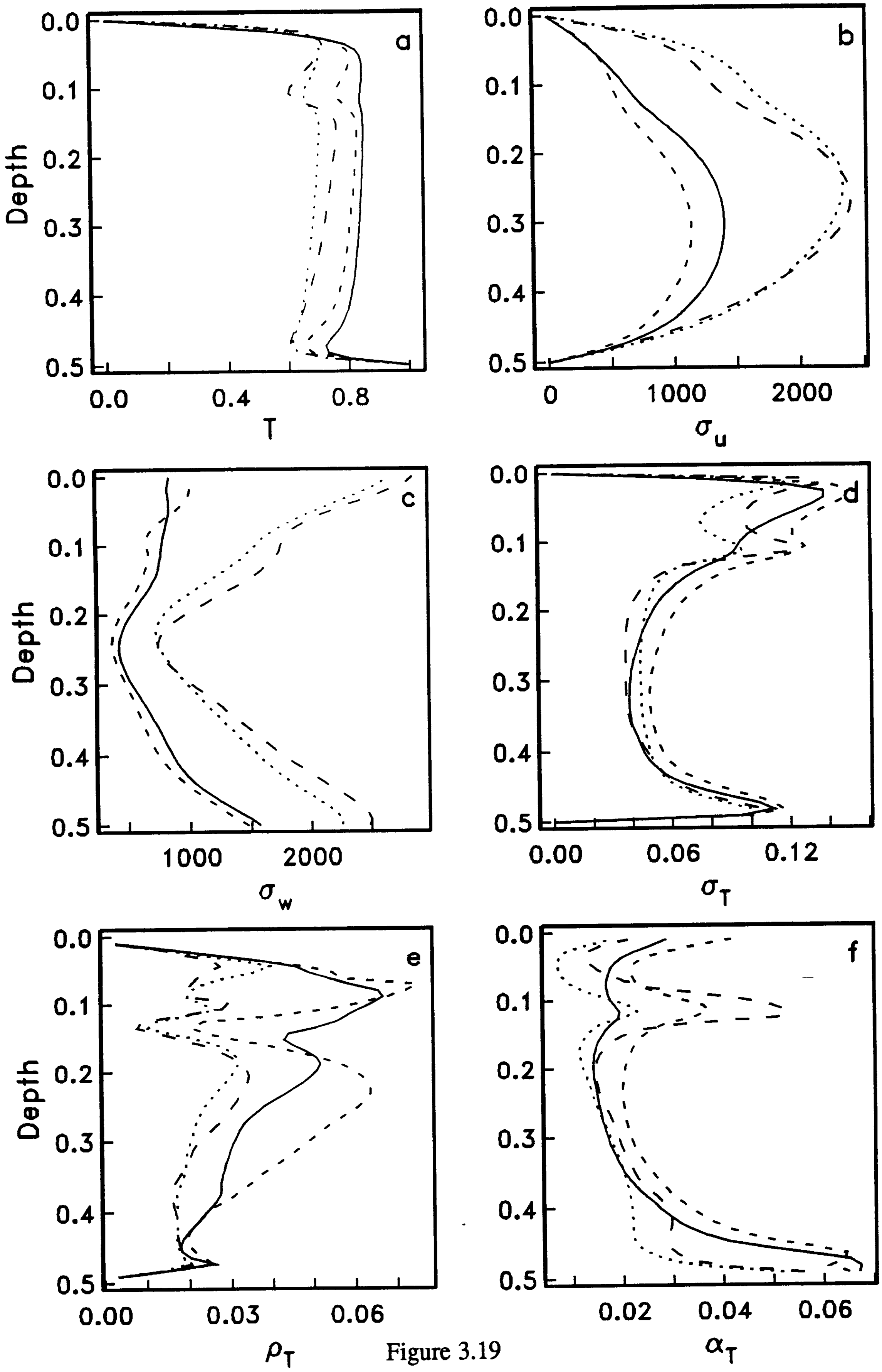
a
b
c
d
e
f
Depth
0.0
0.1
0.2
0.3
0.4
0.5
T
0.0
0.4
0.8
σ_u
0
1000
2000
σ_w
1000
2000
σ_T
0.00
0.06
0.12
ρ_T
0.00
0.03
0.06
α_T
0.02
0.04
0.06

Figure 3.19

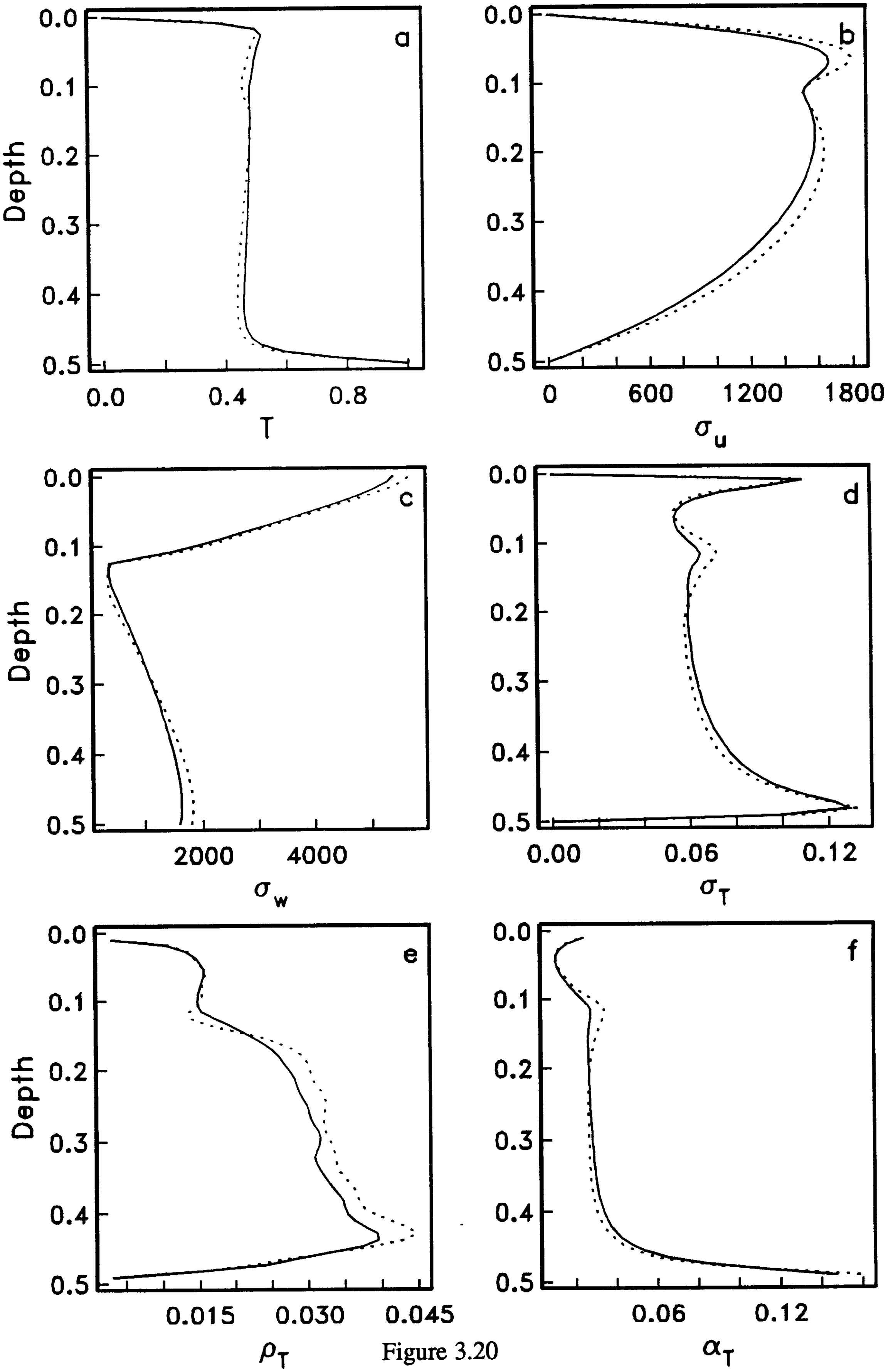
a
Depth
0.0
0.1
0.2
0.3
0.4
0.5
0.0
0.4
0.8
T
b
0.0
0.1
0.2
0.3
0.4
0.5
0
600
1200
1800
σ_u
c
Depth
0.0
0.1
0.2
0.3
0.4
0.5
2000
4000
σ_w
d
0.0
0.1
0.2
0.3
0.4
0.5
0.00
0.06
0.12
σ_T
e
Depth
0.0
0.1
0.2
0.3
0.4
0.5
0.015
0.030
0.045
ρ_T
f
0.0
0.1
0.2
0.3
0.4
0.5
0.06
0.12
α_T

Figure 3.20

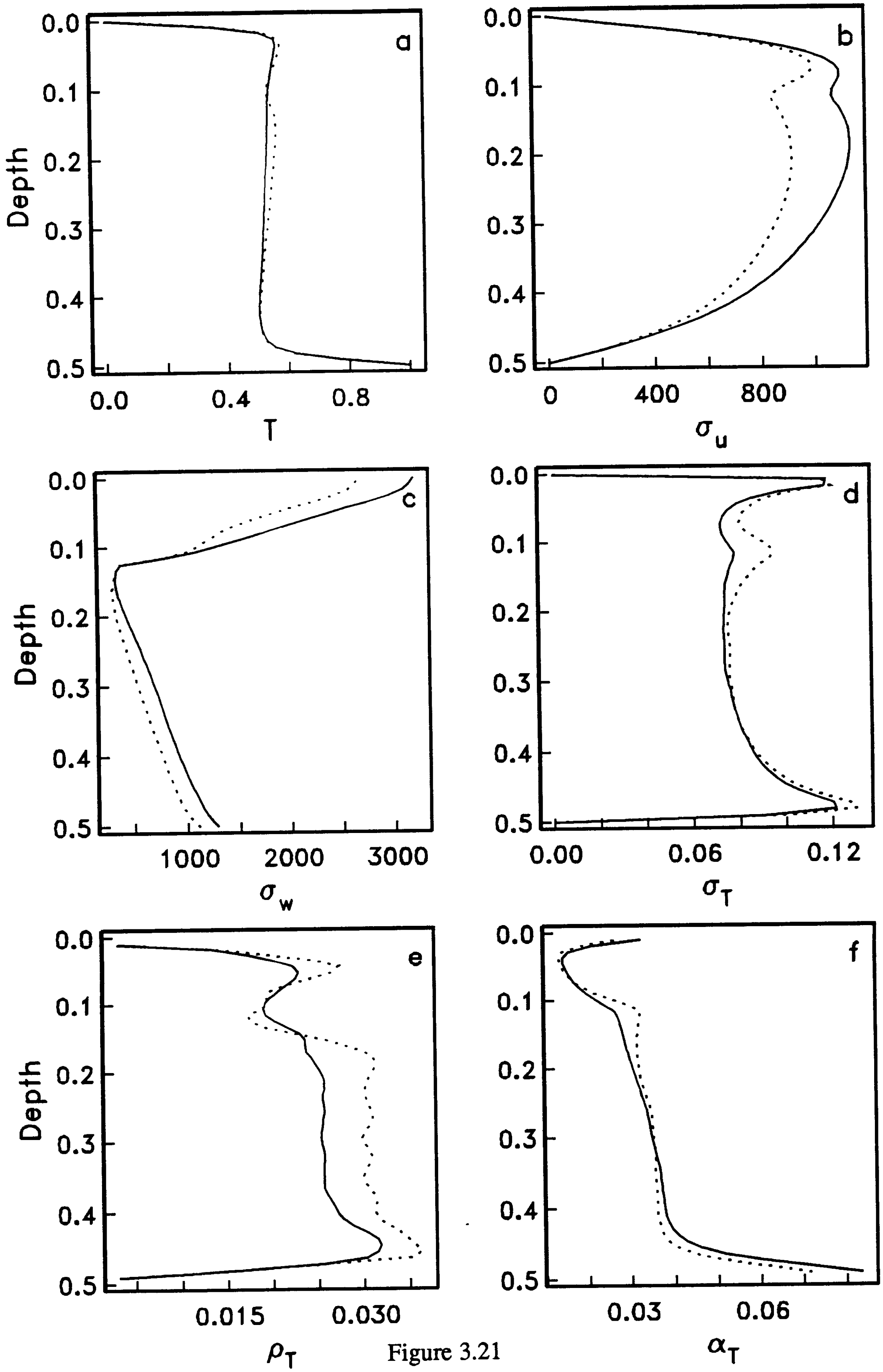
a
b
c
d
e
f
Depth
0.0
0.1
0.2
0.3
0.4
0.5
0.0
0.4
0.8
T
0
400
800
σ_u
1000
2000
3000
σ_w
0.00
0.06
0.12
σ_T
0.015
0.030
ρ_T
0.03
0.06
α_T

Figure 3.21

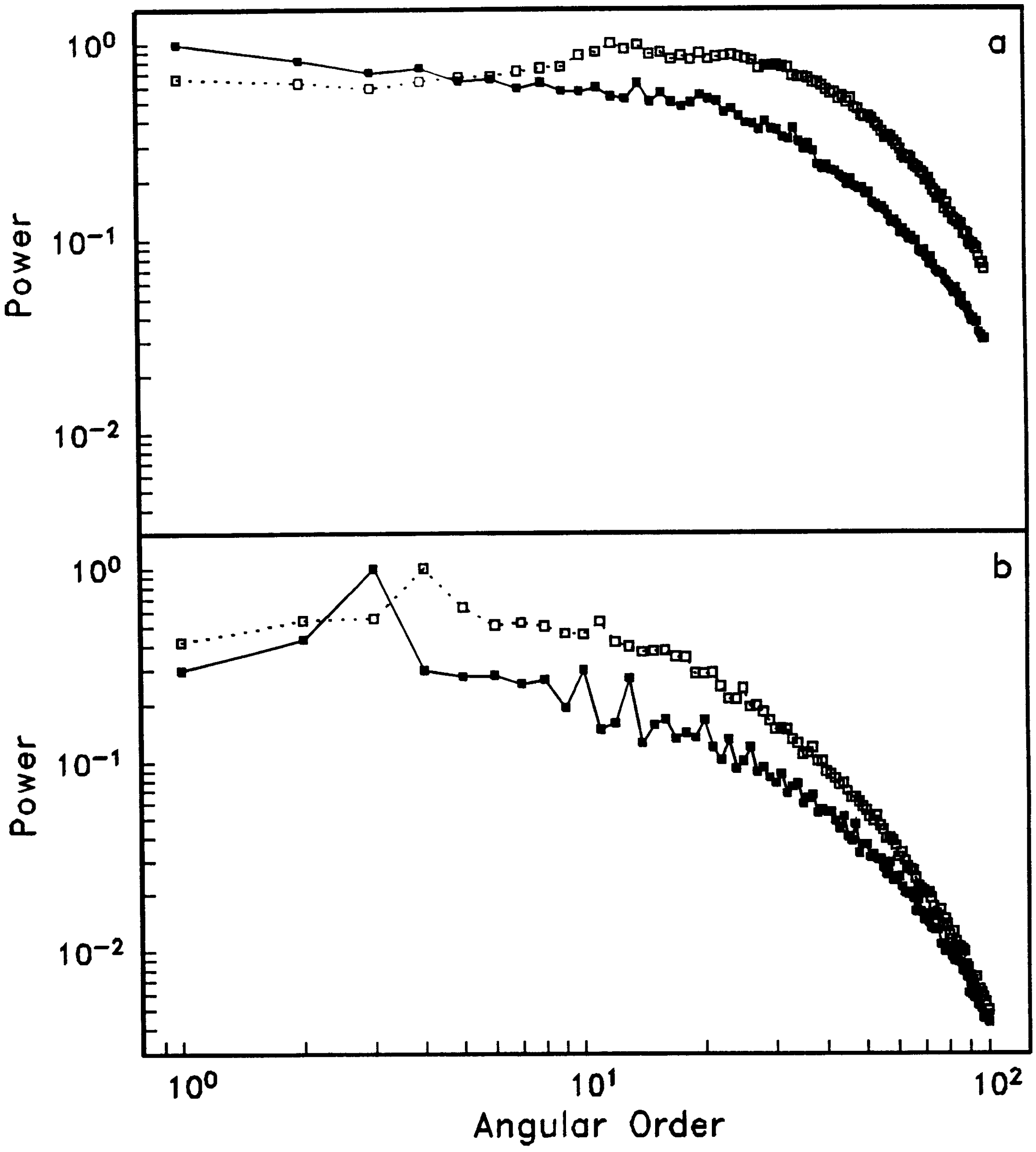

Figure 3.22

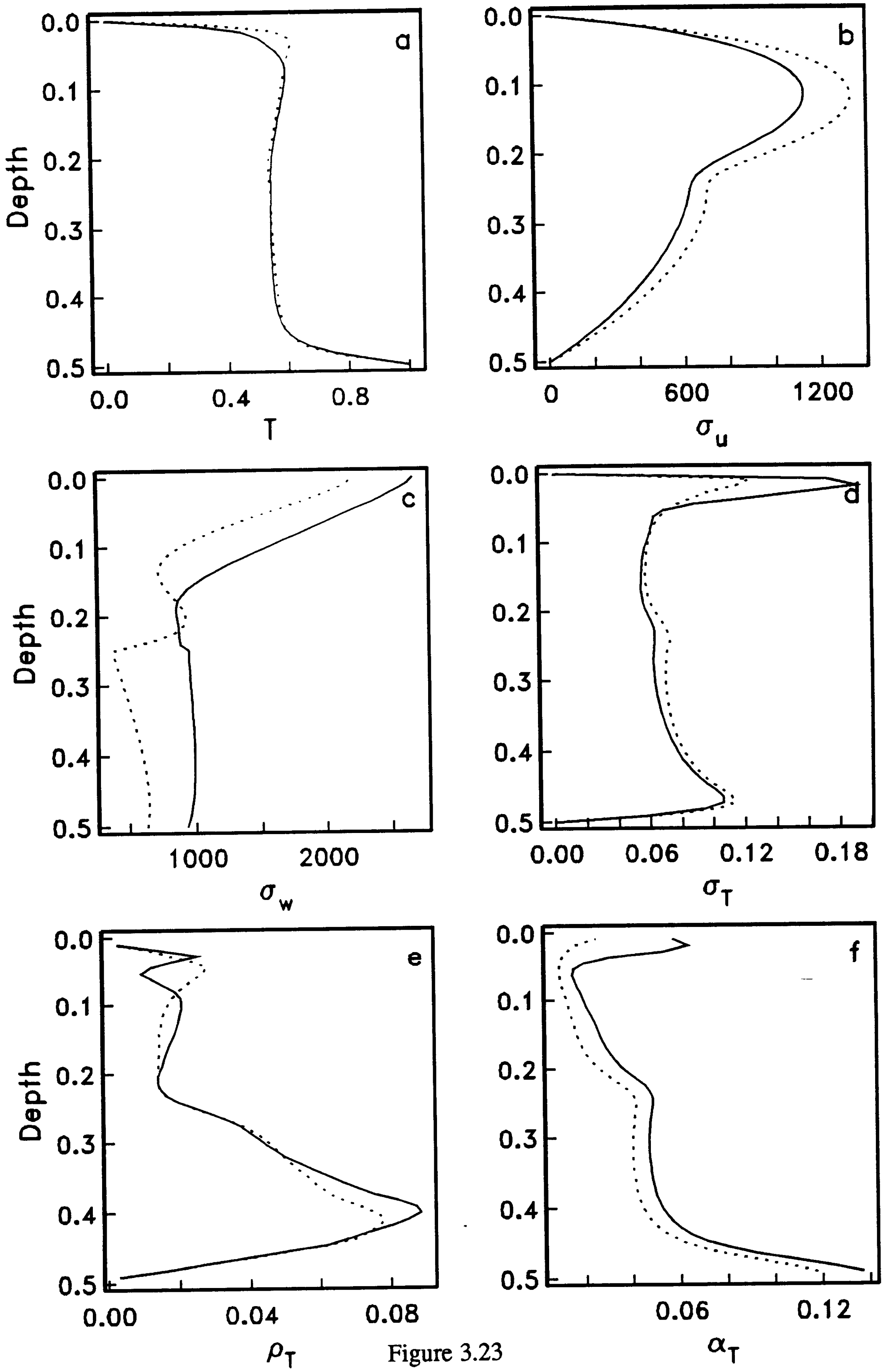
a
Depth
0.0
0.1
0.2
0.3
0.4
0.5
0.0
0.4
0.8
T
b
0
600
1200
σ_u
c
1000
2000
σ_w
d
0.00
0.06
0.12
0.18
σ_T
e
0.00
0.04
0.08
ρ_T
f
0.06
0.12
α_T

Figure 3.23

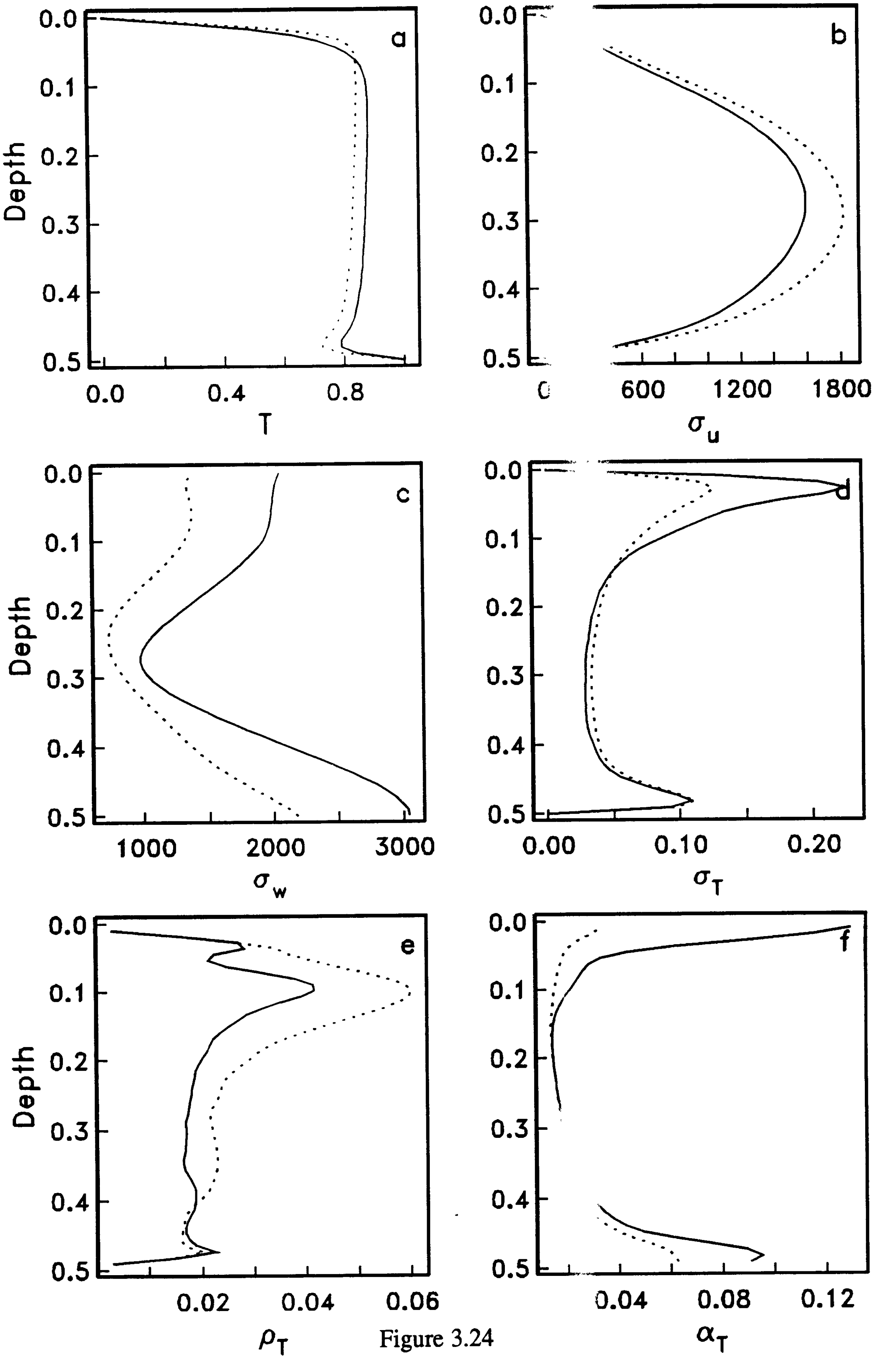
a
b
c
d
e
f
Depth
0.0
0.1
0.2
0.3
0.4
0.5
T
0.0
0.4
0.8
σ_u
600
1200
1800
σ_w
1000
2000
3000
σ_T
0.00
0.10
0.20
ρ_T
0.02
0.04
0.06
α_T
0.04
0.08
0.12

Figure 3.24

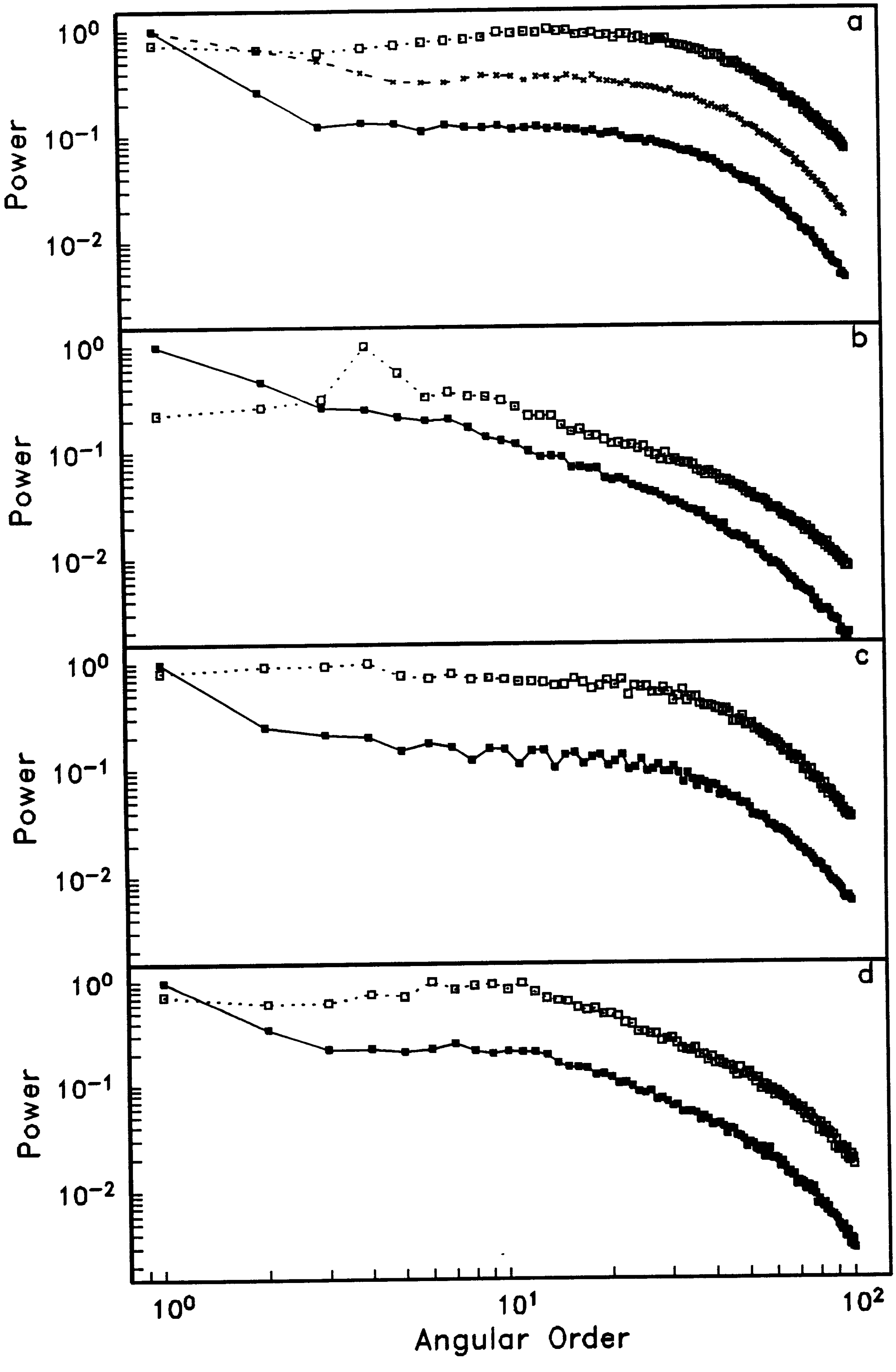
a
b
c
d
Power
Power
Power
Power
10^0
10^{-1}
10^{-2}
10^0
10^{-1}
10^{-2}
10^0
10^{-1}
10^{-2}
10^0
10^{-1}
10^{-2}
10^0
10^1
10^2
Angular Order

Figure 3.25

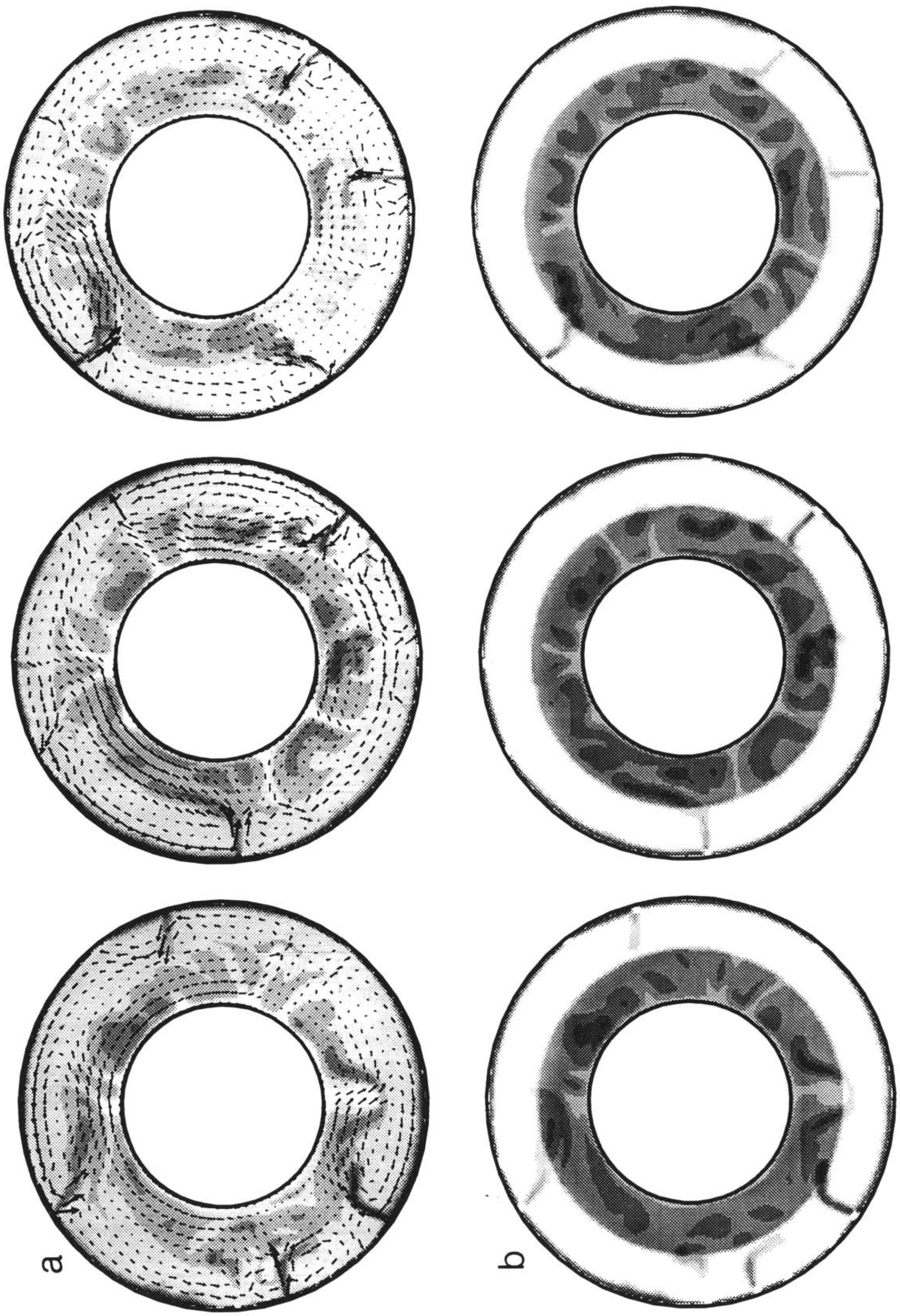

Figure 3.26

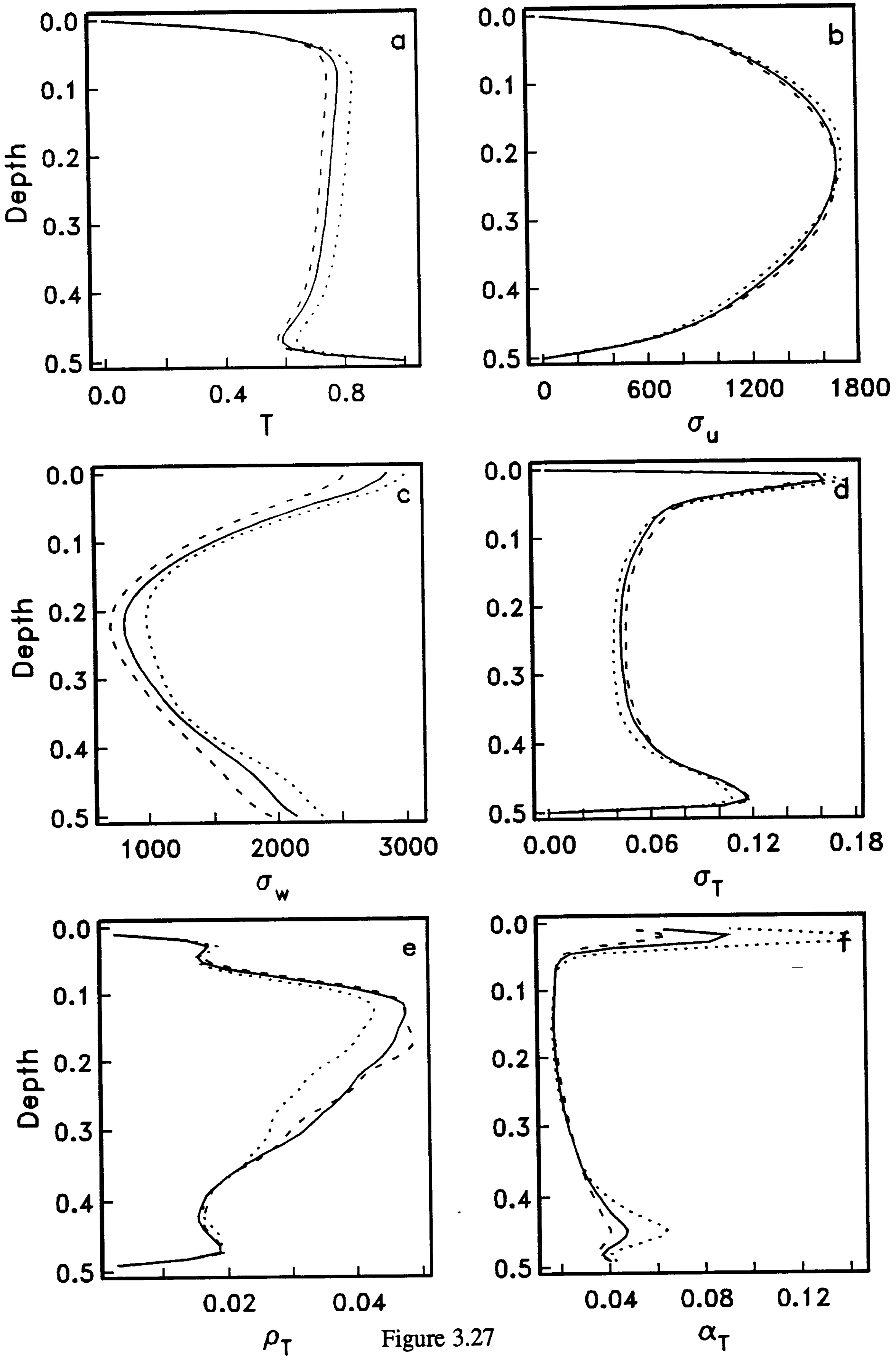
a
Depth
0.0
0.1
0.2
0.3
0.4
0.5
0.0
0.4
0.8
T
b
0
600
1200
1800
σ_u
c
1000
2000
3000
σ_w
d
0.00
0.06
0.12
0.18
σ_T
e
0.02
0.04
ρ_T
f
0.04
0.08
0.12
α_T

Figure 3.27

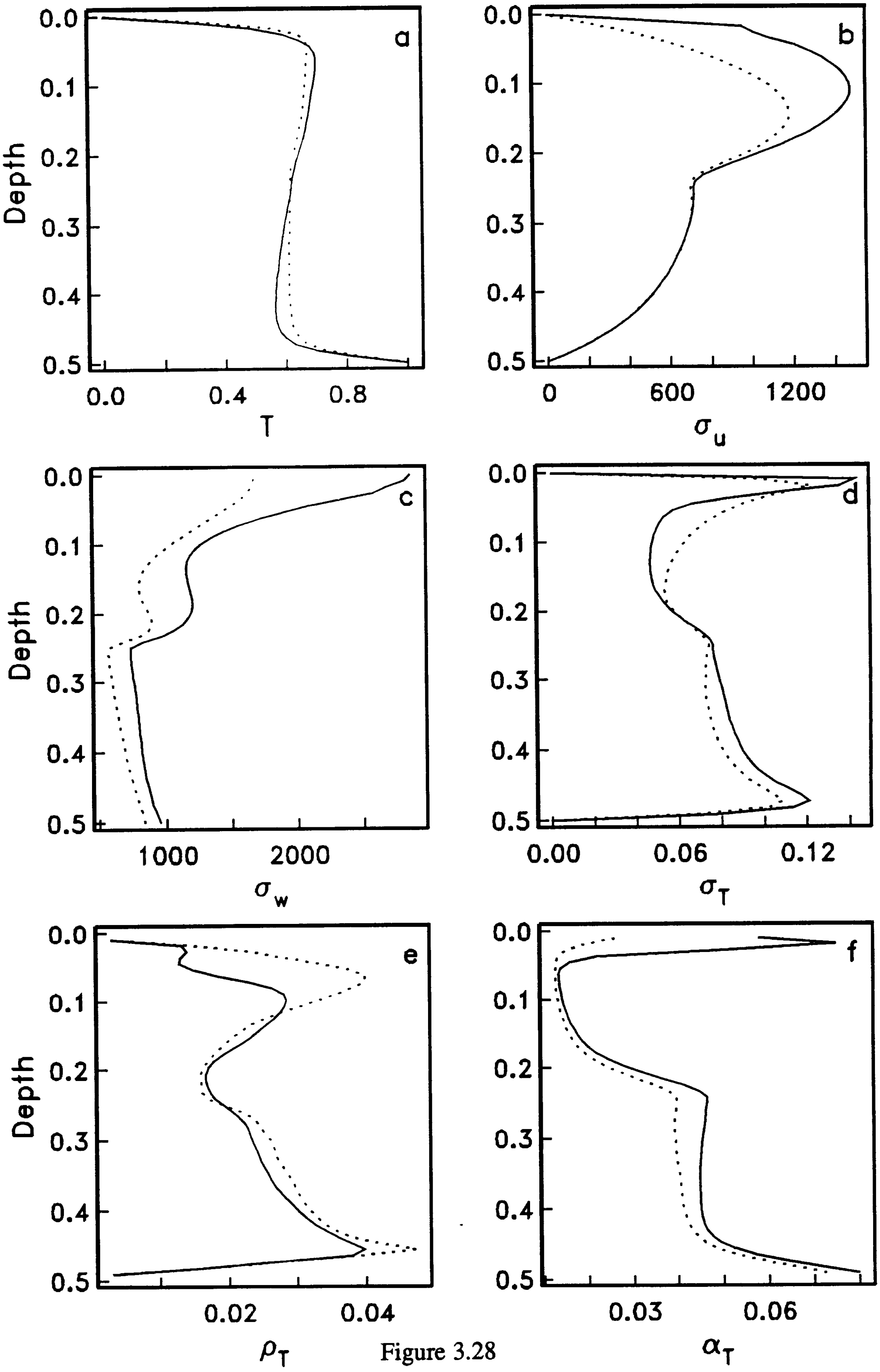
a
Depth
0.0
0.1
0.2
0.3
0.4
0.5
0.0
0.4
0.8
T
b
0.0
0.1
0.2
0.3
0.4
0.5
0
600
1200
σ_u
c
Depth
0.0
0.1
0.2
0.3
0.4
0.5
1000
2000
σ_w
d
0.0
0.1
0.2
0.3
0.4
0.5
0.00
0.06
0.12
σ_T
e
Depth
0.0
0.1
0.2
0.3
0.4
0.5
0.02
0.04
ρ_T
f
0.0
0.1
0.2
0.3
0.4
0.5
0.03
0.06
α_T

Figure 3.28

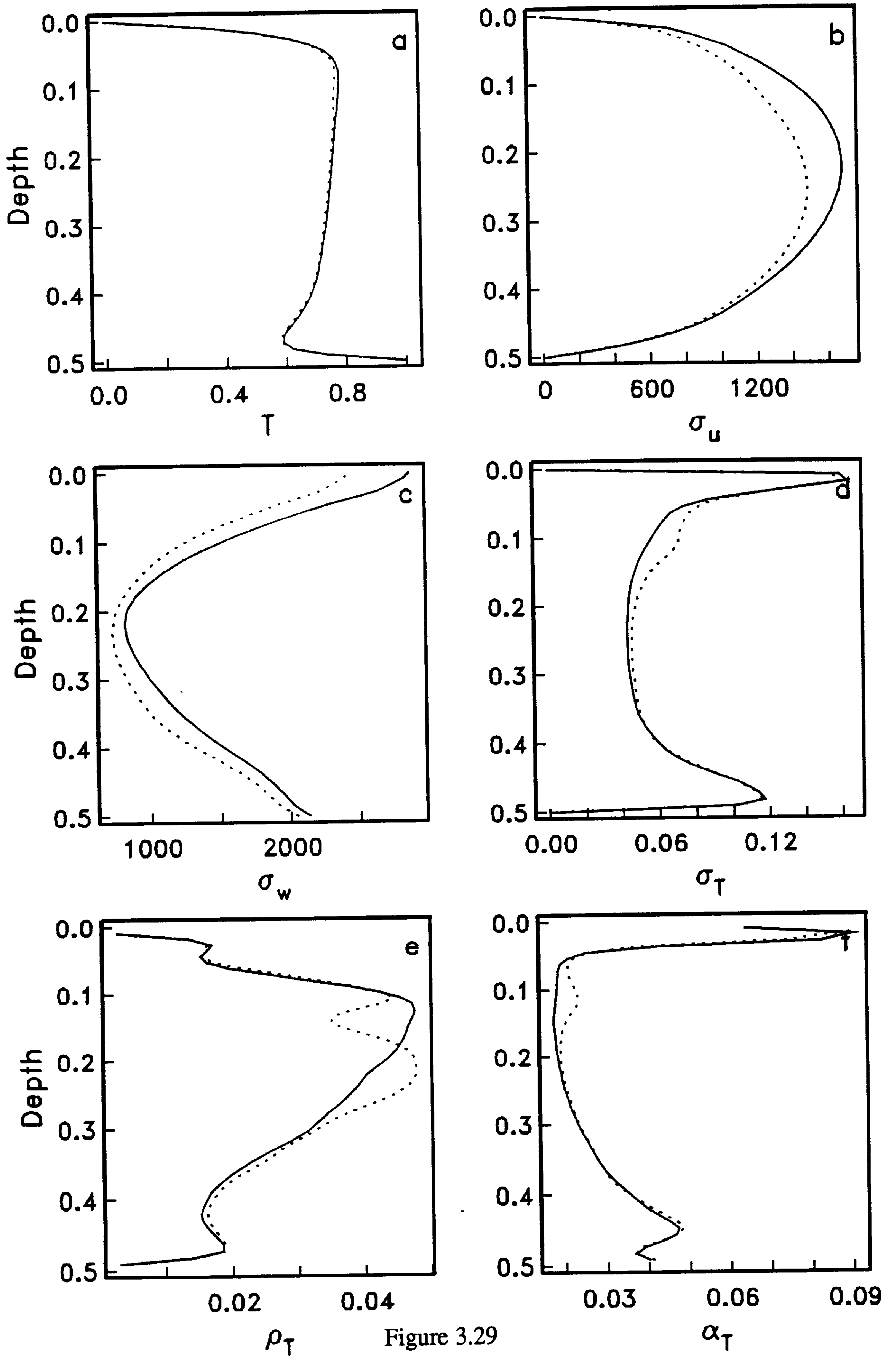
a
b
c
d
e
f
Depth
0.0
0.1
0.2
0.3
0.4
0.5
0.0
0.4
0.8
T
0
600
1200
σ_u
1000
2000
σ_w
0.00
0.06
0.12
σ_T
0.02
0.04
ρ_T
0.03
0.06
0.09
α_T

Figure 3.29

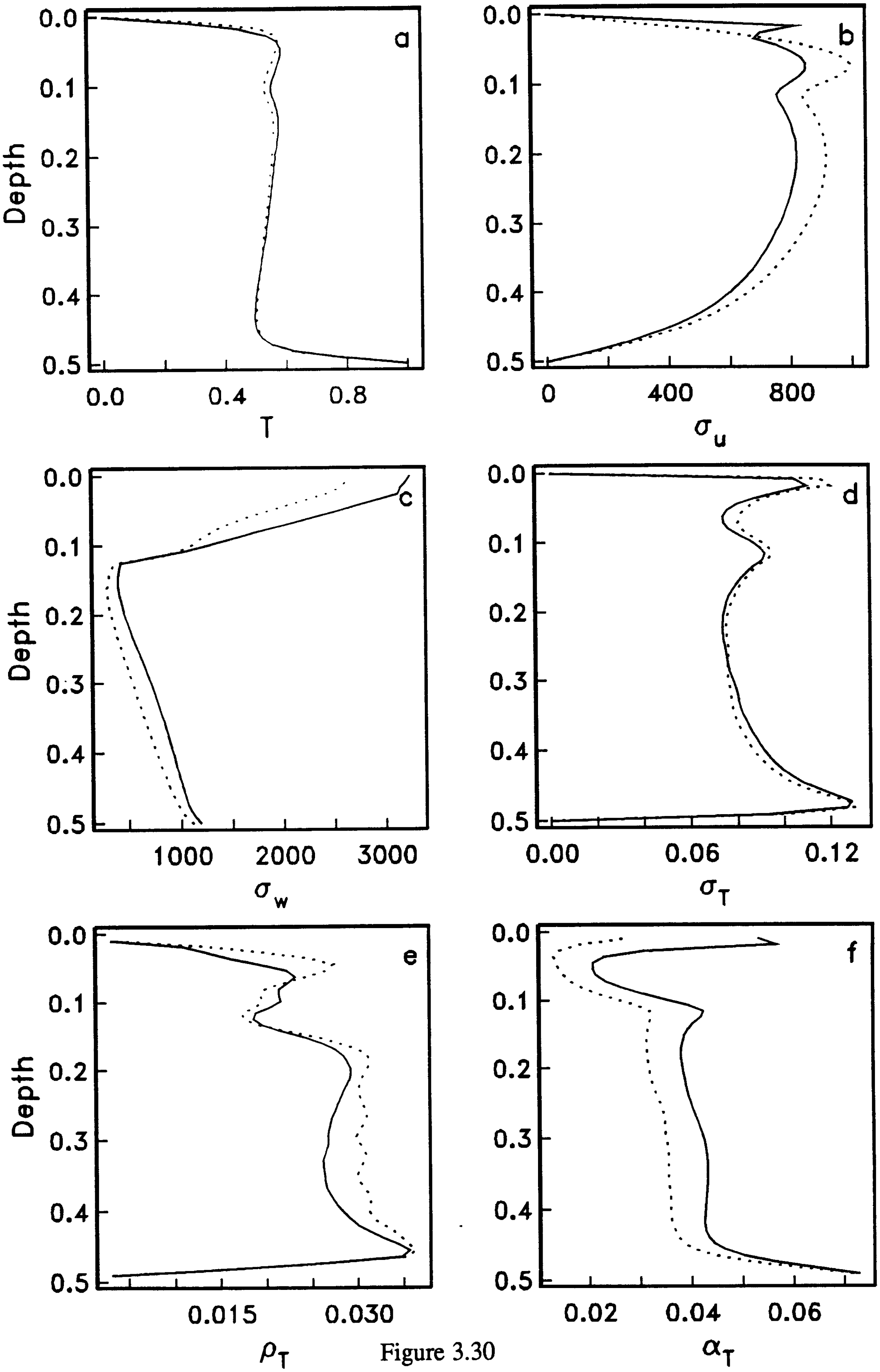
a
b
c
d
e
f
Depth
0.0
0.1
0.2
0.3
0.4
0.5
T
0.0
0.4
0.8
σ_u
0
400
800
σ_w
1000
2000
3000
σ_T
0.00
0.06
0.12
ρ_T
0.015
0.030
α_T
0.02
0.04
0.06

Figure 3.30

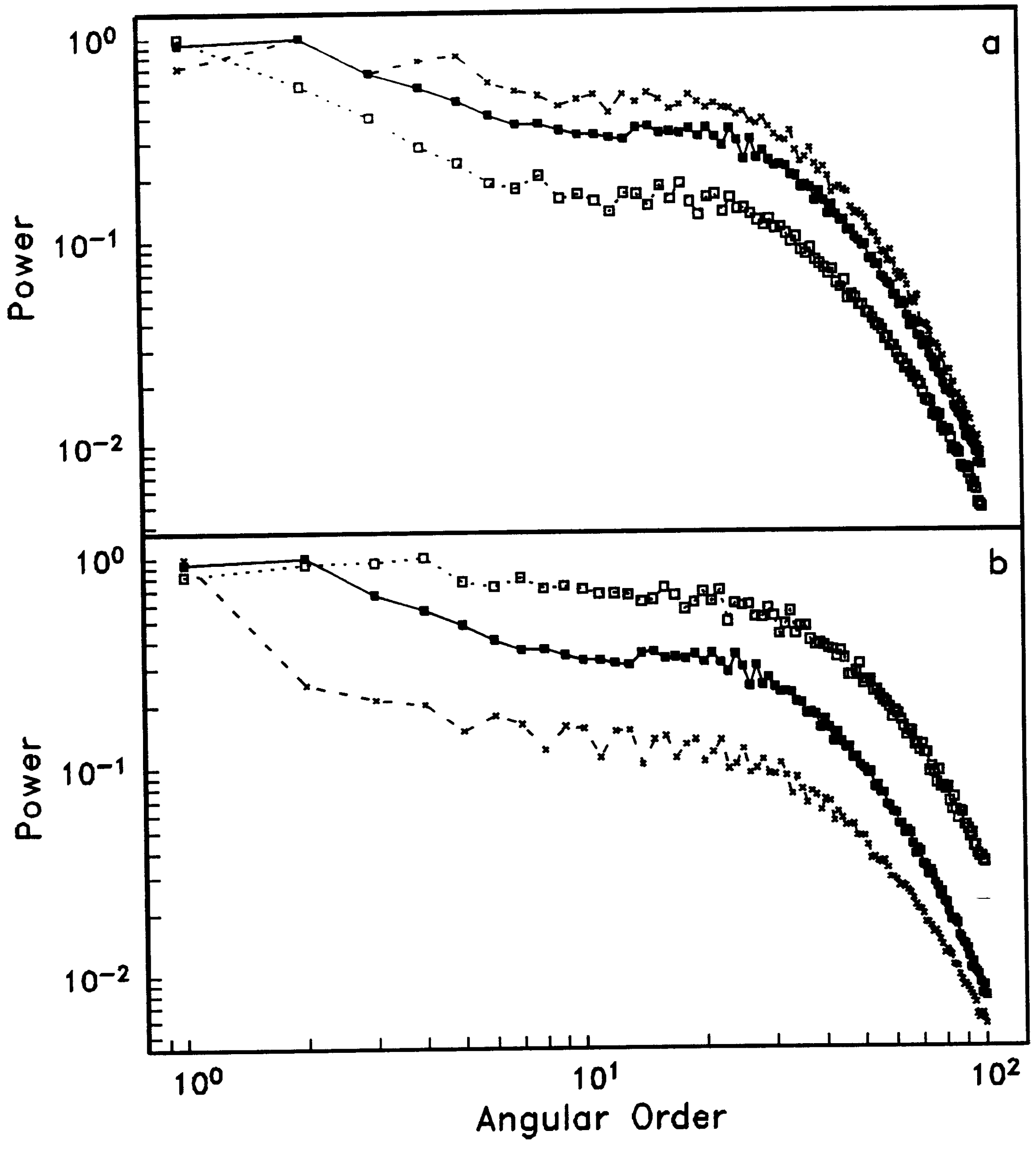
a
b
Power
Power
10^0
10^{-1}
10^{-2}
10^0
10^{-1}
10^{-2}
10^0
10^1
10^2
Angular Order

Figure 3.31

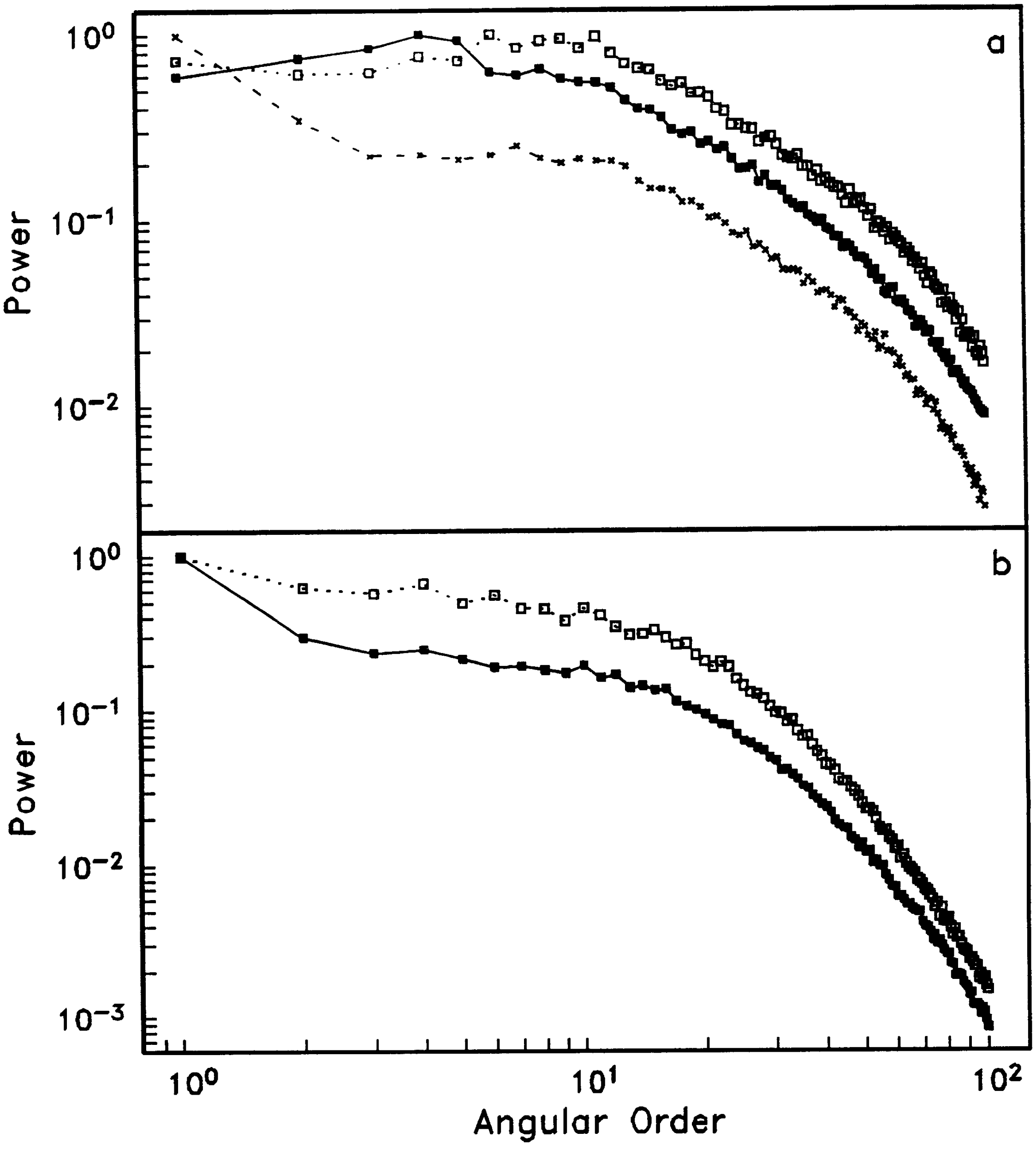

Figure 3.32

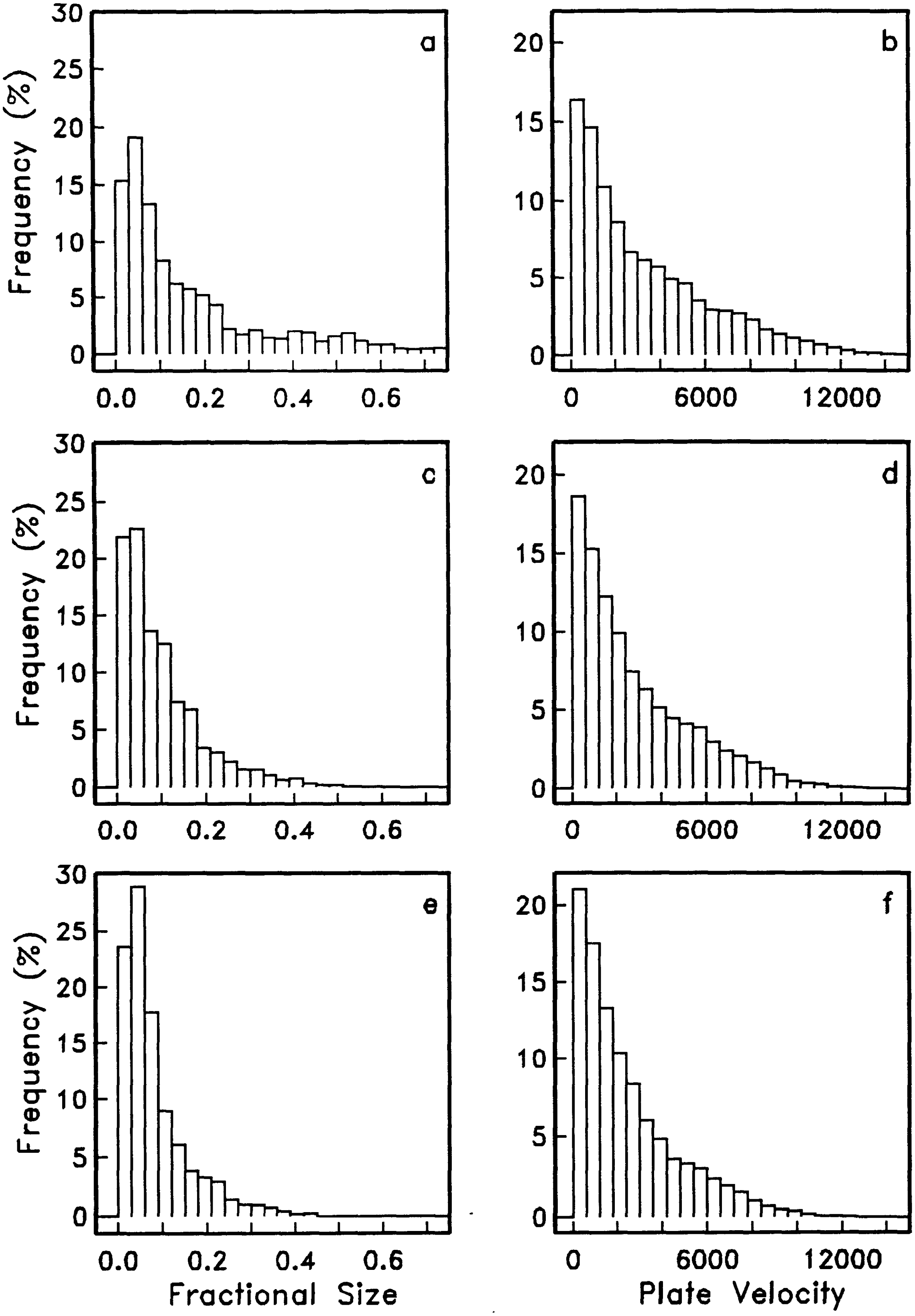
a
b
c
d
e
f
Frequency (%)
0
5
10
15
20
25
30
0.0
0.2
0.4
0.6
Fractional Size
0
5
10
15
20
0
6000
12000
Plate Velocity

Figure 3.33

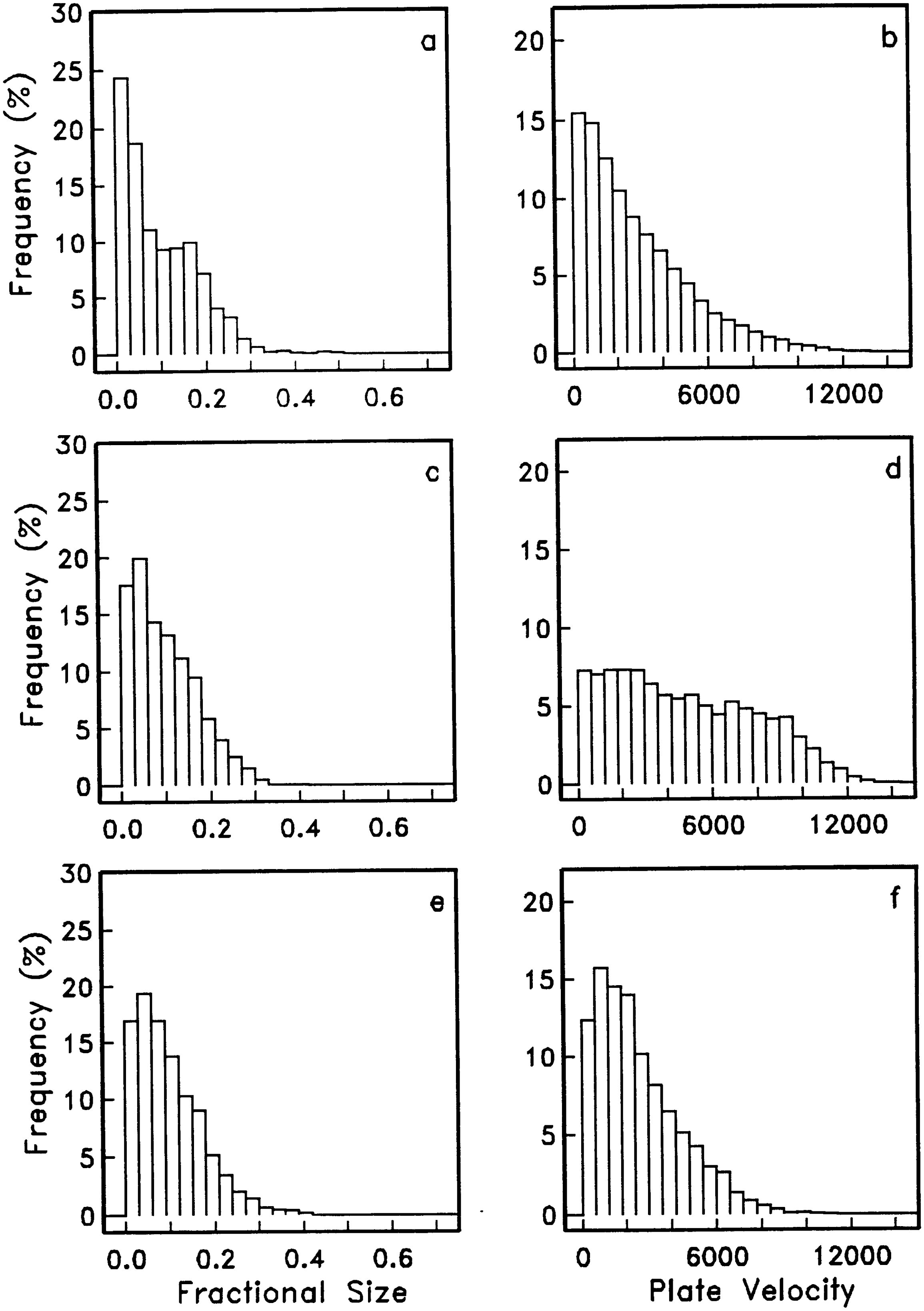
a
b
c
d
e
f
Frequency (%)
0
5
10
15
20
25
30
0.0
0.2
0.4
0.6
Fractional Size
6000
12000
Plate Velocity

Figure 3.34

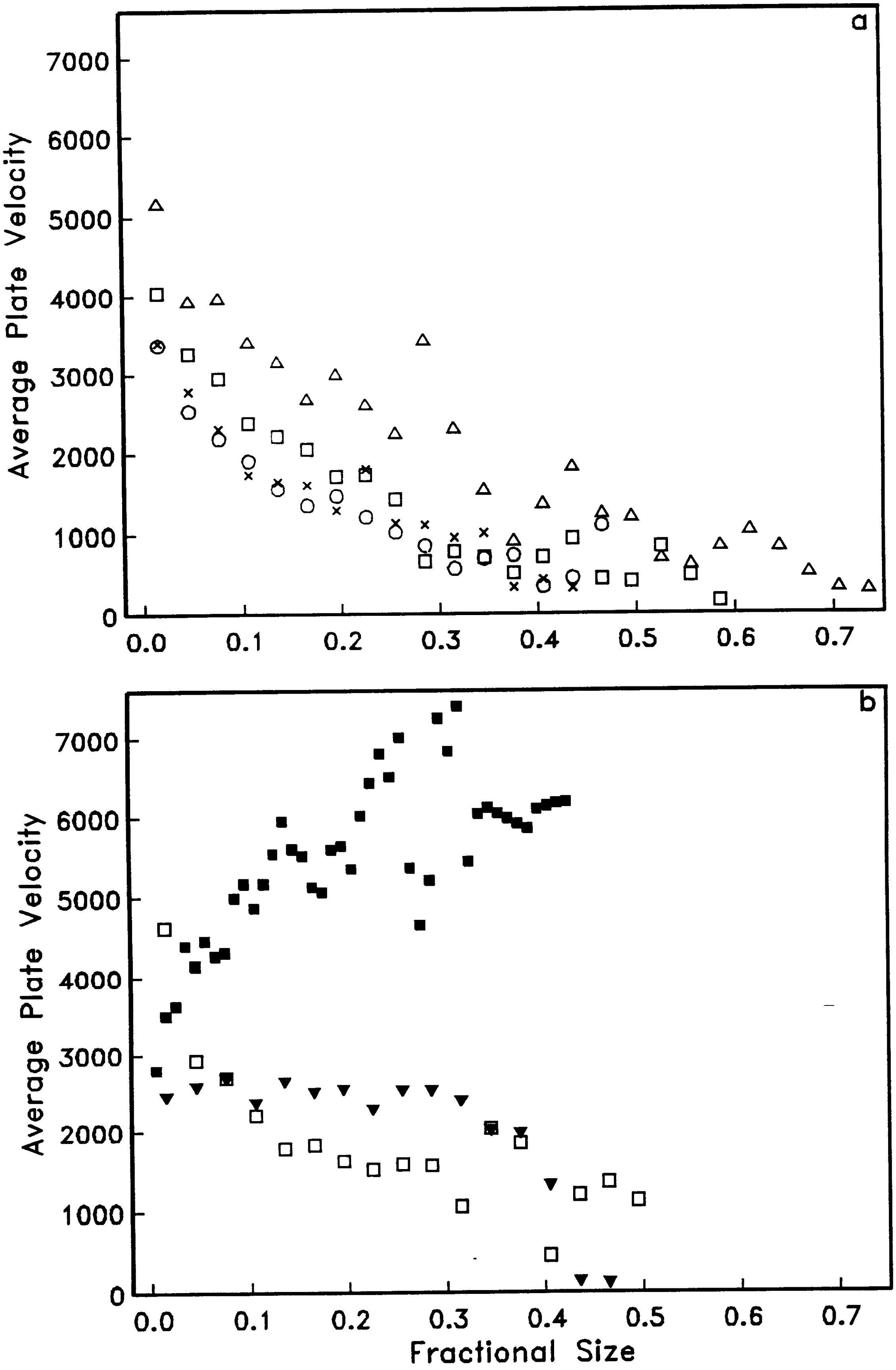
a
b
Average Plate Velocity
0
1000
2000
3000
4000
5000
6000
7000
0.0
0.1
0.2
0.3
0.4
0.5
0.6
0.7
Fractional Size

Figure 3.35

CHAPTER 4

TOMOGRAPHIC EARTH STRUCTURES

INTRODUCTION

One goal of structural seismology is to map the aspherical variations in the seismic wave speeds in sufficient detail to resolve the pattern of the mantle convection. The most fundamental issue, posed forty-three years ago by *Birch* [1951], is the degree to which the large-scale flow is stratified by changes in mineralogical phase or bulk chemistry across the transition zone from depths of 400 to 700 km. The most plausible mineralogical explanation for the jump in elastic parameters at the 660-km discontinuity is the endothermic dissociation of spinel-structured $(Mg,Fe)_2SiO_4$ (γ-olivine) into (Mg,Fe)O (magnesiowüstite) plus perovskite-structured $(Mg,Fe)SiO_3$. The 660-km discontinuity could also mark a compositional boundary between the upper and lower mantle [*Richter and Johnson*, 1974], at least in some average sense [*Jeanloz*, 1991]. Another mechanism for impeding vertical flow is an increase of viscosity with depth. Most radial viscosity structures obtained from modeling the earth's non-hydrostatic geoid [*Hager et al.*, 1985; *Hager and Richards*, 1989; *Ricard and Wuming*, 1991; *King and Masters*, 1992; *Forte et al.*, 1993] exhibit a rapid viscosity increase from the upper to the lower mantle.

Our numerical experiments, presented in chapter 3, indicate that mantle flow stratification due to an endothermic phase transition or due to a step-function viscosity increase show a distinct expression in the two-point correlation diagnostics.

Structural information on a global scale is now available from tomographic models of mantle shear-wave velocities. Data sets with relatively good geographic and depth coverage have been compiled and inverted by several research groups [*Tanimoto*, 1990; *Su and Dziewonski*, 1991; *Dziewonski and Woodward*, 1992; *Masters et al.*, 1992;

Woodward et al., 1993; *Su et al.*, 1994], yielding whole-mantle models with aspherical variations up to spherical harmonic degree twelve [*Su et al.*, 1994]. Although the resolving power of these whole-mantle models is insufficient to image the details of individual upwellings and downwellings, they do constrain the large-scale pattern of mantle flow. In addition, a high-resolution regional tomographic model of the western hemisphere [*Grand*, 1994] has recently become available providing additional information at smaller wavelengths. In this chapter we characterize the seismic models using the two-point correlation functions introduced in chapter 2.

GLOBAL TOMOGRAPHIC MODELS

In most global tomographic inversions, the aspherical variations in shear-wave speed, $\delta\beta$, are represented by a truncated surface spherical harmonic series,

$$\delta\beta(r,\Omega) = \sum_{l=1}^{l_{max}} \sum_{m=-l}^{l} \delta\beta_l^m(r) Y_l^m(\Omega), \tag{4.1}$$

The radii r range from the core-mantle boundary at $b = 3480\,\text{km}$ to the surface at $a = 6371\,\text{km}$, and the angular coordinates $\Omega = (\theta, \varphi)$ range over the unit sphere S_1. In regions where compositional and phase differences can be ignored, $\delta\beta$ is relatively small, typically less than 5% of the mean wave speed $\overline{\beta}(r)$, and can be related to the aspherical temperature variations by the linear approximation $\delta\beta(r,\Omega) = (\partial\beta / \partial T)_P\, \delta T(r,\Omega)$.

Laboratory measurements [*Anderson et al.*, 1992] and seismic observations of slab anomalies [*Creager and Jordan*, 1986] yield reliable estimates of the temperature derivative of shear velocity at upper mantle conditions, but there is considerable uncertainty on the value of $(\partial\beta / \partial T)_P$ in the lower mantle; Debye-Grüneisen theory predicts that it decreases substantially with pressure, perhaps by as much as an order of magnitude between the transition zone and the core-mantle boundary [*Duffy and Ahrens*, 1992].

This uncertainty aside, a good "general circulation model" for mantle flow should be able to reproduce the major features of $\delta\beta(r,\Omega)$. It would appear, however, that the current understanding of mantle convective processes is far too crude to erect such a model; even if constrained by the observed motions of the surficial plates, dynamical calculations can be expected to simulate only the grosser aspects of the flow pattern, not its smaller, more time-dependent geographical features. Moreover, whole-mantle tomography has the resolving power to recover only a low-pass filtered image of mantle structure, with features that are uncertain at the smaller scales.

Distinguishing among competing convection hypotheses must therefore rely on a set of robust, reliably estimated properties of $\delta\beta(r,\Omega)$. We employ the two-point correlation diagnostics defined in chapter 2 to characterize tomographic earth structures in a way that allows a direct comparison to numerical convection experiments. The diagnostic functions (2.3)-(2.5) embody complementary information about the spatial correlation of time-dependent fields. Beyond their utility in assessing the structural differences among mantle convection simulations, demonstrated in chapter 3, the two-point correlation functions of the temperature fields of numerical convection experiments can be constrained by seismic observations.

Seismology can at best provide only a single (present-day) snapshot of the aspherical variation in the shear-wave speeds, $\delta\beta(r,\Omega)$, rather than a time series. Consequently, temporal averaging cannot be done to obtain $C_{\beta\beta}(r,r',\Delta)$ for the real earth. Instead, we must rely on the 3D snapshot estimators

$$\tilde{\sigma}_\beta^2(r) = \frac{1}{4\pi}\int_{S_1} \delta\beta^2(r,\Omega)\,d\Omega = \frac{1}{4\pi}\sum_l \tilde{S}_\beta(r,l) \tag{4.2}$$

$$\begin{aligned} \tilde{R}_\beta(r,r') &= \frac{1}{4\pi\,\tilde{\sigma}_\beta(r)\,\tilde{\sigma}_\beta(r')}\int_{S_1} \delta\beta(r,\Omega)\,\delta\beta(r',\Omega)\,d\Omega \\ &= \frac{1}{4\pi\,\tilde{\sigma}_\beta(r)\,\tilde{\sigma}_\beta(r')}\sum_{l,m} \delta\beta_l^{m*}(r)\,\delta\beta_l^m(r') \end{aligned} \tag{4.3}$$

$$\begin{aligned} \tilde{A}_\beta(r,\Delta) &= \frac{1}{8\pi^2\tilde{\sigma}_\beta^2(r)}\int_{S_1}\int_{S_1} \delta\beta(r,\Omega)\,\delta\beta(r,\Omega')\,\delta(\Omega\cdot\Omega'-\cos\Delta)\,d\Omega\,d\Omega' \\ &= \frac{1}{4\pi\tilde{\sigma}_\beta^2(r)}\sum_l \tilde{S}_\beta(r,l)\,P_l\,(\cos\Delta) \end{aligned} \tag{4.4}$$

where $\tilde{S}_\beta(r,l) = \sum_m |\delta\beta_l^m(r)|^2$ and $P_l(\cos\Delta)$ are Legendre polynomials.

Fortunately, the angular averaging in (4.2)-(4.4) is effective in reducing snapshot variability. A few judicious approximations (e.g., the statistics are Gaussian) can be used to show that the relative standard deviations in $\tilde{\sigma}_f$, $\tilde{\rho}_f$, and $\tilde{\alpha}_f$ owing to temporal fluctuations in $f(r,\Omega,t)$ (for example, shear-velocity or temperature) are proportional to $\tilde{\alpha}_f$. Expressing $\tilde{\alpha}_f$ in radians, we obtain:

$$\mathrm{S.D.}[\tilde{\sigma}_f / \sigma_f] \approx 0.5\alpha_f, \tag{4.5a}$$

$$\mathrm{S.D.}[\tilde{\rho}_f / \rho_f] \approx 0.7\alpha_f, \tag{4.5b}$$

$$\mathrm{S.D.}[\tilde{\alpha}_f / \alpha_f] \approx 0.4\alpha_f \tag{4.5c}$$

Values typical of the low-resolution seismic models [e.g.,*Masters et al.*, 1992; *Su et al.*, 1994] are $0.1 < \tilde{\alpha}_f < 0.2$, implying snapshot-to-snapshot variations of 15% or less for all three diagnostics. This statistical behavior has been numerically confirmed for *Tackley et al.'s* [1993] 3D model, shown in Figure 4.1, which depicts the "ensemble averages" σ_T, ρ_T, and α_T as well as the snapshot estimators $\tilde{\sigma}_T$, $\tilde{\rho}_T$, and $\tilde{\alpha}_T$ for three instants of the simulation. Should the mantle convective regime be distinctly non-Gaussian, such as a bimodal regime regulated by a strong endothermic phase change at 660 km and dominated by periodic, large-scale flushing of upper-mantle material into the lower mantle [e.g., *Machetel and Weber*, 1991], the probability that the snapshot estimates will differ from the ensemble average can be significant.

While σ_f is a useful diagnostic for characterizing both numerical convection experiments and tomographic earth models, using it for comparing between the two is problematic due to the uncertain variation of the temperature coefficient of shear-wave speed, $(\partial\beta / \partial T)_P$, with pressure [*Duffy and Ahrens*, 1992]. R_f and A_f on the other hand are invariant with respect to any radial scaling of $f(r,\Omega,t)$.

Figure 4.2 displays equatorial and polar cross-sections of the rms-normalized shear velocity, $\delta\beta(r,\Omega)/\bar{\sigma}(r)$, for two whole-mantle shear-velocity models, the Harvard model S12_WM13 [*Su et al.*, 1994] (abbreviated HV) and the Scripps model SH10/C17 [*Masters et al.*, 1992] (abbreviated SC). Different data sets and parameterizations were used in the tomographic solutions. The Harvard group obtained spherical-harmonic/Chebyshev coefficients for $l_{max} = 12$ and $n_{max} = 13$ by inverting an extensive collection of long-period waveforms, including both body and surface waves, as well as sets of *SS–S* and *ScS–S* differential travel times measured by *Woodward and Masters* [1991; 1991] and their own *S* and *SS* absolute travel times. The Scripps group used the same differential travel-times in combination with a large compilation of free-oscillation data [*Ritzwoller et al.*, 1988; *Smith and Masters*, 1989], plus absolute times of *S* phases and some higher-order *S* multiples. They discretized the radial distribution of aspherical heterogeneity into eleven vertically homogeneous layers of varying thicknesses and expanded each in a spherical-harmonic series to $l_{max} = 10$. For consistency, we truncated the coefficient series for HV at angular degree and order 10 and expanded the radial variation of SC in Chebyshev polynomials out to order 13.

Figures 4.3 and 4.4 show radial and angular correlation functions and $\tilde{\sigma}_\beta$, $\tilde{\rho}_\beta$, and $\tilde{\alpha}_\beta$, for the two models. The maps of $\tilde{R}_\beta(r,r')$ (Figures 4.3*a*, *b*) are very similar in the upper half of the mantle, with correlation lengths that oscillate by only a few tens of kilometers about a mean of approximately 130 km (Figure 4.4*b*). Below 1500 km depth the HV model shows a rapid increase in the correlation length reaching a maximum of 320 km at 2400 km before falling off towards the core-mantle boundary. The maximum occurs at the level marking the best expression of the high-amplitude, low-degree structures that dominate the lowermost mantle in HV and other tomographic models. In the SC model, these features are compressed into a thinner zone above the core-mantle boundary; consequently, $\tilde{\rho}_\beta$ remains approximately constant to 2400 km, below which it increases to 270 km at the base of the mantle. The angular correlation functions for HV and SC (Figures 4.3*c*, *d*), are largest near the surface, decreasing at depths of 500 km and 400 km, respectively, and show another local maximum near the core-mantle boundary. These characteristics are also evident in $\tilde{\alpha}_\beta$ (Figure 4.4*c*). $\tilde{\sigma}_\beta$ shows maxima near the surface and core-mantle boundary (CMB), with the HV model having a near-surface maximum almost three times bigger than the maximum near the CMB, while for the SC model the maxima are of approximately equal height (Figure 4.4*a*). Figure 4.5 shows angular power spectra for the two models. The radially averaged normalized power spectrum (Figure 4.5*a*) peaks at the lowest angular degrees (l = 2-3) for both models. The spectral roll-off is more pronounced for SC than HV. This is due to the fact that the power in the mid-mantle is distributed nearly uniformly for HV while for SC low angular degrees dominate. The change in the spectral character from a white spectrum to one dominated by angular degrees two and three near the CMB has been documented by the Harvard group [*Su et al.*, 1994] and is also apparent for SC, even though there the change in spectral character occurs at greater depth.

MODEL RESOLUTION AND PARAMETERIZATION

The discrepancies between the two models described in the previous section raise the question of how well resolved the global tomographic models are. *Su et al.* [1994] have performed a series of resolution experiments, where they inverted synthetic data sets calculated for shear-velocity structures specified by a single spherical-harmonic/Chebyshev coefficient ${}_n\delta\beta_l^m$. From their inversion results we calculated the two-point correlation diagnostics shown in Figures 4.6-4.8. Figure 4.6 compares the radial and angular correlation functions computed from the input structure, ${}_8\delta\beta_{11}^6$, with those calculated from the inversion. The radial correlation function is recovered quite well down to depth of 1800 km, while the structure of the angular correlation function is faithfully reproduced throughout the mantle. Figure 4.7 shows $\tilde{\sigma}_\beta$, $\tilde{\rho}_\beta$, and $\tilde{\alpha}_\beta$ for the same test structure as well as for a test structure defined by the spherical-harmonic/Chebyshev coefficient ${}_5\delta\beta_{10}^5$. The test structure with $n = 5$ is recovered faithfully throughout most of the mantle. The amplitude of $\tilde{\sigma}_\beta$ is clearly the most poorly reproduced quantity. This is probably due to the damping associated with the seismic inversion process. Figure 4.8 depicts the recovered angular power spectrum for the ${}_8\delta\beta_{11}^6$ test structure. The radially averaged normalized power spectrum decreases by an order of magnitude away from the target degree l = 11. Power spectra at near-surface depths and especially near the base of the mantle show the most spectral leakage to adjacent degrees. Trade-offs exist between radial and angular smoothness for a tomographic inversion, contributing to differences in the recovery of radial and angular structures.

These experiments clearly show that the resolution of the HV model degrades towards the core-mantle boundary. Similar calculations are not available to us for the Scripps inversion, but we note that this is the region where the difference in the radial correlation functions for the two seismic models becomes large. Disagreements between the two models are evident at higher levels as well; in fact, the radial coherence of the HV and SC heterogeneity fields (cross-correlation coefficient at a specified radius), while high (~0.8) in the high-amplitude regions of the uppermost and lowermost mantle, is weak (0.4-0.6) throughout the mid-mantle region where the rms variation is low. Further work to reconcile the tomographic models, and to assess the ability of the seismic data to constrain details of the two-point correlation function, is clearly warranted. Preliminary results from a study of the Scripps group, who used a temperature field of *Tackley et al.'s* [1993] 3D convection model as a test structure for their inversion, indicate that the major features of the radial correlation function for that model are recovered by the seismic inversion (S. Johnson and G. Masters, unpublished data, 1994).

Above we investigated the effects of data coverage and smoothness constraints imposed by the inversion procedure on synthetic test structures. In this section we illustrate the influence of different model parameterizations on the resulting seismic earth models. We examined two degree-eight tomographic models from earlier Harvard studies [*Dziewonski and Woodward*, 1992; *Woodward et al.*, 1993], both of which explain the seismic data equally well. The first, SH8/WM13 (WM), has the same radial parameterization as HV ($n_{max} = 13$), and its radial correlation function is shown in Figure 4.9*a*. The second, SH8/U4L8 (UL), is parameterized by separate Chebyshev expansions in the upper mantle ($n_{max} = 4$) and lower mantle ($n_{max} = 8$) and therefore develops a discontinuity in $\delta\beta$ at a depth of 670 km. Its radial correlation function, displayed in Figure 4.9*b*, shows a sharp decrease around 670 km depth.

Consider a tomographic model as the output of a filter whose input is the real earth and whose response is determined by the seismic data and the model parameterization. Given a known radial correlation function, R_f^{in}, the effects of a given model parameterization can be calculated as

$$R_f^{\mathrm{Filter}}(r,r') = \frac{\sum_{k,k'} T_k(r)T_{k'}(r')I_{kk'}}{\sqrt{\sum_{k,k'} T_k(r)T_{k'}(r)I_{kk'} \sum_{k,k'} T_k(r')T_{k'}(r')I_{kk'}}}, \tag{4.6}$$

where

$$I_{kk'} = \frac{1}{c_k c_{k'}} \int_b^a \int_b^a T_k(s)T_{k'}(s')w(s)w(s')R_f^{\mathrm{in}}(s,s')\,ds\,ds' \tag{4.7}$$

and $T_k(s)$, $w(s)$ and c_k are the Chebyshev polynomials, Chebyshev weight functions and Chebyshev normalizing integrals, respectively [e.g., *Abramowitz and Stegun*, 1972].

To illustrate the effects of the model parameterization, we use a cosine-squared radial correlation function, R_β^{in}, of constant width throughout the mantle (ρ_β^{in} = 67 km). Figure 4.10*a* shows the filter-response, $\tilde{R}_\beta^{\mathrm{WM}}$, applied to R_β^{in}. Applying the parameterization of the two-layer model to $\tilde{R}_\beta^{\mathrm{in}}$ yields the filter response, $\tilde{R}_\beta^{\mathrm{UL}}$, displayed in Figure 4.10*b*. Comparing Figures 4.9*b* and 4.10*b* we note the similarity between the features around 670 km depth. This is further illustrated in Figure 4.11 where the radial correlation lengths are compared. UL displays a sharp decrease in $\tilde{\rho}_\beta$ confined to a 200-km interval centered on the 670-km discontinuity (Figure 4.11*a*). A very similar feature is obtained by applying the discontinuous parameterization to a constant radial correlation function (Figure 4.11*b*). (The reason the radial correlation lengths decrease toward the boundaries lies in the higher resolution of the Chebyshev basis functions there. The widths of $\tilde{\rho}_\beta^{\mathrm{WM}}$ and $\tilde{\rho}_\beta^{\mathrm{UL}}$ are larger than ρ_β^{in} due to the radial filtering performed.) This experiment suggests that discontinuous model parameterizations should be avoided in tomographic tests of mantle stratification.

FILTERING

The current generation of whole-mantle tomographic models parameterize the shear-velocity structures only up to angular degree $l_{max} \approx$ 10-12 [*Masters et al.*, 1992; *Su et al.*, 1994]. The radial distribution of aspherical heterogeneity is parameterized using either 13 Chebyshev polynomials or vertically homogeneous layers. When comparing results from numerical convection experiments to seismic constraints, we need to low-pass filter the temperature fields to account for the limited seismic resolution. In this section we illustrate the effects of calculating two-point correlation functions from temperature fields truncated at angular degree 10 and radial (Chebyshev) order 13 for different flow models. (For a detailed discussion of the convection experiments see chapter 3.)

Figure 4.12, shows σ_T, ρ_T and α_T for a convection experiment with a 30-fold viscosity increase at mid-depth. The results of truncating the δT snapshots at angular order 10 and radial order 13 prior to calculating two-point correlation diagnostics are shown together with the unfiltered diagnostics. The filtering reduces σ_T and increases α_T, and it distorts the structure in both caused by the viscosity stratification. The change in ρ_T is much smaller, except in the lower boundary layer, where the correlation length increases rapidly owing to the dominance of a few low-degree harmonics. In particular, the rapid rise in ρ_T at the mid-depth viscosity transition is only slightly smoothed by the truncation. The next example (Figure 4.13) shows the same diagnostics for a convection run with an endothermic phase boundary ($P = -0.1$) at $r = 0.875$. Both σ_T and ρ_T preserve the characteristic signature of the phase boundary for the filtered fields, albeit slightly distorted. In particular, the rms-amplitude of the filtered fields is decreased and the minimum in ρ_T is shifted to slightly larger depths. This behavior is also observed for the radial correlation diagnostics calculated for 3D convection experiments with an endothermic phase change [*Jordan et al.*, 1993]. The correlation angle is distorted most significantly both in size and shape. The local maximum in α_T centered around the phase transition, has disappeared entirely. Raising the cut-off in angular and radial order to $l_{max} = n_{max} = 20$ leads to similar modifications in the correlation diagnostics. In particular, the local maximum in the correlation angle associated with the phase transition is still not detectable. Figure 4.14 shows the same diagnostics for a convection run with temperature-dependent viscosity and ten plates whose geometries evolve with time. The amplitude of σ_T is reduced for the low-pass filtered diagnostic, while ρ_T retains its characteristic signature. As for the previous examples, α_T is distorted most significantly, even though the near-surface maximum associated with the presence of plates is retained. Figure 4.15 shows a comparison between the correlation diagnostics calculated for two experiments with temperature-dependent viscosity and ten evolving plates, one run with an endothermic phase boundary ($P = -0.1$) at $r = 0.875$. σ_T, ρ_T, and α_T calculated from the unfiltered fields are shown in Figures 4.15*a*, *c*, and *e*, respectively. Their filtered counterparts are compared in Figures 4.15*b*, *d*, and *f*. The local minimum in ρ_T near the phase transition depth, characteristic of flow stratification can be seen for both unfiltered and filtered diagnostics, while the local correlation maximum in α_T has disappeared after low-pass filtering the temperature fields. The weak expression of the phase transition is preserved for σ_T.

To summarize, the radial correlation length is least affected by truncating the temperature fields at angular degree 10 and radial order 13. With slight distortions, ρ_T retains both shape and amplitude of features characteristic to a given flow regime. The amplitude of σ_T is always reduced for the truncated diagnostic, however, the variation of the function with depth is better preserved. The correlation angle is affected most severely by the low-pass filtering, both shape and amplitude of α_T are distorted. The only characteristic of α_T preserved in the low-pass filtered fields is its increase near the surface associated with the presence of plates, an expression of predominantly horizontal variations in the flow fields. All other features in the correlation diagnostics were due to some form of radial flow stratification; for them the diagnostic features of the radial correlation function are embedded in the low-degree harmonics. This functional is therefore more suitable than σ_T or A_T for testing stratification hypotheses against the seismic models.

REGIONAL TOMOGRAPHIC MODELS

One limitation of global seismic models is their low radial and angular resolution. While the radial correlation function is least affected by low-pass filtering to the resolution typical of today's global tomographic models, an increase in resolution should allow us to interpret more subtle features of the flow diagnostics. This section investigates a recent high-resolution regional tomographic model [*Grand*, 1994] (GR), calculating its two-point correlation functions. *Grand's* [1994] model of mantle shear-velocity structure beneath the Americas and surrounding oceans is parameterized using blocks of horizontal dimensions of roughly 275 by 275 km and vertical dimensions varying from 75 to 150 km. The data consist of *S* and *ScS* waves as well as multibounce phases *SS*, *SSS*, and *SSSS*. Synthetic seismograms were used to measure the travel times accounting for the first-order effects of velocity heterogeneity on the raypaths. The inversion algorithm is designed to explain as much data as possible with shallow mantle heterogeneity (above 320 km depth). The resulting model is slightly smoothed, both laterally and radially using a weighted running mean. Due to the data sampling the model resolution is probably poorest between 400 and 800 km depth [S. Grand, personal communication, 1994].

Figure 4.16 shows the areal coverage of this model. The shaded regions shown in Figures 4.16*a* and 4.16*b* represent blocks for which a velocity heterogeneity was obtained by the inversion for all and for at least half of the 22 depth layers, respectively. These areas comprise 44% and 74% of the earth's surface area, respectively. For simplicity, we denote the models corresponding to these two regions as G44 and G74, respectively. Radial and angular correlation functions calculated for these regions are shown in Figures 4.17 and 4.18. $\tilde{R}_\beta$ and $\tilde{A}_\beta$ were calculated by numerical integration of the velocity anomalies according to equations (4.2)-(4.4). Anomalies of blocks in G74 for which the inversion provided no velocity anomalies were calculated from a smoothest-model spherical harmonic spline interpolation [*Shure et al.*, 1982] (Figure 4.18*a*, *c*). Spherical harmonic splines truncated at angular degree 20, radially expanded using Chebyshev polynomials ($n_{max} = 20$) were used for calculating the correlation functions shown in Figures 4.17*b*, *d* and 4.18*b*, *d*. Both the radial and angular correlation functions calculated for G44 and G74 are very similar. This is further illustrated in Figure 4.19, where $\tilde{\sigma}_\beta$, $\tilde{\rho}_\beta$, and $\tilde{\alpha}_\beta$ are depicted. The radial and angular correlation diagnostics are characterized by correlation maxima near the surface, low correlation lengths between 350 and 800 km depths (below which $\tilde{\rho}_\beta$ increases rapidly from approximately 50 km to 150 km), nearly constant values down to 2500 km and local maxima at the base of the mantle. The rms-variation (Figures 4.19*a*, *b*) is largest near the surface, its amplitude in part probably due to the specifics of the inversion algorithm discussed above. Dashed lines in Figure 4.19 show the correlation diagnostics calculated from the continuously parameterized model for two levels of angular and radial truncation ($l_{max} = n_{max} = 20$ and $l_{max} = 20$, $n_{max} = 13$). These diagnostics are similar to those calculated from the layered model, with $\tilde{\alpha}_\beta$ showing the largest difference, illustrating the effects of filtering on the angular correlation function. Figure 4.20 shows $\tilde{\sigma}_\beta$, $\tilde{\rho}_\beta$, and $\tilde{\alpha}_\beta$ for different areal coverages. The diagnostics for G44 and G74 are expanded to angular degree and radial order 20. We also calculated diagnostics for the S12_WM13 [*Su et al.*, 1994] (HV) using the same regions as well as those calculated from the complete global model. For both GR and HV the characteristic features are similar for the two subsets, which themselves are close to the global diagnostics (for HV).

DISCUSSION

In this chapter we have investigated the utility of characterizing tomographic models of seismic velocity anomalies using two-point correlation functions. Unlike for numerical convection experiments, only a single snapshot of the earth's seismic heterogeneity field is available to us. Fortunately, the angular averaging performed when calculating the correlation diagnostics successfully reduces their variability (Figure 4.1). While $\tilde{\sigma}_\beta$, $\tilde{R}_\beta$, and $\tilde{A}_\beta$ contain complementary information about the earth's heterogeneity, $\tilde{R}_\beta$ clearly is the most useful, especially when searching for signatures of radial stratification. Several factors limit the utility of the other diagnostics: First, an attractive property of $\tilde{R}_\beta$, and $\tilde{A}_\beta$ not shared by $\tilde{\sigma}_\beta$ is their invariance with respect to a radially varying function such as the temperature derivative of shear velocity, whose depth-dependence is uncertain in the lower mantle. This property becomes important when comparing the correlation diagnostics of the shear velocity heterogeneity to those obtained from temperature fields of numerical convection experiments. Second, synthetic inversion experiments for the HV model using simple test structures indicate that $\tilde{\sigma}_\beta$ is more poorly recovered than $\tilde{R}_\beta$, and $\tilde{A}_\beta$, especially its amplitude (Figure 4.7*a*). Third, calculating correlation diagnostics from temperature fields filtered to the limited resolution of tomographic models reveals that the amplitude of the rms-variation is reduced by this low-pass filtering. The shape of σ_T is affected to a lesser degree. Even more affected than σ_T, is the angular correlation function. Low-pass filtering of convection runs removes all features diagnostic of radial flow stratification from α_T. The radial correlation length is distorted slightly, but retains most of its characteristics of radial flow stratification (Figures 4.12-4.15).

With these caveats in mind, Figure 4.21 shows a comparison of $\tilde{\sigma}_\beta$, $\tilde{\rho}_\beta$, and $\tilde{\alpha}_\beta$ for the global tomographic models HV and SC truncated at angular degree 10 and radial order 13 together with the regional model G74. The diagnostics of the regional model are probably fairly close to what global averages would look like (Figure 4.20). All three models show increased values of $\tilde{\sigma}_\beta$ near the surface and CMB, however, the size of these maxima, the ratio of the maxima, and the values in the interior varies between the different models (Figure 4.21*a*). As discussed before, the angular truncation of these models is too severe to expect the detection of any features indicative of radial stratification. Features that might be associated with horizontal scales in the earth's mantle are the local maxima near the surface and CMB (Figure 4.21*c*). For all models, the radial correlation length between 350 and 800 km depth is relatively constant, albeit by about a factor of two smaller for G74. Below that depth, $\tilde{\rho}_\beta$ for G74 increases rapidly to a correlation length of 150 km constant throughout most of the lower mantle and increases in D" to a maximum of 260 km. Below 1200 km depth, G74 and SC differ only by 20-30 km. HV on the other hand shows an increase starting at 1600 km depth to a maximum of 320 km at a depth of 2500 km. While some of these features, such as the rapid rise in G74 from 800 km to 1200 km depth, or a similar increase in HV below 1600 km depth are intriguing, the differences in $\tilde{\rho}_\beta$ between the three models suggest caution in putting too much stock in any one feature. Is the mantle below 1200 km depth characterized by a constant correlation length of ~150 km with an increase in D" as suggested by G74 and SC and is the increase in HV below 1600 km depth a result of its deteriorating resolution as evident from Figure 4.7? Is the rapid increase in G74 starting around 800 km depth real, and why are its values of $\tilde{\rho}_\beta$ between 350 and 800 km depth less than half those observed for the global models? This could be due to the fact that the depth range between 400 and 800 km is most poorly resolved for G74 [S. Grand, personal communication]. Alternatively, the discrepancies might be due to the different data sets or the different approximations used to make the inverse problem tractable. Figure 4.22, which shows the coherency (cross-correlation coefficient at a specified radius) between two seismic models, reiterates this point. The coherency of GR with either HV or SC only exceeds 0.5 in the uppermost and lowermost mantle, while the lower-resolution global models show a slightly higher coherency (note however, that some of the data used to construct HV and SC were identical). Some of the questions regarding which (if any) of the seismic models resembles the earth's mantle most closely may be addressed by looking at the correlation diagnostics of resolution tests similar to those performed for the HV model, a process we have initiated. However, ultimately it will be desirable to directly invert seismic observations for the two-point correlation functions rather than calculating these from tomographic models.

REFERENCES

Abramowitz, M., and I. A. Stegun, *Handbook of mathematical functions with formulas, graphs, and mathematical tables*, 1046 pp., Dover, New York, 1972.

Anderson, O. L., D. Issak, and H. Oda, High-temperature elastic constant data on minerals relevant to geophysics, *Rev. Geophys.*, *30*, 57-90, 1992.

Birch, F., Remarks on the structure of the mantle, and its bearing upon the possibility of convection currents, *Trans. Am. Geophys. Union*, *32*, 533-534, 1951.

Creager, K. C., and T. H. Jordan, Slab penetration into the lower mantle beneath the Mariana and other island arcs of the Northwest Pacific, *J. Geophys. Res.*, *91*, 3573-3589, 1986.

Duffy, T. S., and T. J. Ahrens, Sound velocities at high pressure and temperature and their geophysical implications, *J. Geophys. Res.*, *97*, 4503-4520, 1992.

Dziewonski, A. M., and R. L. Woodward, Acoustic imaging at the planetary scale, in *Acoustical Imaging*, edited by H. Ermert, and H.-P. Harjes, *vol.*, *19*, pp. 785-797, Plenum, New York, 1992.

Forte, A. M., A. M. Dziewonski, and R. L. Woodward, Aspherical structure of the mantle, tectonic plate motions, nonhydrostatic geoid, and topography of the core-mantle boundary, in *Dynamics of Earth's deep interior and Earth rotation*, edited by J. L. LeMouel, D. E. Smylie, and T. Herring, *Geophysical Monograph*, *72*, pp. 135-166, 1993.

Grand, S. P., Mantle shear structure beneath the Americas and surrounding oceans, *J. Geophys. Res.*, *99*, 11591-11621, 1994.

Hager, B. H., R. W. Clayton, M. A. Richards, R. P. Comer, and A. M. Dziewonski, Lower mantle heterogeneity, dynamic topography and the geoid, *Nature*, *313*, 541-545, 1985.

Hager, B. H., and M. A. Richards, Long-wavelength variations in Earth's geoid; physical models and dynamical implications, *Philos. Trans. R. Soc. London, Ser. A*, *328*, 309-327, 1989.

Jeanloz, R., Effects of phase transitions and possible compositional changes on the seismological structure near 650 km depth, *Geophys. Res. Lett.*, *18*, 1743-1746, 1991.

Jordan, T. H., P. Puster, G. A. Glatzmaier, and P. J. Tackley, Comparisons between seismic Earth structures and mantle flow models based on radial correlation functions, *Science*, *261*, 1427-1431, 1993.

King, S. D., and T. G. Masters, An inversion for radial viscosity structure using seismic tomography, *Geophys. Res. Lett.*, *19*, 1551-1554, 1992.

Machetel, P., and P. Weber, Intermittent layered convection in a model mantle with an endothermic phase change at 670 km, *Nature*, *350*, 55-57, 1991.

Masters, T. G., H. Bolton, and P. Shearer, Large-scale 3-dimensional structure of the mantle, *Eos Trans. AGU*, *73*, 201, 1992.

Ricard, Y., and B. Wuming, Inferring the viscosity and 3-D density structure of the mantle from geoid, topography and plate velocities, *Geophys. J. Int.*, *105*, 561-571, 1991.

Richter, F. M., and C. E. Johnson, Stability of a chemically layered mantle, *J. Geophys. Res.*, *79*, 1635-1639, 1974.

Ritzwoller, M., T. G. Masters, and F. Gilbert, Constraining aspherical earth structure with low-degree interaction coefficients: application to uncoupled multiplets, *J. Geophys. Res.*, *93*, 6369-6396, 1988.

Shure, L., R. L. Parker, and G. E. Backus, Harmonic splines for geomagnetic modelling, *Phys. Earth Planet. Inter.*, *28*, 215-229, 1982.

Smith, M. F., and T. G. Masters, Aspherical structure constraints from free oscillation frequency and attenuation measurements, *J. Geophys. Res.*, *94*, 1953-1976, 1989.

Su, W.-J., and A. M. Dziewonski, Predominance of long-wavelength heterogeneity in the mantle, *Nature*, *352*, 121-126, 1991.

Su, W.-J., R. L. Woodward, and A. M. Dziewonski, Degree 12 model of shear velocity heterogeneity in the mantle, *J. Geophys. Res.*, *99*, 6945-6980, 1994.

Tackley, P. J., D. J. Stevenson, G. Glatzmaier, and G. Schubert, Effects of an endothermic phase transition at 670 km depth in a spherical model of convection in the Earth's mantle, *Nature*, *361*, 699-704, 1993.

Tanimoto, T., Long-wavelength S-wave velocity structure throughout the mantle, *Geophys. J. Int.*, *100*, 327-336, 1990.

Woodward, R. L., A. M. Forte, W.-J. Su, and A. M. Dziewonski, Constraints on the large-scale structure of the earth's mantle, in *Evolution of the earth and planets*, edited by E. Takahashi, R. Jeanloz, and D. Rubie, *Geophysical Monograph*, *74*, pp. 89-109, 1993.

Woodward, R. L., and T. G. Masters, Global upper mantle structure from long-period differential travel times, *J. Geophys. Res.*, *96*, 6351-6377, 1991.

Woodward, R. L., and T. G. Masters, Lower-mantle structure from long-period differential travel times, *Nature*, *352*, 231-233, 1991.

FIGURE CAPTIONS

Fig. 4.1. (*a*) Rms temperature variation, (*b*) radial correlation length, and (*c*) horizontal correlation angle, as a function of depth for the 3D convection run with an endothermic phase transition of *Tackley et al.* [1993]. The ensemble averages (σ_T, ρ_T, and α_T) are shown as solid lines, the snapshot estimates ($\tilde{\sigma}_T$, $\tilde{\rho}_T$, and $\tilde{\alpha}_T$) for three snapshots widely separated in time are shown as dashed lines.

Fig. 4.2. Cross-sections of rms-normalized shear-velocity heterogeneity for the global tomographic models S12_WM13 [*Su et al.*, 1994] (HV) (top row) and SH10/C17 [*Masters et al.*, 1992] (SC) (bottom row). Inset maps denote the great-circle along which the cross-sections were taken. Grayscale varies from fast (dark) to slow (light) dimensionless shear-velocity heterogeneity $\delta\beta/\sigma_\beta \in [-0.5, 0.5]$.

Fig. 4.3. (*a*), (*b*) Radial correlation functions, $\tilde{R}_\beta(z,z')$, and (*c*), (*d*) angular correlation functions, $\tilde{A}_\beta(z,\Delta)$, as functions of depth z and angular lag Δ for HV (*a*), (*c*) and SC (*b*), (*d*). Both models are truncated at angular degree l = 10 and radial (Chebyshev) order 13. $\tilde{R}_\beta(z,z')$ and $\tilde{A}_\beta(z,\Delta)$are unity on the loci $r = r'$, and $\Delta = 0$, respectively, and decrease away from these axes of symmetry. Contours are in increments of 0.2.

Fig. 4.4. (*a*) Rms shear-velocity heterogeneity, $\tilde{\sigma}_\beta$, (*b*) radial correlation length, $\tilde{\rho}_\beta$, and (*c*) horizontal correlation angle, $\tilde{\alpha}_\beta$, as a function of depth for HV (solid) and SC (dashed). Both models are truncated at angular degree l = 10 and radial (Chebyshev) order 13.

Fig. 4.5. Angular power spectrum, $\tilde{S}_\beta(z,l)$ for HV (solid lines, filled symbols) and SC (dashed lines, open symbols). (*a*) Radial average of normalized spectrum, $\tilde{S}_\beta/\tilde{\sigma}_\beta^2$. (*b*)

$\tilde{S}_\beta(z=100\,\mathrm{km},l)$, (*c*) $\tilde{S}_\beta(z=670\,\mathrm{km},l)$, (*d*) $\tilde{S}_\beta(z=1400\,\mathrm{km},l)$, (*e*) $\tilde{S}_\beta(z=2100\,\mathrm{km},l)$, and (*f*) $\tilde{S}_\beta(z=2800\,\mathrm{km},l)$. All plots are normalized to a maximum power of unity.

Fig. 4.6. Resolution test for HV for a test structure specified by a single spherical-harmonic/Chebyshev coefficient ${}_n\delta\beta_l^m$, $n=8$, $l=11$, $m=6$. (*a*), (*c*) Radial and angular correlation function of the input structure. (*b*), (*d*) $\tilde{R}_\beta$ and $\tilde{A}_\beta$ and of the fields recovered by inversion of the seismic data.

Fig. 4.7. (*a*), (*b*) Rms shear-velocity heterogeneity, $\tilde{\sigma}_\beta$, (*c*), (*d*) radial correlation length, $\tilde{\rho}_\beta$, and (*e*), (*f*) horizontal correlation angle, $\tilde{\alpha}_\beta$, as a function of depth, z for two different test structures inverted with the HV data set and parameterization. Input structure (solid), structure recovered by inversion of the seismic data (dashed). (*a*), (*c*), (*e*) Test structure ${}_8\delta\beta_{11}^6$; (*b*), (*d*), (*f*) test structure ${}_5\delta\beta_{10}^5$.

Fig. 4.8. Angular power spectrum, $\tilde{S}_\beta(z,l)$, for the test structure ${}_8\delta\beta_{11}^6$ recovered from the resolution test for HV. (*a*) Radial average of normalized spectrum, $\tilde{S}_\beta / \tilde{\sigma}_\beta^2$. (*b*) $\tilde{S}_\beta(z=100\,\mathrm{km},l)$, (*c*) $\tilde{S}_\beta(z=670\,\mathrm{km},l)$, (*d*) $\tilde{S}_\beta(z=1400\,\mathrm{km},l)$, (*e*) $\tilde{S}_\beta(z=2100\,\mathrm{km},l)$, and (*f*) $\tilde{S}_\beta(z=2800\,\mathrm{km},l)$. All plots are normalized to a maximum power of unity.

Fig. 4.9. Radial correlation functions for two differently parameterized degree-eight models of the Harvard group. (*a*) SH8/WM13 [*Woodward et al.*, 1993] (WM), radially parameterized by continuous Chebyshev polynomials (n = 13). (*b*) SH8/U4L8 [*Dziewonski and Woodward*, 1992] (UL), radially parameterized by separate Chebyshev expansions in the upper mantle (n = 4) and lower mantle (n = 8).

Fig. 4.10. Radial correlation functions obtained by applying different parameterization filters to a cosine-squared radial correlation function of constant width throughout the mantle (ρ_β^{in} = 67 km). (*a*) WM parameterization, (*b*) UL parameterization.

Fig. 4.11. Radial correlation length, ρ_β, for the radial correlation functions shown in Figures 4.9 and 4.10. (*a*) WM (solid) and UL (dashed). (*b*) Applying different parameterization filters to a cosine-squared radial correlation function of constant width throughout the mantle (ρ_β^{in} = 67 km); WM parameterization (solid) and UL parameterization (dashed).

Fig. 4.12. (*a*) Rms temperature variation, σ_T, (*b*) radial correlation length, ρ_T, and (*c*) horizontal correlation angle, α_T, as a function of normalized depth $z = 1 - r$ for the same convection run shown in Figures 2.1-2.4. Dashed lines show the results of truncating the δT snapshots at angular degree 10 and radial order 13 prior to averaging; solid lines show the diagnostics calculated from the unfiltered fields.

Fig. 4.13. (*a*) Rms temperature variation, σ_T, (*b*) radial correlation length, ρ_T, and (*c*) horizontal correlation angle, α_T, as a function of normalized depth $z = 1 - r$ for a convection run with an endothermic phase transition at $r = 0.875$ with a phase buoyancy parameter $P = -0.1$. Dashed lines show the results of truncating the δT snapshots prior to averaging at angular degree 10 and radial order 13 (short dashed) and angular degree 20 and radial order 20 (long dashed), respectively; solid lines show the diagnostics calculated from the unfiltered fields.

Fig. 4.14. (*a*) Rms temperature variation, σ_T, (*b*) radial correlation length, ρ_T, and (*c*) horizontal correlation angle, α_T, as a function of normalized depth $z = 1 - r$ for a convection run with ten plates whose geometries evolve with time. Viscosity varies according to equation (3.2). Dashed lines show the results of truncating the δT snapshots at angular degree 10 and radial order 13 prior to averaging; solid lines show the diagnostics calculated from the unfiltered fields.

Fig. 4.15. (*a*), (*b*) Rms temperature variation, σ_T, (*c*), (*d*) radial correlation length, ρ_T, and (*e*), (*f*) horizontal correlation angle, α_T, as a function of normalized depth $z = 1 - r$ for

two convection runs with ten plates whose geometries evolve with time and an endothermic phase transition at $r = 0.875$. Viscosity varies according to equation (3.2). (*a*), (*c*), (*e*) diagnostics calculated from the unfiltered fields. (*b*), (*d*), (*f*) results of truncating the δT snapshots at angular degree 10 and radial order 13 prior to averaging. Phase buoyancy parameter $P = -0.0$ (solid) and $P = 0.1$ (dashed).

Fig. 4.16. Coverage maps for the regional tomographic shear-velocity model of *Grand* [1994] (GR) parameterized by 22 layers of constant slowness anomaly blocks. Shaded regions show locations where the tomographic model contains a velocity anomaly in all 22 layers (G44) (*a*), in at least 11 layers (G74) (*b*).

Fig. 4.17. (*a*), (*b*) Radial correlation functions, $\tilde{R}_\beta(z,z')$, and (*c*), (*d*) angular correlation functions, $\tilde{A}_\beta(z,\Delta)$, as functions of depth, z, and angular lag, Δ, for G44. (*a*), (*c*) Model parameterized by 22 layers of constant slowness anomaly blocks. (*b*), (*d*) Model parameterized by spherical harmonics truncated at $l_{max} = 20$ and Chebyshev polynomials truncated at $n_{max} = 20$. $\tilde{R}_\beta(z,z')$ and $\tilde{A}_\beta(z,\Delta)$ are unity on the loci $z = z'$, and $\Delta = 0$, respectively, and decrease away from these axes of symmetry. Contours are in increments of 0.2.

Fig. 4.18. (*a*), (*b*) Radial correlation functions, $\tilde{R}_\beta(z,z')$, and (*c*), (*d*) angular correlation functions, $\tilde{A}_\beta(z,\Delta)$, as functions of depth, z, and angular lag, Δ, for G74. (*a*), (*c*) Model parameterized by 22 layers of constant slowness anomaly blocks. (*b*), (*d*) Model parameterized by spherical harmonics truncated at $l_{max} = 20$ and Chebyshev polynomials truncated at $n_{max} = 20$. $\tilde{R}_\beta(z,z')$ and $\tilde{A}_\beta(z,\Delta)$ are unity on the loci $z = z'$, and $\Delta = 0$, respectively, and decrease away from these axes of symmetry. Contours are in increments of 0.2.

Fig. 4.19. (*a*), (*b*) Rms shear-velocity heterogeneity, $\tilde{\sigma}_\beta$, (*c*), (*d*) radial correlation length, $\tilde{\rho}_\beta$, and (*e*), (*f*) horizontal correlation angle, $\tilde{\alpha}_\beta$, as a function of depth, z , for *Grand's*

[1994] tomographic model. (*a*), (*c*), (*e*) G44; (*b*), (*d*), (*f*); G74. Model parameterized by 22 layers of constant slowness anomaly blocks (solid); model parameterized by spherical harmonics and Chebyshev polynomials with $l_{max} = 10$, $n_{max} = 13$ (short dashed) and $l_{max} = 20$, $n_{max} = 20$ (long dashed).

Fig. 4.20. (*a*), (*b*) Rms shear-velocity heterogeneity, $\tilde{\sigma}_\beta$, (*c*), (*d*) radial correlation length, $\tilde{\rho}_\beta$, and (*e*), (*f*) horizontal correlation angle, $\tilde{\alpha}_\beta$, as a function of depth. (*a*), (*c*), (*e*) Model GR truncated at $l_{max} = 20$ and $n_{max} = 20$ with G44 (solid) and G74 (short dashed). (*b*), (*d*), (*f*) Model HV with an areal coverage according to Figures 4.16*a*. (solid) and 4.16*b*. (short dashed). Functions calculated for the complete global model (HV) are shown by the long dashed lines.

Fig. 4.21. (*a*) Rms shear-velocity heterogeneity, $\tilde{\sigma}_\beta$, (*b*) radial correlation length, $\tilde{\rho}_\beta$, and (*c*) horizontal correlation angle, $\tilde{\alpha}_\beta$, as a function of depth. Model G74 (solid), global models truncated at $l_{max} = 10$ and $n_{max} = 13$ HV (short dashed) and SC (long dashed). Dotted line marks the upper mantle–lower mantle transition. For a better comparison between the models we display $\tilde{\rho}_\beta$ of G74 truncated at $l_{max} = 20$ and $n_{max} = 20$

Fig. 4.22. Coherency, $\tilde{\psi}$, of two seismic heterogeneity fields, as a function of depth. (*a*) GR and HV, (*b*) GR and SC, and (*c*) HV and SC. HV and SC were truncated at $l_{max} = 10$ and $n_{max} = 13$. Areal coverage according to Figures 4.16*a* (solid) and 4.16*b* (short dashed). For comparison, the coherency between the global fields HV and SC is also shown (long dashed).

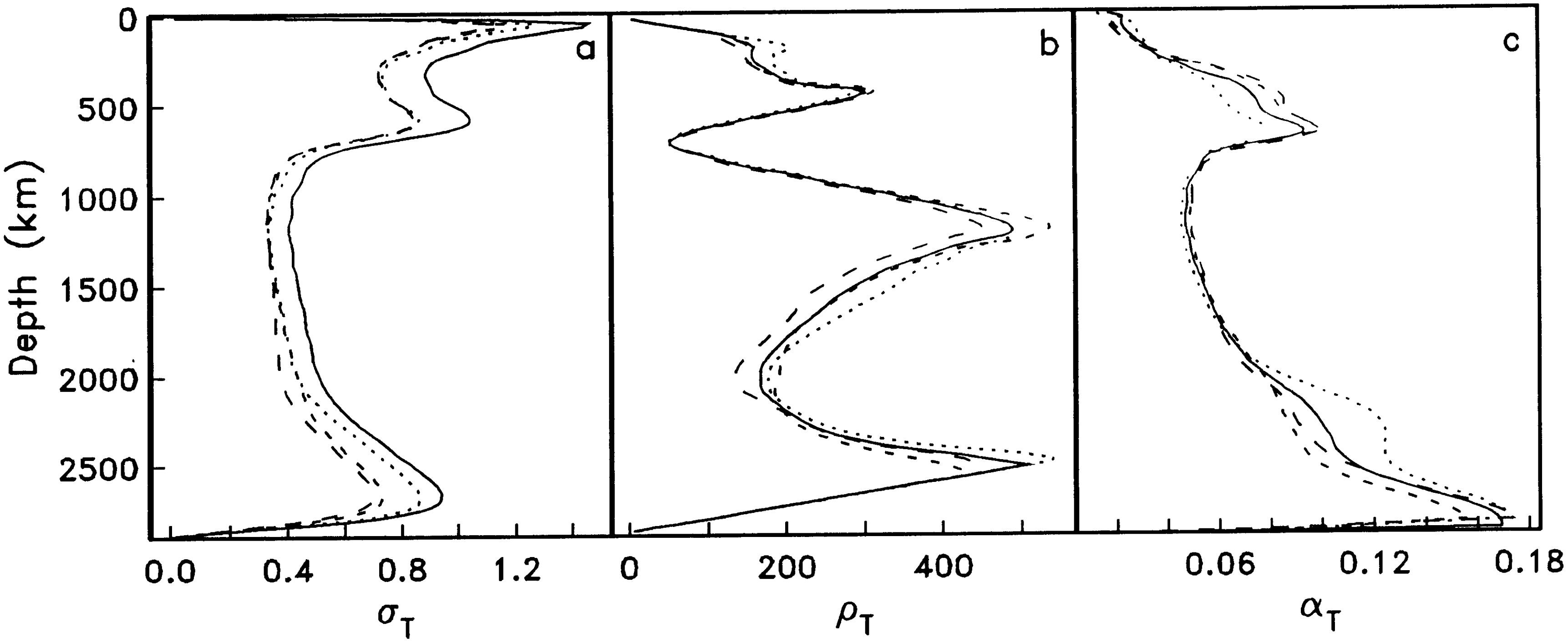
Depth (km)
0
500
1000
1500
2000
2500
a
b
c
0.0
0.4
0.8
1.2
σ_T
0
200
400
ρ_T
0.06
0.12
0.18
α_T

Figure 4.1

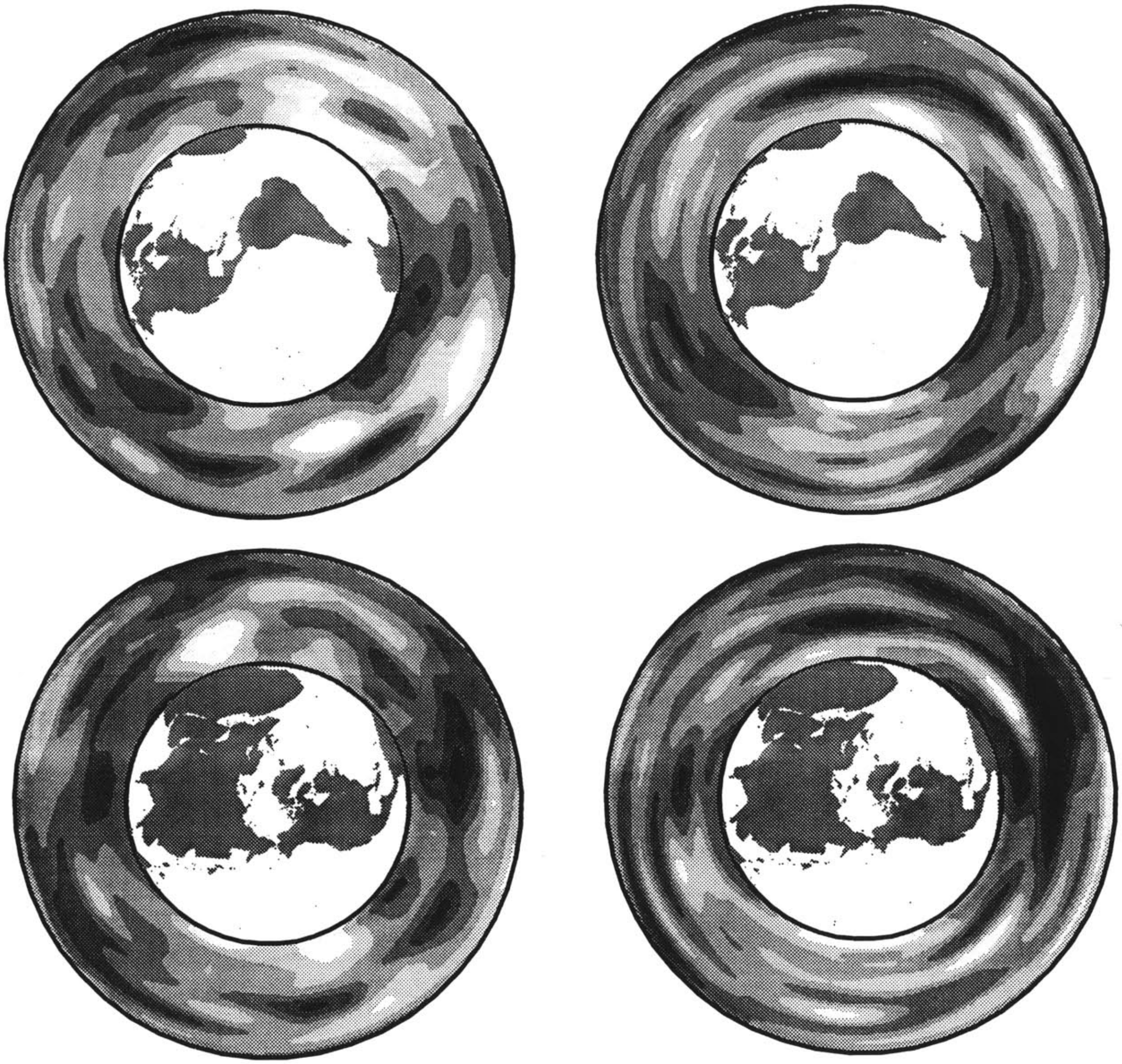

Figure 4.2

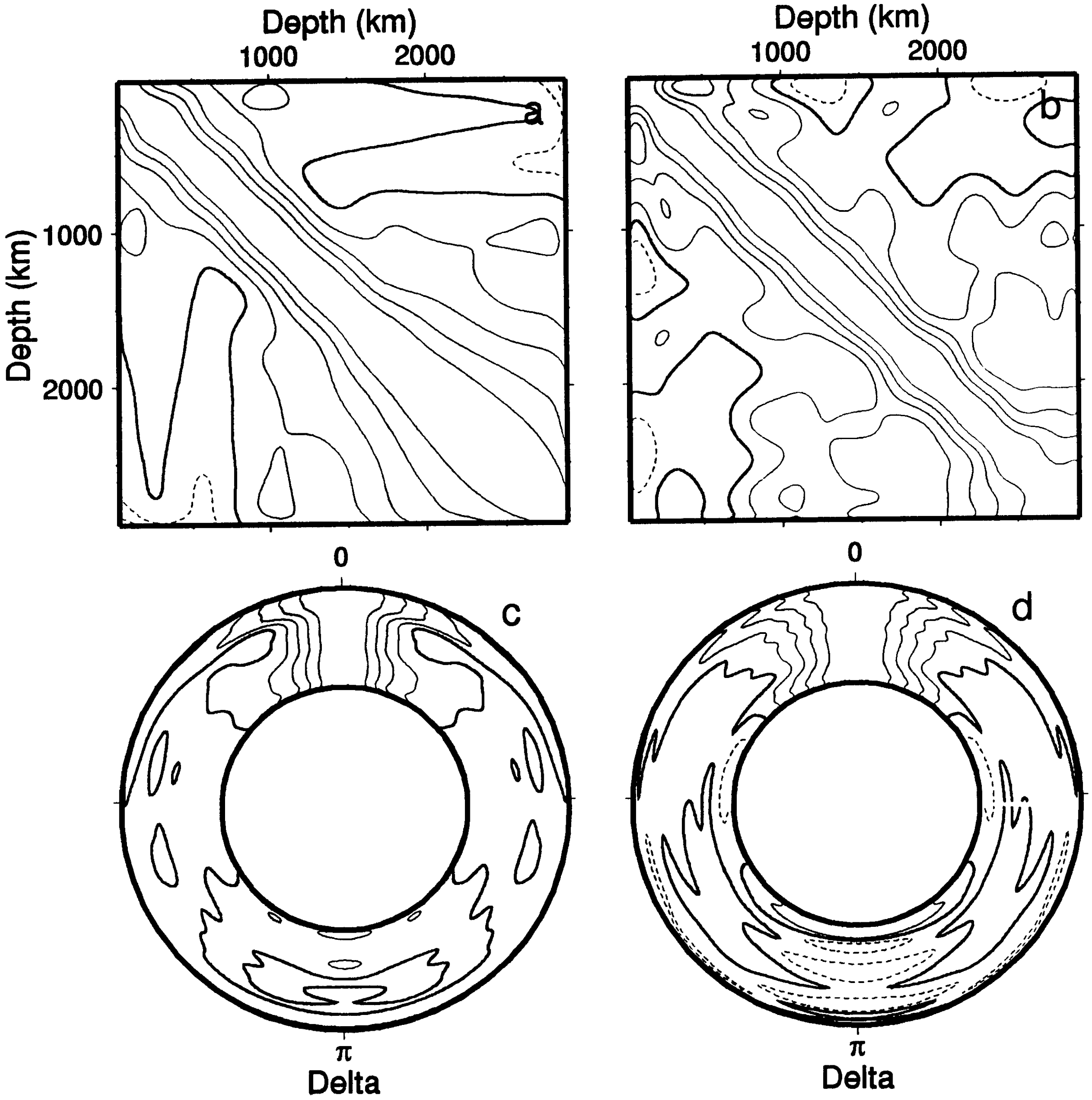
Depth (km)
1000
2000
a
Depth (km)
1000
2000
b
Depth (km)
1000
2000
0
c
π
Delta
0
d
π
Delta

Figure 4.4

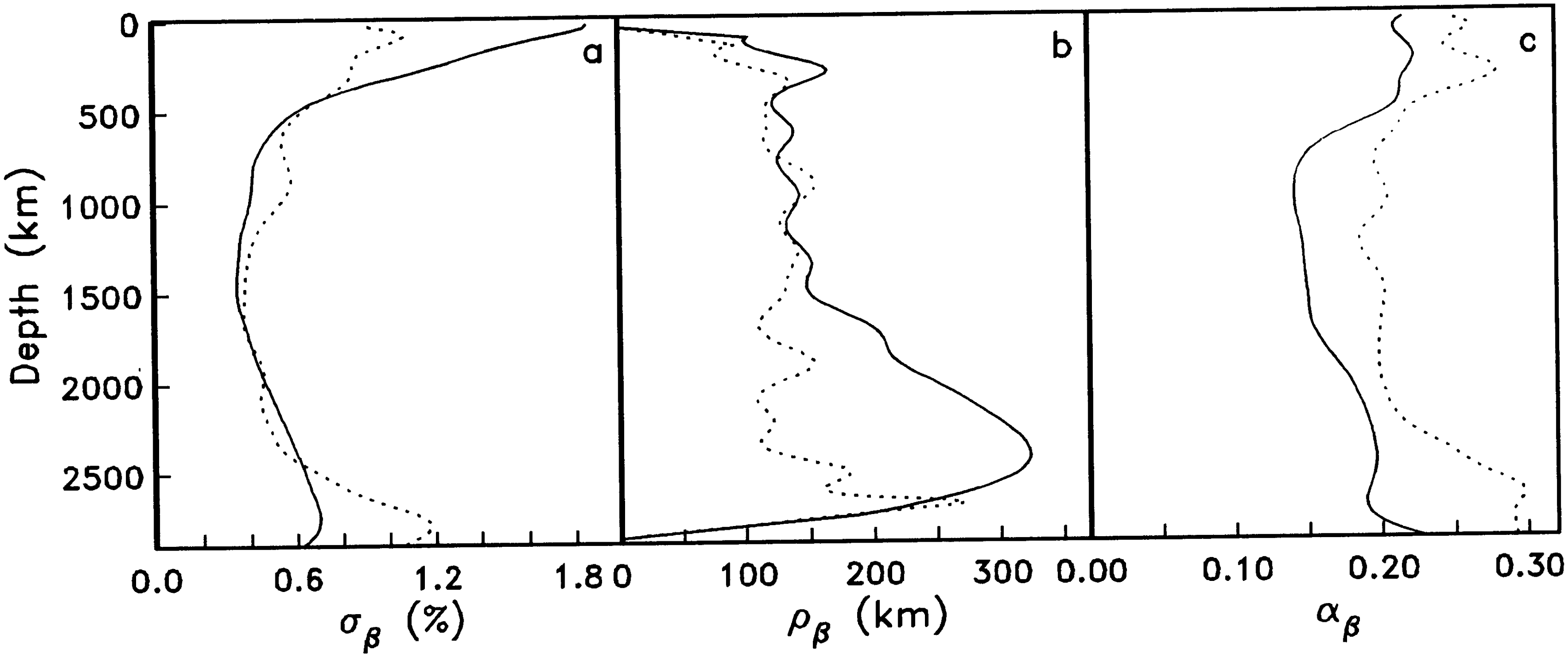

Depth (km)
0
500
1000
1500
2000
2500
a
b
c
0.0
0.6
1.2
1.8
0
100
200
300
0.00
0.10
0.20
0.30
σ_β (%)
ρ_β (km)
α_β

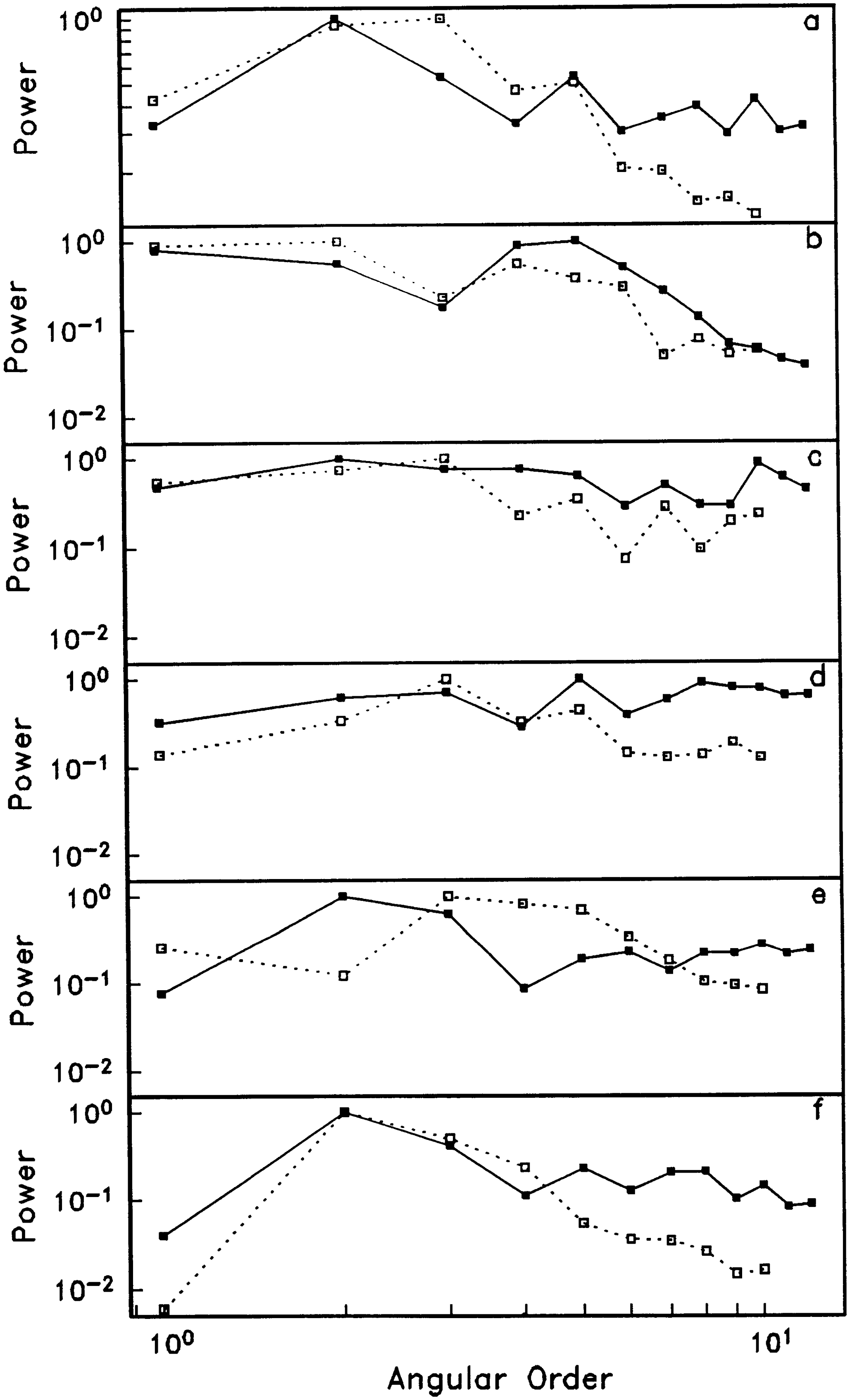

Figure 4.5

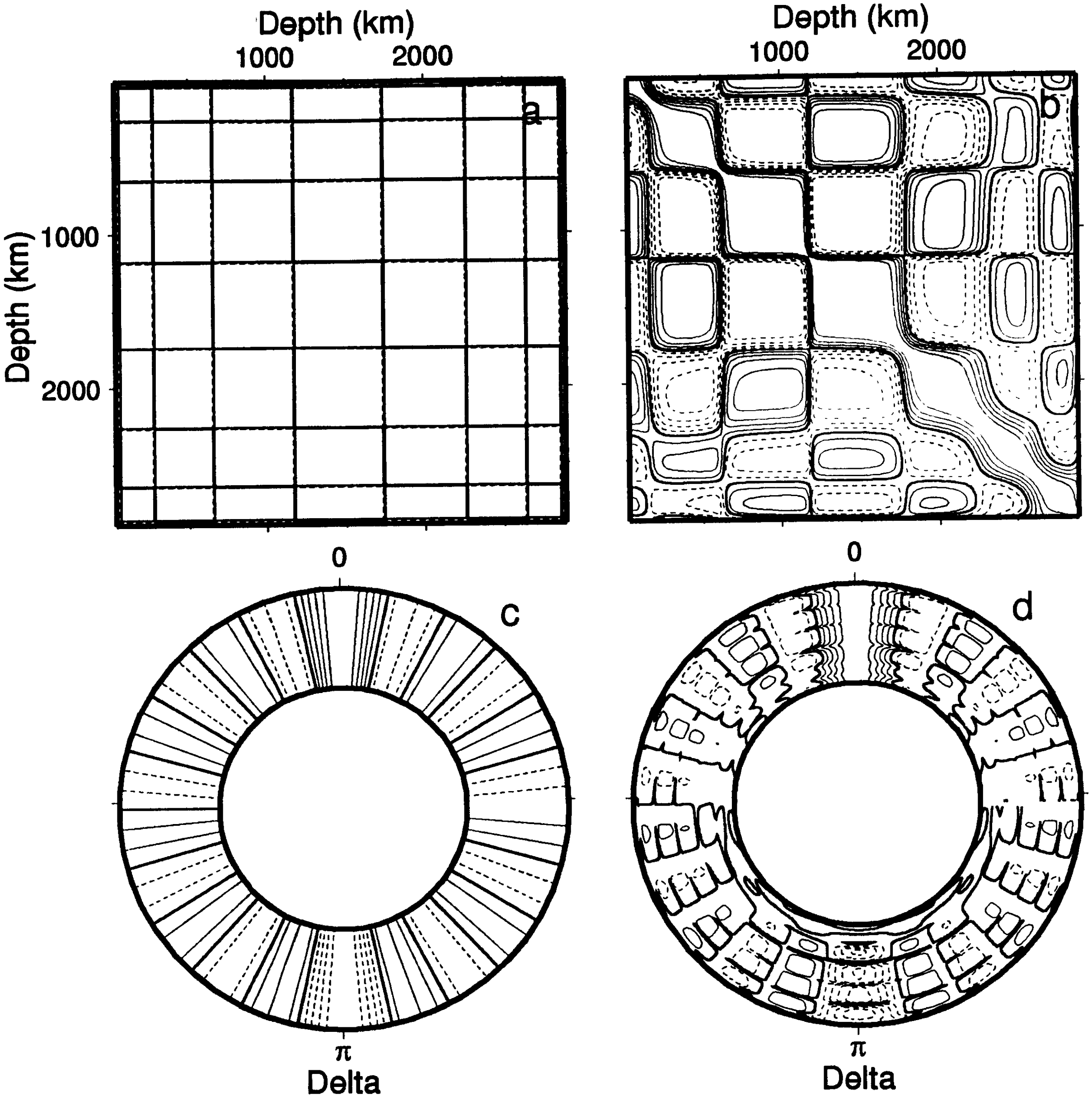
Depth (km)
1000
2000
Depth (km)
1000
2000
a
Depth (km)
1000
2000
b
0
c
0
d
π
Delta
π
Delta

Figure 4.6

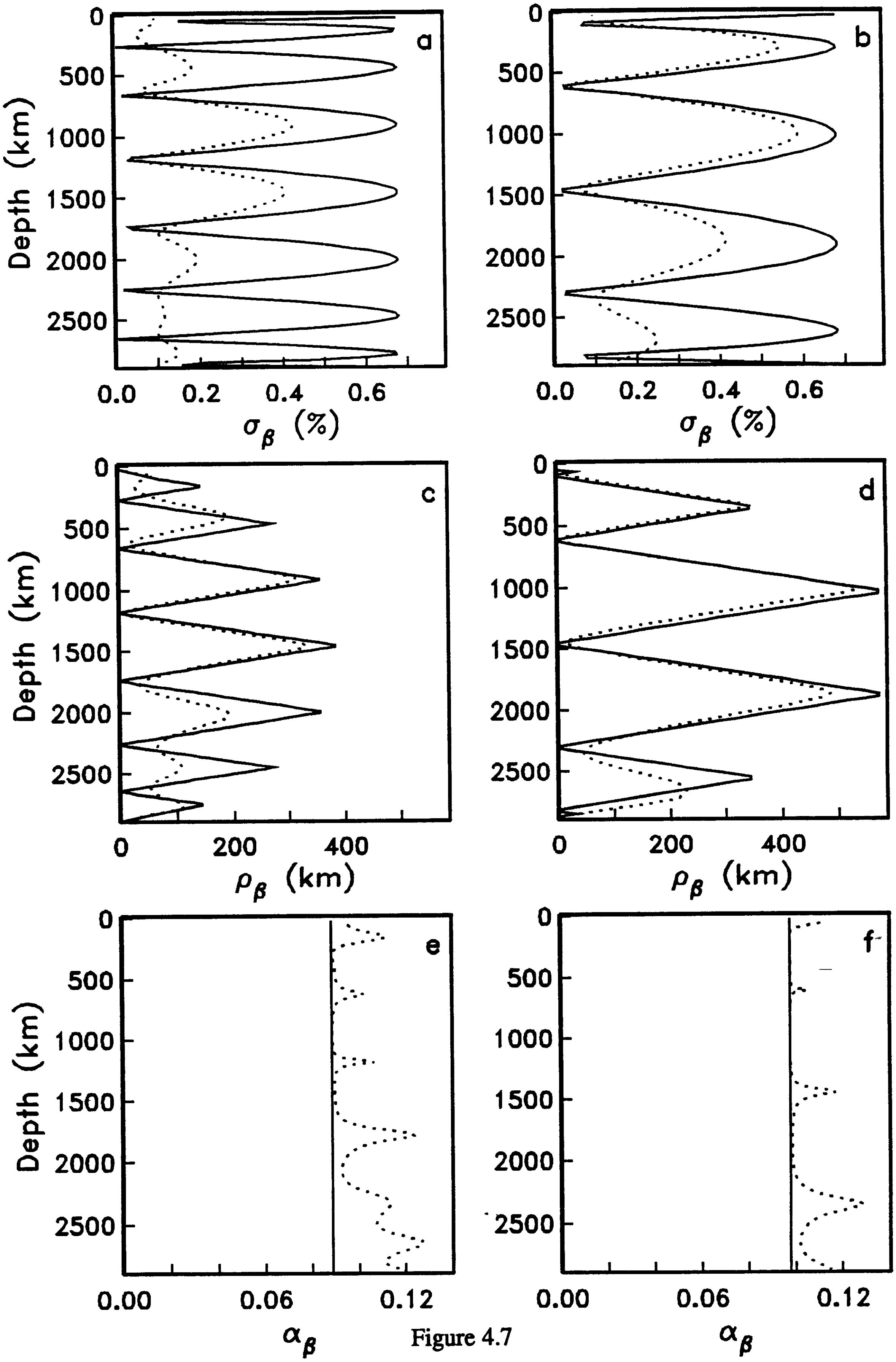
a
b
c
d
e
f
Depth (km)
0
500
1000
1500
2000
2500
0.0
0.2
0.4
0.6
σ_β (%)
0
200
400
ρ_β (km)
0.00
0.06
0.12
α_β

Figure 4.7

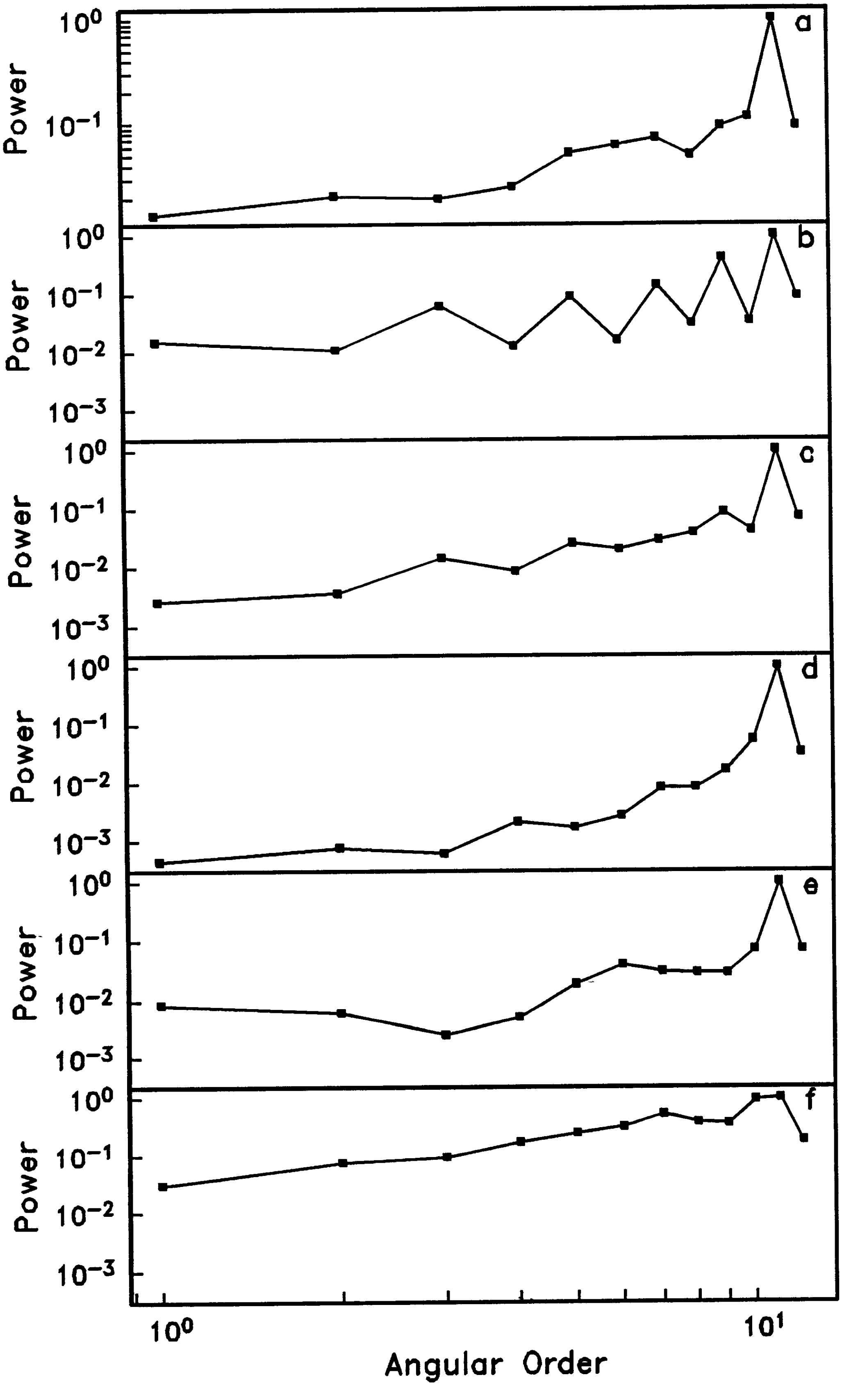

Figure 4.8

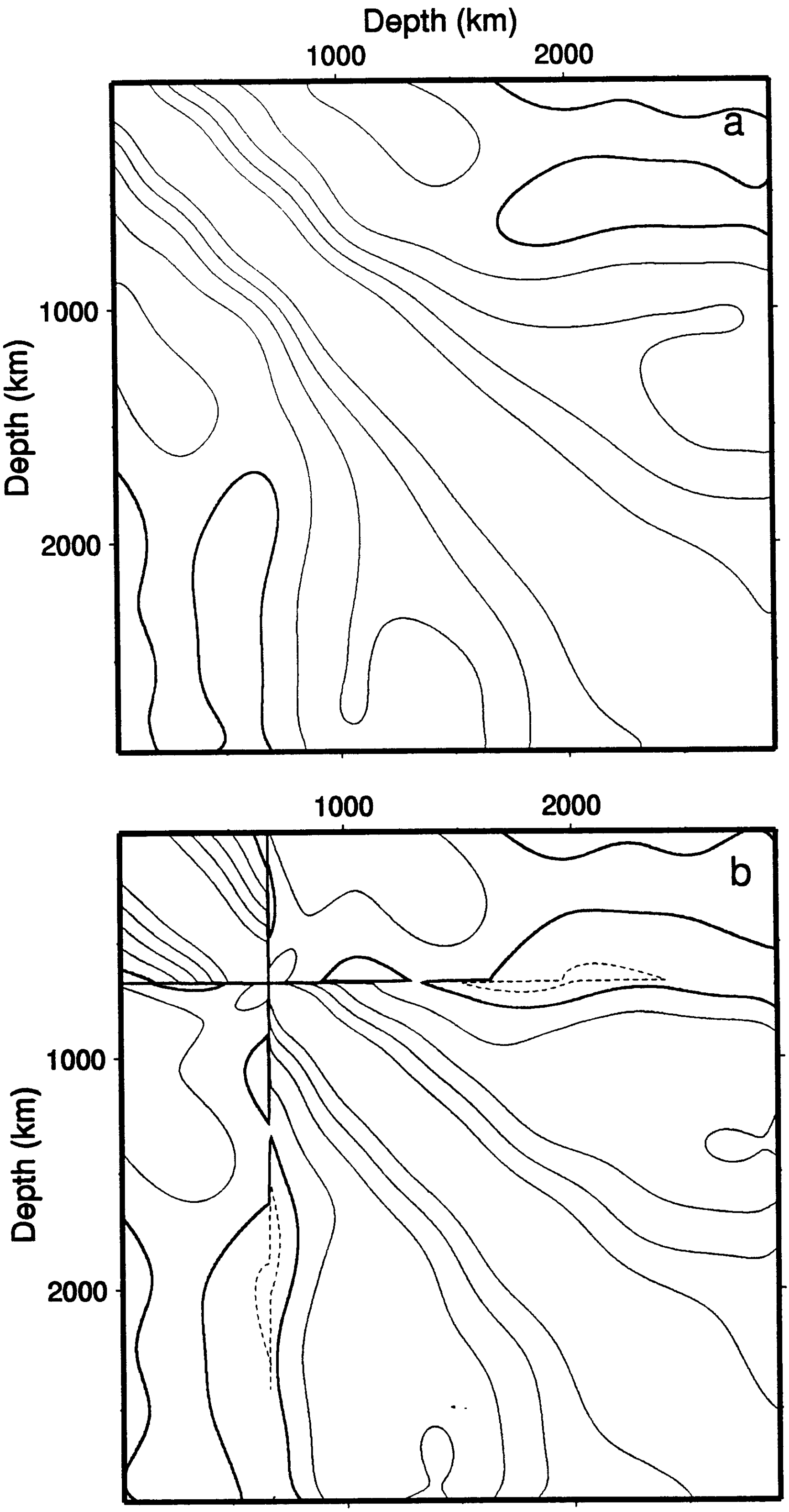
Depth (km)
1000
2000
a
1000
2000
Depth (km)
1000
2000
b
1000
2000
Depth (km)

Figure 4.9

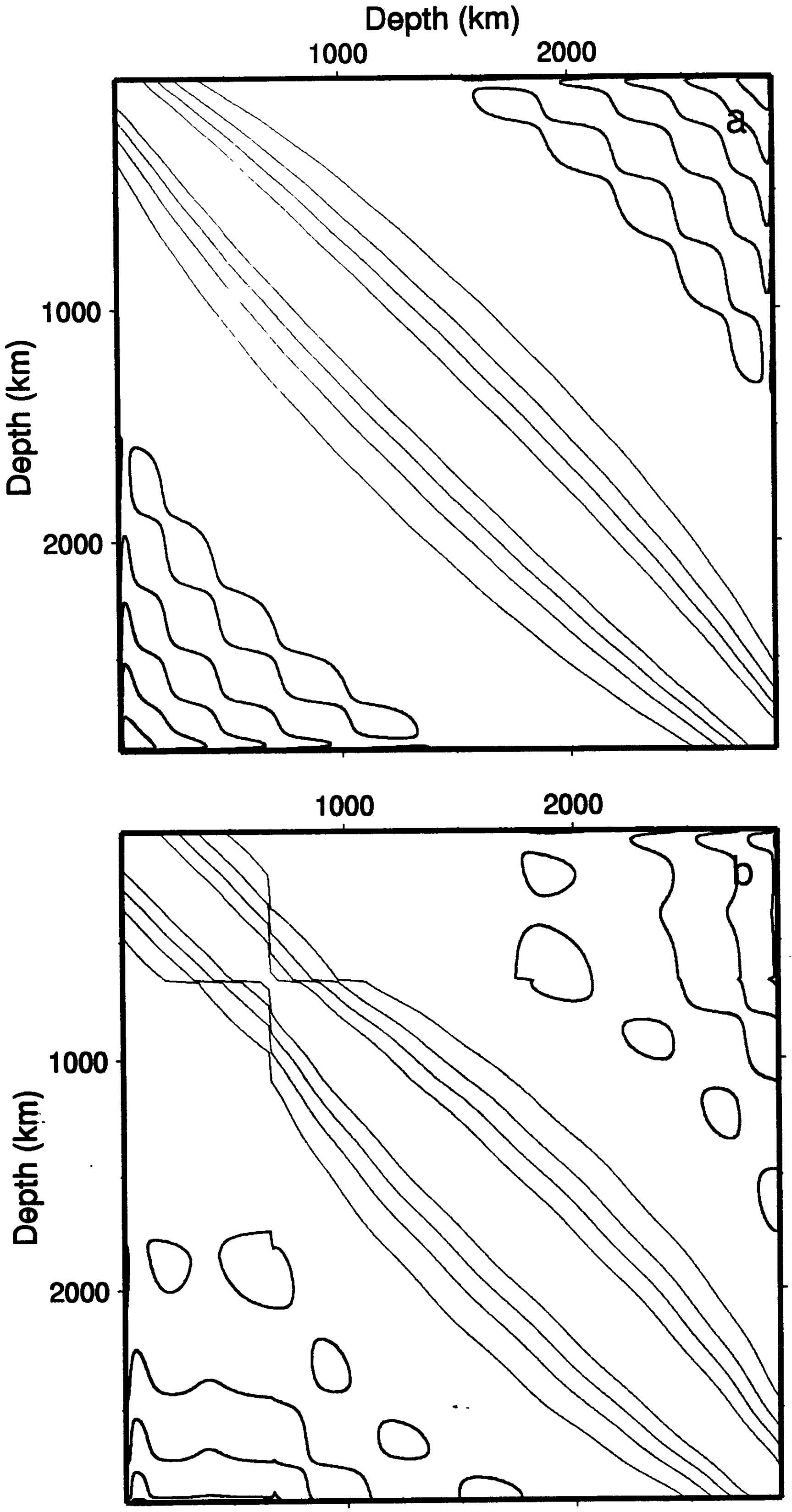
Depth (km)
1000
2000
a
Depth (km)
1000
2000
1000
2000
b
Depth (km)
1000
2000

Figure 4.10

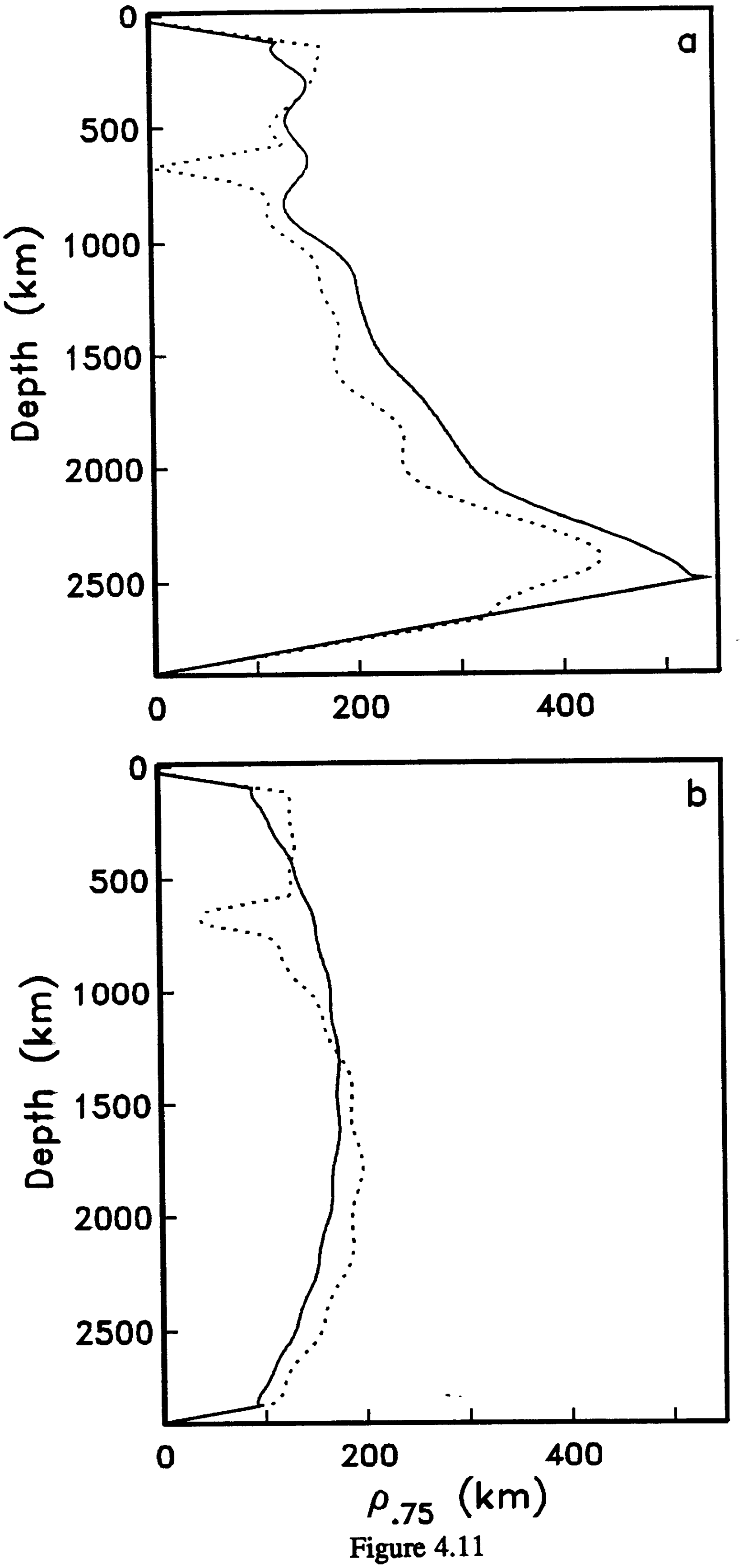
0
500
1000
1500
2000
2500
Depth (km)
a
0
200
400
0
500
1000
1500
2000
2500
Depth (km)
b
0
200
400
$\rho_{.75}$ (km)

Figure 4.11

Figure 4.12

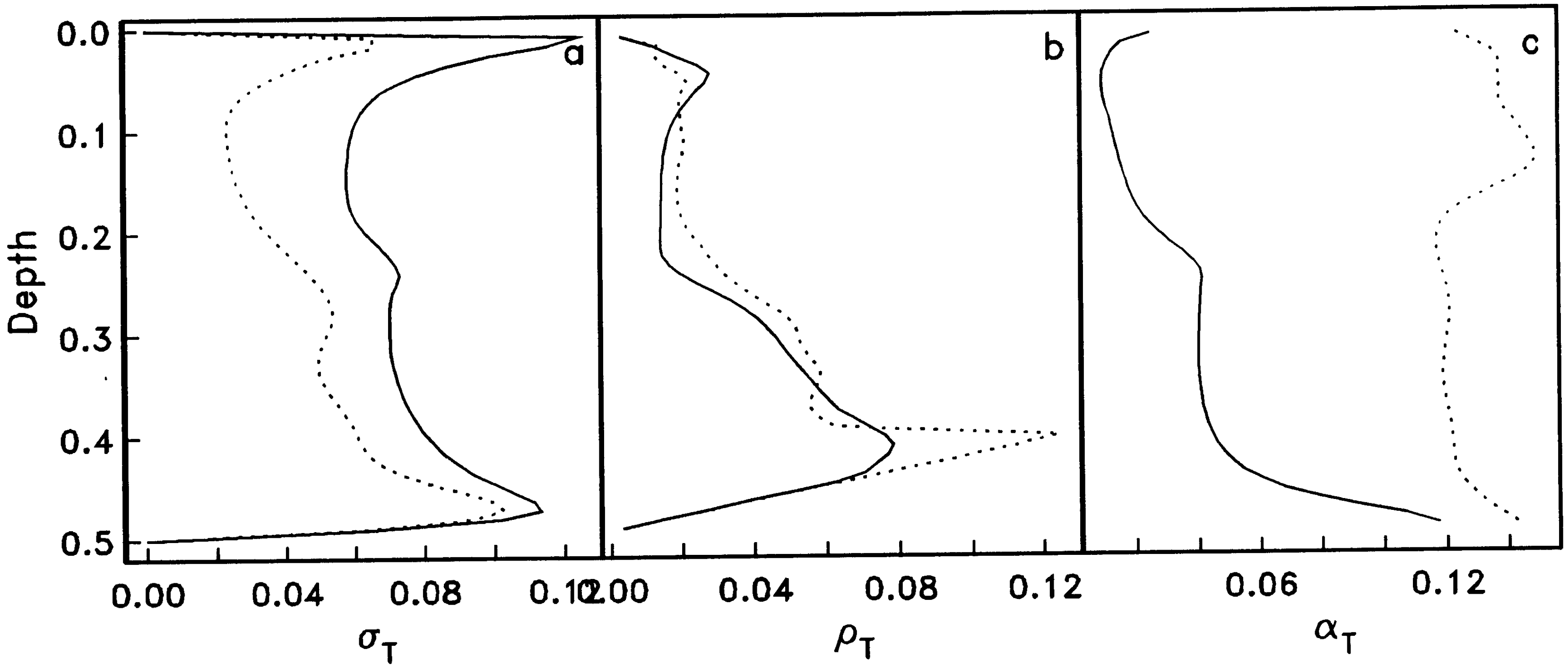

Depth
0.0
0.1
0.2
0.3
0.4
0.5
a
b
c
0.00
0.04
0.08
0.12
0.00
0.04
0.08
0.12
0.06
0.12
σ_T
ρ_T
α_T

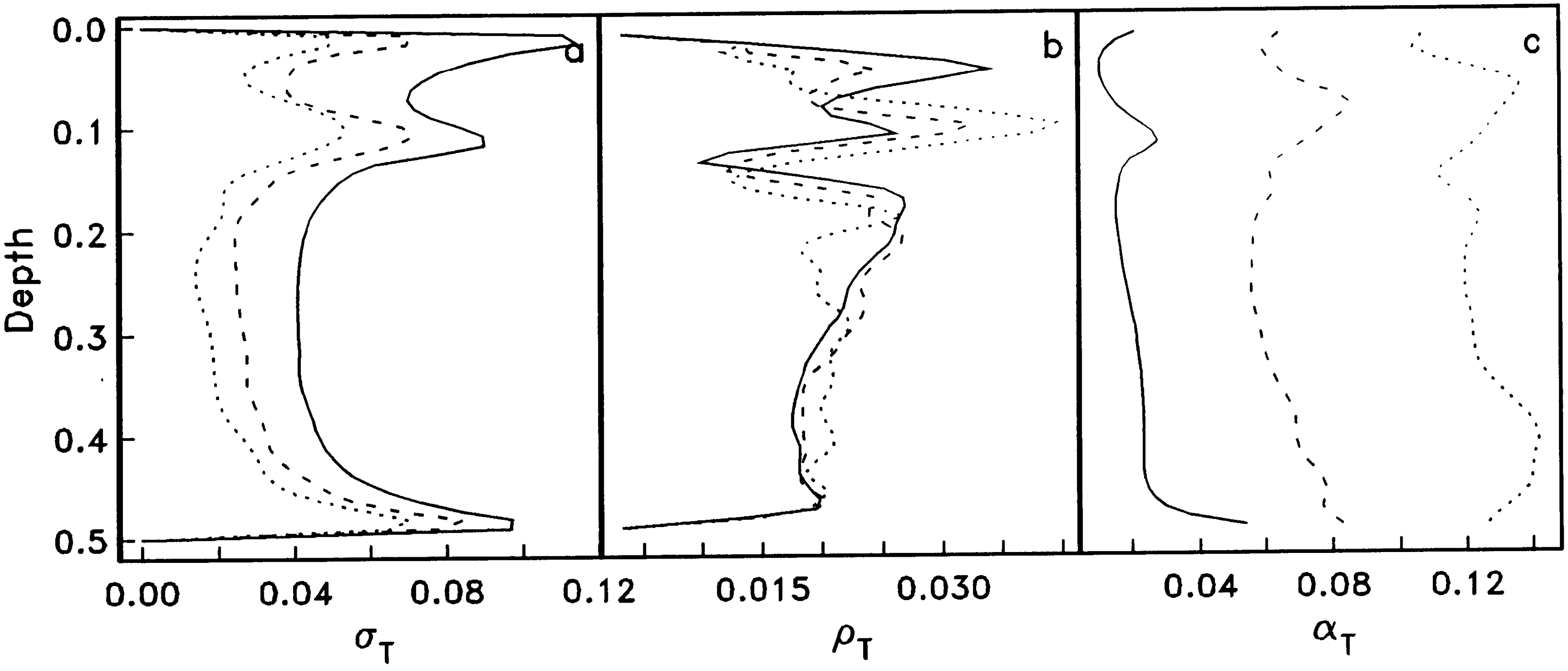
a
b
c
Depth
0.0
0.1
0.2
0.3
0.4
0.5
0.00
0.04
0.08
0.12
σ_T
0.015
0.030
ρ_T
0.04
0.08
0.12
α_T

Figure 4.13

Figure 4.14

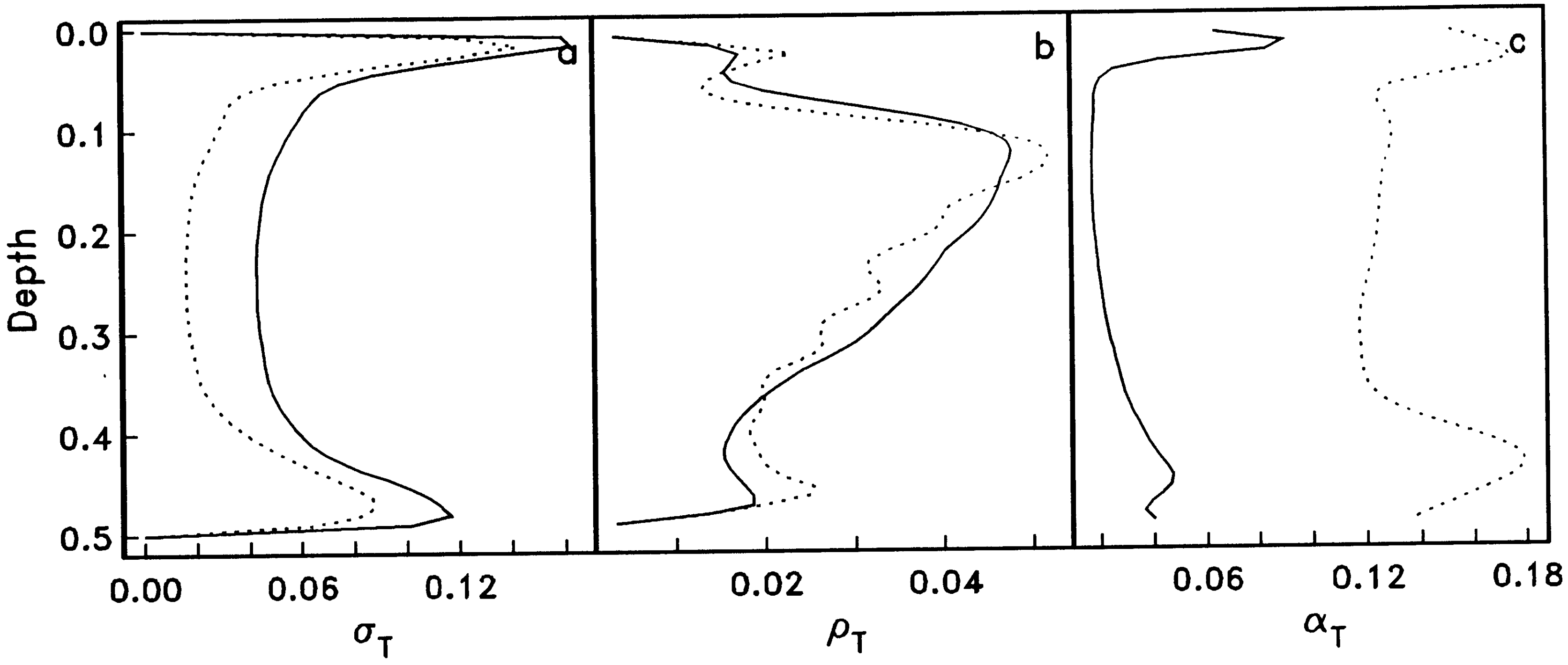
Depth
0.0
0.1
0.2
0.3
0.4
0.5
a
b
c
0.00
0.06
0.12
σ_T
0.02
0.04
ρ_T
0.06
0.12
0.18
α_T

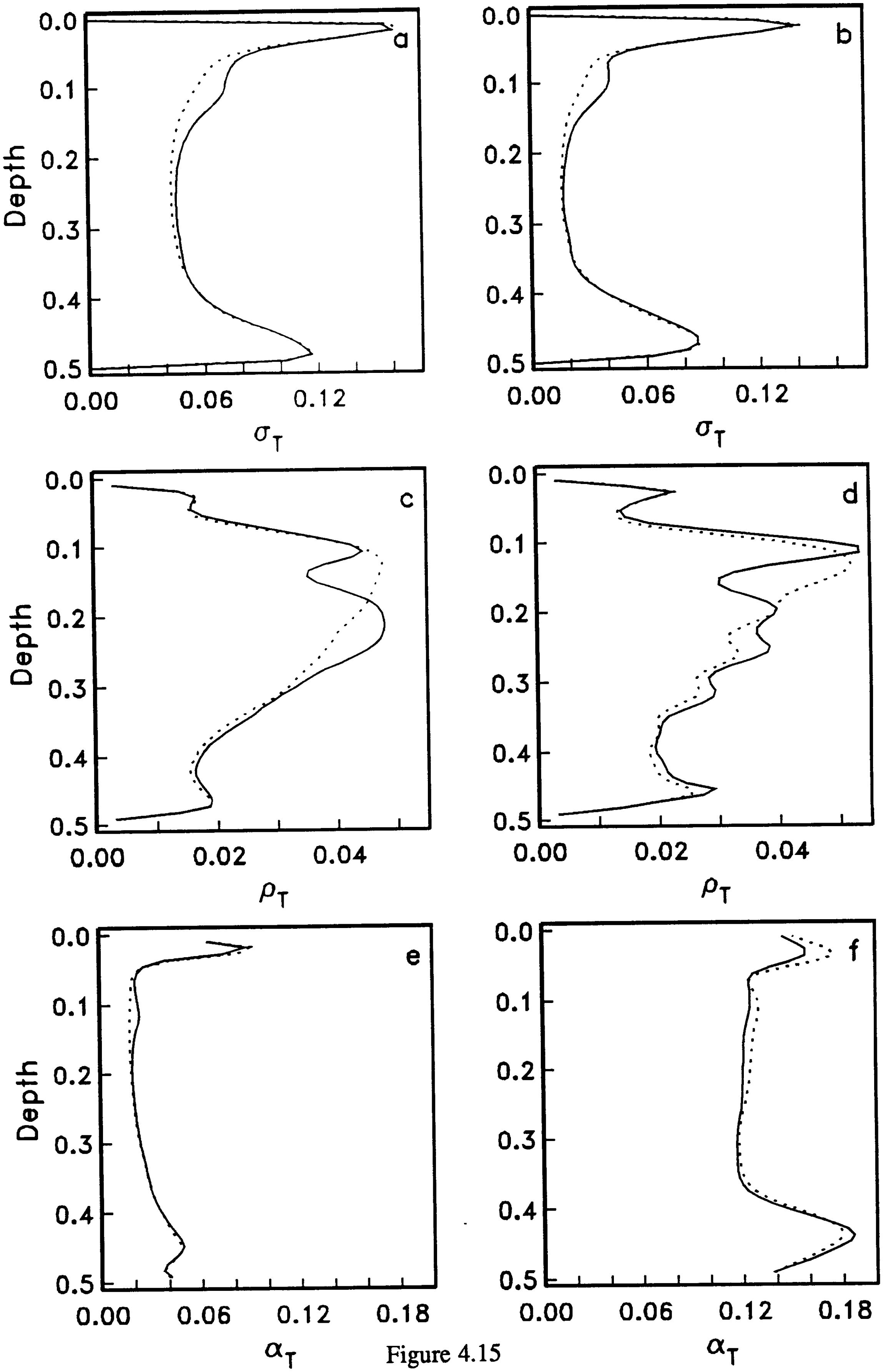
a
b
c
d
e
f
Depth
0.0
0.1
0.2
0.3
0.4
0.5
0.00
0.06
0.12
0.18
0.02
0.04
σ_T
ρ_T
α_T

Figure 4.15

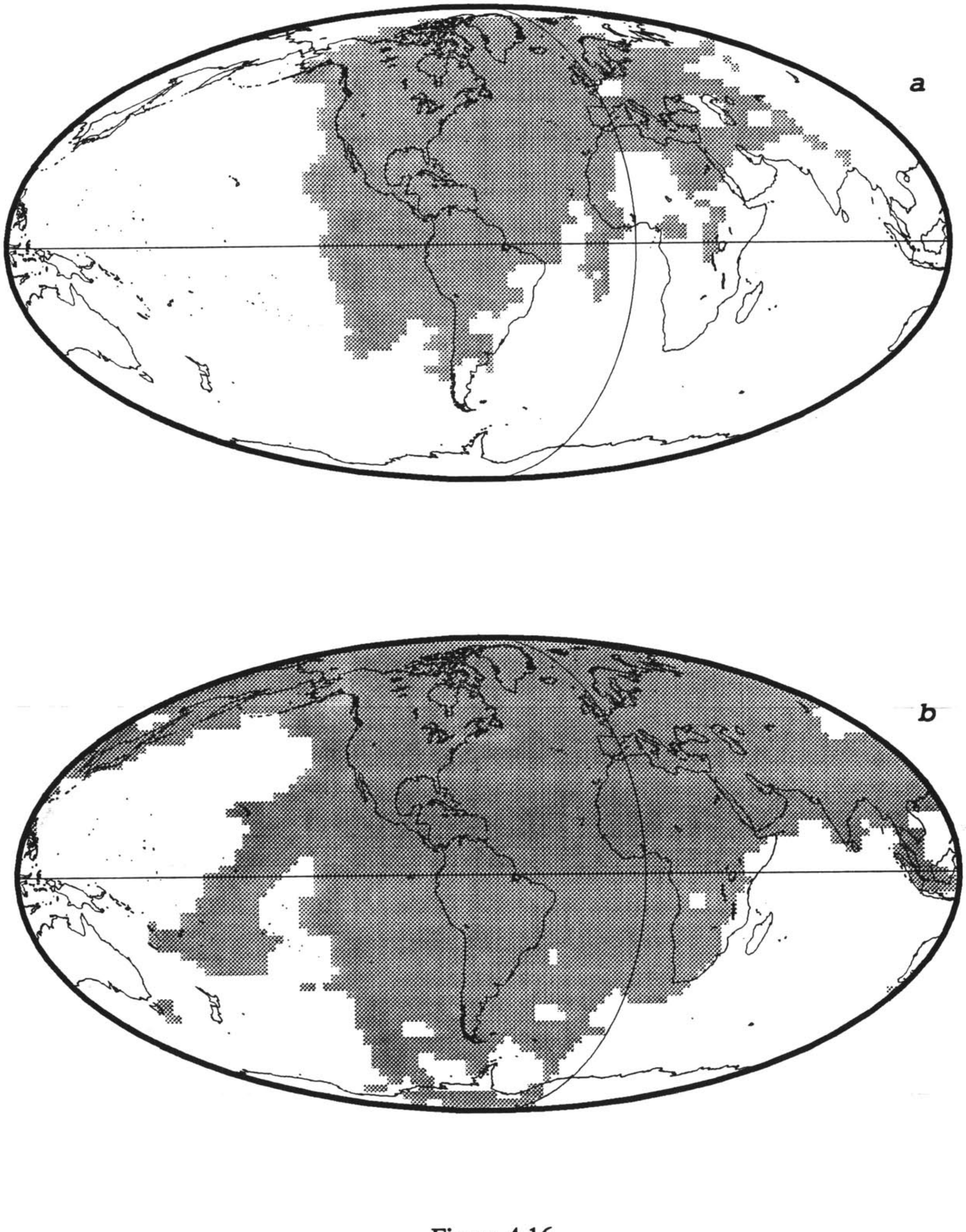

Figure 4.16

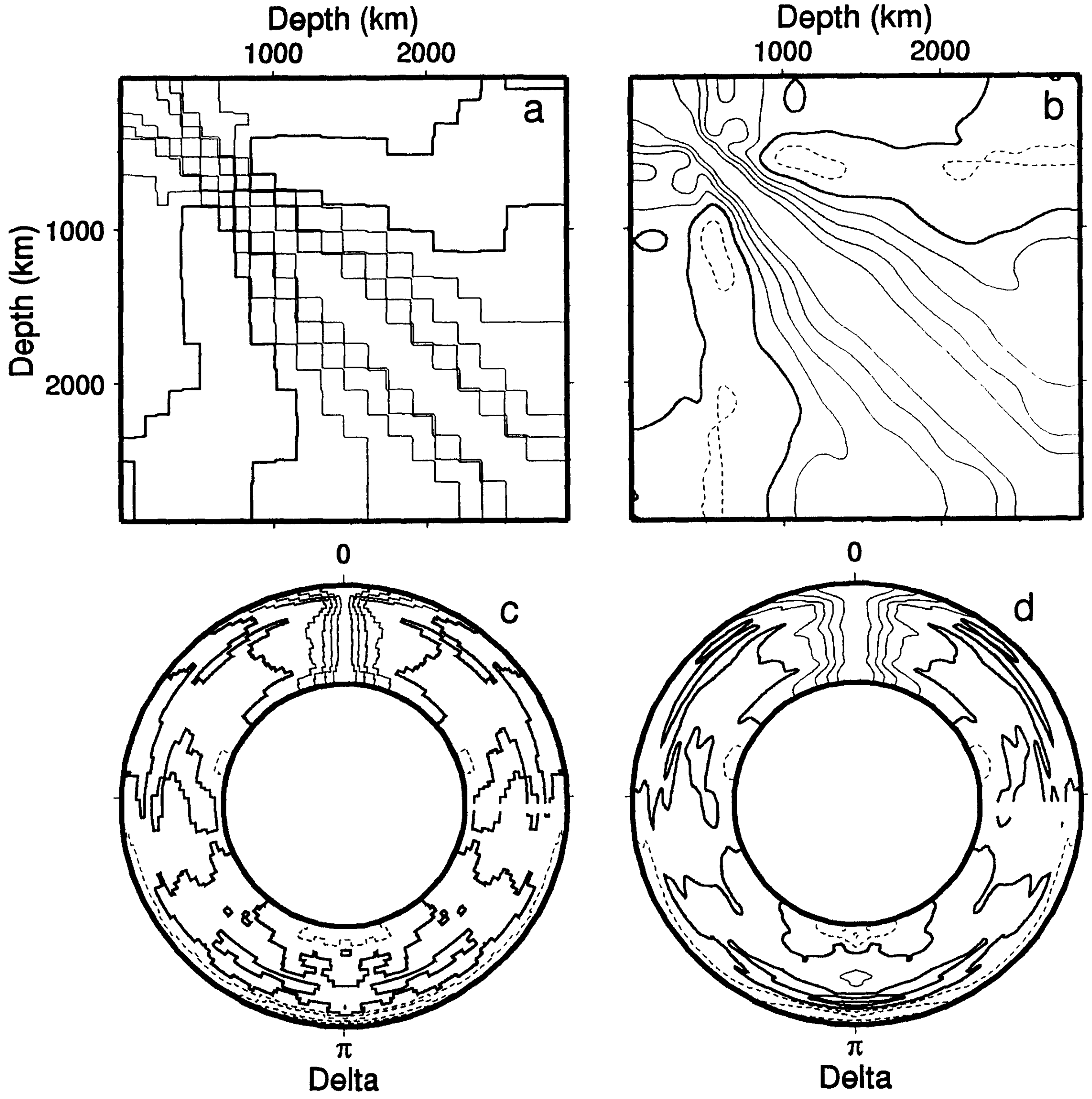
Depth (km)
1000
2000
a
Depth (km)
1000
2000
b
Depth (km)
1000
2000
0
c
π
Delta
0
d
π
Delta

Figure 4.17

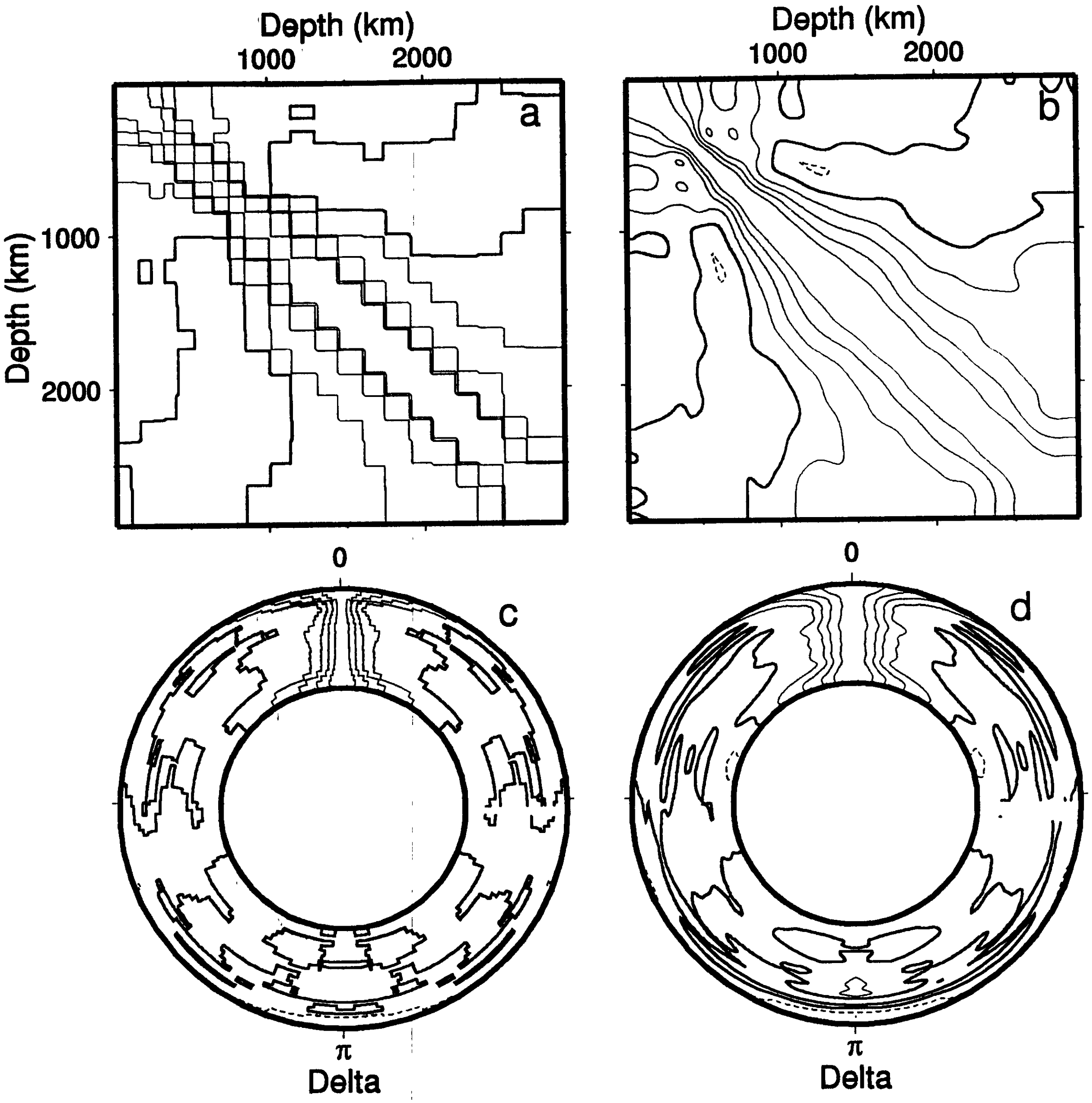
Depth (km)
1000
2000
a
Depth (km)
1000
2000
b
Depth (km)
1000
2000
0
c
π
Delta
0
d
π
Delta

Figure 4.18

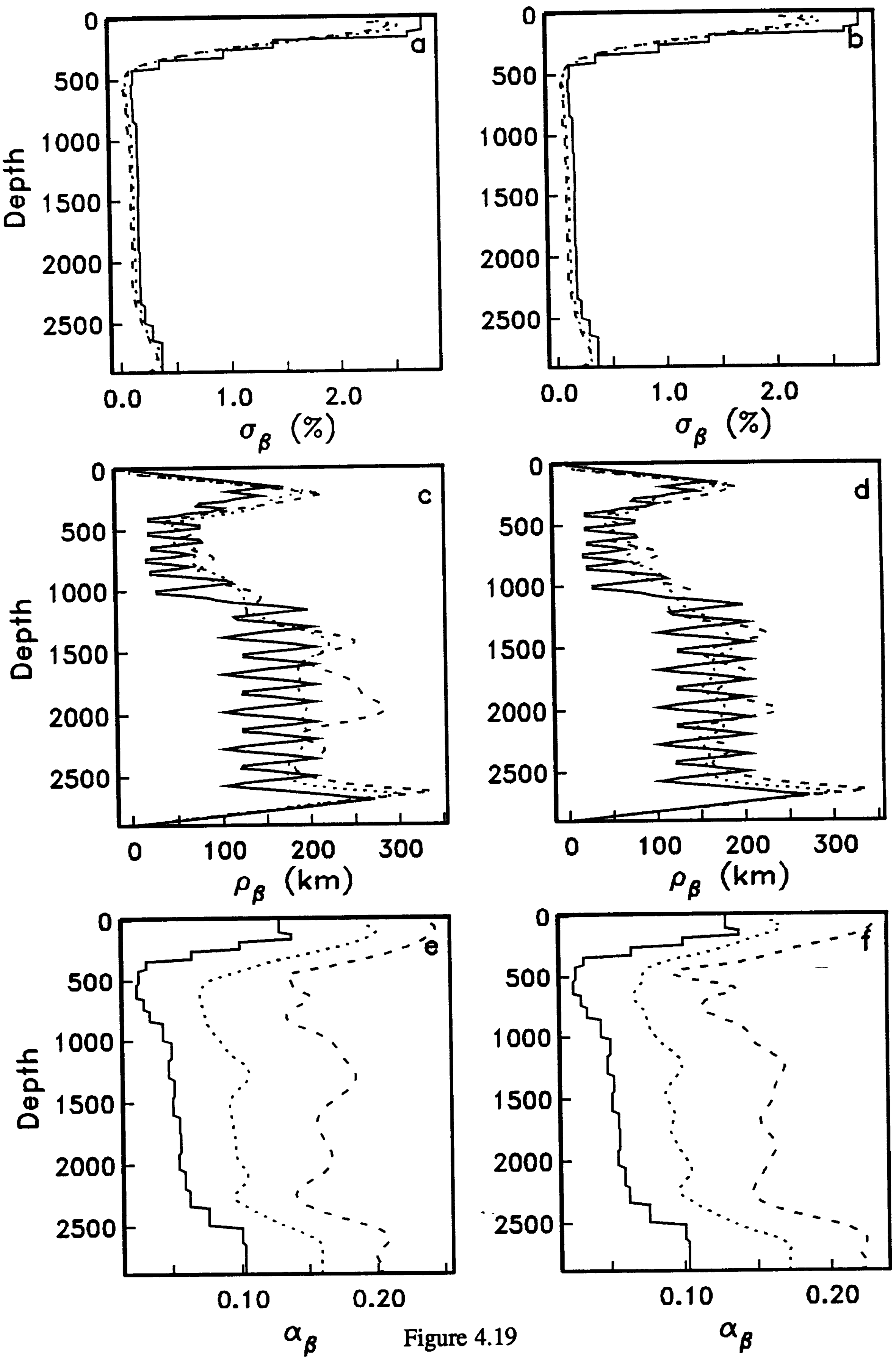
a
b
c
d
e
f
Depth
0
500
1000
1500
2000
2500
0.0
1.0
2.0
σ_β (%)
0
100
200
300
ρ_β (km)
0.10
0.20
α_β

Figure 4.19

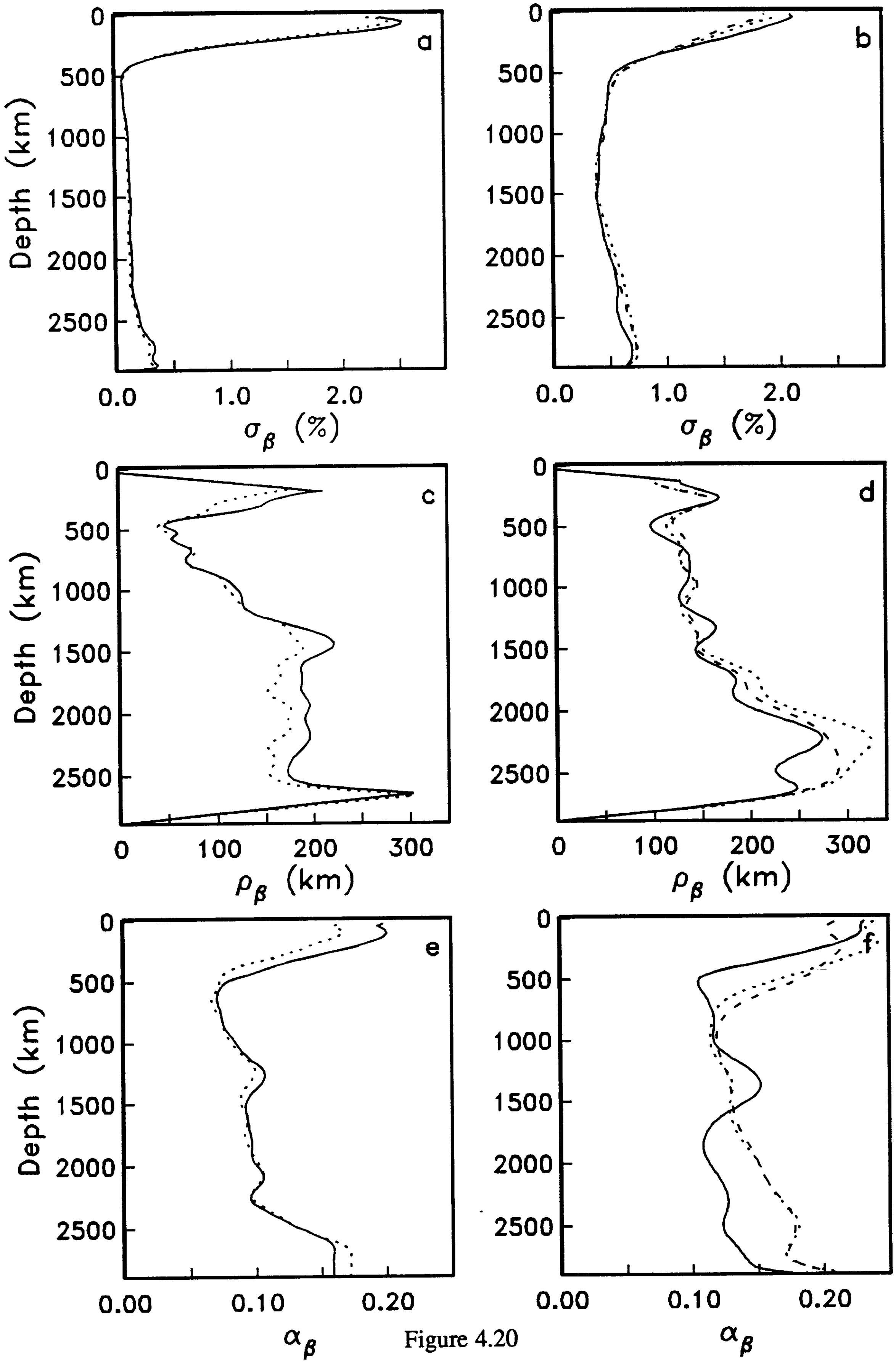
a
b
c
d
e
f
Depth (km)
0
500
1000
1500
2000
2500
0.0
1.0
2.0
σ_β (%)
0
100
200
300
ρ_β (km)
0.00
0.10
0.20
α_β

Figure 4.20

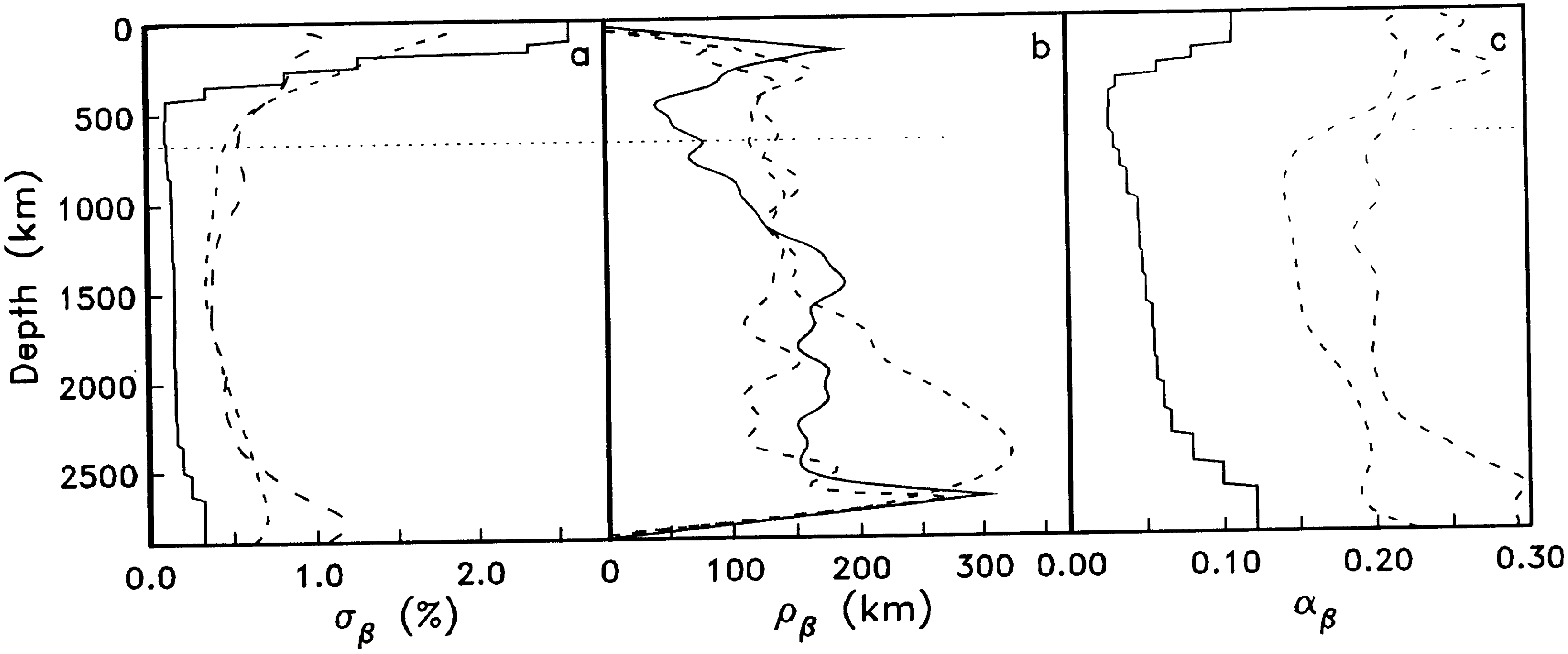
a
b
c
0
500
1000
1500
2000
2500
Depth (km)
0.0
1.0
2.0
σ_β (%)
0
100
200
300
ρ_β (km)
0.00
0.10
0.20
0.30
α_β

Figure 4.21

Figure 4.22

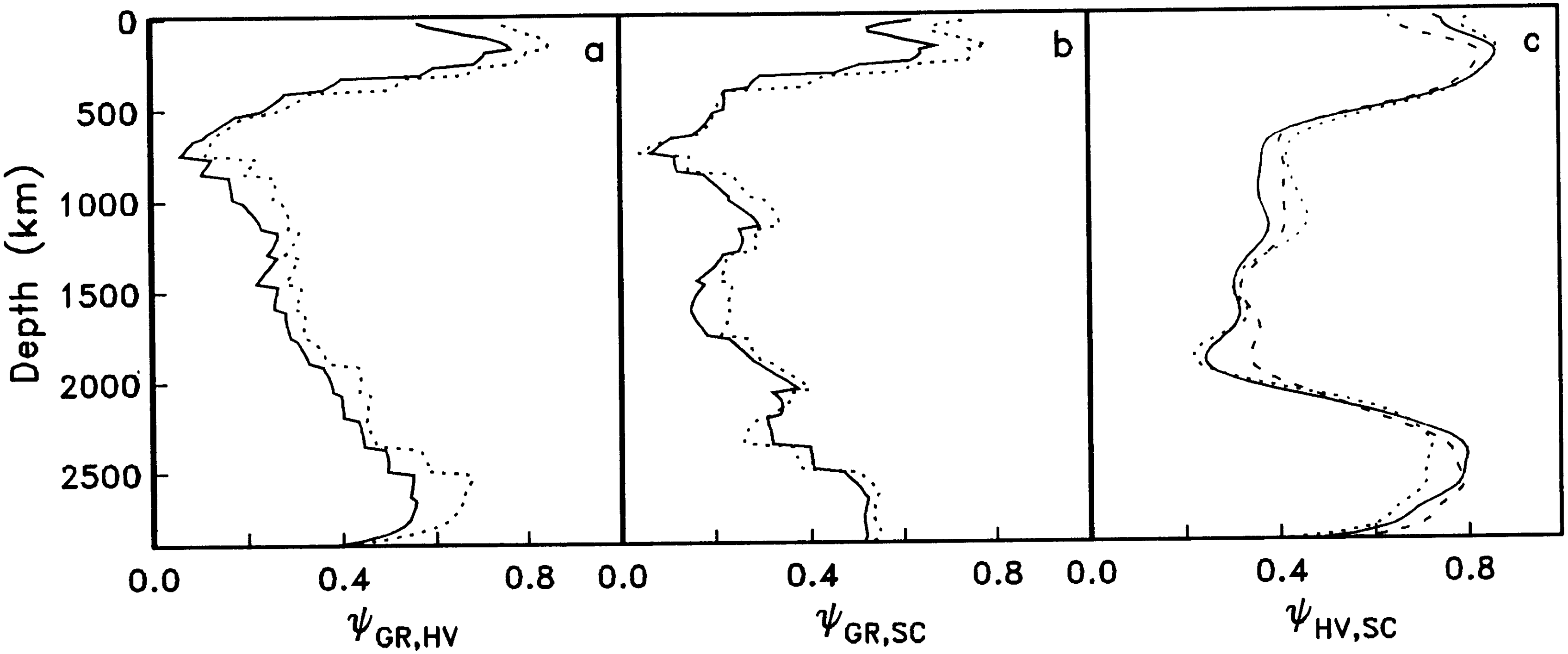
Depth (km)
0
500
1000
1500
2000
2500
a
b
c
0.0
0.4
0.8
0.0
0.4
0.8
0.0
0.4
0.8
$\psi_{GR,HV}$
$\psi_{GR,SC}$
$\psi_{HV,SC}$

CHAPTER 5

SUMMARY AND CONCLUSIONS

In this study we have used two-point correlation functions to characterize the average properties of numerical mantle convection experiments and tomographic earth structures. We have investigated a large number of mantle flow models and quantified the influence of Rayleigh number, internal heating rate, radial viscosity variations, temperature-dependent rheology, phase changes, and plates, both isolated and in combination. Each of these effects alters the flow structure and is clearly expressed in the two-point correlation diagnostics.

Chapter 2 introduces the complete spatio-temporal two-point correlation functions of the temperature and flow velocity fields as tools for studying high-Rayleigh number fluid flow and illustrates the concepts with an example calculation. Diagnostics of the temperature field reveal the characteristic flow features as well as V-diagnostics and are more easily relatable to geophysical observables. We investigate the influence of geometry on the flow by comparing the second-order statistics of a 2D cylindrical calculation with a 3D spherical shell experiment [*Tackley et al.*, 1993] for a flow with an endothermic phase change. The characteristic features of the flow are expressed in the correlation functions for both geometries.

In chapter 3 we apply this formalism to characterize the second-order statistics of mantle convection experiments investigating a large number of different effects. For isoviscous flows in an annulus, we show how radial averages of σ_T, ρ_T, and α_T scale with Rayleigh number for various internal heating rates. A rapid 10-fold to 30-fold viscosity increase with depth yields weakly stratified flows, quantified by σ_u, which measures the rms-radial flux. The horizontal flux diagnostic σ_w reveals the sensitivity of the flow organization on the depth of the viscosity jump (a viscosity discontinuity located at mid-depth leads to horizontal return flow, while one at $r = 0.875$ does not). In the T-diagnostics, a rapid viscosity increase with depth is documented as an increase of σ_T, ρ_T, and α_T in the high-viscosity region.

For numerical experiments with a temperature-dependent rheology, we employ a mobilization scheme for the upper boundary layer that allows us to study the influence of weak, low-viscosity upwellings and strong, high-viscosity downwellings, while preserving a mobile upper boundary layer. Temperature dependence does not appreciably perturb the σ-diagnostics or α_T in the convecting interior. Changes in the radial correlation length are two-fold. First, the greater viscosity of cold downwellings leads to an increase in the height and width of the radial correlation maximum near the top. Second, the increase in ρ_T associated with a viscosity jump is markedly reduced.

An endothermic phase transition manifests itself in the correlation diagnostics as a local minimum in σ_u and ρ_T and a local maximum in σ_T and α_T around the phase transition depth. Temperature-dependent rheology reduces the amount of layering; however, the phase-change induced layering is still apparent in the two-point correlation diagnostics, with ρ_T being the most sensitive indicator of a phase transition. When the phase change coincides with a rapid viscosity increase, the effects of the latter are more important in organizing the flow.

We also investigate the influence of surface plates on the flow organization. Plates whose geometries evolve with time are modeled using a temperature-dependent rheology combined with weak zones (small regions of low viscosity) advected by the flow. The two-point correlation diagnostics obtained from these flows are similar to the temperature-dependent runs with a mobilized upper boundary layer. Differences include an increase in σ_w and α_T near the surface, and a shift of the maximum in σ_u to shallower depths. The main influence of plates is to organize the large-scale flow structure, best documented in the angular power spectrum, which has more power concentrated at low wave numbers for the models with plates. We also quantify some statistics of the plate system, such as plate-size and relative plate-velocity distributions. Average plate velocities decrease nearly monotonically with increasing plate size for cases without a viscosity stratification, whereas viscously stratified systems exhibit a more uniform average plate-velocity distribution.

We have undertaken this systematic study of different effects on the flow structure to establish a data base for a quantitative comparison between mantle convection models and tomographic earth structures based on the same set of diagnostics. The radial correlation function is best suited for such a comparison, as it is least sensitive to the angular and radial filtering necessary when comparing results from convection calculations to the low-resolution images obtained from seismic tomography. R_T can be directly compared with $\tilde{R}_\beta$ estimated from tomographic models where the mapping of shear-speed variations into temperature variations is linear with a coefficient of proportionality that depends only on depth. This should be a good approximation in the mantle's interior away from chemical boundary layers.

In chapter 4 we calculate the two-point moment functions for global and regional models of seismic shear velocity heterogeneity. The tomographic models show relatively constant radial correlation lengths between 350 and 800 km depth, although the exact values of ρ_β differ. Below 1200 km depth, two of the three models agree within 20-30 km. Above this depth, the other two models agree. The discrepancy between the seismic heterogeneity fields can be quantified by the coherency, ψ, (cross-correlation coefficient at a specified radius) between any two models. This analysis indicates low coherencies except in the uppermost and lowermost mantle, where $\psi > 0.5$. The variability between the correlation functions derived from the different seismic models makes an interpretation of individual features of $\tilde{R}_\beta$ difficult.

Despite their differences, tomographic models still provide valuable constraints on the types of mantle flow models consistent with the observed radial correlation functions. Figure 5.1 shows radial correlation lengths, $\tilde{\rho}_\beta$, for the three seismic models (G74, HV, and SC) and ρ_T-profiles for various convection experiments filtered to the global tomographic resolution. For reference, the range of correlation lengths encompassed by the seismic models is shown as a gray-shaded area. Common to the convection runs are a temperature-dependent rheology and ten surface plates. In addition, the numerical experiments shown in Figure 5.1*b* have a step-function viscosity increase at $r = 0.875$, while those depicted in Figure 5.1*c* exhibit an endothermic phase change at that depth (and $\eta_0 = 1$). The convection models with a 30-fold viscosity increase ($P = 0.0$ and $P = -0.1$) are most consistent with the seismic results, while a viscosity jump by a factor 100 is marginally consistent (long dashed). None of the ρ_T-profiles for the convection experiments without viscosity stratification show a morphology similar to that of the seismic models. Whereas the $\tilde{\rho}_\beta$-profiles increase with depth, ρ_T for cases with a weak endothermic phase boundary ($P = 0.0$ and $P = -0.1$) decreases with depth, and the run with $P = -0.2$ (long dashed) shows two local maxima well outside the range spanned by the seismic models. For runs without viscous stratification, the endothermic phase change manifests itself as a distinct local minimum in ρ_T at the phase transition depth. Such a minimum in ρ_T is absent for the experiment where the phase change and viscosity jump coincide.

To quantify the magnitude of flow stratification, we define a stratification index for the average radial mass flux as $S(|u|) = 1 - |u|_S/|u|_0$, where $|u|_S$ is the value at the stratification boundary and $|u|_0$ is a reference value. For a completely stratified flow, $|u|_S = 0$ and $S(|u|)$ is unity, while for $|u|_S = |u|_0$, the stratification index is zero. Using a definition for $|u|_0$ based on a reference run, used by *Solheim and Peltier* [1994], is problematic for convection experiments with varying viscosity and/or internal heating, where the proper choice of parameters for the reference case is difficult. Instead, we choose $|u|_0$ as the mean of radially averaged fluxes above and below the stratification boundary away from boundary layers. This definition of $|u|_0$ allows us to obtain an estimate for S from each convection experiment individually. Figure 5.2 shows a plot of $S(|u|)$ versus $S(\rho)$, the stratification index for the radial correlation length (calculated analogously), for a suite of convection models spanning a wide range of rheologies with varying phase change strengths, at Rayleigh numbers $Ra_{B_{eff}} = 1 \times 10^6$ - 5×10^6 and internal heating rates ranging from 52% to 85%. $S(\rho)$ can also be calculated for the tomographic models; the range spanned by the models G74, HV, and SC is shown as dark gray-shaded bands. Light shaded bands outline the additional range of $S(\tilde{\rho}_\beta)$ allowed assuming that half the correlation length in the seismic models at 670 km depth is due to noise. To allow a comparison between $S(\rho_T)$ and $S(\tilde{\rho}_\beta)$ stratification indices were calculated from the diagnostics obtained by low-pass filtering the temperature fields to $l_{max} = n_{max} = 20$ (Figure 5.2*a*) and $l_{max} = 10$, $n_{max} = 13$ (Figure 5.2*b*), respectively. For small values of $S(|u|)$, $S(\rho_T)$ increases more rapidly than $S(|u|)$, beyond $S(|u|) \cong 0.1$, $S(\rho_T)$ increases approximately linearly with a slope smaller than unity. Except for a completely stratified run, $S(|u|)$ is less than 0.5. Experiments falling outside the gray-shaded bands for both levels of filtering are (in order of decreasing $S(|u|)$): the rigorously stratified case, two experiments with $P = -0.2$, a run with $P = -0.15$, an experiment with a 30-fold viscosity increase at $r = 0.875$ and a strong endothermic phase change ($P = -0.15$), and two experiments with $P = -0.1$ and $P = 0.0$. For the same value of P, both $S(|u|)$ and $S(\rho)$ are smaller for the runs with temperature-dependent rheology than their temperature-independent counterparts, consistent with the findings discussed in chapter 3 (Figure 4.19). All experiments inconsistent with the constraints provided by $S(\tilde{\rho}_\beta)$, also fail to be consistent with the overall morphology of the $\tilde{\rho}_\beta$-profiles shown in Figure 5.1, indicating that the stratification index provides a crude but effective discriminant. The range spanned by $S(\tilde{\rho}_\beta)$ (for models G74, HV, and SC) suggests that the present-day mantle is at most weakly stratified with $S(|u|) \leq 0.1$. While it is possible to calculate an instantaneous radial flow velocity field for a model of seismic heterogeneity directly [*Hager and Clayton*, 1989; *Phipps-Morgan and Shearer*, 1993], those calculations involve a scaling of seismic anomalies to density, the choice of a radial viscosity model, and to date do not incorporate the effects of lateral viscosity variations. The approach presented here provides an alternative route for determining $S(|u|)$.

Is there a relationship between the stratification index $S(|u|)$ and the temporal variability of the radial flux at the stratification boundary, $|\tilde{u}|_S$? Figure 5.3 depicts histograms of $|\tilde{u}|_S$ for unstratified flows (Figures 5.3*a*, *b*), viscously stratified flows (Figures 5.3*c*, *d*), and flows stratified by a strong endothermic phase-change (Figures 5.3*e*,*f*). The latter two runs show a distinct asymmetry in the flux histograms, which is due to episodic "avalanching" events occurring for these strongly phase-change modulated flows. A simple measure for the asymmetry of the flux distributions is: $A(|\tilde{u}|_S) = 1 - |\tilde{u}|_S^{med} / \langle |\tilde{u}|_S \rangle$, where $|\tilde{u}|_S^{med}$ and $\langle |\tilde{u}|_S \rangle$ are the median flux and mean flux, respectively. For distributions symmetric about the mean, the asymmetry index is zero. Figure 5.4 shows $A(|\tilde{u}|_S)$ as a function of $S(|u|)$ for the same suite of runs depicted in Figure 5.2. All models with $S(|u|) \leq 0.1$ also have small $A(|\tilde{u}|_S)$. The runs characterized by strong episodicity have stratification indices greater than 0.2. For the same values of P, experiments with temperature-dependent viscosity have smaller values of $A(|\tilde{u}|_S)$ than their temperature-independent counterparts, as strong, cold downwellings are capable of penetrating the phase boundary more readily, leading to a larger mean flux and smaller avalanches. Results from 3D calculations with an endothermic phase change [*Tackley et al.*, 1993] exhibit less episodicity than comparable 2D runs. These results suggest that strong episodicity only occurs for highly stratified flows. As the stratification index for the present day mantle as constrained by the seismic models discussed above is small, it appears unlikely that the earth's mantle is in a regime where long periods of separate upper mantle - lower mantle convection are interrupted by short episodes of whole mantle style convection as advocated by some workers [*Machetel and Weber*, 1991; *Peltier and Solheim*, 1992].

As seismology provides only a single snapshot of the convecting mantle we cannot rule out that today's mantle is in an avalanching cycle of an episodic regime, leading to small values of $S(\tilde{\rho}_\beta)$ (and by inference $S(|u|)$). However, as both temperature-dependent rheology and three-dimensionality reduce episodicity, this scenario appears unlikely. Other geophysical observations can help us to discriminate further between the styles of mantle convection. As already discussed in chapter 3, plates are an important part of the earth's convecting system, and should therefore be incorporated in numerical models. Convection experiments with plates whose geometries evolve with time also allow a comparison of the numerical models with a set of observations that extend over a period of time - the plate tectonic record. While in this thesis the convection experiments with plates and temperature-dependent rheology are primarily discussed in terms of two-point correlation functions, we shall illustrate some of the diagnostic potential of the plate system statistics. Figure 5.5 shows histograms of fractional plate size and relative plate velocity for two convection experiments and for the earth's plate tectonic system over the last 120 Ma compiled by *Lithgow-Bertelloni et al.* [1993]. The first convection model (Figures 5.5*a*, *b*) has a strong endothermic phase transition ($P = -0.2$) at $r = 0.875$ and has plate-size and plate-velocity histograms peaked at the smallest bins. In contrast, the size and velocity histograms of the second experiment (Figures 5.5*c*, *d*) show less asymmetry. This model has a 30-fold viscosity increase at $r = 0.875$ and a weak endothermic phase change ($P = -0.1$) at that depth. Figures 5.5*e*, *f* show the size and velocity distributions for the earth's plate tectonic system over the last 120 Ma. It is evident that the histograms of the plate tectonic record are more similar to the convection model with a high-viscosity lower layer than to the model with a strong endothermic phase boundary. The asymmetry of the plate-size and plate-velocity distributions is further quantified using the same definition for the asymmetry index as above (i.e., using the ratio of median and mean of the distribution) and is shown in Figure 5.6 for all convection experiments with evolving plates together with the value for the earth (star). Common to the convection models closest to the earth's value is a 30-fold viscosity increase at $r = 0.875$ (triangles). Models plotting further away either have a constant background viscosity (filled squares), a viscosity increase at $r = 0.75$, or a 100-fold viscosity jump (open squares). While these results are intriguing, it must not be forgotten that the convection calculations are two-dimensional and an assessment of the importance of three-dimensionality for these plate system statistics (analogous to that presented in chapter 2 for the two-point correlation functions) awaits the development of 3D spherical shell calculations with temperature-dependent viscosity and evolving plates.

In this thesis we have developed a formalism for quantifying the average properties of numerical convection models based on two-point correlation functions. The same approach can be used to describe tomographic earth structures. As long as thermal anomalies are predominantly responsible for seismic velocity heterogeneity, a direct comparison between ρ_T and $\tilde{\rho}_\beta$ is meaningful. Such a comparison indicates that a viscosity increase at 670 km depth by a factor 30-100 is consistent with the tomographic models investigated, while a constant viscosity mantle clearly is not. (Should the increase in $\tilde{\rho}_\beta$ below 1600 km for HV turn out to be an artifact due to the degrading resolution, these bounds may be further tightened.) This result corroborates findings from geoid modeling [*Hager*, 1984; *Hager and Richards*, 1989; *King and Masters*, 1992; *Forte et al.*, 1993], which indicate a viscosity increase with depth of one or two orders of magnitude. Whether it will be possible to use our approach for distinguishing between details of these different radial viscosity structures is doubtful, unless the range permitted by the seismic models can be reduced substantially. What does seem possible, however, is to rule out convection models without a viscosity increase with depth. This can be done on the basis of the overall morphology of the radial correlation diagnostic for such flows, as well as on the basis of the stratification indices, $S(|u|)$ and $S(\rho)$. These stratification indices furthermore indicate that the present-day style of convection is dominantly whole-mantle ($S(|u|) \leq 0.1$). Together with $A(|\tilde{u}|_S)$ they furthermore suggest that it is unlikely for the earth to be in an intermittently layered regime as proposed by *Machetel and Weber* [1991] and *Peltier and Solheim* [1992] and invoked as a mechanism for explaining geochemical observations [*Stein and Hofmann*, 1994]. Independent evidence comparing plate system statistics from numerical convection calculations to the earth's plate tectonic record also favors models with a 30-fold viscosity increase in the lower mantle.

REFERENCES

Forte, A. M., A. M. Dziewonski, and R. L. Woodward, Aspherical structure of the mantle, tectonic plate motions, nonhydrostatic geoid, and topography of the core-mantle boundary, in *Dynamics of Earth's deep interior and Earth rotation*, edited by J. L. LeMouel, D. E. Smylie, and T. Herring, *Geophysical Monograph, 72*, pp. 135-166, 1993.

Hager, B. H., Subducted slabs and the geoid; constraints on mantle rheology and flow, *J. Geophys. Res.*, *89*, 6003-6015, 1984.

Hager, B. H., and R. W. Clayton, Constraints on the structure of mantle convection using seismic observations, flow models, and the geoid, in *Mantle convection; plate tectonics and global dynamics*, edited by R. W. Peltier, *The Fluid Mechanics of Astrophysics and Geophysics*, *4*, pp. 657-763, Gordon and Breach, New York, 1989.

Hager, B. H., and M. A. Richards, Long-wavelength variations in Earth's geoid; physical models and dynamical implications, *Philos. Trans. R. Soc. London, Ser. A*, *328*, 309-327, 1989.

King, S. D., and T. G. Masters, An inversion for radial viscosity structure using seismic tomography, *Geophys. Res. Lett.*, *19*, 1551-1554, 1992.

Lithgow-Bertelloni, C., M. A. Richards, Y. Ricard, R. J. O'Connell, and D. E. Engebretson, Toroidal-poloidal partitioning of plate motions since 120 MA, *Geophys. Res. Lett.*, *20*, 375-378, 1993.

Machetel, P., and P. Weber, Intermittent layered convection in a model mantle with an endothermic phase change at 670 km, *Nature*, *350*, 55-57, 1991.

Peltier, W. R., and L. P. Solheim, Mantle phase transitions and layered chaotic convection, *Geophys. Res. Lett.*, *19*, 321-324, 1992.

Phipps-Morgan, J., and P. M. Shearer, Seismic constraints on mantle flow and topography of the 660-km discontinuity: Evidence for whole mantle convection, *Nature*, *365*, 506-511, 1993.

Solheim, L. P., and W. R. Peltier, Avalanche effects in phase transition modulated thermal convection: A model of earth's mantle, *J. Geophys. Res.*, *99*, 6997-7018, 1994.

Stein, M., and A. W. Hofmann, Mantle plumes and episodic crustal growth, *Nature*, *372*, 63-68, 1994.

Tackley, P. J., D. J. Stevenson, G. Glatzmaier, and G. Schubert, Effects of an endothermic phase transition at 670 km depth in a spherical model of convection in the Earth's mantle, *Nature*, *361*, 699-704, 1993.

FIGURE CAPTIONS

Fig. 5.1. (*a*) Radial correlation lengths, $\tilde{\rho}_\beta$, for tomographic models G74 (solid), HV (short dashed), and SC (long dashed). The range of correlation lengths encompassed by the three tomographic models is shown as a gray-shaded area. (*b*), (*c*) Radial correlation lengths, ρ_T, for convection experiments with temperature-dependent viscosity and ten plates. (*b*) Step-function viscosity increase at r = 0.875. 30-fold viscosity increase (solid); 30-fold viscosity increase and endothermic phase change ($P = -0.1$) (short dashed); 100-fold viscosity increase (long dashed). (*c*) Convection experiments with $\eta_0 = 1$ and an endothermic phase change at r = 0.875. $P = 0.0$ (solid), P = –0.1 (short dashed), and $P = -0.2$ (long dashed). All temperature fields were truncated at $l_{max} = 10$ and $n_{max} = 13$.

Fig. 5.2. Radial mass flux stratification index, $S(|u|)$, versus radial correlation length stratification index, $S(\rho)$, at r = 0.875, for a suite of convection experiments spanning a wide range of rheologies with varying phase change strength. Reference values were computed as the mean of radial averages above and below the stratification boundary (300 km and 600 km thick, respectively) beginning 70 km away from that boundary. Dark-shaded bands outline the range of $S(\tilde{\rho}_\beta)$ allowed by the tomographic models G74, HV, and SC. Light shaded bands outline the additional range of $S(\tilde{\rho}_\beta)$ allowed assuming that half the correlation length in the seismic models at 670 km depth is due to noise. (*a*) $S(\rho_T)$ calculated from temperature fields truncated at $l_{max} = 20$ and $n_{max} = 20$. (*b*) $S(\rho_T)$ calculated from temperature fields truncated at $l_{max} = 10$ and $n_{max} = 13$. Filled symbols represent experiments with temperature-dependent viscosity with 10 plates, open symbols temperature-independent runs.

Fig. 5.3. Histograms of the snapshot estimator of radial flux, $|\tilde{u}|_S$, at r = 0.875 for numerical convection experiments. (*a*), (*c*), (*e*) Temperature-dependent viscosity and ten

plates. (*b*), (*d*), (*f*) Temperature-independent viscosity. (*a*), (*b*) $\eta_0 = 1, P = 0.0$. (*c*), (*d*) 30-fold viscosity increase at $r = 0.875, P = 0.0$. (*e*), (*f*) $\eta_0 = 1, P = -0.2$.

Fig. 5.4. Radial mass flux stratification index, $S(|u|)$, versus asymmetry measure of the flux distribution, $A(|\tilde{u}|_S)$, at $r = 0.875$, for a suite of convection experiments spanning a wide range of rheologies with varying phase change strengths. Filled symbols represent experiments with temperature-dependent viscosity and 10 plates, open symbols temperature-independent runs. The runs for which the $|\tilde{u}|_S$-histograms are shown in Figure 5.3 are depicted as circles.

Fig. 5.5. Histograms of fractional plate size and relative plate velocity normalized by the rms-velocity of the plate system. (*a*), (*b*) Convection run with temperature-dependent viscosity, ten plates, and an endothermic phase change $P = -0.2$ at $r = 0.875$. (*c*), (*d*) Convection run with temperature-dependent viscosity, ten plates, a 30-fold viscosity increase, and an endothermic phase change $P = -0.1$ at $r = 0.875$. (e), (f) Earth's plate tectonic system for the past 120 Ma from the plate-tectonic reconstruction of *Lithgow-Bertelloni et al.* [1993].

Fig. 5.6. Asymmetry measure of the plate size distribution, $A(\textit{Plate Size})$, versus $A(\textit{Plate Velocity})$. Filled squares denote convection experiments with $\eta_0 = 1$ and varying P. Open triangles represent convection experiments with a 30-fold viscosity increase at $r = 0.875$ and varying P. The star denotes the point pair for the earth using the plate tectonic reconstruction of *Lithgow-Bertelloni et al.* [1993] for the past 120 Ma.

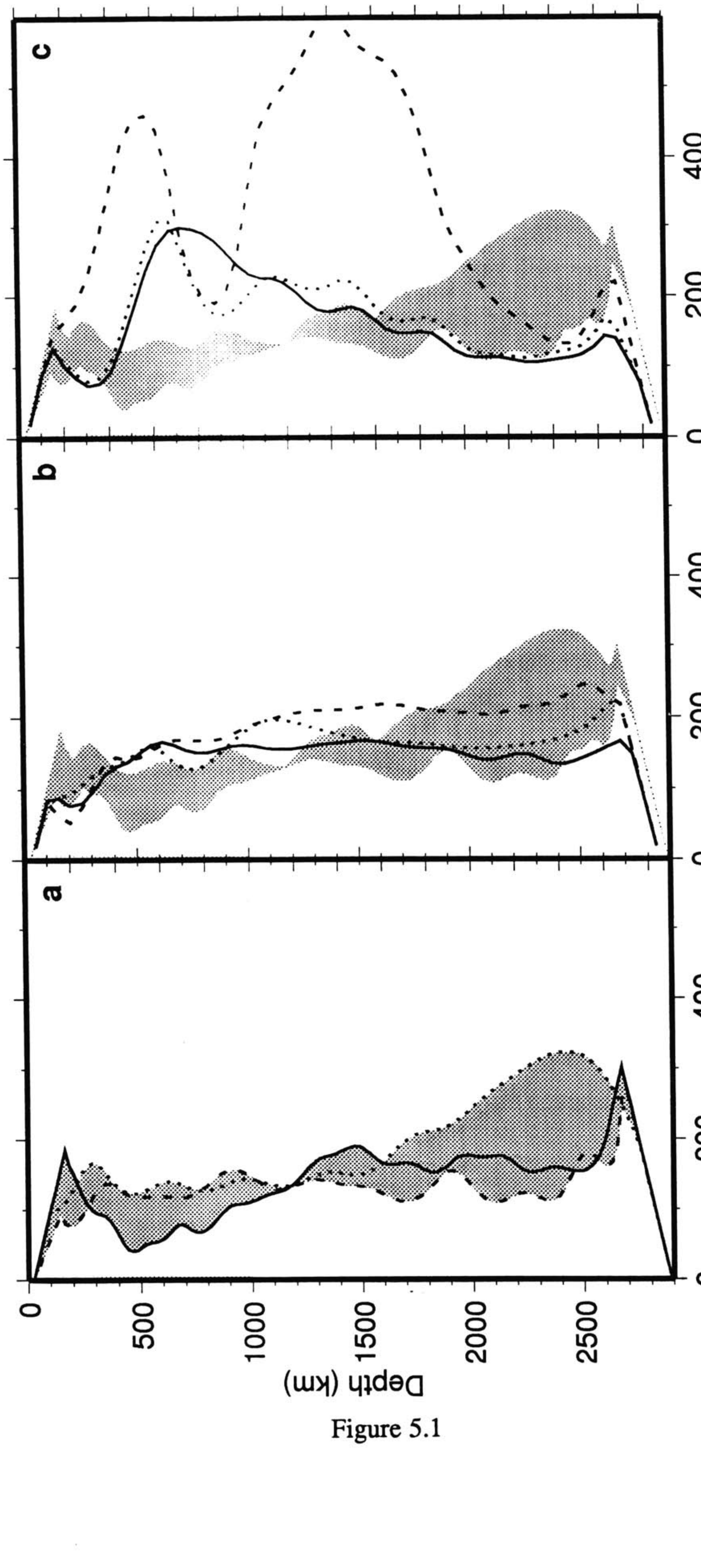
a
b
c
Depth (km)
0
500
1000
1500
2000
2500
ρ_β (km)
ρ_T (km)
ρ_T (km)
0
200
400

Figure 5.1

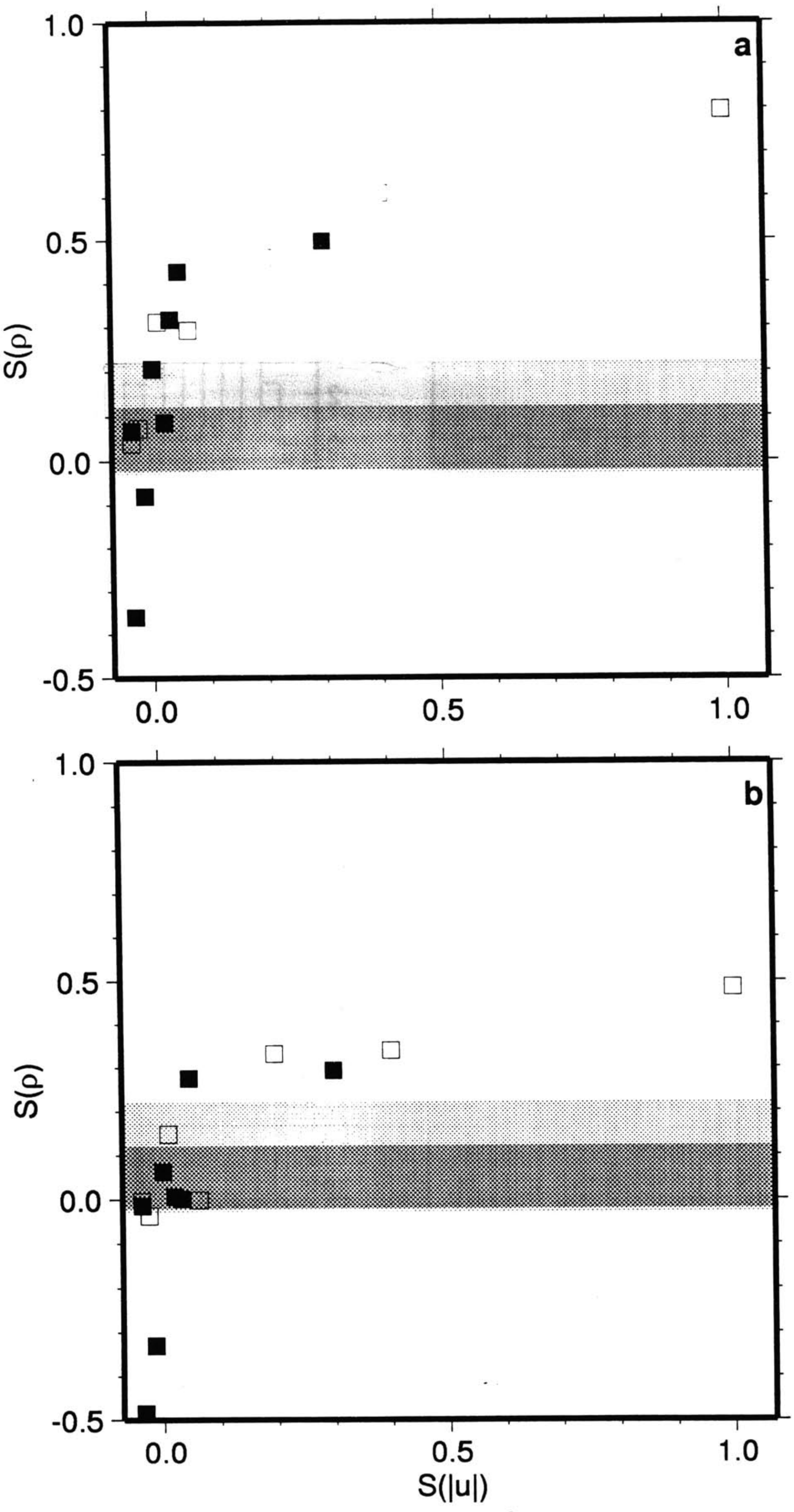

Figure 5.2

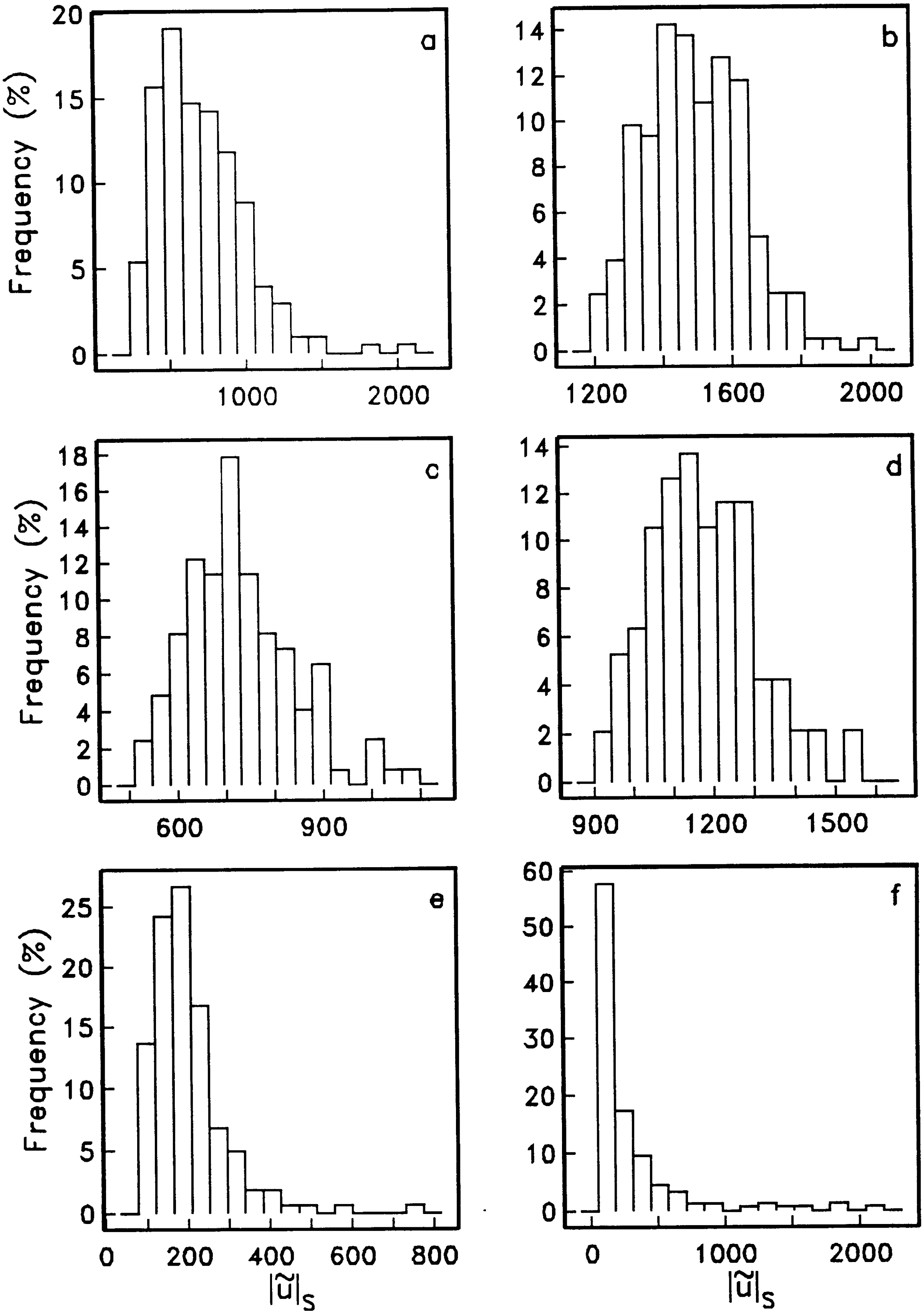
a
b
c
d
e
f
Frequency (%)
0
5
10
15
20
1000
2000
0
2
4
6
8
10
12
14
1200
1600
2000
0
2
4
6
8
10
12
14
16
18
600
900
0
2
4
6
8
10
12
14
900
1200
1500
0
5
10
15
20
25
0
200
400
600
800
0
10
20
30
40
50
60
0
1000
2000
$|\tilde{u}|_s$
$|\tilde{u}|_s$

Figure 5.3

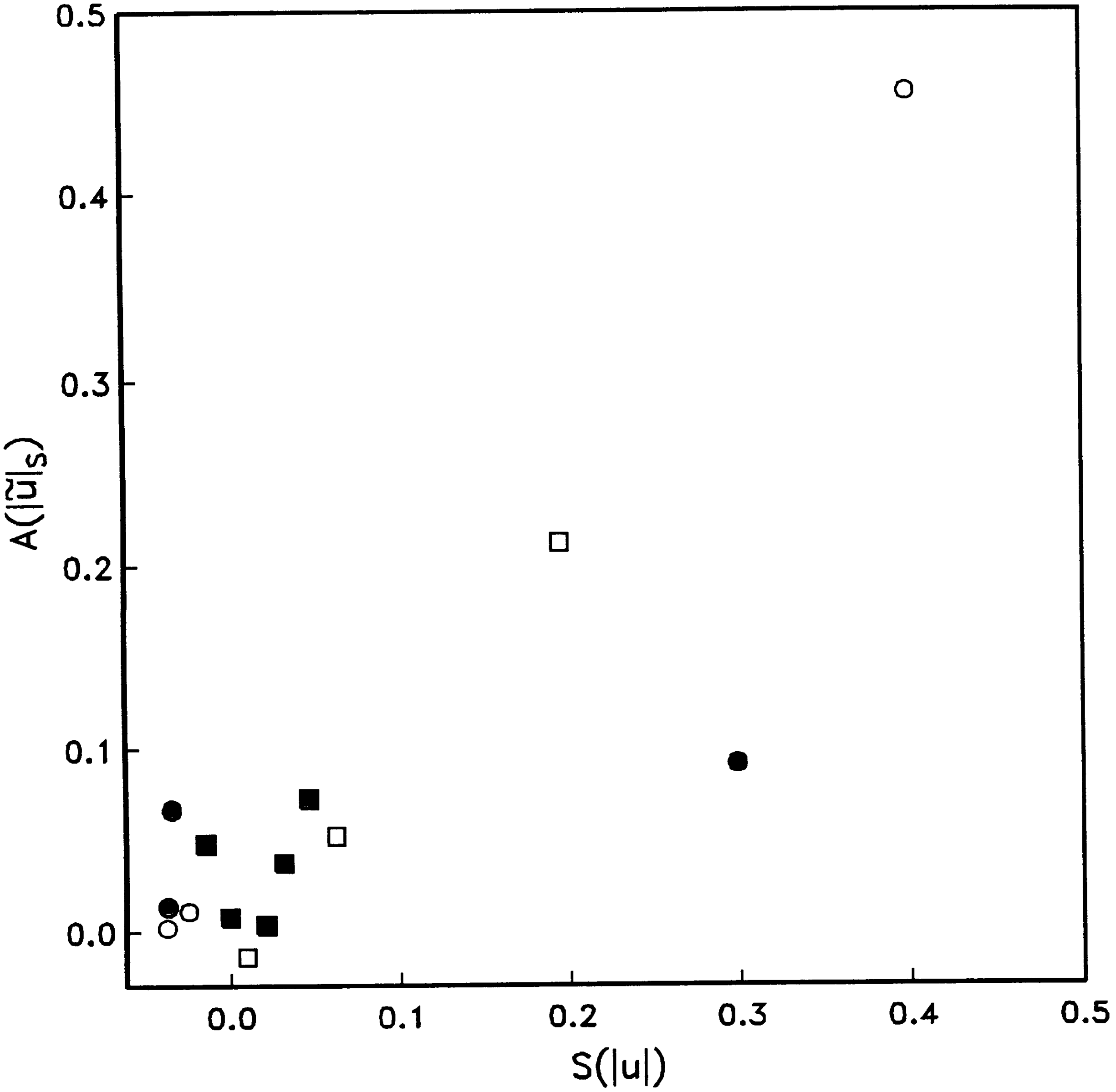

Figure 5.4

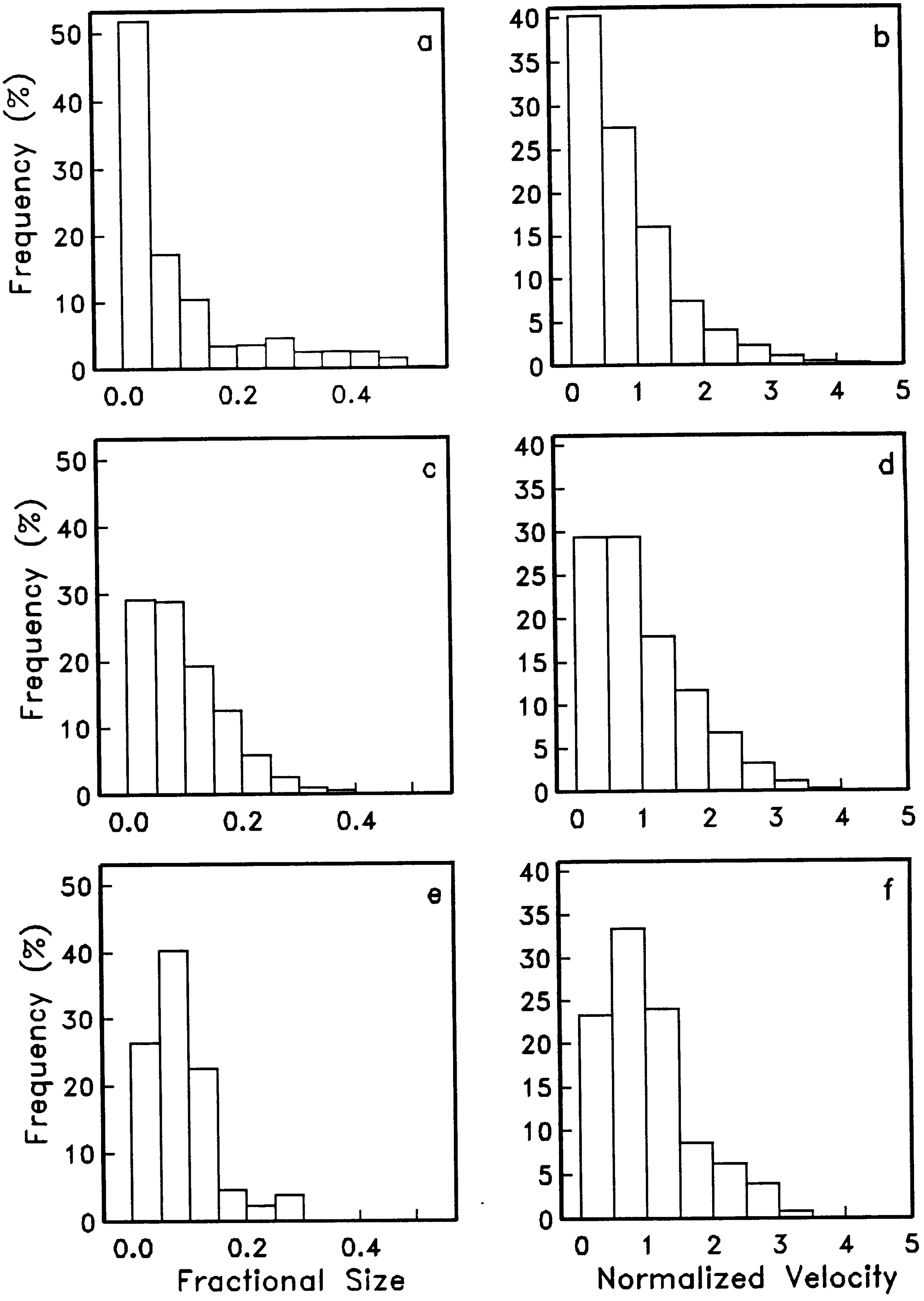
a
b
c
d
e
f
Frequency (%)
0
10
20
30
40
50
0
5
10
15
20
25
30
35
40
0.0
0.2
0.4
0
1
2
3
4
5
Fractional Size
Normalized Velocity

Figure 5.5

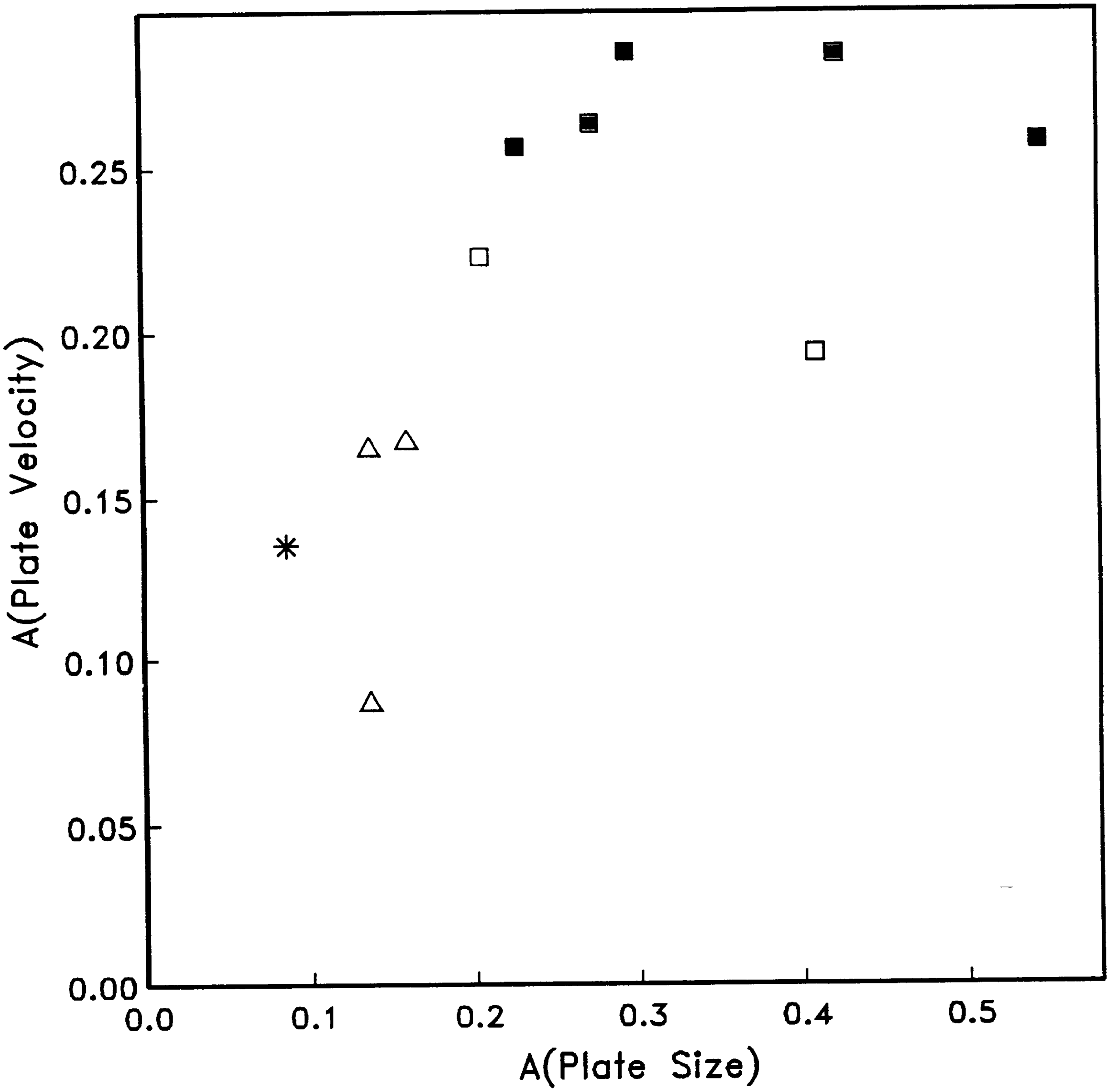
0.25
0.20
0.15
0.10
0.05
0.00
A(Plate Velocity)
0.0
0.1
0.2
0.3
0.4
0.5
A(Plate Size)

Figure 5.6

APPENDIX A

FIELD EQUATIONS OF MANTLE CONVECTION

The governing equations of mantle convection are derived from the principles of conservation of mass, momentum and energy. Since the mantle has a very high Prandtl number, inertial and Coriolis forces are negligible. With the Boussinesq approximation the fluid is effectively incompressible and the conservation equations take the form [*McKenzie et al.*, 1974]:

$$\nabla \cdot \mathbf{u} = 0, \tag{A.1}$$

$$\nabla \cdot \tau = -\nabla P + \mathbf{f}, \tag{A.2}$$

$$\frac{\partial T}{\partial t} + \mathbf{u} \cdot \nabla T = \kappa \nabla^2 T + \frac{H_M}{c_p}, \tag{A.3}$$

where $\mathbf{u}$ and τ and P are the flow velocity, deviatoric stress tensor, and non-hydrostatic pressure, respectively. T, t, κ, H_M and c_p are the temperature, time, thermal diffusivity, heating rate per unit mass and heat capacity, respectively. The body force, $\mathbf{f}$, consists of a thermal buoyancy term plus buoyancy forces, associated with density changes due to the deflection of a phase transition present, viz.

$$\mathbf{f} = \rho_r \alpha (T - T_r) g \hat{\mathbf{r}} + \Delta\rho g \hat{\mathbf{r}} \tag{A.4}$$

Consistent with the Boussinesq approximation phase-change effects enter only in the momentum equation; the latent heat term scales with dissipation number and is thus ignored [*Christensen and Yuen*, 1985]. The effect of latent heat release on the propensity for layering, however, is small [*Christensen and Yuen*, 1985].

We solve these equations in cylindrical coordinates (r, φ) subject to the boundary conditions:

$$T\big|_{r=a} = T_r, \quad T\big|_{r=b} = T_b, \quad u\big|_{r=a} = u\big|_{r=b} = \left.\frac{\partial (w/r)}{\partial r}\right|_{r=a} = \left.\frac{\partial (w/r)}{\partial r}\right|_{r=b} = 0 \tag{A.5}$$

and nondimensionalize using the following characteristic scales (primed variables are dimensionless):

$$r = ar'; \quad T = (T_b - T_r)T' + T_r; \quad t = \frac{a^2}{\kappa}t'; \quad \mathbf{u} = \frac{\kappa}{a}\mathbf{u}'; \quad p = \frac{\kappa\eta}{a^2}p'; \quad \tau = \frac{\kappa\eta}{a^2}\tau' \tag{A.6}$$

where, b and a are the inner and outer radii of the cylindrical shell, and $\mathbf{u} = (u, w)$ are the radial and angular components of velocity, respectively. Substituting (A.6) in (A.1)-(A.4) and subsequently dropping the primes, yields:

$$\nabla \cdot \mathbf{u} = 0, \tag{A.7}$$

$$\nabla \cdot \tau = -\nabla P + \zeta^{-3} Ra_B \left(T - \frac{Ra_P}{Ra_B}\Gamma\right)\hat{\mathbf{r}}, \tag{A.8}$$

$$\frac{DT}{Dt} = \nabla^2 T + \zeta^{-2}\frac{Ra_H}{Ra_B}, \tag{A.9}$$

where $\zeta = (a-b)/a$, $Ra_B = \rho_r g \alpha (a-b)^3 (T_b - T_r)/\kappa\eta$, $Ra_P = \Delta\rho g (a-b)^3/\kappa\eta$, and $Ra_H = Ra_B H_M (a-b)^2/\kappa c_p (T_b - T_r)$ are the Benard-Rayleigh number, the phase-boundary Rayleigh number, and the internal-heating Rayleigh number, respectively. Γ denotes the phase-progress function.

The narrow phase-loop width for the transformation of spinel-structured $(Mg,Fe)_2SiO_4$ (γ-olivine) into (Mg,Fe)O (magnesiowüstite) plus perovskite-structured $(Mg,Fe)SiO_3$ poses difficulties for an accurate numerical representation of the phase transition effects. An implementation used by many researchers, known as the "phase-function method" [*Richter*, 1973], is based on a phase progress function, $\Gamma(r,\varphi)$, that describes the relative fraction of the heavier phase at any point in the fluid. In order to model the narrow phase loop observed and phase boundary deformations at Rayleigh numbers appropriate for the earth, extremely high grid resolution is necessary. Even in two dimensions, however, the highest resolution experiments to date [*Solheim and Peltier*, 1994], have a phase-loop width at least a factor of six larger than the results from laboratory experiments indicate [*Ito and Takahashi*, 1989]. An alternative approach is to ignore the effects associated with the phase boundary deflection and to include only the buoyancy forces due to the phase change. This approach is known as the "effective thermal expansivity method" [*Christensen and Yuen*, 1985], or when the buoyancy effects are collapsed onto the phase boundary as the "sheet-mass anomaly method" [*Tackley et al.*, 1993]. The latter approach has the advantage of a zero-width phase loop. As long as the characteristic size of convective features is large compared to the phase boundary deflections, this approximation is sufficient to describe the effects of the phase change [*Tackley et al.*, 1994].

We have implemented both approaches for parameterizing the effects of a phase transition on the flow. Following *Richter* [1973] and *Christensen and Yuen* [1985], we express the phase function as

$$\Gamma(r,T)=\frac{1}{2}[1+\tanh\frac{r_t-r-\gamma(T-T_t)/\rho_r g}{d}], \tag{A.10}$$

where the contributions from the non-hydrostatic pressure on the phase function have been ignored. The phase transition occurs over a finite depth interval, d, with a Clapeyron slope, γ, at radius r_t and temperature T_t. Using the same characteristic scales as above (equation A.6), we obtain the dimensionless equation

$$\Gamma(r,T)=\frac{1}{2}[1+\tanh\frac{r_t-r-\gamma(T-T_t)}{d}], \tag{A.11}$$

where again the primes have been dropped. The Clapeyron slope is non-dimensionalized by $a\rho_r g/(T_b-T_r)$.

In the "sheet-mass anomaly method" [*Tackley et al.*, 1993] the effects associated with the phase boundary deflection are ignored and only buoyancy forces due to the phase change are incorporated. In dimensionless form the phase function takes the form

$$\Gamma(r)=-\gamma(T-T_t)\delta(r-r_t), \tag{A.12}$$

where $\delta(r)$ is the Dirac-delta function.

A comparison between the two methods described above can be found in Figure 3.18.

REFERENCES

Christensen, U. R., and D. A. Yuen, Layered convection induced by phase transitions, *J. Geophys. Res.*, *90*, 10, 1985.

Ito, E., and E. Takahashi, Postspinel transformations in the system Mg2SiO4-Fe2SiO4 and some geophysical implications, *J. Geophys. Res.*, *94*, 10637-10646, 1989.

McKenzie, D. P., J. M. Roberts, and N. O. Weiss, Convection in the earth's mantle: towards a numerical simulation, J. Fluid Mech., 63, 465-538, 1974.

Richter, F. M., Finite Amplitude Convection Through a Phase Boundary, *in International Symposium on Geophysical Theory and Computers, 9th. R. Astron. Soc., Geophys. JVol.*, 1973.

Solheim, L. P., and W. R. Peltier, Avalanche effects in phase transition modulated thermal convection: A model of earth's mantle, *J. Geophys. Res.*, *99*, 6997-7018, 1994.

Tackley, P. J., D. J. Stevenson, G. Glatzmaier, and G. Schubert, Effects of an endothermic phase transition at 670 km depth in a spherical model of convection in the Earth's mantle, *Nature*, *361*, 699-704, 1993.

Tackley, P. J., D. J. Stevenson, G. A. Glatzmaier, and G. Schubert, Effects of multiple phase transitions in a 3-D spherical model of convection in the Earth's mantle, *J. Geophys. Res.*, *99*, 15877-15901, 1994.

TABLES

Table A.1. Physical and geometrical parameters

Parameter	Value
Inner shell radius b	3.0×10^6 m
Outer shell radius a	6.0×10^6 m
Temperature contrast ΔT	1200 K
Reference density ρ_r	3.5×10^3 kg/m^3
Gravitational acceleration g	10 m/s^2
Thermal diffusivity κ	1.0×10^6 m^2/s
Thermal expansivity α	2.5×10^{-5} K^{-1}
Dynamic viscosity η	10^{22} Pa s
Density jump across phase boundary	3.68×10^2 kg/m^3

ACKNOWLEDGMENTS

Many people contributed to the success of this final product, thanking all of them in the proper fashion would require another roughly 200 pages and take another six-plus years. In light of the late hour, I will limit myself to the following paragraphs.

Hans Stolte rescued me from a career in the humanities by allowing me to join his already crowded Physik Leistungskurs. The math and physics he taught me became a solid foundation to build on. At Oregon, Gene Humphreys gave me the opportunity to work on interesting research problems in mantle tomography and encouraged me to apply to MIT. In addition, he showed me that it is exciting to go a step beyond modeling seismic heterogeneity and to try to understand the underlying dynamical processes. Gene became my early role model as a seismodynamicist. He also taught me some basketball moves. John Nabelek convinced me that the weather in Boston would not be all that bad. From those days in Eugene, I want to thank my fellow students Francois Saucier, Ken Dueker, and Chuck Wicks for interesting Friday afternoon group meetings.

Tom Jordan convinced me that MIT would be the best place to study geophysics. Not only is he a great salesman and motivator, he is also a first-rate scientist. From his quantitative approach to scientific problems, I profited tremendously. Now I carry a large bag of tricks. Tom provided an excellent environment for doing work and was very responsive to the needs of his students - be it another disk drive for Pierre or faster CPUs for my own work. Through numerous parties, Friday lunches, and late nights at the Third and Charles, Tom contributed much to the spirit of our research group. He also allowed me to change the focus of my thesis research at the end of my fourth year. Through several teaching assistantships, Tom gave me the opportunity to get my feet wet doing some teaching.

Brad Hager provided valuable guidance and advice to a normal-mode seismologist turned convection modeler. His insights, often prefaced with "shooting from the hip, ...", were usually right on target. Through a seminar and bag-lunch meetings he helped

broaden my knowledge as an earth scientist. Trying to convince Brad made me work harder.

In addition, I want to thank John Grotzinger, Rick O'Connell, and Dan Rothman for being on my thesis committee and for many useful comments and suggestions.

My understanding of convection modeling benefited from discussions with Gary Glatzmaier and Paul Tackley. Paul deserves special praise for promptly satisfying my many requests to dig up output files, and helpful discussions about phase changes. Scott King and Shijie Zhong provided me with their convection codes, preprints, and benchmark comparisons. Dave Yuen was another continuous source of pre-publication manuscripts. On the seismological side, Wei-jia Su, Bob Woodward, Adam Dziewonski, Guy Masters, and Steve Grand allowed me to use their tomographic models prior to publication. Bob and Wei-jia generously shared some software. Carolina Lithgow-Bertelloni made the results from her plate-tectonic reconstructions available.

First-year office mates Lind Gee and Greg Beroza made certain my MIT career started off on the right track. With daily afternoon questions, they prepared me well for my general exam. Greg and Eva Huala provided me with an opportunity to practice my German. Lind patiently answered numerous questions about seismology and computers. She also helped expand my cooking skills by sharing several of her favorite recipes. Mark Murray was the resident expert on inverse theory and vintage movies.

More recently, Mark Simons and Will Wilcock shared an office with me. Will together with Anne Sheehan and Cecily Wolfe were always ready to organize hiking and cross-country skiing trips - one of which ended in a road-side snow bank, another almost in a creek. Downhill skiing was organized by Gail Christenson, John Goff, or Kurt Feigl - unfortunately it often rained in the White Mountains. More recently, under the able planning of Jim Gaherty the weather has much improved. Jim and Jen Edwards provided local entertainment tips and hosted March Madness parties. Speaking of basketball, the company of fellow Postglacial Rebounders Nic Fiszman, Jim Gaherty, Ray LeBeau, Garrett Ito, Jeff Vroom, Rafi Katzman, Jess Adkins, and Pete Kaufman at DuPont and the Thirsty Ear was always fun. Pete Kaufman also occasionally provided take-your-life-inyour-hands taxi service in his turbo-charged vehicle. Sue Smrekar made the sculling class on the cold Charles river more enjoyable. America's pastime, baseball and its recreational cousin softball, were explained to me with great knowledge and patience by Mike Bergman and Steve Shapiro. The former is an expert cook and host of numerous Sunday brunches, the latter was a "perfect" AGU roommate. In addition, Steve was an excellent co-TA in 12.002. In addition, his efforts as ConMan czar were much appreciated. Maybe someday I will manage to spend a weekend with Steve and Karen Jo in Rangeley. Steve's father, Irwin, deserves special mention. Not only did he ask me an easy question after my first AGU talk (when I was about to faint), he also found time to attend my Real Seismology seminar and my thesis defense party.

The other members of Tom's group, who never got mad at me for being such a CPU-hog, deserve special recognition. Thank you Bob Cicerone, Nic Fiszman, Jim Gaherty, Pierre Ihmle, Mamoru Kato, and Steve Shapiro! Other contemporaries at MIT included Carolyn Ruppel, Randy Mackie, Sang-Mook Lee, Nori Namiki, Pat McGovern, Paolo Harabaglia, Lana Panasyuk, and John Olson.

Special thanks to Dave Krowitz and Linda Meinke for keeping the computers running smoothly, to Beverly Kozol-Tattlebaum for making access to Tom easy, and to Anita Killian, Katherine Ware, Marie Senat, Libby Kurten, Dan Burns, and Debbie Sykes for administrative support. Anita was also my housemate at 22 Warner St. Together with Janice Huxley, my long-time housemate at this address, we had many weekly dinners. Janice brought in Steve Jens who kept the washing machine running, always had great Celtics tickets, and helped me give Dave Boulifard a hard time.

Paula Waschbusch made this last year of graduate school, which is supposed to be the hardest, go by in a breeze. She did not get mad at me for my frantic last minute conference preparations and reminded me not to forget the observational constraints. Paula, you have been wonderful!

Last, but certainly not least, I want to thank my parents for encouraging me to pursue my career goals, even though that meant seeing me move to a different continent. Through care packages of Leberwurst, Stollen, and other goodies they supplied me with all the essentials at my home away from home. Thanks to my grandma for her delicious Christmas cookies and to my aunt and uncle for introducing me to the life in the U.S.

This research was supported by the National Science Foundation under grants EAR-90105419 and EAR-9316032.